JOHANNES GUTENBERG UNIVERSITÄT MAINZ

MAX-PLANCK-INSTITUT FÜR POLYMERFORSCHUNG

Max Planck Graduate Center mit der Johannes Gutenberg-Universität

Stimuli-responsive Polymeric Photocatalysts: Smart, Controllable, and Recyclable Materials for Photocatalytic Reactions

Dissertation

zur Erlangung des akademischen Grades
„Doktor der Naturwissenschaften (Dr. rer. nat)“
im Promotionsfach Chemie
des Fachbereichs Chemie, Pharmazie und Geowissenschaften
der Johannes Gutenberg-Universität Mainz

vorgelegt von

Rong Li

Mainz, December 2023

The thesis was carried out from July 2020 until December 2023 within the Department of Physical Chemistry of Polymers at the Max Planck Institute for Polymer Research, Mainz.

Dekan: Prof. Dr. Eva Rentschler

Gutachter 1:

Gutachter 2:

Date of oral examination:

Affidavit

I hereby declare that I wrote the dissertation submitted without any unauthorized external assistance and used only sources acknowledged in this work. All textual passages which are appropriate verbatim or paraphrased from published and unpublished texts, as well as all information obtained from oral sources, are duly indicated, and listed in accordance with bibliographical rules. In carrying out this research, I complied with the rules of standard scientific practice as formulated in the statutes of Johannes Gutenberg-University Mainz to ensure standard scientific practice.

……

(Rong Li)

Acknowledgment

Completing this PhD thesis has been a collaborative effort, and I'm grateful to many who played a crucial role. My sincere thanks to my supervisor, for her unwavering support and guidance throughout these three and a half years at the Max Planck Institute for Polymer Research. I also appreciate my group leader's scientific mentorship and the opportunities he provided in the world of photocatalysis. Thanks to technicians for their kind help with TEM measurements and helpful discussions. Many thanks to my colleague for the amazing cover figure he made for my publications. Special appreciation to my colleagues and friends from the institute for their support and camaraderie. I am grateful to my dissertation committee for their time and constructive comments. Financial support from the Max Planck Graduate Center (MPGC) and the opportunities it provided in workshops, seminars, and conferences are sincerely acknowledged. Lastly, heartfelt thanks to my parents, my partner, and friends for their unwavering support and understanding. This thesis is a testament to the collective effort that shaped my academic and personal growth.

Abstract

The emergence of visible-light photocatalysis has provided a sustainable and promising approach to enable chemical transformations under mild conditions. Inspired by natural photosynthesis, various visible-light photocatalytic materials have been developed and investigated, such as molecular photocatalysts and polymeric photocatalysts. These materials have facilitated a great number of chemical reactions, including aqueous pollutant degradation, water splitting, photodynamic therapy, and organic synthesis. However, rapid separation and recovery of photocatalytic materials with controllable photocatalytic reactivity remains challenging for novel designs of photocatalytic systems. This work aims to design smart photocatalytic materials with switchable reactivity and efficient recyclability, enabling sustainable applications as well as potential cancer therapy. Here, several stimuli-responsive polymeric photocatalytic systems have been developed to address specific application occasions.

Firstly, the realization of enhanced recyclability and efficiency of photocatalytic materials has been addressed. Here, the photoactive diphenyl benzothiadiazole (Ph_2BT) moiety has been modified with a polymerizable methacrylate functional group, resulting in a photocatalytic monomer. This photocatalytic monomer can be copolymerized with pH-responsive and classical monomers in a controlled manner, producing the final pH-responsive photocatalytic nanoparticles. These pH-responsive polymeric photocatalytic nanoparticles have been applied for photocatalytic reduction, oxidation, and redox reactions, where high conversion and selectivity was obtained. Furthermore, these particles can be easily recovered from the reaction medium by altering the pH value and reused for repeated cycles without losing their efficiency, demonstrating a stable, switchable, and recyclable photocatalytic system.

Secondly, the production of recoverable photocatalytic materials that can respond to an orthogonal magnetic stimulus has been investigated. Although pH alternation has offered an efficient approach to recycling photocatalytic materials, an external energy supply for centrifugation is still required for the recycling procedure. Therefore, we have implanted magnetic nanoparticles with photocatalytic polymer chains to produce

recoverable hybrid materials excluding the centrifugation process. Here, magnetic nanoparticles have been encapsulated into photocatalytic polymers that have facilitated photocatalytic oxidation reactions and can be easily reused for repeated cycles. This project highlighted the importance of creating straightforward photocatalytic platforms that can be easily recovered in response to an orthogonal stimulus to enable sustainable applications.

Lastly, the pH switchability of the aforementioned system has encouraged us to further explore pH-sensitive photocatalytic systems to facilitate tumor microenvironment targeted therapeutic applications. Solid tumors are ubiquitously featured by the dysregulated pH, where the extracellular microenvironment (pH_e 6.5-6.9) is slightly lower than normal tissues (pH 7.2-7.4). Therefore, we have designed a photocatalytic nanoparticle system that can specifically respond to this subtle pH change, allowing the targeted activation of photocatalytic moieties at the tumor site. Upon visible light irradiation, reactive oxygen species (ROS) are generated that can either directly kill the cancer cells or further activate prodrugs with ROS-sensitive linkers to generate active anti-cancer therapeutics. Here, these photocatalytic nanoparticles can respond to an extremely subtle pH change from 6.8-6.5, resulting in the disassembly of nanoparticles (D_h ~100 nm, pH 6.8) into free polymer chains or oligomers (D_h ~10 nm, 6.5). These free photocatalytic polymers or oligomers can further activate several prodrug model compounds with different ROS-sensitive linkages, demonstrating a versatile platform for targeted therapeutic applications.

Overall, this thesis intends to create smart, controllable, and recyclable stimuli-responsive photocatalytic systems that can be switched on/off and recycled in response to external stimuli.

Zusammenfassung

Das Aufkommen der Photokatalyse mit sichtbarem Licht hat einen nachhaltigen und vielversprechenden Ansatz für chemische Umwandlungen unter milden Bedingungen ermöglicht. In Anlehnung an die natürliche Photosynthese wurden verschiedene photokatalytische Materialien für sichtbares Licht entwickelt und untersucht, wie z. B. molekulare Photokatalysatoren und polymere Photokatalysatoren. Diese Materialien haben eine Vielzahl chemischer Reaktionen ermöglicht, darunter den Abbau wässriger Schadstoffe, Wasserspaltung, photodynamische Therapie und organische Synthese. Die schnelle Abtrennung und Rückgewinnung von photokatalytischen Materialien mit kontrollierbarer photokatalytischer Reaktivität stellen jedoch eine Herausforderung für neuartige Designs photokatalytischer Systeme dar. Diese Arbeit zielt darauf ab, intelligente photokatalytische Materialien mit schaltbarer Reaktivität und effizienter Rezyklierbarkeit zu entwickeln, die nachhaltige Anwendungen sowie eine potenzielle Krebstherapie ermöglichen. Hier wurden mehrere stimuli-responsive polymere photokatalytische Systeme entwickelt, um spezifische Anwendungsfälle zu adressieren.

Erstens wurde die Realisierung einer verbesserten Recyclingfähigkeit und Effizienz photokatalytischer Materialien in Angriff genommen. Hier wurde die photoaktive Diphenylbenzothiadiazol (Ph2BT)-Einheit mit einer polymerisierbaren Methacrylat-Funktionsgruppe modifiziert, was zu einem photokatalytischen Monomer führte. Dieses photokatalytische Monomer kann mit auf den pH-Wert ansprechenden und klassischen Monomeren kontrolliert copolymerisiert werden, wodurch die endgültigen auf den pH-Wert ansprechenden photokatalytischen Nanopartikel entstehen. Diese auf den pH-Wert reagierenden polymeren photokatalytischen Nanopartikel wurden für photokatalytische Reduktions-, Oxidations- und Redoxreaktionen eingesetzt, wobei eine hohe Umwandlung und Selektivität erzielt wurde. Darüber hinaus können diese Partikel durch Änderung des pH-Werts leicht aus dem Reaktionsmedium zurückgewonnen und für wiederholte Zyklen wiederverwendet werden, ohne ihre Effizienz zu verlieren, was ein stabiles, umschaltbares und recycelbares photokatalytisches System darstellt.

Zweitens wurde die Herstellung von rückgewinnbaren photokatalytischen Materialien untersucht, die auf einen orthogonalen magnetischen Stimulus reagieren können. Obwohl die pH-Änderung einen effizienten Ansatz für das Recycling photokatalytischer Materialien darstellt, ist für das Recyclingverfahren immer noch eine externe Energiezufuhr für die Zentrifugation erforderlich. Daher haben wir magnetische Nanopartikel in photokatalytische Polymerketten eingebaut, um wiederverwertbare Hybridmaterialien ohne Zentrifugationsprozess herzustellen. Hier wurden magnetische Nanopartikel in photokatalytische Polymere eingekapselt, die photokatalytische Oxidationsreaktionen erleichterten und leicht für wiederholte Zyklen wiederverwendet werden können. Dieses Projekt hat gezeigt, wie wichtig es ist, einfache photokatalytische Plattformen zu schaffen, die als Reaktion auf einen orthogonalen Stimulus leicht wiederverwendet werden können, um nachhaltige Anwendungen zu ermöglichen.

Schließlich hat uns die pH-Schaltbarkeit des oben erwähnten Systems ermutigt, pH-sensitive photokatalytische Systeme weiter zu erforschen, um gezielte therapeutische Anwendungen in der Mikroumgebung von Tumoren zu ermöglichen. Solide Tumore sind allgegenwärtig durch einen dysregulierten pH-Wert gekennzeichnet, bei dem die extrazelluläre Mikroumgebung (pHe 6,5-6,9) etwas niedriger ist als bei normalen Geweben (pH 7,2-7,4). Daher haben wir ein photokatalytisches Nanopartikelsystem entwickelt, das spezifisch auf diese geringe pH-Änderung reagieren kann und die gezielte Aktivierung photokatalytischer Komponenten an der Tumorstelle ermöglicht. Bei Bestrahlung mit sichtbarem Licht werden reaktive Sauerstoffspezies (ROS) erzeugt, die entweder die Krebszellen direkt abtöten oder „Prodrugs“ mit ROS-sensitiven Linkern aktivieren können, um aktive Anti-Krebs-Therapeutika zu erzeugen. Hier können diese photokatalytischen Nanopartikel auf eine äußerst subtile pH-Änderung von 6,8 bis 6,5 reagieren, was zur Zersetzung der Nanopartikel (D_h ~100 nm, pH 6,8) in freie Polymerketten oder Oligomere (D_h ~10 nm, 6,5) führt. Diese freien photokatalytischen Polymere oder Oligomere können mehrere Prodrug-Modellverbindungen mit unterschiedlichen ROS-sensitiven Bindungen aktivieren und stellen somit eine vielseitige Plattform für gezielte therapeutische Anwendungen dar.

Insgesamt zielt diese Arbeit darauf ab, intelligente, kontrollierbare und recycelbare, auf Stimuli reagierende photokatalytische Systeme zu schaffen, die als Reaktion auf externe Stimuli ein- und ausgeschaltet und recycelt werden können.

Table of Contents

1 Introduction 12
1.1 Motivation and Aim of this Work 12
1.2 State of Art 15
1.2.1 Photocatalysis 15
1.2.2 Molecular Photocatalysts 17
1.2.3 Conjugated Polymer Photocatalysts 21
1.2.4 Classical Polymer-based Photocatalysts 25
1.2.5 Stimuli-responsive Polymer Photocatalysts 30
1.2.6 Photodynamic Therapy (PDT) 52
1.3 Characterization Techniques 54
1.3.1 Gel Permeation Chromatography (GPC) 54
1.3.2 Ultraviolet-Visible (UV-Vis) Spectroscopy 54
1.3.3 Fourier Transform Infrared (FTIR) Spectroscopy 55
1.3.4 Gas Chromatography-Mass Spectroscopy (GCMS) 55
1.3.5 Nuclear Magnetic Resonance (NMR) Spectroscopy 56
1.3.6 Cyclic Voltammetry (CV) 58
1.3.7 Transmission Electron Microscopy 59
1.3.8 Electron Paramagnetic Resonance (EPR) 60
2 pH-triggered Recovery of Organic Polymer Photocatalytic Particles for the Production of High Value Compounds and Enhanced Recyclability 62
2.1 Motivation 62
2.2 Photocatalytic Reactions 74
2.2.1 Photocatalytic $K_2Cr_2O_7$ Reduction 74
2.2.2 Photocatalytic Sulfide Oxidation 77
2.2.3 2-Furoic Acid Oxidation 83
2.2.4 Photocatalytic Alkylation of 3-Methylindole and β-Nitrostyrene 86
2.3 Conclusion 89
2.4 Experimental Section 90
2.4.1 Materials 90
2.4.2 Characterization Methods 90
2.4.3 Synthesis of Photocatalytic Monomer 90
2.4.4 Synthesis of non-pH-responsive Polymer Photocatalytic Nanoparticles 92
2.4.5 Synthesis of pH-responsive Polymer Photocatalytic Nanoparticles 93

2.4.6 Photocatalytic $K_2Cr_2O_7$ Reduction 94
2.4.7 Photocatalytic Sulfide Oxidation 95
2.4.8 Photocatalytic Alkylation of 3-Methylindole and β-Nitrostyrene 95
3 Magnetically Recyclable Polymer Photocatalytic Materials for Sustainable Photocatalysis 97
3.1 Motivation 97
3.2 Synthesis and Characterization of Magnetic Photocatalytic Polymer Nanoparticles 99
3.3 Conclusion 119
3.4 Experimental section 120
3.4.1 Materials 120
3.4.2 Characterization Techniques 120
3.4.3 Preparation of Diblock Copolymer POEGA-*r*-EY-*b*-PCEA and Amphiphilic Diblock Copolymer POEGA-*r*-EY-*b*-PBzMA 120
3.4.4 Synthesis of Diblock Copolymer POEGA-*s*-EY-*b*-PDHMA Stabilized Fe_3O_4 Nanoparticles 122
3.4.5 Surface Modification of Fe Nanoparticles 122
3.4.6 Encapsulation of Fe Nanoparticles with Photocatalytic Amphiphilic Polymers 122
3.4.7 Surface Modification of Fe_3O_4 Nanoparticles 123
3.4.8 Encapsulation of Fe_3O_4 Nanoparticles with Photocatalytic Amphiphilic Polymers 123
3.4.9 Photocatalytic Reactions 123
4 Therapeutic Applications of Responsive Organic Photocatalytic Polymers, Enabling *in situ* Prodrug Activation 125
4.1 Motivation 125
4.2 Synthesis and Characterization of pH-responsive Photocatalytic Polymer Nanoparticles for Therapeutic Applications 128
4.3 Photocatalytic Reactions 136
4.4 Conclusion 145
4.5 Experimental Section 146
4.5.1 Materials 146
4.5.2 Characterization Techniques 146
4.5.3 Synthesis of Aminoethyl Methacrylate (AMA) 147

4.5.4 Synthesis of Photocatalytic Methacrylamide Monomer 2-(2-(2,4,5,7-tetrabromo-6-hydroxy-3-oxo-3H-xanthen-9-yl)benzamido)ethyl Methacrylamide (EYAEMA) 147
4.5.5 Synthesis of Photocatalytic Methacrylamide Monomer 2-(2-(2,4,5,7-tetrabromo-6-hydroxy-3-oxo-3H-xanthen-9-yl)benzamido)ethyl Methacrylate (EYAEMA) 148
4.5.6 Synthesis of pH-responsive Monomer 2-(Azepan-1-yl)ethyl Methacrylate (AEMA) 148
4.5.7 Synthesis of Thiol Ketal (TK) 149
4.5.8 Synthesis of Ethyl 3-(piperidin-1-yl)acrylate 149
4.5.9 Synthesis of 2-(2-Chloro-2-oxoacetoxy)ethyl Methacrylate 149
4.5.10 Synthesis of 4-Ethyl-3,14-dioxo-3,4,12,14-tetrahydro-1H-pyrano[3',4':6,7] indolizino [1,2-b]quinolin-4-yl (2-(methacryloyloxy)ethyl) Oxalate (pro-CPT) 150
4.5.11 Synthesis of 5-Fluoro-1-(4-(4,4,5,5-tetramethyl-1,3,2-dioxaborolan-2-yl)benzyl)pyrimidine-2,4(1H,3H)-dione 150
4.5.12 Preparation of pH-responsive Polymer PEG-*b*-PAEMA, Dual-responsive Polymers PEG-*b*-PAEMA-*b*-EYAEMA and PEG-*b*-PAEMA-*b*-EYHEMA 151
4.5.13 Preparation of pH-responsive Prodrug Polymer PEG-*b*-PAEMA-*s*-PCPT 153
4.5.14 Photocatalytic Activation of Prodrug Model Compounds Using EY Disodium Salt 153
4.5.15 Photocatalytic Activation of Prodrug Model Compounds Using Polymeric Photocatalyst 154
4.5.16 Cytotoxicity Assay 156
4.6 Additional Trail 157
4.6.1 Experimental section 169
5 Summary and Perspective 170
Appendix 173
A1. List of Figures 173
A2. List of Tables 181
A3. ^{1}H and ^{13}C NMR spectra 182
A4. Reference 191
A5. List of Publications 199

1 Introduction

1.1 Motivation and Aim of this Work

Energy as a basic need for human lives is crucial for our daily life and economic development. The continuous growth of global population and economic development has led to an exponentially increased demand for energy.[1] To date, fossil fuels still dominate the primary energy supplies worldwide, which not only leads to the fast depletion of the limited reserves of fossil resources but also accounts for environmental problems (i.e. climate change). Therefore, switching from fossil fuels to renewable energy sources to fulfill the great energy demand is a key challenge.[2] Among renewable energy sources, sunlight is regarded as an abundant and sustainable energy resource that can be converted into electric and chemical energies.[1,3,4] More strikingly, solar power is enormous, more energy is delivered to the earth by the sun in 1 h than the annual energy consumption of the whole planet.[3] Inspired by nature's photosynthesis, photocatalysis has appeared as a promising solution to address the challenges above of fossil fuels by converting and storing renewable light energy as chemical energy in the form of solar fuels or high-value chemicals.

The term “photocatalysis” describes reactions taking place in the presence of a catalyst, so-called photocatalyst, and light. Extensive investigations in photocatalysts have been carried out in the last five decades. The scope of photocatalytic materials is broad including inorganic semiconductors, conjugated polymer photocatalysts, and molecular photocatalysts. Among the developed photocatalytic materials, homogeneous molecular photocatalysts (i.e. transition metal complexes and organic dyes) are of particular interest due to their high efficiency and tunability. However, these traits of molecular photocatalysts are at the cost of their stability and recyclability. To address these issues, classical polymer photocatalysts have emerged recently as a highly tunable and stable alternative that combines the merits of homogeneous and heterogeneous photocatalysts.[5] However, novel designs of photocatalysts with controllable photocatalytic reactivity and/or rapid and simple recovery are still not yet maximized.

This thesis aims to design smart photocatalytic materials with switchable reactivity and efficient recyclability, allowing sustainable photocatalysis and further expanding the application to potential cancer therapy. Here, two stimuli-responsive polymeric photocatalytic systems have been developed to achieve the rapid separation and recovery of the photocatalytic materials in response to external stimuli. Further to enhance the recyclability of the materials, an ultra pH-sensitive photocatalyst has been designed to allow a potential tumor-targeted therapy via pH-modulated photocatalytic reactivity. This thesis has been constructed based on the following principles:

1. pH-triggered enhancement of efficiency and recovery: Rapid separation and recovery of photocatalytic materials is critical for sustainable applications, which minimizes the cost of manufacturing and waste treatment. Taking lessons from pH-modulated conformational changes in nature, the pH value can switch the wettability of pH-responsive polymeric systems containing tertiary amine groups through a protonation-deprotonation process. Besides, ion-ion interactions are regarded as the strongest non-covalent bond in chemistry, which can accelerate the diffusion of the reactant towards the oppositely charged photocatalyst. In Chapter 2, the synthesis of pH-responsive photocatalytic nanoparticles and their applications in various photocatalytic reactions have been investigated and meanwhile, the enhanced photocatalytic efficiency and recyclability have been demonstrated.

2. Magnet-triggered recovery: Although pH-responsive photocatalytic nanoparticles have been developed to enhance the recyclability of the photocatalytic materials, there is still an external energy input (electricity for centrifugation) required to facilitate efficient recycling. Therefore, it is desired to design systems that can be directly separated from the reaction medium by an external stimulus, such as magnetism, where no additional energy is needed for the recovery process. This recycling process via a magnetic separation technique delivers a more sustainable approach. In Chapter 3, coating magnetic nanoparticles with photocatalytic polymer chains has been achieved and the application as well as

recycling of these hybrid materials for photocatalytic hydroxylation reactions has been investigated.

3. Tumor-specific photocatalyst: Further to improve the sustainability of photocatalytic materials, we are also interested in therapeutic applications of photocatalytic materials. An intrinsic subtle pH difference is exhibited between healthy tissues and the cancer microenvironment. The creation of amphiphilic block copolymers with switchable hydrophobicity offers the possibility of self-assembly and disassembly, which could modulate the activation of the photocatalytic units by controlling their accessibility. Polymers containing tertiary amino groups can be reversibly protonated and deprotonated in response to the pH value of the aqueous solution, which can be tuned to overlap with the subtle pH difference between tumor and healthy tissue. Photocatalysts are capable of generating reactive oxygen species (ROS) that can subsequently cleave the ROS-sensitive prodrugs, resulting in active therapeutics via a cascade reaction. In Chapter 4, the targeted prodrug activation using pH-responsive photocatalytic polymer systems has been demonstrated.

This thesis has been constructed based on these three projects supplemented with an introductory theory, a briefly summarized principles of applied characterization techniques, together with a summary and perspective at the end.

1.2 State of Art

1.2.1 Photocatalysis

Global energy consumption has skyrocketed in the last decades due to thriving urbanization and industrialization, where fossil fuels (coal, oil, and natural gas) account for approximately 85% of primary energy supplies.[6] Serious concerns for the future scarcity of fossil fuels have boosted intensive research in finding alternative energy sources to address the limited reserves of fossil fuels and rising environmental concerns. As early as 1972, two pioneers Fujishima and Honda[7] reported the electrochemical photolysis of water to produce oxygen and hydrogen for the first time, opening a new era of utilizing abundant and sustainable water and sunlight to generate hydrogen as a clean energy source. In addition to the production of clean energy sources (e.g., H_2, CH_4, CH_3OH, etc.), light-mediated chemical reactions such as aqueous pollutant remediation, CO_2 reduction, and chemical redox reactions have also been targeted as more environmentally friendly alternatives to thermal-driven transformations.

Taking lessons from natural photosynthesis, the emergence of photocatalysis has facilitated the conversion of eco-friendly solar energy to high value chemicals or electric energy. The term “photocatalysis” first appeared in some scientific communications in the early 1910s[8] and it has been generally used in chemical literature to describe two different processes (photocatalytic and photosynthetic processes), despite these processes differ in their thermodynamics (see Figure 1).[9,10] To clarify the concept in a more strict definition, photosynthesis describes the process by which a material utilizes light energy to drive thermodynamically forbidden reactions, where the Gibbs free energy change is positive ($\Delta G > 0$). In this case, the material may be considered as photocatalyst only if the input light energy is converted into chemical energy and accumulated in the product (e.g., materials for water splitting and CO_2 reduction). Conversely, materials can also use light to promote thermodynamically favourable chemical conversions ($\Delta G < 0$) without storing the photo-chemical energy. These materials only use the input light energy to overcome the activation barrier of the chemical transformations but do not change the thermodynamics, which fits the strict definition of photocatalyst.

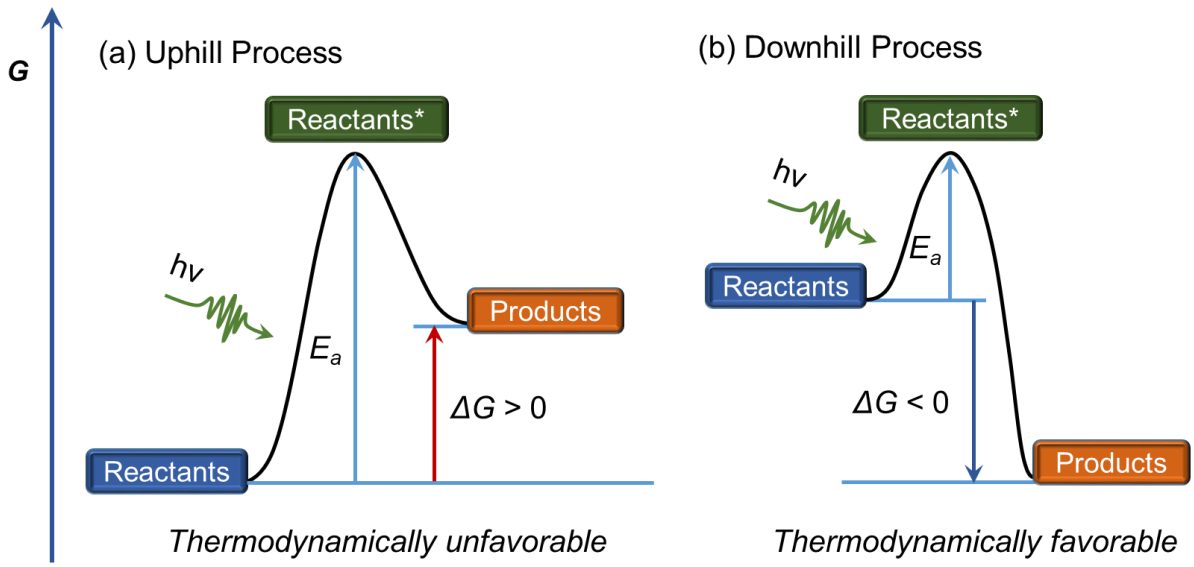

Figure 1. Thermodynamics of uphill and downhill photocatalysis: (a) the uphill process; (b) the downhill process. Adapted from Ref. [10] with permission.

Among all types of photocatalysts, semiconductors are regarded as the most representative and intensively investigated photoactive materials. Although not all photocatalysts are semiconductors, the general mechanisms of photocatalytic processes can be described and translated based on semiconducting materials. Three elemental steps are generally involved in a typical photocatalytic process in the presence of a semiconductor (Figure 2). Initially, upon illumination, photons can promote electrons from the fully occupied valence band (VB) to the unoccupied conduction band (CB) of the semiconductor, leading to the separation of electrons and holes. Besides, a significant portion of photons can also be reflected (as high as 30-40% by silicon films) and/or scattered by semiconducting materials, especially common in white powers, where no energy gain or loss occurs. After the bandgap excitation, charge separation occurs followed by the migration of these charge carriers to the surface. Eventually, these charge carriers can further interact with the absorbed donor and/or acceptor molecules. It is worth noting that the separation of electrons and holes is a short-lived state, where they can either recombine radiatively (photoluminescence) or non-radiatively to release energy.

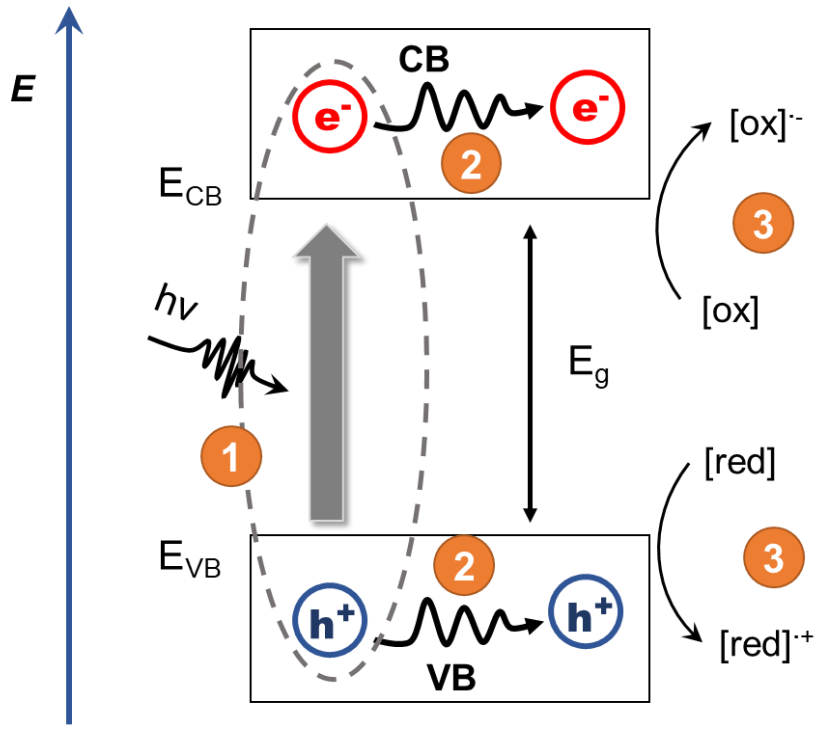

Figure 2. A typical photocatalytic process of semiconducting photocatalytic materials. Three steps are involved in the photocatalytic process: (1) light absorption and excitation; (2) charge separation and migration; (3) electron transfer between the semiconductors.

Bearing the general mechanism of photocatalysis in mind, in the following sub-chapters the existing implementations of photocatalysis are discussed more in detail based on the types of photocatalytic materials involved. Since the thesis is based on visible-light organic photocatalysts, traditional semiconducting photocatalysts[11,12] such as TiO_2, ZnO, NiO, WO_3, CdS, etc. are out of the scope of the state of art. Here, four categories of photocatalytic materials, including molecular photocatalysts; conjugated polymer photocatalysts; classical polymer-based photocatalysts; and stimuli-responsive photocatalysts, as well as the therapeutic application of photocatalysts known as photodynamic therapy will be covered.

1.2.2 Molecular Photocatalysts

As the simplest construction of photocatalysts, two molecular systems based on transition metal complexes or organic dyes have emerged as many of the most

commonly employed visible light photocatalysts for homogeneous photocatalysis and their photochemistry has been well investigated (Figure 3).

Transition metal complex photocatalysts are designed by coordinating Lewis basic ligands to Lewis acidic central metal. The reactivity of these complexes is highly tunable by selectively varying the structure or activity of ligands.[13] As a general rule, complexes are more strongly reducing when electron-donating substituents are presented on the ligands, conversely, electron-withdrawing groups make complexes stronger oxidants.[14] Polypyridyl complexes of ruthenium and iridium[15,16] are investigated most intensively among their analogues, because of their exceptional ability to generate stable and long-lived photoexcited states (e.g. 1100 ns for tris(2,2′-bipyridine) ruthenium(II) ($Ru(bpy)_3^{2+}$)) upon the illumination of visible light. Over four decades, these materials have been employed to accomplish water splitting and CO_2 reduction to methane, as well as act as components of organic light-emitting diodes or photosensitisers in photodynamic therapy. Until the last decade, their potential in catalyzing organic synthesis has been further explored, where chemical transformations can be facilitated under exceptionally mild conditions. To give an overview of the photochemistry of transition metal complexes, the prototypical photoredox catalyst $Ru(bpy)_3^{2+}$ is described as an example (Figure 3a). Upon irradiating with visible light, an electron is excited from the metal-centered t_{2g} orbital to a ligand-centered π^* orbital through a metal-to-ligand charge transfer (MLCT). Subsequently, an electron in singlet excited state transfers to the long-lived triplet excited state through an intersystem crossing (ISC), which then engages with single-electron transfer (SET) events with organic substrates. Remarkably, these photoexcited species can act as both strong oxidizing agents (accepting an electron to t_{2g} orbital) and reducing agents (expelling an electron from π^* orbital) simultaneously (Figure 3a). In particular, chemical transformations such as amine α-functionalization, C-C bond formations, asymmetric aldehyde alkylations, and dehalogenations in the presence of complex photocatalysts have been highlighted in the literature.[15,16]

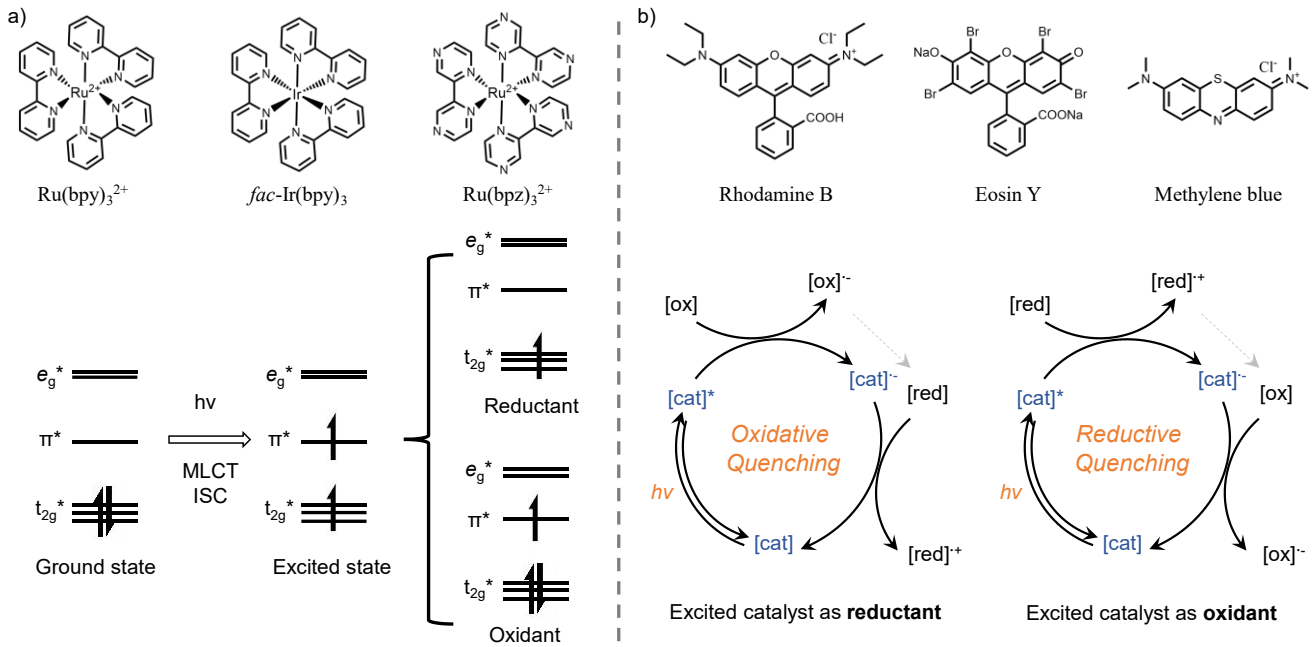

Figure 3. Selection of important molecular photocatalysts and their simplified functional principles: (a) metal complex. (b) organic dyes.

Although transition metal complexes exhibit extraordinary performance towards various chemical transformations, their high cost and potential toxicity lead to a shift to cheaper, metal-free, easily accessible, and tunable organic dyes. These molecules are generally constructed with heterocycles with planar extended π-systems, typified by acridiniums, diaryl ketones, xanthenes, thiazines, and cyanoarenes.[17] The application of organic dyes in organic synthesis has progressed rapidly, especially in the formation of C-C bonds, C-X bonds, thiol-ene reactions, etc. The photophysical process (Figure 3b) is initiated upon irradiating light to excite the organic dyes. Similar to transition metal complexes, an electron is promoted to an excited state from the ground singlet state (S_0) of the organocatalyst, and within picoseconds, the electron is relaxed to the first singlet excited state (S_1). Through ISC the S_1 can proceed to the triplet state (T_1), resulting in a significantly extended lifetime from nanosecond to millisecond regime. Both S_1 and T_1 can participate in organic reactions through either energy transfer (EnT) or SET mechanism. Reactive species can be generated through an energy transfer process, for instance, triplet oxygen molecules can be sensitized to singlet oxygen, and these activated species can further participate in chemical transformations. This

mechanism differs from SET photoredox process, where substrates are directly promoted to their excited state instead of undergoing an electron transfer redox process. Among organic dyes, eosin Y, Rose Bengal, rhodamine B, and methylene blue are readily available and even outperform transition metal complexes on some occasions, therefore they have been widely employed in chemical transformations.

As an example of a molecular photocatalyst, the photochemistry of eosin Y[18–21] has been well-established, and eosin Y exhibits outstanding performance for chemical transformations. Eosin Y absorbs green light with a characteristic peak at 539 nm and a molar extinction coefficient Ɛ = 60803 $M^{-1}cm^{-1}$. Once excited by visible light, eosin Y undergoes a rapid IC from the singlet state (^{1}EY*) to the triplet state (^{3}EY*). This excited state of eosin Y (^{3}EY*) is both a stronger reductant and a stronger oxidant compared to its ground state analogue (EY), which has been demonstrated by redox potentials of the excited state. These redox potentials are derived based on the standard redox potentials of the ground state, which are determined by cyclic voltammetry, and the triplet excited state energy. Typical reduction reactions achieved by eosin Y are reduction of phenacyl sulfonium salts,[22] reduction of nitrobenzene,[23] and desulfonylation.[24] Additionally, oxidation reactions such as oxidative iminium ion formation,[25] bromination,[26] hydroxylation,[27] cyclization of thioamides,[28] desulfurization,[29] aldoximes and primary amides into nitriles,[30] and oxidation of silyl enol ethers[31] have been catalyzed by eosin Y. Moreover, eosin Y can also facilitate redox reactions e.g. arylation reaction,[32] trifluoromethylation,[33] and enantioselective α-alkylation of aldehydes in combination with organocatalyst.[34,35] In addition to redox (electron transfer) reactions, the photoexcited ^{3}EY* state can also undergo an energy transfer process[31] to return back to its ground state. Therefore, the easy accessibility, simple functionalization, biocompatibility, strong absorption of visible light and suitable redox potential values make eosin Y an attractive photocatalyst for chemical reactions, therefore it was selected as one of the photocatalysts employed in this thesis.

To date, molecular photocatalysts have shown outstanding performance in catalyzing a broad range of reactions in a homogenous manner, with excellent activity, high selectivity, and well-defined active sites. However, these materials also suffer from

several inherent drawbacks in terms of difficulties in separation and recycling from the reaction mixture, which increases the production cost and pollution. Moreover, homogeneous systems are often less stable and degrade over time because of photobleaching or solvolysis. Furthermore, these small molecules are only soluble in a limited range of solvents, which can limit their applications. Therefore, the formation of a heterogeneous photocatalyst by either incorporating the photoactive species into a conjugated network or immobilizing homogeneous small molecular photocatalysts to a secondary species is of great interest that can in principle facilitate their recovery and recycling as introduced following.

1.2.3 Conjugated Polymer Photocatalysts

Conjugated polymer photocatalysts, featured by their designable structures, high chemical stability, low cost for synthesis, and readily recyclability, have been targeted as tunable and reusable alternatives to molecular photocatalysts. More in detail, these materials consist of earth-abundant elements, and monomers can be modified with certain properties, enabling the translation of functions to polymer properties such as solubility and morphology. By altering the monomer formulations or modifying monomers, their optical properties (absorbance in visible light regime) as well as redox potential can be tuned. Additionally, they are chemically stable against photobleaching outperforming molecular photocatalysts. Moreover, the fully conjugated polymer backbone leads to unique properties in charge carrier separation and transport processes where the recombination process is prevented. All these factors make conjugated polymer photocatalysts an extremely attractive class of photoactive materials. Therefore, conjugated polymer photocatalysts have been widely applied in various photocatalytic reactions, including water pollutant degradation,[36–38] antibacterial treatment,[39–42] photodynamic therapy,[43–45] hydrogen evolution,[46–48] carbon dioxide reduction,[49–51] and organic transformations.[52–54]

In this subchapter, the basics of three representative conjugated polymer photocatalysts: graphitic carbon nitrides (g-C_3N_4), conjugated porous polymers (CPPs), and covalent organic framework (COFs) are discussed briefly.

Graphitic Carbon Nitrides (g-C_3N_4)

g-C_3N_4 is a class of 2-dimensional frameworks constructed by carbon and nitrogen elements with conjugated heptazine rings (Figure 4a). Since first reported in 2009 by Wang and Antonietti[55] for water splitting, g-C_3N_4-based photocatalysts have been intensively explored because of five main outstanding features:

(1) Semiconducting materials consist of carbon and nitrogen light elements with suitable valence band maxima (VBM) and conduction band minima (CBM), allowing redox reactions.

(2) The band gap is approximately 2.7 eV enabling absorption of blue light, thereby facilitating visible light photocatalysis.

(3) g-C_3N_4 is extremely stable against thermal (up to 600 °C) and chemical changes, because of the strong covalent carbon nitrogen bonds. Besides, these materials can be produced at a relatively low cost (~ a few euros per kg, considering the cost of starting materials and efforts for the synthesis) and easily separated from the reaction medium, therefore they can be reused multiple times increasing the sustainability.

(4) g-C_3N_4 is more bio-compatible compared to transition metal complexes.

(5) g-C_3N_4 shows tolerance against most chemical functionalities, thus protecting functional groups before chemical synthesis is not required.

Apart from the aforementioned conjugated structure, several different materials are also considered as “carbon nitride” such as mesoporous graphitic carbon nitride (mpg-CN) with a high surface area and ionic structured potassium poly(heptazine imide) (K-PHI). The most common way to prepare g-C_3N_4 is through the thermolysis of melamine or other nitrogen-rich precursors at 550-600 °C, except for K-PHI prepared by heating the mixture of 5-amino tetrazole or triazole in LiCl/KCl eutectics to 550-600 °C.

Similar to traditional semiconducting materials, g-C_3N_4 can be activated by light with photon energy equal to or greater than 2.7 eV, where an electron is promoted from VB to the CB, leaving a hole in the VB (Figure 4b). When applying these materials to chemical transformations, the redox potential of the materials is extremely crucial

to evaluate the feasibility of the reactions. In general, the VBM of g-C_3N_4 is located at around + 1.6 eV and CBM at – 1.1 eV vs. normal hydrogen electrode (NHE), respectively. Notably, the redox potential allows g-C_3N_4 to drive many photocatalytic processes such as photocatalytic hydrogen evolution, CO_2 reduction, and pollutant degradation (Figure 4c).[56]

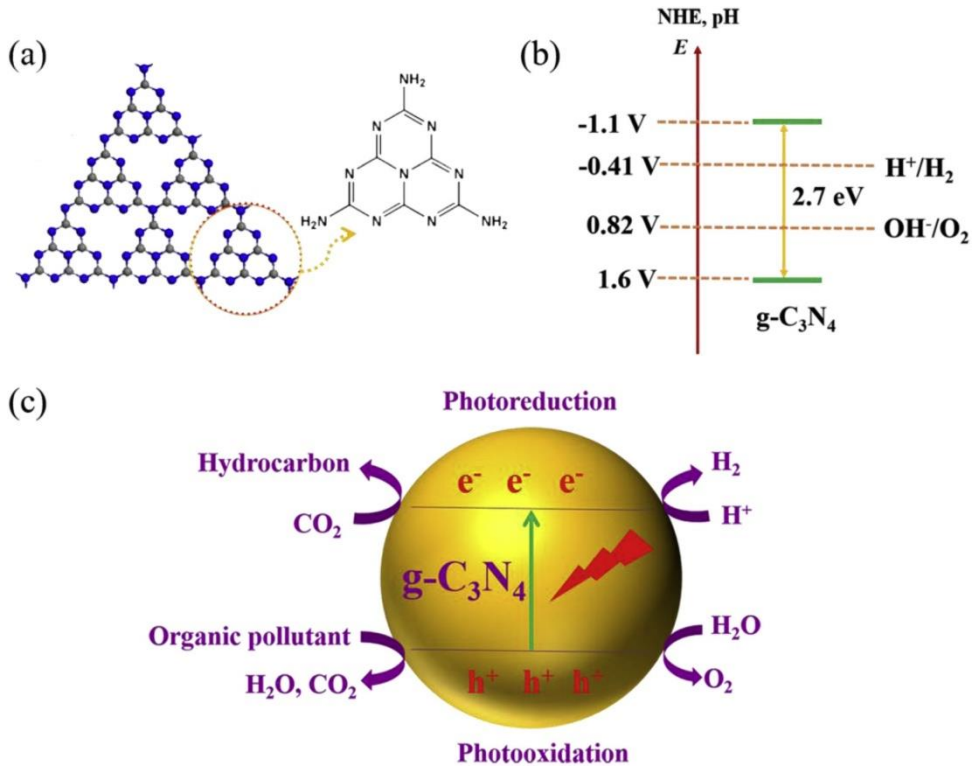

Figure 4. (a) Tri-s-triazine-based structure of g-C_3N_4. Color scheme: gray balls - C atoms, blue ones - N atoms. (b) Band structure of g-C_3N_4. (c) Photocatalysis of g-C_3N_4. Reproduced from Ref. [56] with permission.

Conjugated Porous Polymers (CPPs)

Conjugated porous polymers (CPPs) are comprised of π-conjugated three-dimensional rigid microporous polymer networks, which merge the advantages of porous materials and conjugated polymers. The three-dimensional nature of CPPs offers opportunities to design the morphologies and surface properties, as well as additional traits such as high stability, recyclability, and selectivity. CPPs can be synthesized with a great number of approaches, such as metal-assisted cross-coupling reactions (e.g., Suzuki-, Yamamoto-, Heck-, Sonogashira-, Negishi-, Glaser-, and oxidative polymerization),

acid- and base-catalyzed polymerization, and thermo-driven polymerization. Generally, CPPs consist of sp^2 hybridized polymer backbones with p_z orbitals perpendicular to the polymer chain, generating π-delocalization thereby an energy band gap simplified as the gap between HOMO (the highest occupied molecular orbital)–LUMO (lowest unoccupied molecular orbital). With light irradiation, an electron is promoted from the HOMO to the LUMO generating an active electron-hole pair. Subsequently, they migrate to the surface of the catalyst, leading to redox reactions at the surface. Since first reported as visible-light photocatalyst in 2013,[57] CPPs have been applied to drive a great number of photoredox reactions such as dehalogenation of haloketones, oxidative coupling of amines, water splitting, reduction of 4-nitrophenol, [2+2] cycloaddition, and enantioselective α-alkylation.[58]

Covalent Organic Framework (COFs)

COFs are newly designed crystalline porous organic polymers with low densities, where organic molecular building blocks are connected by covalent bonds through reticular chemistry. COFs are entirely composed of earth-rich light elements such as B, C, N, and O and have been widely employed in heterogeneous catalysis, gas storage and separation, energy storage, and optoelectronic devices.[59,60] This design principle offers the opportunity to apply versatile COFs as heterogeneous photocatalysts to promote chemical reactions.[61] Semiconducting COFs share the common features of other conjugated polymer photocatalysts as aforementioned. Moreover, structures of COFs can be engineered to achieve fast electron-hole separation and transportation, suppressing electron-hole recombination. Especially, the high crystallinity and porous structure can accelerate charge migration through pre-organized pathways to the surface and avoid the charge trapping by defects, commonly presented in amorphous materials. Besides, the extended π-conjugation in-plane along with the well-defined interlayer π-stacking enables the enhanced light-absorbing capacity as well as high charge carrier mobility.[60,62] A great number of photocatalytic applications have been facilitated by COFs, including photocatalytic hydrogen and oxygen evolution, CO_2 reduction, pollutant degradation, and selective organic reactions.

Despite conjugated polymer photocatalysts possessing fascinating features such as designable structures, high chemical stability, low cost for synthesis, and readily recyclability, their structural construction has limited their application to heterogeneous photocatalysis. Without post-functionalization or treatment, conjugated polymer photocatalysts are generally hydrophobic because of the hydrophobicity of monomer building blocks, which restricts their water-compatibility. Therefore, considerable efforts have been invested in a more tunable alternative where photocatalytic moieties are in a pseudo-homogeneous state with a broad spectrum of compatible solvents.

1.2.4 Classical Polymer-based Photocatalysts

Compared to conjugated polymer photocatalysts, the emergence of classical polymer-based photocatalysts that combine classical polymers with photocatalytic monomers has offered opportunities to enable both efficient homogeneous and heterogeneous photocatalysis. Additionally, it also provides the possibility to overcome the trade-off between the solvation of photocatalytic species (homogeneous photocatalysis) and recyclability (generally heterogeneous photocatalysis). Here, photocatalytic moieties are often solvated and easily accessible resulting from careful selection of the polymer matrix, facilitating efficient photocatalysis. Molecular photocatalysts can be either attached to the polymer support or modified with polymerizable functional groups (e.g., vinyl, acrylate, methacrylate, methacrylamide, etc.) and subsequently copolymerized during the synthesis of the polymer materials. A great number of polymer constructions, such as linear polymers, polymer particles, and cross-linked polymers have been designed as polymeric support, enabling the recyclability of photocatalytic materials. Here in this subchapter, various approaches of attaching small molecule photocatalysts to the most commonly studied polymer supports will be discussed briefly and corresponding photocatalyzed reactions will also be touched slightly.

Linear Polymers

As the simplest form of polymers, linear polymers can either be dissolved to create a homogeneous solution or they can be dispersed in the solvent resulting in a heterogeneous system. Depending on the targeted application condition, linear polymers can also be designed with relative complexity by copolymerizing multiple

blocks. Here, some typical examples of linear polymers as photocatalytic molecule support have been demonstrated.

As early as 2011, the copolymerization of molecular photocatalysts to form linear polymer by free radical polymerization was pioneered by Hisaeda and coworkers,[63] where styrene, a B_{12} derivative, and a Ru complex were utilized as monomers (Figure 5). The resultant linear polymer has been applied for the photocatalytic dehalogenation of phenethyl bromide, which shows a better performance compared with free photocatalyst and B_{12} due to colocalization of the reactive species through copolymerization. Therefore, copolymerization is a more economically efficient approach to reducing the loading of photocatalytic units.

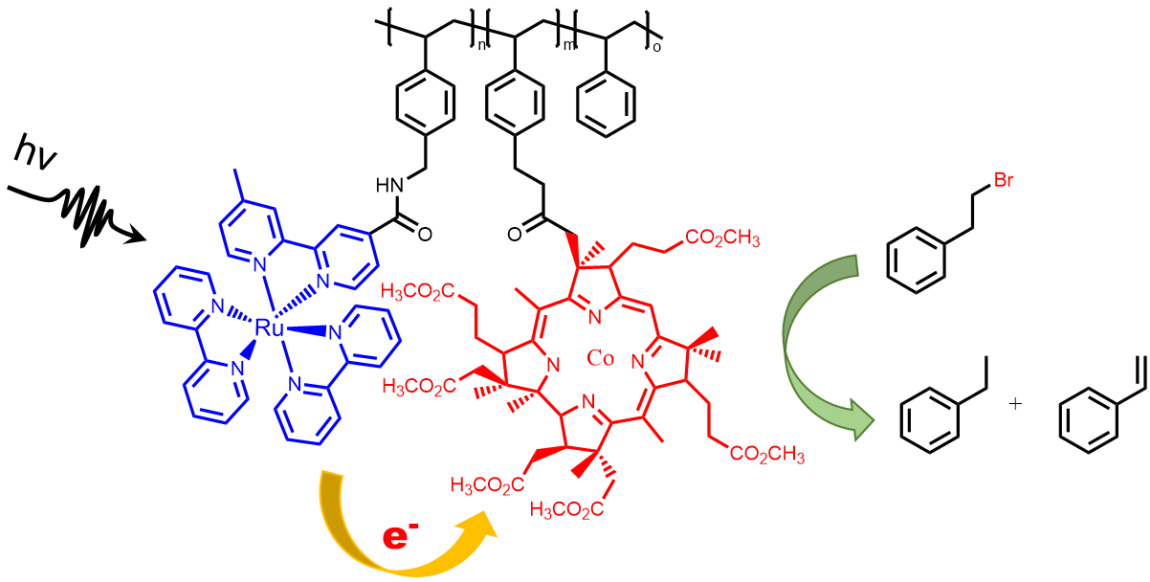

Figure 5. Chemical structure of the statistical copolymer of styrene, styrene-based B_{12}, and Ru complex photocatalyst. The photocatalytic reaction is facilitated by the polymer photocatalyst. Reproduced from Ref. [63] with permission.

In addition to free radical polymerization, linear polymer photocatalysts have also been prepared by ring-opening polymerizations. Thomas *et al.*[64] synthesized polylactides (PLA) bearing a unit of Ru-containing complex by ring-opening polymerization to form a cell-penetrating photosensitizer for photodynamic therapy. Here, the Ru complex possesses a hydroxyl group on the ligand that can react with $Zn(N(SiMe_3)_2)_2$ producing an active zinc alkoxide. Subsequently, this zinc alkoxide further initiated and controlled

the LA polymerization. This linear photosensitizer conjugate outperformed the nonfunctionalized analogue in cellular absorption, thereafter enhanced photodynamic therapy.

Fustin *et al*.[65] investigated the optimization of the synthetic structural design of polymeric photosensitizer with a minimal amount of molecular photosensitizer loading. Here, the BODIPY photocatalytic unit has been incorporated into amphiphilic diblock copolymers either at the hydrophobic end or in between the hydrophilic and hydrophobic segments by azide-alkyne click chemistry. These amphiphilic linear polymers bearing a BODIPY moiety readily self-assembled in aqueous conditions with their non-photoactive analogue to form vesicles around 90 nm in diameter, respectively. Despite similar polymer architectures have been formed independent of the location of the photocatalytic unit, significantly greater phototoxicity at low light levels has been achieved by incorporating photoactive molecules at the junction compared to at the hydrophobic core.

Polymer Particles

Polymer particles are of great interest, acting as supporting materials because of their easy and cheap production using multiple synthetic routes. A broad range of functionalities can be implanted by surface modification. Attaching photocatalytic units onto or into the polymer particles is particularly attractive, allowing easy recycling of photocatalytic materials and suppressed photobleaching.

The fixation of molecular photocatalyst to Merrifield resins (chloromethylated styrene-divinylbenzyne copolymer beads) was pioneered by Neckers and coworkers in 1975.[66] Rose Bengal molecules with a carboxylic acid group were incorporated onto the surface of Merrifield resins with chloromethane surface groups by a nucleophilic displacement reaction. These beads with RB bound on the surface outperformed free RB molecules when used to catalyze C=C bond cleavage in DCM, because of the improved solubility and photostability. However, self-quenching has been observed when a higher amount of RB molecules was attached. The authors also further treated the particles with pyridine after immobilizing RB in order to promote the hydrophilicity of the beads. These hydrophilic particles were used for the oxidation of 2-furoic acid in methanol, where

better performance was obtained with free RB dyes (49% conversion) compared with beads only modified with RB (14% conversion). Moreover, the efficiency was significantly enhanced using pyridine functionalized particles with 89% conversion. Therefore, the good solvation of photocatalytic moieties enables efficient photocatalysis.

More recently, diaryporphyrin photosensitizer functionalized poly(methyl methacrylate) (PMMA) particles have been investigated for photodynamic therapy.[67] These core-shell nanoparticles were synthesized by emulsion polymerization of MMA and diaryporphyrin sensitizer monomers bearing quaternary ammonium salts. While polymerization, hydrophobic PMMA segments formed the core with hydrophilic segments (chains bearing the quaternary ammonium salts) as the shell. However, when applied for photodynamic therapy free diarlyporphyrin compound outperformed these particles, which could be a consequence of incorporating the photosensitizer into the core instead of the shell due to its high hydrophobicity. The photosensitizers were less accessible in the core of the particles and, thereafter less efficient. This finding demonstrates that photoactive moieties must be located in proper positions to enable efficient performance.

Crosslinked Polymers

The production of crosslinked polymers is similar to linear polymers but adds a secondary monomer with multiple reactive centers additionally, creating coupled linear chains as polymer networks. These systems have been used in various photocatalytic applications due to their chemical stability, tunable solvent compatibility, and ease of recovery.

As an example, Huber *et al*.[68] have synthesized PMMA microgels that contained molecular photocatalysts. The molecular photocatalyst was first functionalized with a polymerizable vinyl group that allows copolymerization with MMA monomers in the presence of a crosslinker (Figure 6). These photocatalytic microgels have been utilized to undertake photocatalytic [4 + 2] cycloaddition reactions with extremely low photocatalyst loading at 0.06 mol% compared to the substrate. These photocatalytic microgels enabled reactions with high conversion and selectivity. Moreover, these

materials were more stable against photobleaching and can be recycled after use compared with molecular photocatalysts.

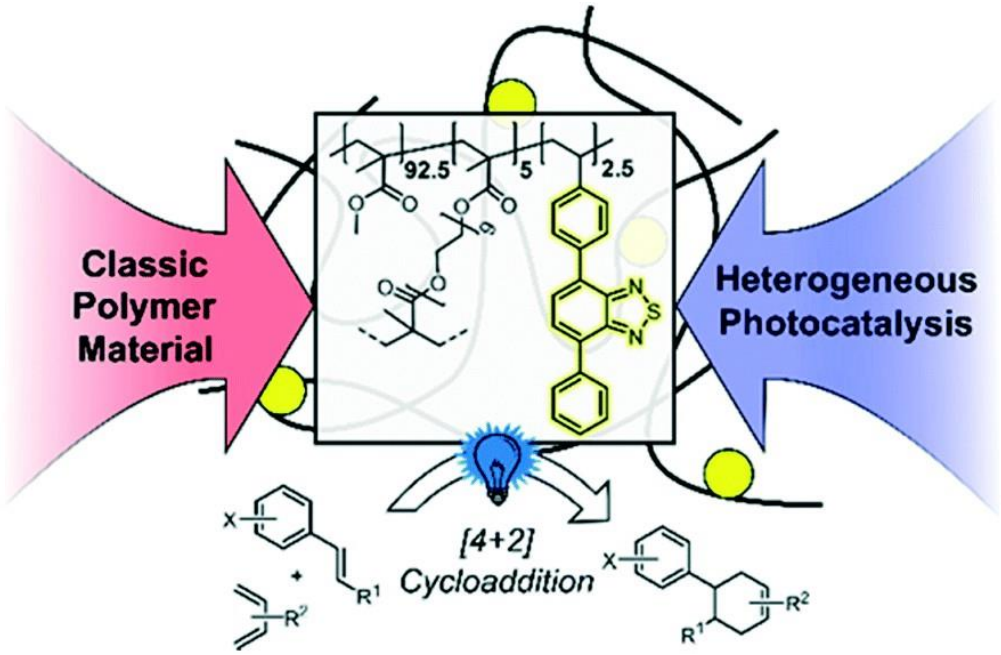

Figure 6. Illustration of PMMA-based photocatalyst copolymer microgel and its application in photocatalytic [4 + 2] cycloaddition. Reproduced from Ref. [68] with permission from the Royal Society of Chemistry.

Further to copolymerization, photocatalytic moieties can also be attached to the crosslinked polymers by coordination. Shen *et al*.[69,70] have synthesized crosslinked vinylpyridine-based polymers before the attachment of Ir complex, where pyridine groups acted as chelating sites. These materials were featured with high efficiency and functional group tolerance when catalyzing Beckermann rearrangement reactions[69] or cyclization of tertiary anilines with maleimides[70]. Besides, these crosslinked polymers bearing with Ir complex can be simply recovered by centrifugation with slightly decreased efficiency but negligible loss of Ir.

Many examples of attaching molecular photocatalysts to crosslinked polymers have been discussed in detail in a recent review.[5] Here, some typical approaches to incorporating photocatalytic units are described very briefly. For example, Li *et al*.[71] have fixed iodic boron-dipyrromethene (BODIPY) photocatalyst onto crosslinked

porous polymers by copper-catalyzed azide-yne “click” reaction. Yoo *et al*.[72] have functionalized the molecular photocatalyst with divinyl groups that can act as crosslinkers to prepare crosslinked photocatalytic polymers. In addition, divinyl group modified molecular photocatalysts have also been reported by Tobin *et al*.[73] and Ferguson *et al*.[74], respectively, facilitating the production of crosslinked photocatalytic polymers.

1.2.5 Stimuli-responsive Polymer Photocatalysts

This subchapter is based on a published mini-review ‘Temperature- and pH-Responsive Polymeric Photocatalysts for Enhanced Control and Recovery, *Angew. Chem. Int. Ed.* **2022**, 61, e202211132’.

Although the emergence of classical polymer photocatalysts has facilitated the production of highly tuneable and readily recyclable photocatalysts, the ability to undertake photocatalysis in a controlled manner and rapid recycling is still not maximized. Especially, pseudo-homogeneous polymeric photocatalysts are particularly attractive as they are able to facilitate efficient photocatalytic reactions in a homogeneous manner, where the polymers are fully solvated/swollen, and the photoactive centers are easily accessible towards mass diffusion and light penetration. However, one of the critical challenges within pseudo-homogeneous photocatalysts is the requirement of a rapid separation and efficient recycling of the catalyst, in order to minimize the production costs, reduce waste generation (e.g., organic solvents for product extraction or polymer precipitation), and diminish the metal contamination (in terms of metal-based photocatalysts) in final products. To overcome the trade-off between efficient homogeneous photocatalysis and recyclability, photocatalytic materials can be designed with switchable solubility or dispersibility in response to external stimuli. Ideally, the photocatalytic species are in a swelling state, where the photocatalytic centers are readily accessible, resulting in efficient catalysis, whereas upon the application of an external stimulus the catalytic systems could undergo a conformational change, leading to phase separation and thereafter, easy recycling. Moreover, altering the solubility of the materials results in a controlled activation and deactivation of the catalyst by regulating the accessibility to the catalytic sites. This

feature of orthogonally switchable functions or activities is typical of biological systems that can modulate their activity dynamically by external triggers.

As an example, enzymes can alter their internal structures/conformation and, therefore, functionalities upon the application of inhibitors,[75,76] cofactors,[77] and environmental changes (i.e. temperature,[78] pH,[79–81] light,[82] and ionic strength[83]). Taking lessons from nature catalysts, different types of artificial smart materials have been developed with tunable physical properties in response to external stimuli, including light, temperature, pH value, salts, magnetic field, and mechanical force. A wide range of variations in physical properties can be observed, for instance changes in solubility, shape, volume, color, aggregation state, magnetic properties, and mechanical properties. The emergence of stimuli-responsive photocatalytic systems has fully taken advantage of the dynamic behavior of smart materials. It is possible to controllably switch the photocatalyst from an active “on” state to an inert “off” state, providing the opportunity to manipulate photocatalytic reactions temporally, spatially, and orthogonally to other processes.

In this section, some of the latest investigations on polymer/oligomer-based triggerable and switchable photocatalytic systems in the field of heterogeneous catalysis are discussed. Considering the complexity of photocatalytic reactions and conditions involved in previous works, the comparison of photocatalysis efficiency and the analysis of detailed chemical mechanisms regarding catalytic reactions are out of the scope of this thesis. In the following, the progress in three types of stimuli-responsive heterogeneous photocatalysis (temperature, pH, and magnetic) will be discussed in terms of the recycling of the materials and/or the dynamic control of the photocatalytic activity.

Thermo-responsive Polymer Photocatalytic Systems

Temperature is the most widely used physical stimulus in smart materials. A great number of thermo-responsive classical polymers are featured by either upper critical solution temperature (UCST) or lower critical solution temperature (LCST). Typically, applications of thermo-responsive systems are based on LCST poly(N-isopropylacrylamide) (PNIPAM) systems, because of their easy production and

transition temperature (ca 32 °C) in the range of body temperature. At temperatures below LCST, PNIPAM is hydrophilic and fully solvated in water. Whereas at temperature above LCST, PNIPAM polymers become hydrophobic and undergo a phase transition forming globules or aggregations. This temperature induced phase transition has been exploited in the field of heterogeneous photocatalysts to enable *in situ* control of the photocatalysis and several thermo-responsive photocatalysts based on PNIPAM polymers have been produced. Here, a high catalytic performance is observed when the photocatalytic centres are homogeneously solvated/distributed in the reaction medium in a non-aggregate state of the material; whilst a suppressed reactivity is obtained after the formation of aggregations. In the pseudo-homogenous state, the accessibility of reactants and light to the active catalytic sites is higher in comparison to the aggregated state.[84,85] However, the aggregation is a continuous process and heat can also be supplied as an extra source of energy in addition to light. Further to switching the hydrophilicity of the polymer systems, it can in principle accelerate the diffusion of chemical species. As a result, an acceleration in the reaction rate may also be seen in the loose aggregation state that creates a confined preferential microenvironment for the reactive species.[86] In most cases, these two effects are combined, resulting in switchable photocatalysis modulated by switchable accessibility of the active catalytic centres. Aggregates formed through physical interactions, e.g. π-π stacking[87] and amphiphilic self-assembly,[88] have also been utilized to induce enhanced photocatalysis, because of the aggregation-induced triplet excited state generation or charge carrier migration, which is not discussed in this review. Furthermore, the phase transition from hydrophilic to hydrophobic could induce a phase separation of the polymers that can be used for the recovery of the photocatalytic polymer.

Linear polymers are the simplest form of a polymer, they can be dissolved either completely creating a homogenous system or dispersed in a heterogeneous system. Koizumi *et al*.[86] used PNIPAM to produce a temperature-controlled photooxygenation polymer containing benzophenone as the photocatalytic molecule (Figure 7). This photocatalytic polymer was simply synthesized by radical copolymerization of NIPAM and 4-allyloxybenzophenone (BP). The photooxygenation of the material exhibited a

heat-induced enhancement below 17 °C and suppression above 22 °C. This off-on-off behavior of poly(NIPAM-*co*-BP) was driven by a temperature-induced conformational change of the polymer from coil to micelle to globule state. When the temperature was in the range of 5-17 °C, loose aggregations of poly(NIPAM-*co*-BP) were formed. This micelle state could extend the lifetime of the $^1O_2$ because of the increased hydrophobic domain, leading to an enhancement of photooxygenation. It is also possible to expect an additional effect, resulting from the increased diffusion rate of the mass transportation that is triggered by the elevated temperature in the loose aggregation state. With further increasing the temperature above 22 °C, the polymer transforms from a micellar state to a globule state containing a hydrophobic precipitated core that blocks access to photoactive sites, resulting in a suppression in photoactivity. A slightly lower LCST temperature (29 °C) was observed compared to pure PNIPAM polymer chains (32 °C), which is possibly due to the increased hydrophobicity from the BP units (6 Mol.%). It suggests that LCST can be tuned according to the interest of application by adjusting the doping of BP units. After use, this material can be easily recovered by heating up to 40 °C, followed by centrifugation. These features suggest the combination of PNIPAM and small photocatalyst molecules is a simple and effective approach to produce smart photocatalysts. As a preliminary investigation of combining small molecule photocatalysts with stimuli-responsive polymers, authors have provided insights by taking advantage of the macromolecular structure change to achieve dynamic control over the photocatalytic reaction and the recycling of the material.

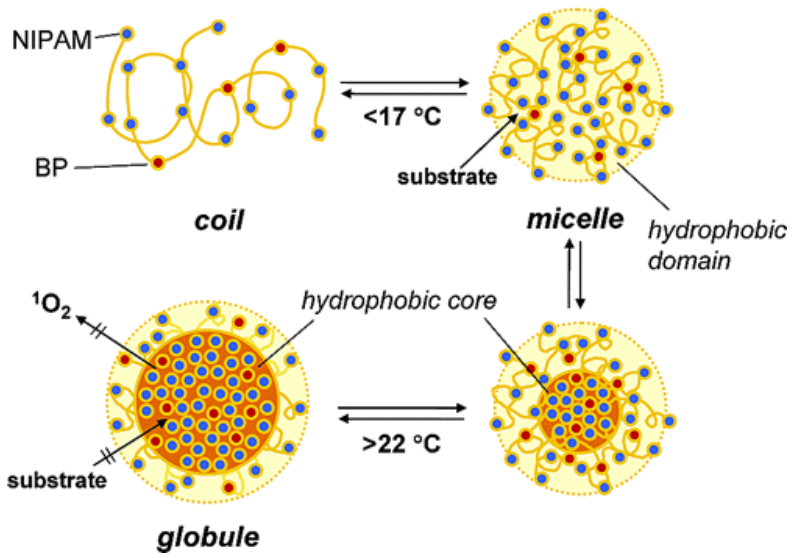

Figure 7. Structure of poly(NIPAM-*co*-BP) and changes in the structure of poly(NIPAM-*co*-BP) in water as a function of temperature. Reproduced with permission from Ref. [86] with permission.

Apart from the aforementioned simple photooxygenation, the application of tagging organic small molecule photocatalyst onto NIPAM polymer chains has been further investigated by Sumerlin and coworkers[89]. Here, an eosin Y (EY)-derived NIPAM polymer photocatalyst was demonstrated for the synthesis of polymeric bioconjugates. EY was modified with acrylate functional group, enabling the copolymerization with NIPAM monomers via RAFT polymerization. This copolymer photocatalyst was utilized for grafting N, N-dimethylacrylamide (DMA), and 4-acryloylmorpholine (NMO) polymers from a protein modified macroCTA via photoelectron/energy transfer reversible addition−fragmentation chain transfer (PET-RAFT) polymerization. A comparable efficiency as the unmodified EY was obtained using poly(EY-NIPAM). Post polymerization, the photocatalyst was removed by heating the reaction mixture to 37 °C and filtrating. This straightforward photocatalyst removal protocol allows small volume reactions and significantly lowers the cost of purification. Moreover, the polymerization can be performed in the presence of a protein in biologically benign conditions, demonstrating its usefulness as a biocompatible photocatalyst for advanced bioconjugate manufacturing.

In addition to pure organic photocatalysts, several Zn-based porphyrin temperature-sensitive photocatalytic systems[90–92] have been reported. Generally, the central porphyrin rings were easily functionalized with four initiators for the chain extension of NIPAM via atom transfer radical polymerization (ATRP), forming star-shaped polymers. These photocatalytic materials exhibited a LCST behavior, and their temperature dependent dye degradation was investigated. These materials could be recovered and reused over 8 cycles with negligible loss of reactivity. The recovery was achieved by simply increasing the temperature, resulting in a heterogeneous separation of the photocatalyst. Moreover, the central porphyrin can also be further modified by different functional end groups, for example, azide (N_3) and alkyne that can enable click reactions.[92] This method involved a two-step reaction: the formation of NIPAM arms through ATRP followed by the azide-yne click reaction between two photocatalytic units. However, the investigations of these photocatalytic materials have been limited to dye degradation reactions.

Stimuli-responsive cross-linked gel systems can be synthesized in a similar manner to linear polymers, but in the presence of an appropriate cross-linker. These network systems are generally more robust and can be recovered more easily. Moreover, because of the possibility of controlled swelling and shrinkage, they have been targeted as an effective class of smart heterogeneous photocatalysts.

Recently, Chen *et al.*[93] synthesized PNIPAM gels containing 10-phenylphenothiazine (PTH) photocatalyst units that were functionalized with an acrylamide group. PNIPAM was selected because of its good solubility in many organic solvents, as well as its LCST behavior in water. The Gel-PTH was synthesized by radical polymerization of NIPAM and PTHMA monomers with the addition of N,N'-methylenebis(acrylamide) (MBAA) as the cross-linker. The swelling behavior of the gels was characterized by storage moduli (*G*'), ensuring a strong and stable structure for easy handling and removal. In addition to light, this gel material can also be switched ON/OFF by using temperature as a second external trigger. Here, upon elevating the temperature a reduction in the gel size as well as a transparent-to-opaque transition was observed. This decreased accessibility of the active photocatalytic sites within the material in

response to heat, allowing the control of the reactivity. The authors employed this material to selectively catalyze the radical controlled polymerization (RCP) of a variety of monomers, including acrylamide, acrylate, methacrylate, vinyl ester and vinyl amide. The polymer chain propagation can be stopped and restored by tuning the temperature of the reaction medium. Here, temperature acts as a trigger to obtain an orthogonal and spatial control of the polymerization procedure. As the gel is around 1 cm in size, it can be removed easily and efficiently reused over six cycles without diminished performance in polymerization rate.

The dimension and production of thermo-responsive photocatalyst gels were further extended by Ferguson *et al.* by producing NIPAM microgels containing a N-(4-(7-phenylbenzo[c][1,2,5]thiadiazol4-yl)phenyl) (PhBTPH) moiety as a photocatalyst (Figure 8).[84] Here, PhBTPH was functionalized with an acrylamide group that roughly matched the propagation rate of the NIPAM monomer, enabling a homogeneous distribution of the photocatalytic units across the microgel network. The authors synthesized dual-responsive microgels through a free-radical precipitation polymerization technique. The size of these microgels experienced a significant decrease after the application of heat, leading to the inaccessibility of the active photocatalytic sites implemented in the network. In detail, photocatalytic PNIPAM microgels were fully solvated in aqueous solution at room temperature (25 °C), enabling efficient pseudo-homogeneous photocatalysis where the photocatalytic PhBTPH units were easily accessible towards substrate diffusion as well as light penetration. Upon heating up to 40 °C, the microgels were turning hydrophobic and phase separated from the aqueous solution, which strongly scattered light as illustrated by a significant change in the optical properties of the microgels in Figure 8c. Meanwhile, this phase separation led to a constraint mass diffusion to the photoactive centers.

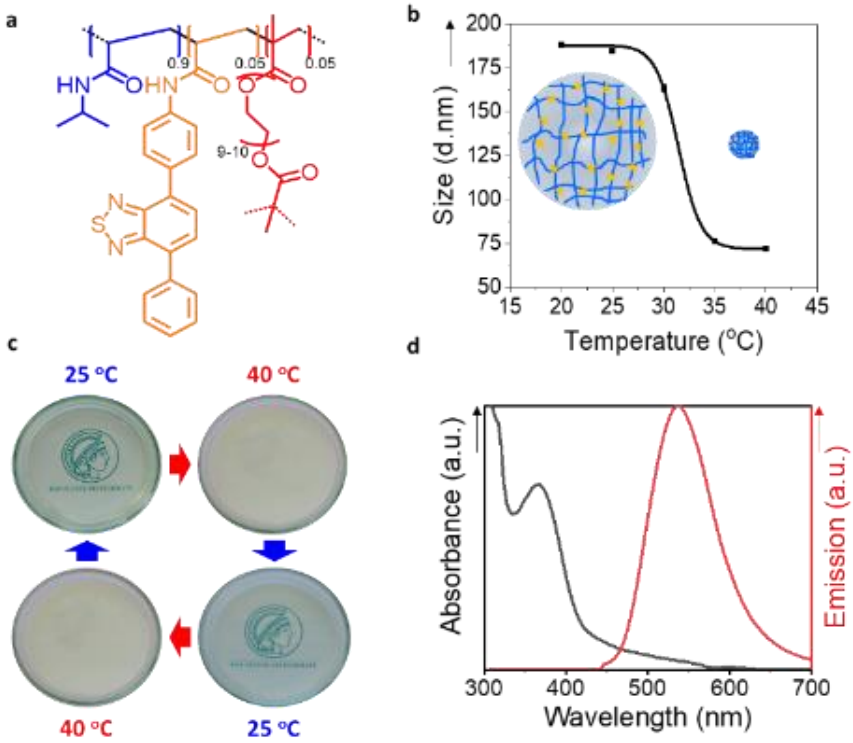

Figure 8. Photocatalytic temperature-responsive microgels. (a) structure of cross-linked photocatalytic microgel. (b) Temperature-dependent shrinking of microgel. (c) Controllable optical properties of photocatalytic microgel as a function of temperature. (d) Temperature dependent photocatalytic conversion of the enzyme cofactor NADH to NAD^+. Reproduced with permission from Ref. [84] with permission.

Taking advantage of this alternation in macromolecular structure of photocatalytic microgels triggered by heat, the authors were able to switch on/off of the photocatalytic materials. The controlled activation of these gels triggered by temperature was investigated by the selective photooxidation of the enzyme cofactor NADH. The dynamic behavior of this biorthogonal material provided precise control over the reaction, where the reaction can proceed at low temperature, otherwise can be stopped upon heating up. Additionally, these microgels were further used for other redox reactions, including disulfide formation mimicking the enzyme-controlled post-translational peptide modifications undertaken in cells. In principle, the conformational change and aggregation induced by heat can be used for the recycling of the microgel.

The recovery and reusability of these gels should also be taken into consideration for further investigations.

Further to PNIPAM-based photocatalytic systems, several thermomorphic phase-selective systems (TMSs) coupled with iridium and ruthenium-based photocatalysts have been developed. TMSs consist of at least two solvents featured with a highly temperature-dependent miscibility gap, exhibiting two liquid phases at lower temperatures and one single phase at elevated temperatures. Under reaction conditions, substrates and catalysts are solvated in one single liquid phase, enabling homogenous photocatalysis; whilst under separation conditions, products and catalysts are separated into two different liquid phases.[94] A number of thermomorphic phase selective photocatalysts have been produced by attaching polyisobutylene (PIB) to the ligands of the metal complexes that have a strong preference for one solvent in a biphasic system, facilitating efficient photocatalysis and easy recycling of photocatalyst.

Priyadarshani *et al.*[95] demonstrated a PIB functionalized $Ru(bpy)_3PF_6$ complex system, utilized as a soluble recyclable photoredox catalyst. Here, PIB (M_n=2.3 kDa) was initially functionalized with a halogen atom prior to being grafted to the bipyridine ligands in the presence of an alkylating agent, affording at least one PIB chain per bipyridine ligand. After being coupled with PIB, these ligands coordinated with metal ions. This complex photocatalyst was utilized for the free radical polymerization of acrylate monomers in heptane a good solvent for both the photocatalyst and acrylate monomers. Upon the extension of the polymer chains, polyacrylate polymers become insoluble in heptane and self-separate from the photocatalyst with negligible Ru contamination. This significant reduction in Ru leaching, compared to the unmodified $Ru(bpy)_3PF_6$ photocatalyst, is due to the high affinity of the PIBs for the solvent. The photocatalyst complexes can be recycled for at least three times obtaining polymer yields greater than 70%. Moreover, the PIB-Ru catalyst system that consists of 2 PIB per bipyridine ligand displayed an additional phase selective solubility in a thermomorphic heptane/DMF system. One single phase of the photocatalyst was obtained in a heptane/DMF mixture at high temperature, while upon cooling a phase separation occurred resulting in a biphasic system separating the photocatalyst from DMF. DMF,

as a very powerful solvent for a variety of reactions, can effectively expand the application of this homogeneous photocatalyst with simple recyclability.

The production of thermomorphic phase-selective photocatalyst was further investigated by Rackl *et al.* (Figure 9). [96] They have developed single PIB polymer chain bonded iridium complexes that exhibit an almost identical optical property to its parent complex fac-Ir(ppy)$_3$. Different from the aforementioned PIB coupling strategy, the authors synthesized the catalyst core structure prior to the attachment of the PIB chain. This PIB tagged photocatalyst was used in a biphasic thermomorphic system of heptane and acetonitrile that exhibits a UCST behavior. Initially, the substrates and reagents were dissolved in the acetonitrile at room temperature and to this a non-miscible phase of heptane containing PIB tagged photocatalyst was added. This biphasic reaction mixture was heated exceeding the UCST to obtain a monophasic solution, allowing homogeneous photocatalysis. After the reaction was completed, the system was simply cooled to room temperature, returning to a two-phase system that was separated to yield the product and recover the photocatalytic material. The catalyst was reused for at least 10 cycles, giving a constant high yield of product with comparable efficiency to the parent Ir photocatalyst. Moreover, the authors incorporated this system into a flow system to obtain continuous recycling of the photocatalyst. This flow system was applied in the photocatalytic E/Z isomerization of cinnamyl acetate, where high selectivity was obtained with an effective reduction of catalyst loading by a factor of 30.

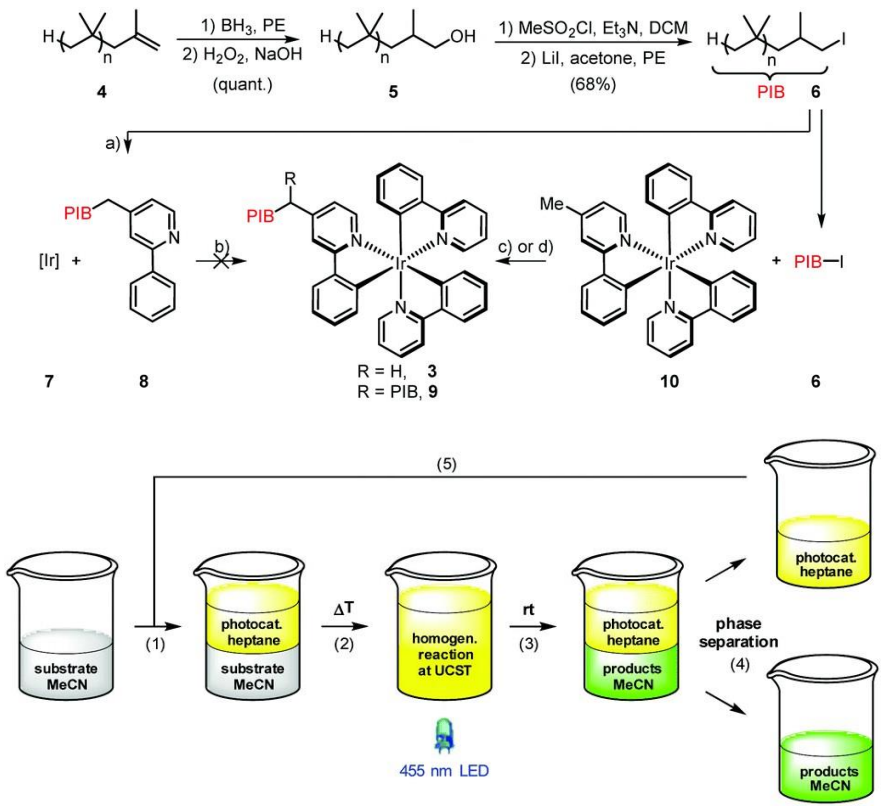

Figure 9. PIB coupling to Ir-based photocatalyst. Method developed by Rackl *et al*.[96] for photocatalysis in a biphasic system with easy separation of products and recyclability of photocatalyst. Figure reproduced from Ref. [96] with permission.

TMSs based on PIB tagged metal complexes demonstrate a versatile strategy for the recovery and reuse of homogeneous transition metal catalysts. However, these polymer-based systems display a molecular mass distribution without an accurate structure, which could lead to possible problems regarding solubility limitations and catalyst leaching. More recently, long alkyl chains have been proven to be capable of generating thermomorphic phase-selective effects. A long alkyl chain ($C_{17}H_{35}$-) bound 2-phenylpyridine Ir complex that possesses an accurate molecular weight has been designed and used for a wide scope of trifluoromethylation of aromatic and heterocyclic compounds with 43-82% yield. This material showed negligible loss of activity after 5 cycles.[97] Moreover, it should be addressed that these systems require high temperatures (70 or 85 °C) in addition to light irradiation, which might be disadvantageous for temperature-sensitive photochemical reactions.

pH-Responsive Polymer Photocatalytic Systems

pH-responsive polymers can also be employed to create responsive photocatalytic systems, to control their catalytic activity and facilitate their recovery by tuning the pH value of the reaction medium. Commonly, pH-responsive polymers are polyelectrolytes containing weakly ionizable groups, which can either accept or donate protons responding to the change in environmental pH.[98–100] At high pH conditions, polyacids are ionized, leading to a drastic change in hydrophilicity and electrostatic repulsion of the polymer chains. Examples are poly(acrylic acid) (PAA) and poly(methacrylic acid) (PMA).[101] On the contrary, polybases are protonated in neutral or acidic conditions, leading to an electrostatic repulsion and swelling of the polymeric materials. Examples are poly(dimethylamino ethylmethacylate) (PDMAEMA)[102], poly(diisopropylamino ethylmethacylate) (PDIAEMA)[103], and poly(4 or 2-vinylpyridine) (P4VP or P2VP)[104]. This controllable swelling of these polymeric materials has been incorporated into photocatalytic systems, facilitating the dynamic control of the photoactivity and recovery of the photocatalytic materials. Ideally, light and reactants are free to reach the catalytic centers in the swollen state of the materials that facilitates efficient photocatalysis. Conversely, when the polymeric matrix is in a contracted state, the diffusion of the reactants and accessibility of reactive sites is hindered, resulting in a less efficient catalysis. The influence of pH variations on chemical reactions should be especially taken into consideration. For instance, a vast number of reactions[17] prefer to take place under basic conditions, therefore an increase in pH value by itself favors the chemical reactions to proceed. Because of this complexity, the investigation of reaction kinetics variations in response to pH changes is difficult. Given the system displays a pH-responsive swelling-shrinking behavior that cannot provide comprehensive and precise information for the control of the reactions, complementary results to exclude the effect of pH variation on the reaction itself are expected. As a result, this pH induced phase transition is more commonly employed to facilitate the recovery of the photocatalytic materials.

Conjugated polymers consisting of fully π-conjugated systems are appealing candidates for upscaling heterogeneous photocatalysis, because of their robustness, nontoxicity, and high visible-light activity. Considering the upscaling in more industrial

applications, water, in particular, is considered a green and economically friendly solvent for photocatalysis. Despite of their high photocatalytic performance, conjugated polymer systems often suffer from poor water solubility/dispersibility. Therefore, a great number of investigations have been carried out in order to improve their water-compatibility.[105–111] Herein, we would like to introduce two simple approaches through the addition of acid to improve the water-compatibility of conjugated systems.

A simple protonation approach of the pristine hydrophobic conjugated polymer networks has been reported by Zhang and coworkers (Figure 10).[111] Sonogashira cross-coupling of 1,3-dibromoazulene and 1,4-dibromobenzene with 1,3,5-triethynylbenzene as a cross-linker was utilized for the synthesis of two conjugated microporous polymers (CMPs), which differ in the molar ratio of two monomers to cross-linker. These CMPs contain azulene units that can be protonated in the presence of acid, resulting in the formation of a stable resonance aromatic six-π-electron tropylium cation. The authors took advantage of this easy method and protonated these two CMPs using TFA, creating two hydrophilic CMPs that were well-dispersed in water. These hydrophilic CMPs were employed for the photocatalytic reduction of Cr^{VI} pollutant to less toxic Cr^{III} and nearly full conversion was achieved after 1 h under the irradiation of a 23 W household energy-saving lightbulb. Furthermore, in the presence of a metal cation Fe^{III} or Cu^{II} as a co-catalyst, cascade catalytic cycles of Cr^{VI} reduction were accomplished without loss of activity after 5 runs, where the promoted electron in the conduction band of CMP is utilized to reduce either Fe^{III} or Cu^{II} to Fe^{II} or Cu^{I}, respectively; this resultant reduced metal cation further reduces Cr^{VI}, obtaining Cr^{III} and the pristine Fe^{III} or Cu^{II} cation. All these aspects demonstrate that these materials are promising water-compatible heterogeneous photocatalysts. Notably, these two hydrophilic CMPs possess different valence bands and conduction bands that gives the opportunity to choose a suitable photocatalyst according to the potential required for chemical reactions. It should also be mentioned that both the porosity and the pore volumes were reduced after protonation. This reduction was suspected to be caused by that trifluoroacetate as a counterion largely incorporated into the network to balance the tropylium cations. Additionally, the incorporation of the trifluoroacetate anions on

the tropylium cations inside the protonated polymer network could also decrease the thermal stability of the material. At elevated temperatures, an increased mobility of trifluoroacetate anions is expected, leading to a reduction in the stability of the networks. Although the authors demonstrated efficient Cr^{VI} reduction using TFA protonated CMPs, the oxidation half-reaction has not been specified. In addition, after protonation

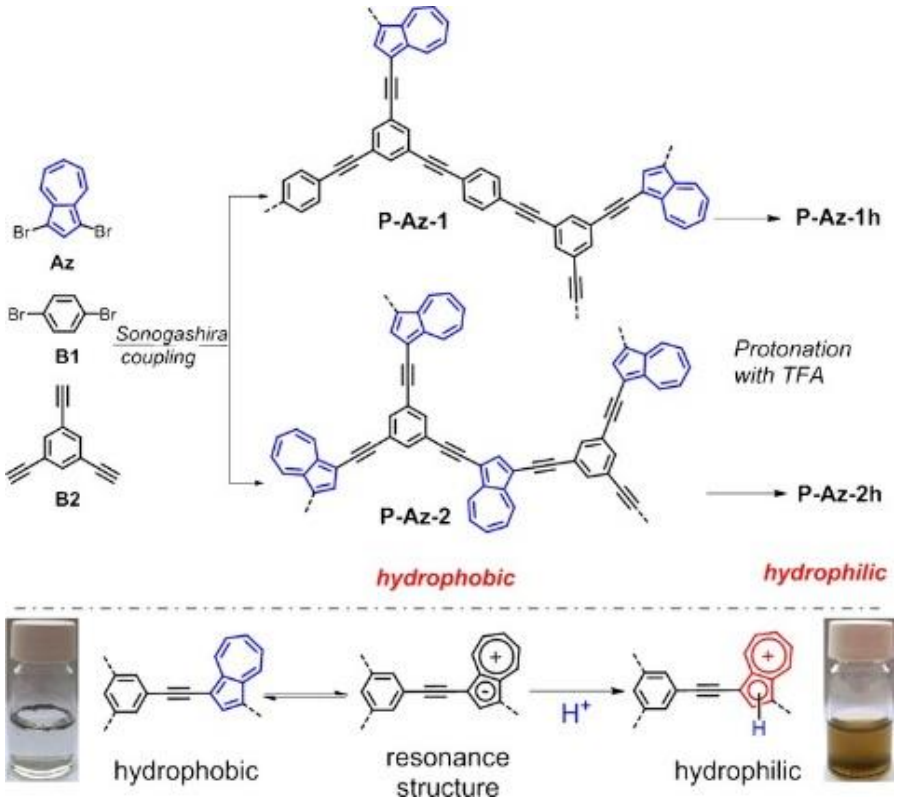

Figure 10. Synthetic pathway and modification method for hydrophilic, conjugated, microporous polyazulene networks. Reproduced from Ref. [111] with permission.

Further to the aforementioned system, CO_2 has also been applied to reversibly tune the photoactivity of conjugated polymers as a special source of acid. Byun *et al*. modified the production of conjugated polymer photocatalysts with switchable hydrophilicity without compromising its recyclability (Figure 11).[112] Here, a tertiary amine was implemented into the conjugated linear polymer through a post-modification of hydrophobic P-BT-Br with diethylamine (DEA). The resulting P-BT-DEA was hydrophobic under neutral and basic conditions. In this complex, the tertiary amine acted as a proton acceptor upon being treated with CO_2 gas, generating bicarbonate

salts in aqueous solutions, and facilitating a good polymer dispersion in water. The bicarbonate salts can be eliminated by treating the solution with N_2 under mild conditions, leading to the precipitation and recycling of the hydrophobic P-BT-DEA. This CO_2-responsive photocatalyst was used for the effective dye degradation and photo-redox reactions, including photo-oxidation of 2-furoic acid, photo-reduction of 4-nitrophenol (4-NP), as well as the coupling of caffeine with aryldiazonium tetrafluoroborate. The efficient coupling of caffeine and aryldiazonium tetrafluoroborate as a model reaction of arylation of heteroarenes enables the direct production of biologically active compounds. Moreover, the PBT-DEA-CO_2 could be reused for up to six 24 h cycles without a loss of conversion efficiency. This simple and reversible approach for switching the polymer solubility can be utilized as a versatile and powerful tool for functional photocatalyst synthesis in future investigations.

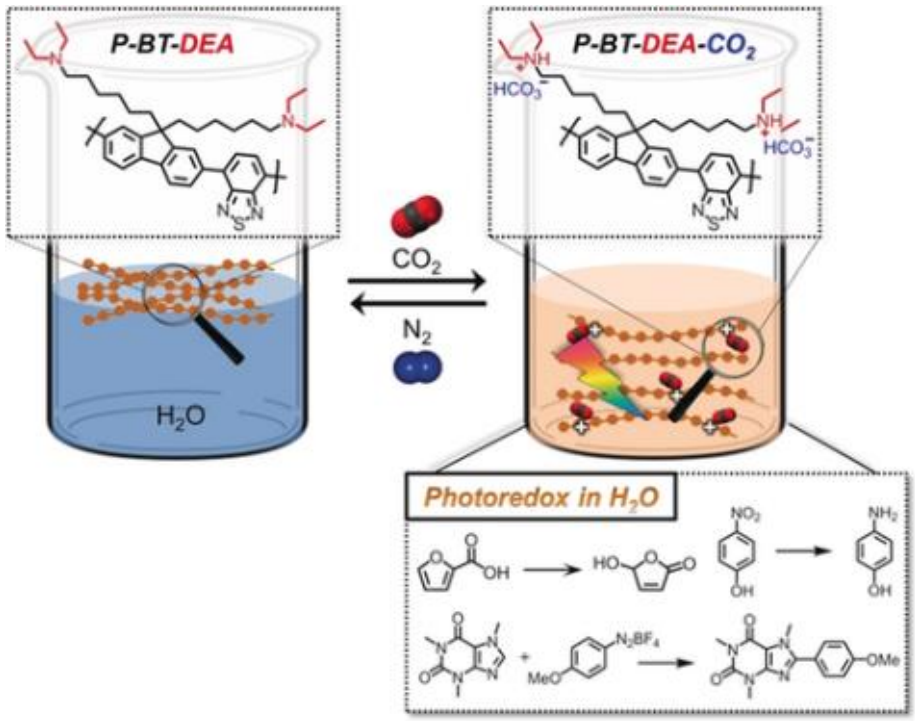

Figure 11. Schematic illustration of the switchable hydrophilicity of the conjugated polymer photocatalyst through CO_2/N_2 exchange, and its photocatalytic applications in water. Reproduced from Ref. [112] with permission.

In the case of photodynamic therapy, pH variations across the tumor microenvironment can be used to selectively activate the photosensitizer at the tumor site, enabling a targeted treatment. For example, acid-responsive AB2 Y-shape metallo-supramolecular micelles, containing iron-tetraphenylporphyrins (Fe-TPP) as a photosensitizer, have been fabricated by Wang *et al.* and used for photodynamic therapy.[113] The micelles were formed through the metal-ligand interaction between Fe-TPP and histidine. Histidine is an essential amino acid and it contains an imidazole group that can act as an acid-labile ligand because of its weak base nature. Prior to the coordination process, histidine and photosensitizer were modified with hydrophobic PLA chains and hydrophilic PEG chains, respectively. At physiological pH (~7.4), two histidine-PLA chains were coordinated to one Fe-TPP, creating Y-shape supramolecular micelles (MSM), which can also be used for drug encapsulation. Once subjected in tumor microenvironment (pH<6), imidazole groups were protonated, and thereafter, this metallo-coordinated micelles were disassociated, revealing the photocatalytic sites, and releasing the drugs. This disassembly was confirmed by dynamic light scattering (DLS) (increased hydrodynamic size and polydispersity index) and TEM (clasped NPs). The photodynamic activity of MSM was characterized by singlet oxygen generation using 9, 10-anthracenediyl-bis(methylene) dimalonic acid (AMDA) as a trapping agent. However, the singlet oxygen generation of MSM has not been compared at pH 7.4 and pH 5.7. Moreover, at pH 7.4, the photobleaching rate of MSM was faster than the non-responsive version (PDP). It is unclear what may cause this difference in these materials in terms of singlet oxygen generation at pH 7.4; however, the formation of PDP was through binding instead of coordination. In addition, it could be expected that the photosensitizers are located at the interface of the hydrophilic PEG shell and hydrophobic PLA core in both cases, which may facilitate an identical accessibility of the oxygen and light towards the reactive centers. Therefore, the binding could reduce the photoactivity of Fe-TPP, conversely the coordination approach demonstrates an efficient method for micelle formation without compromising Fe-TPP activity. The acid-labile photodynamic efficiency of MSM needs to be further addressed. Furthermore, the location and distribution of the photosensitizer should be

taken into consideration for further investigations to have pH targeted activation for photodynamic therapy.

A more straightforward approach was reported by Chen and coworkers[114], who utilized ATRP to produce a pH-responsive amphiphilic block copolymer using a zinc teraaminophthalocyanine derivative as the photocatalytic unit. Methacrylate modified zinc tetraaminophthalocyanine photocatalyst (ZnPc) monomers were copolymerized with pH-responsive DIPAEMA monomers using a hydrophilic PEG-Br chain as initiator. At a pH value greater than 6, the PDIPAEMA block was deprotonated and highly hydrophobic, leading to a micelle formation through the self-assembly of these amphiphilic polymer chains. Whilst at a pH value less than 6, these micelles disassembled because the tertiary amine of the PDIPAEMA units became protonated. This protonation significantly increased hydrophilicity that led to a full solvation of the diblock copolymer and thereafter, the dissociation of the micelles. Herein, the authors took advantage of this pH induced conformational change to switch “on” and “off” of the photocatalytic units. The block copolymer photosensitizer was utilized to oxidize L-tryptophan at pH 5.5 and 7.4, respectively, with an 8-fold increase in yield observed at pH 5.5. This increased photoactivity at lower pH was attributed to the higher accessibility to the photosensitizer in the dissolved form compared with the micelles. Moreover, this pH sensitive photosensitizer is capable of responding to subtle pH changes in the range of tumor microenvironment, demonstrating a potential application in the field of photodynamic therapy.

In addition to micelle formation and dissociation, the aggregation behavior of pH responsive systems has also been addressed. Zou *et al.*[85] demonstrated the use of DMAEMA to produce pH-responsive and recoverable photocatalysts containing a Pt porphyrin derivative (Figure 12). Four pH-responsive PDMAEMA chains were extended from the hydrophobic Pt-porphyrin center, creating a star-shaped unimolecular micelle(UM). At pH 2, the tertiary amine groups of PDMAEMA arms were fully protonated, resulting in UMs with excellent water dispersibility, unconstrained mass transfer, and high active site accessibility. When the pH was elevated above the p*K*a (~7.5) of PDMAEMA at pH 10, the PDMAEMA chains were deprotonated and became

more hydrophobic, leading to the aggregation of UMs. This research also investigated the “on/off“ switch of the photocatalytic activity and the recyclability of the photocatalyst, using the pH-induced reversible dispersion/aggregation behavior of the UMs. The photocatalytic water-splitting was studied at pH 2 and 10, respectively. A 12-fold enhancement in H_2 evolution was observed at pH 2, and the authors claimed that the formation of stable UMs dispersions and high accessibility to the active catalytic sites are the reasons for the significant improvement in performance. However, the effect of pH on photocatalytic hydrogen evolution has not been clarified and further control experiments using non-responsive photocatalysts for hydrogen evolution under both acidic and basic conditions may help support the claim.

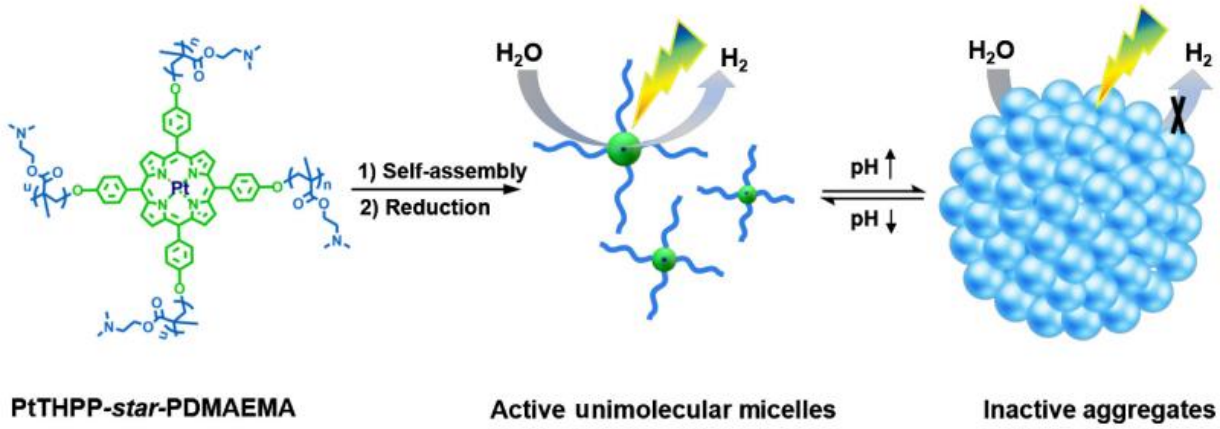

Figure 12. Schematic representation of switchable unimolecular micelles with single Pt atoms. The dispersed UMs are catalytically active, whereas the photocatalytic activity of the aggregated UMs is sharply reduced. Reproduced with permission from Ref. [85].

Apart from the aforementioned temperature-sensitive photocatalyst for PET-RAFT polymerization, the implementation of pH-responsive photocatalyst has emerged as an alternative powerful technique for spatiotemporal, composition, and sequence control of the polymer synthesis, in particular, under aqueous conditions. Huang *et al.*[115] have prepared pH-sensitive hollow microspheres immobilized with Zn-based porphyrin (ZnTPP) as a heterogeneous photocatalyst. Briefly, a SiO2-poly(glycidyl methacrylate-co-methacrylic acid) (PGMA-*co*-PMAA) core-shell structure was prepared prior to attaching ZnTPP moieties to the azide-modified PGM-N_3 shell via alkyne-azide click

chemistry. Following etching the SiO_2 core using HF solution, pH-sensitive hollow microspheres were obtained. The resulting microspheres self-aggregated at a pH value lower than 4.3, where the carboxylic groups COOH were protonated. Whereas at neutral or basic conditions, the PMAA moieties became deprotonated, affording a homogenous dispersion and porous shell structure due to increased hydrophilicity and charge repulsion. The authors investigated whether this structural and conformational change could be used to control the photoactivity of the photocatalytic units. These photocatalytic microspheres were utilized for the PET-RAFT polymerization of N,N-dimethylacrylamide (DMA) under three different pH values of 9.0, 7.0, and 5.0, respectively. A longer induction period and a slower propagation rate were observed at pH 5.0 in comparison to reactions performed at pH 7.0 and 9.0, which was attributed to the poor accessibility to the photocatalytic moieties compared with the completely dispersed and porous form. It should be noted that a reasonable propagation of polymer was still possible at pH 5.0, which may result from the distribution of the photocatalytic sites concentrated on the surface of the microspheres.

The use of an external trigger has been demonstrated to be a powerful and versatile approach to controlling photocatalytic reactions and recovering photocatalytic materials efficiently. So far, most of the photocatalytic control has been achieved through the modification of the physical environment of the photocatalytic sites; however, the modification of the nature of the photocatalytic center could also be used to induce switchability. These initial investigations into stimuli-responsive photocatalysis have addressed their potential to produce a near limitless range of smart materials and can be translated into more industrially relevant applications.

Magnetic Polymer Photocatalysts

Further to temperature and pH, investigations on seeking a more orthogonal stimulus to trigger the recovery of photocatalytic materials have been undertaken, especially the development of magnetic-responsive photocatalysts has exhibited great performance.[116–121] A decade ago, Zhang and coworkers[116] produced water-soluble magnetic-functionalized g-C_3N_4 hybrid materials via in situ decorating spinel $ZnFe_2O_4$ nanoparticles on g-C_3N_4 sheets with a one-step solvothermal approach. The authors found that the loading of $ZnFe_2O_4$ can enhance the catalytic performance of the materials. A possible mechanism could be the synergistic effect of g-C_3N_4 and $ZnFe_2O_4$, the smaller particle size, and the high wettability, leading to the effective electron-hole pair separation thereby enhancing photocatalytic efficiency.

In addition to carbon nitrides, Djellabi et al.[120] have introduced Fe_3O_4 nanoparticles into conjugated polymer mixtures, resulting in a soft-magnetically recoverable photoactive material that enables Cr(VI) reduction, MB oxidation, and bacteria inactivation. The incorporation of Fe_3O_4 not only facilitated the recovery of the photocatalytic materials but also participated in the electron transfer process in the presence of H_2O_2 known as the Fenton reaction (reduction of Fe(III) to Fe(II) of Fe_3O_4) that further enhanced the efficiency. However, the implantation process of the Fe_3O_4 into the conjugated polymer photocatalyst has not been described.

More recently, Bayarkhuu et al.[117] have synthesized magnetic conjugated polymer photocatalysts comprising conjugated polyelectrolytes with crosslinkable vinyl groups and hydrophilic Fe_3O_4 nanoparticles (see Figure 13). Water-dispersible Fe_3O_4 nanoparticles were incorporated and stabilized in the conjugated structure during the crosslinking process of conjugated polyelectrolytes. The solvent compatibility of the resultant materials can be tuned by anion exchange, thereby these materials can be applied in a wide range of solvents from water to toluene. Magnetic conjugated polymers with hydrophilic anions have efficiently degraded tetracycline in water, whereas these materials coupled with hydrophobic anions displayed high efficiency for photooxidative amine coupling in acetonitrile.

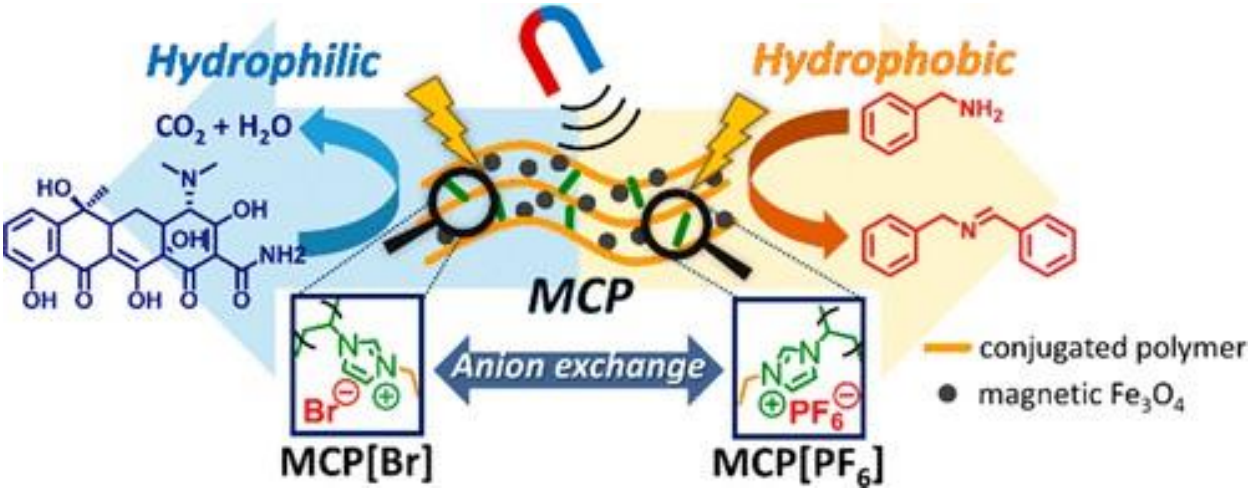

Figure 13. Illustration of magnetic conjugated polymer (MCP) with controllable wettability via anion exchange and the nanoparticles were used for hydrophilic and hydrophobic substrates. Reproduced with permission from Ref. [117].

The combination of magnetic nanoparticles with conjugated polymer photocatalysts has facilitated the efficient recycling of photocatalytic materials by applying an orthogonal stimulus magnetism. It should be noted that magnetic materials e.g., Fe_3O_4 can be involved in the electron transfer process, therefore photocatalytic reactions and material constructions should be carefully selected and designed. However, the implantation of magnetism into stimuli-responsive polymer based photocatalytic materials enabling multi-functionalization has not yet been investigated.

Perspective

The combination of stimuli-responsive systems with heterogeneous photocatalysts enables the production of a new class of catalysts featured by switchability, adaptability, and excellent recyclability. To date, a variety of photoactive species have been implemented into a broad range of smart polymeric systems from linear polymers to gel matrices. The dynamic control over the photocatalytic performance of these materials can be generally achieved by regulating the accessibility of the photoactive sites according to the external environment. The switchable solubility/dispersibility of the stimuli-responsive photocatalyst provides a precise temporal control regarding the on/off of the photocatalytic reactions. However, neither the regulation of the reaction rate in a continuous manner nor the quantity of the catalytic activity has been obtained.

Moreover, no discussion regarding the changes in actual physicochemical processes upon the application of external triggers that occur in the photocatalysts, including photon absorption, exciton diffusion, and free charge generation, have been provided by the state-of-art investigations. Temperature-responsive photocatalytic polymers are still the most frequently and intensively investigated systems, especially for the systems based on PNIPAM. A number of new polymers with transition temperatures in a broad range from 20 to 50 °C[122] have been developed recently, providing new possibilities to produce a palette of catalytic systems with different transition temperatures. Compared to temperature, fewer of the known smart photocatalytic systems are triggered by pH value changes, which should be further implemented and investigated. Especially, the orthogonal dynamic control over the photocatalytic reactions through the pH variation is desired. Moreover, the production of switchable photocatalytic systems based on changing the nature of active centers still needs to be further investigated. For example, by directly altering photoactive sites in response to external stimuli, it is possible to tune the optical properties of photocatalysts, which may be interesting for selective photocatalysis or cascade photocatalytic reactions. In addition to heat and pH, many other triggers (i.e., salts, electric fields, etc.) could be implemented. For instance, the solubility of ionic liquid based polymers in water significantly depends on the counter ions of the polymers.[123] Therefore, counter ion-exchange can be utilized to switch the water solubility of ionic liquid based photocatalytic polymers, enabling the recovery of the photocatalyst and possible control of the photoactivity. Furthermore, the development of a flow device has opened the way in the direction of up-scaling photocatalytic reactions with continuous product separation and catalyst recovery. However, most of these investigations are limited to the study of simple model reactions, including photooxygenation, dye degradation, and 4-nitrophenol degradation, thus the production of more practically or technologically relevant compounds with high values (i.e., solar fuels or medicines) applying these materials would be extremely desirable. Stimuli-responsive polymer photocatalysts are an exciting and sustainable class of hybrid materials with highly tunable potential, allowing the translation to more industrially relevant applications. Moreover, pH-responsive photocatalytic materials can also be specifically designed to match the intrinsic pH difference between the

bloodstream and the tumor extracellular microenvironment, where the activity of photocatalytic materials can be switched on/off according to the pH of the tissue. This exhibits the potential to employ photocatalytic materials for targeted cancer treatment (e.g., photodynamic therapy and prodrug activations).

1.2.6 Photodynamic Therapy (PDT)

Photochemotherapy of cancer, often known as “photodynamic therapy (PDT)”, involves the administration of a tumor-localizing photosensitizing agent (photosensitizer PS or photocatalyst) that is subsequently activated by light of a specific wavelength. The excited energy state can generate highly cytotoxic singlet oxygen ($^1O_2$) and radicals ($O_2^{-\cdot}$ and $HO^{\cdot}$), leading to cell death via apoptosis or necrosis. This demonstrates a non-invasive way of cancer treatment as a special application of photocatalysis.

Two types of photodynamic reactions can occur in PDT depending on the nature of the primary steps (Figure 14). Type I reactions are direct reactions between the excited state of PS (PS*) and substrates (e.g., cell membranes or molecules), where hydrogen atoms are abstracted, or electron transfer is involved. This interaction generates free radicals and radical ions that can further react with other molecules such as oxygen, resulting in reactive oxygen species (ROS). The Type II reaction involves energy transfer from the PS* to the molecular oxygen directly, producing $^1O_2$. ROS generation via Type II reaction is mechanistically simpler than via Type I reactions, therefore most treatments are believed to undergo through the Type II mechanism instead of Type I. Three interrelated mechanisms, including direct cytotoxicity to tumor cells, tumor vasculature damage, and the development of systemic immunity induced by a robust inflammatory reaction, are used to demonstrate the antitumor effects of PDT. The performance of PDT highly depends on various parameters such as the type and dose of PS used, the time intervals of PS administration and light exposure, tumor oxygen concentration, light dose in total, and its fluence rate, etc. Therefore, the optimization of PDT conditions requires a coordinated interdisciplinary effort, which has been profoundly demonstrated previously.[124]

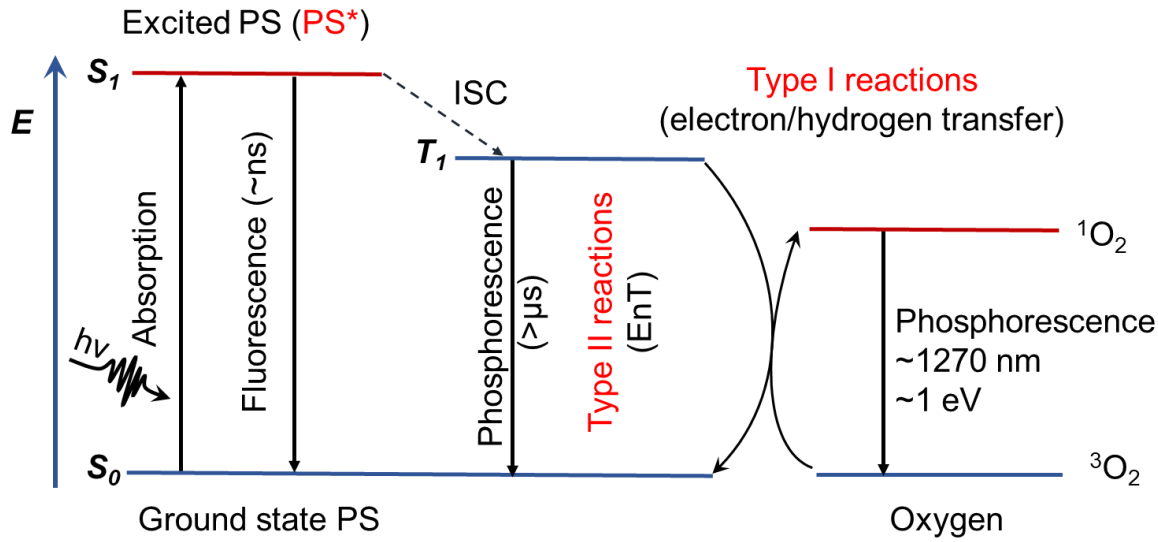

Figure 14. Photosensitization processes are illustrated by a modified Jablonski diagram. Light exposure takes a photosensitizer molecule from the ground singlet state (S_0) to an excited singlet state (S_1). The molecule in S_1 may undergo intersystem crossing to an excited triplet state (T_1) and then either form radicals via a type 1 reaction or, more likely, transfers its energy to molecular oxygen ($^3O_2$) and form singlet oxygen ($^1O_2$), which is the major cytotoxic agent involved in PDT.

1.3 Characterization Techniques

In this subchapter, the most relevant characterization techniques employed in this thesis are briefly outlined. The working principles of the measurements are explained, which allows us to demonstrate and correlate the properties of the materials through the data collected.

1.3.1 Gel Permeation Chromatography (GPC)

Gel permeation chromatography (GPC), also known as size exclusion chromatography (SEC), is commonly used to determine the molar mass and molecular weight distribution (MWD) of polymers. In a typical GPC measurement, the polymer sample is dissolved in a good solvent to ensure good solvation and expansion of polymer chains. This diluted polymer solution is injected into a column packed with porous gel with a pore size distribution of 50-10^5 nm. This porous stationary gel can separate polymer chains by their hydrodynamic volume in solution (generally referred to as the molecular size). Smaller molecules can diffuse into most of the pores in the beads, resulting in an increased retention time. Upon excluding through the column, the polymer chains separated by sizes are measured by the refractive index detector and/or UV detector by their elution time. As a relative measurement method, a series of calibration standards (dispersity $Đ \leq 1.1$) with known molar masses are also eluted through the porous column to establish a quantitative relationship between the elution time and the molar mass. Therefore, the number-(M_n), weight-(M_w), viscosity-(M_v), and z-(M_z) averaged molar mass of polymers can be determined, subsequently allowing the calculation of their dispersity Đ via M_w/M_n. In this work, GPC was applied as an important technique to determine the molar mass and dispersity of photocatalytic polymers.

1.3.2 Ultraviolet-Visible (UV-Vis) Spectroscopy

UV-Vis spectroscopy is an analytic method measuring the amount of discrete wavelengths of UV and/or visible light, which have been absorbed by or transmitted through a sample compared to a reference or blank sample. Light carries a certain amount of energy, inversely proportional to its wavelength that can promote electrons in a substrate to an excited state. Depending on the different bonding environments of

the electrons in a substrate, a specific amount of energy is required to promote the electrons from the ground state (valence band) to an excited state (conduction band) that is detected as absorption. Therefore, the absorption wavelengths differ in different substances. The absorption intensity (*A*) is a function of the intensity of the incident monochromatic radiation before and after passing through the measurement cell (I_0/I), as described in Beer-Lambert law:

$$A = log\frac{I_0}{I} = \varepsilon \cdot c \cdot d$$

where $\mathcal{E}$, *c*, and *d* are molar absorption coefficients, concentration of the sample solution, and the thickness of the measurement cell (commonly quartz cuvette), respectively.

In this work, UV-Vis spectroscopy has been used to characterize the absorption band of the photocatalytic materials, as well as monitor the reaction kinetics by colorimetric methods.

1.3.3 Fourier Transform Infrared (FTIR) Spectroscopy

Chemical bonds can specifically absorb infrared radiation through discrete molecular vibrations and rotations. Therefore, infrared spectroscopy is widely utilized to investigate the molecular structure and the surrounding environment of materials. The majority of molecules show infrared (IR) absorption in the mid-IR range (400-4000 cm^{-1}), thus in Fourier transform infrared (FTIR) spectra the transmittance is usually plotted against the wavenumber in the mid-IR range representing a molecular 'fingerprint' of the substance. As an extremely sensitive and solid-state compatible method, only a small quantity of samples (< 10 mg) is required. In this work, FTIR was used to identify the specific functional groups of the photocatalytic polymers and nanoparticles.

1.3.4 Gas Chromatography-Mass Spectroscopy (GCMS)

Gas chromatography-mass spectroscopy (GCMS) is a powerful analytical tool that combines gas chromatography (GC) and mass spectroscopy (MS). It can separate different pure compounds from a sample mixture depending on their volatility. By flowing an inert gas stream (mobile phase: helium, nitrogen, carbon dioxide, and

hydrogen), the evaporated sample passes through a stationary phase in the column, resulting in separated compounds. These compounds are transported into the mass detector directly, where a stream of electron beams is utilized to ionize the compounds generating various fragments. The mass-to-charge ratio (*m*/*z*) of each fragment is recorded, thereafter different compounds in a sample mixture can be identified by comparing to the substance library or sample standards. GC-MS was utilized as an important analytic method in this work to monitor photocatalytic reaction conversions, and kinetic profiles and identify possible products.

1.3.5 Nuclear Magnetic Resonance (NMR) Spectroscopy

Nuclear magnetic resonance (NMR) spectroscopy is an advanced technique for the molecular structural characterization of a sample at the atomic level. In addition to chemical structures, NMR spectroscopy can also determine reaction dynamics, phase changes, conformational and configurational alternations, and diffusion potential.[125] Most atomic nuclei possess an intrinsic nuclear spin (*I*) and angular momentum *P* that is proportional to the magnetic moment μ.[126] When exposed to an external magnetic field (B), some nuclei exist in specific nuclear spin states that are quantum-mechanically allowed. Their energy difference (ΔE) can be described by the following equation:

$$\Delta E = \frac{\mu B}{I}$$

When a suitable radio frequency pulse is applied perpendicular to the static magnetic field, the spins can resonate with the irradiated pulse, thereafter they can be specifically excited and deflected (Figure 15). Consequently, a precession of the spins is generated, and it is comparable to that of a spinning top whose movement has been disturbed by a brief bump. The frequency of this precession in the xy plane, depending on the strength of the external magnetic field, is the actual measurement quantity and is called the Larmor frequency. The nuclear spins in the excited state can be detected till return to their equilibrium state, which is parallel to the external magnetic field (longitudinal or T_1 relaxation). In practical measurement, the detected signal falls faster because the precession of nuclear spins differs in resonance frequencies. The coherence fades over time, therefore the spins point in different directions and the signals can cancel each

other out (transversal or T_2 relaxation). The resonance frequency of a specific nuclear spin highly depends on the chemical environment of the nucleus because the frequency can be affected by electron shielding. This leads to the so-called chemical shifts, demonstrating the frequency of the signal relative to a fixed standard.[127–129] In this thesis, liquid NMR spectroscopy has been employed to determine the chemical structures of organic small molecules and polymers.

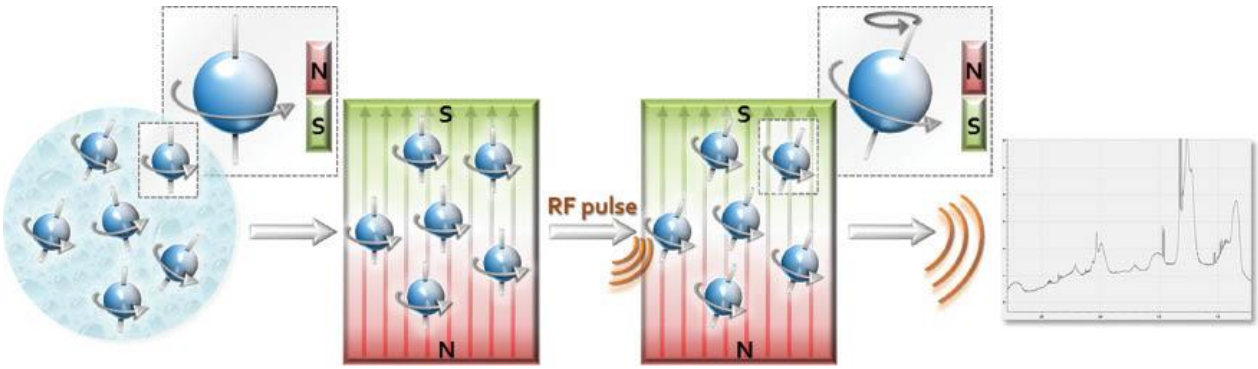

Figure 15. Simplified illustration of the NMR methodology. The nuclear spins found in organic molecules behave similarly to small magnets. While they are statistically oriented in solution, they preferentially align parallel in the external magnetic field. Together they result in a macroscopic magnetization of the spins in the z direction. The spins rotate through targeted excitation of the spins using radio frequency. The macroscopic magnetization is brought horizontal and rotates in the static field after the pulse is switched off. The immediate environment of the nuclear spin (e.g., chemical bonds, electrostatic interactions, solvent matrix, etc.) determines its resonance frequency, which is ultimately reproduced as a signal in the NMR spectrum. Specific molecules can therefore be identified by their characteristic signal patterns.[127]

1.3.6 Cyclic Voltammetry (CV)

Cyclic voltammetry (CV) is an electrochemical method usually applied to study oxidation and reduction processes of electroactive species, which occurs at the interface of electrode and solution and the standard potential can be obtained according to the Nernst equation:

$$aA + ne^- \leftrightarrow bB$$

$$E = E^{0\prime} - \frac{2.303RT}{nF} log \frac{[B]^b}{[A]^a}$$

Here, A is the reactant, B is the product, E is the electrode potential, $E^{0\prime}$ is the formal potential, R is the gas constant (8.3145 $J \cdot K^{-1} \cdot mol^{-1}$), T is temperature, n is the number of moles of electrons involved, F is the Faraday constant (96.485 $C \cdot mol^{-1}$), and $\frac{[B]^b}{[A]^a}$ is the ratio of products to reactants.

In a typical CV measurement setup, an electrochemical cell (Figure 16a) is used, where a polished working electrode (e.g. glassy carbon, platinum, and gold), a reference electrode (e.g. saturated Hg_2Cl_2 solution), and a counter electrode (e.g. Pt wire) are connected to the potentiostat and immersed in an electrolyte solution (e.g. $[NBu_4][PF_6]$ in CH_3CN). During the measurement, the working electrode potential ramps linearly versus time, while the reference electrode potential remains as constant. The electroactive substance, which is either dissolved in the electrolyte solution or pre-deposited on the electrode, can be oxidized or reduced when sufficient potential is applied. The current is measured between the working electrode and the counter electrode, whereas the potential is measured between the working electrode and the reference electrode. The current (I) is plotted as a function of the applied potential (E), giving the cyclic voltammogram with oxidation processes shown as upward peaks and reduction processes shown as downward peaks according to the IUPAC convention (Figure 16b).[130]

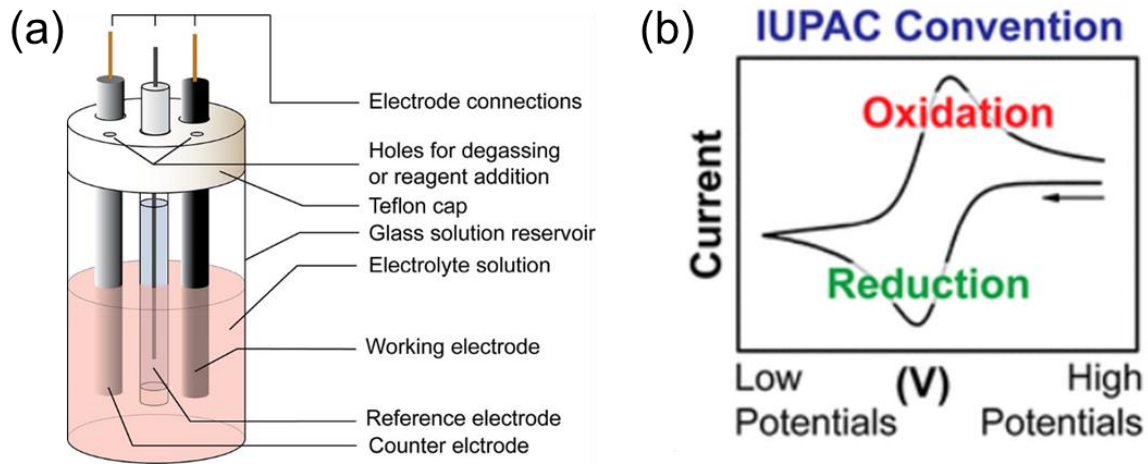

Figure 16. Schematic illustrations of (a) a typical electrochemical cell and (b) a typical voltammogram obtained by CV measurements. Reproduced with permission from Ref.[130]

Here, CV has been applied to determine the highest occupied molecular orbital (HOMO) and the lowest unoccupied molecular orbital (LUMO) levels of photocatalytic materials.

1.3.7 Transmission Electron Microscopy

In a conventional transmission electron microscope (TEM), an electron beam with a uniform current density is emitted from the electron gun to an ultrathin specimen and the energy of the electron is between 60 and 150 keV (usually 100 keV), which could also be up to 200 keV-3 MeV regarding high-voltage electron microscopy.

The electrons are elastically and inelastically scattered by the sample atoms, which therefore requires an extremely thin specimen. The specimen thickness is generally in the range of 5 nm-0.5 μm for a 100 keV electron beam, determined by the density and chemical composition of the sample, as well as the desired resolution.[131] According to the classical Rayleigh criterion of a light microscope, the smallest distance that can be distinguished between two points, known as the image resolution δ, is expressed approximately by

$$\delta = \frac{0.61\lambda}{\mu \, sin\beta}$$

where λ is the incident wavelength, μ represents the refractive index of the viewing medium, and β stands for the semi-angle of magnifying lens. In order to simplify the

equation, $\mu sin\beta$, sometimes termed as numerical aperture (NA) is approximated to unity, resulting in the resolution equal to around half of the wavelength of the irradiation.[132] While the resolution of a light microscope is greatly limited by the incident light wavelength. Due to de Broglie's great contribution finding that the wavelength of electrons is related to the electron energy, the approximation equation between electron wavelength and energy can be expressed as follows:

$$\lambda \approx \frac{1.22}{E^{1/2}}$$

where *E* means the energy of the incident electrons in electron volts (eV), thus the wavelength λ ~ 0.004 nm (4 pm) for a 100 keV electron beam, which is much smaller than the radius of an atom.[132] Therefore TEM is extremely useful in providing high-resolution images down to the atomic level details, in which the elastic and inelastic scattering produces the contrast, allowing better understanding of the properties of the materials.[131,132] TEM was used to obtain the detailed morphologies of the materials synthesized in this work, in order to visualize the morphologies of the photocatalytic nanoparticles.

1.3.8 Electron Paramagnetic Resonance (EPR)

Electron paramagnetic resonance (EPR), also known as electron spin resonance (ESR) is a practical form of spectroscopy utilized to investigate molecules or atoms with an unpaired electron. While measurement, the sample is subjected to a very strong magnetic field with electromagnetic radiation applied monochromatically. Similar to NMR, the geometry of a molecule can be observed by EPR through its magnetic moment and difference in electron and nucleus mass. Therefore, EPR is very useful for the detection and identification of free radical species, point defects in solids or localized crystal imperfections, molecules with unpaired electrons in ground states such as NO, NO_2, and O_2, as well as proteins with paramagnetic ions (e.g., Mn^{2+}, Fe^{3+} and Cu^{2+}). The unpaired electrons of these samples can occupy either +1/2 or – 1/2 m_s spin value in the presence of an external magnetic field due to the Zeeman effect. Therefore, these samples can absorb a single or range of wavelengths of electromagnetic radiation,

where the resonant absorption occurs if the microwave frequency (v) can meet the following requirement:

$$\Delta E = h\nu = g_e \mu_B B$$

here g_e is the spectroscopic splitting factor: g_e = 2.002319304386(20), μ_B is Bohr magneton, and *B* is the magnetic field. In a typical EPR measurement, the microwave frequency is fixed at a constant value (9-10 GHz), and a magnetic field is swept to find the resonance conditions, generating a graph of the absorption as a function of the magnetic field.[133] In this thesis, EPR spectroscopy has been applied to detect and confirm the generation of singlet oxygen during photocatalytic processes.

2 pH-triggered Recovery of Organic Polymer Photocatalytic Particles for the Production of High Value Compounds and Enhanced Recyclability

This chapter is based on a published article 'pH-triggered Recovery of Organic Polymer Photocatalytic Particles for the Production of High Value Compounds and Enhanced Recyclability, *Angew. Chem. Int. Ed.* **2023**, 62, e202217652'.

Pseudo-homogeneous polymeric photocatalysts are an emerging class of highly efficient and tunable photocatalytic materials, where the photocatalytic centers are easily accessible. The creation of highly efficient photocatalytic materials that can be rapidly separated and recovered is one of the critical challenges in photocatalytic chemistry. Here, we describe pH-responsive photocatalytic nanoparticles that are active and well-dispersed under acidic conditions but aggregate instantly upon elevation of pH, enabling easy recovery. These responsive photocatalytic polymers can be used in various photocatalytic transformations, including Cr^{VI} reduction and photoredox alkylation of an indole derivative. Notably, the cationic nature of the photocatalyst accelerates the reaction rate of an anionic substrate compared to uncharged species. These photocatalytic particles could be readily recycled allowing multiple successive photocatalytic reactions with no clear loss in activity.

2.1 Motivation

Taking lessons from natural photosynthesis, the emergence of visible light photocatalysts has facilitated the conversion of abundant solar energy to high value chemicals or electrical energies. To date, photocatalytic systems have been employed for a large number of applications, including aqueous pollutant degradation,[36,37,134,135] photodynamic therapy,[44,136–138] hydrogen evolution,[46,139–141] and organic transformations.[142–146] In particular, the wide scope of photocatalytic reactions (e.g. C−C coupling reactions,[147] C=C bond cleavage,[148] trifluoromethylation of arenes,[149] heterocycle formation,[150] and enantioselective alpha-alkylation[151]) is of great importance for organic chemistry to overcome the activation energy associated with a particular reaction under mild reaction conditions. Many investigations are undertaken with molecular homogeneous photocatalysts, including precious transition metal-based photocatalysts[15] and organic photoredox catalysts,[152] which have been

targeted as highly tunable alternatives to inorganic photocatalysts but at the expense of stability and efficiency.[153,154]

The merger of molecular photocatalysts and heterogeneous polymers has helped realize efficient photocatalysis with enhanced stability compared to their molecular form. Classical polymer-based photocatalysts have been targeted as a highly tunable and versatile class of heterogeneous photocatalysts, taking advantage of their easy production, broad functionalities, and flexibility in design.[5] Among these materials, pseudo-homogeneous polymeric photocatalysts are particularly attractive as they are capable of facilitating efficient photocatalytic reactions in a homogeneous manner, where the polymers are in a fully solvated/swollen state and photocatalytic moieties are readily accessible towards light penetration and mass diffusion. In addition to maintaining an efficient performance, investigations regarding the recycling of pseudo-homogeneous polymeric photocatalysts have also been carried out via either precipitating photocatalytic polymers in organic solvent[155] or extracting the products from the polymer solution.[156] One of the main challenges within these materials is to obtain a rapid separation and high recyclability of the catalysts, in order to avoid organic solvent waste and reduce the production/recycling cost.

In biological systems, protein conformational change, ligand exchange, and other structural rearrangements in response to environmental triggers have been widely utilized to manipulate the biochemical activity of living systems.[157–160] Mimicking the stimuli-responsive conformational changes in nature, the integration of pH-responsive moieties into polymer structures provides an opportunity to induce a phase transition of polymers in aqueous conditions by a minute change in environmental pH. These pH-triggered phase transitions have been successfully demonstrated by the simple reversible protonation/deprotonation of polyelectrolytes.[161,162] For example, polyacids are ionized at high pH conditions and polybases are protonated at neutral or acidic conditions. The resulting drastic increase in hydrophilicity and electrostatic repulsion of the polymer chains can be applied to enhance the water compatibility of polymers. Conversely, the reverse process of polyacid ionization or polybase protonation promotes polymer hydrophobicity, leading to phase separation and recovery of polymer chains from the aqueous solution.

However, only a few examples of pH-responsive and photoactive polymers[85,111,112] have been demonstrated, although incorporating pH-responsive moieties to polymer

structures shows the ability to gain control of the water-compatibility and/or recycling of the materials. As an example, Byun *et al.* [112] reported a CO_2-triggered system, where the wettability of a post-functionalized photocatalytic conjugated linear polymer has been enhanced by the addition of CO_2 into the solvent and this photocatalytic material is recycled through a simple CO_2/N_2 switching. Gas exchange provides an orthogonal control on the water-compatibility switching of this system, whereas it is a time-consuming process, and the post-functionalization is limited to conjugated polymer photocatalysts. Besides, the undefined contraction and aggregation of linear polymer chains could lead to insufficient recovery of the conjugated polymer, indicated by the declined conversion of the recycling experiments. Recently, a pH-triggered aggregation of unimolecular micelles, consisting of a Pt-porphyrin photocatalytic center and four poly(dimethylaminoethyl methacrylate) (PDMAEMA) arm chains, has been demonstrated by Zou *et al.*[85]. However, only one reactive center can be incorporated per micelle and the size of the micelle aggregations was still in nm scale (< 200 nm). Here, we demonstrate enhanced recycling of photocatalytic materials via an instant aggregation of polymeric photocatalyst nanoparticles triggered by pH changes, where the particles can be reversibly switched from the nm scale to the macro scale (visible by eye).

Ideally, the photocatalytic moieties should be solvated/swollen and easily accessible, to obtain efficient photocatalysis; whilst upon external stimuli can undergo conformational changes, leading to aggregation and/or precipitation, which facilitates the easy recycling of photocatalysts. A core-shell polymer nanoparticle system that can be homogeneously dispersed in aqueous conditions and stabilized by hydrophilic polymer brushes could be utilized as a polymeric platform for photocatalytic units. Upon elevating pH, the stabilizing block becomes contracted, and nanoparticles aggregate/precipitate. In order to ensure an efficient photocatalytic performance and control, the photocatalytic moieties should be incorporated in the polymer brushes anchored on the surface of the hydrophobic core. A simple approach to switch the wettability of the nanoparticles can be achieved by protonating/deprotonating the stabilizing block according to the environment pH value.

Here in this chapter, we have produced pH-responsive polymer core-shell nanoparticles containing photocatalytic active centers distributed within the corona of the nanoparticles. The reversible protonation-deprotonation of tertiary amine-tethered

polymer brushes was applied to tune the hydrophobicity of the stabilizing shell triggered by pH alternation (Figure 17). The efficient photocatalytic performance of switchable photocatalytic nanoparticles has been demonstrated by photocatalytic reactions in aqueous medium under visible light irradiation, including photo-reduction of toxic Cr(VI) inorganic water contamination and various organic transformations, including sulfoxidation, 2-furoic acid oxidation, and Friedel-Crafts alkylation of an indole derivative. These nanoparticles undergo stark aggregations upon elevation of the pH value of the medium, as the polymer shell turns highly hydrophobic after turning neutral, which facilitates rapid and easy recycling of the photocatalytic materials.

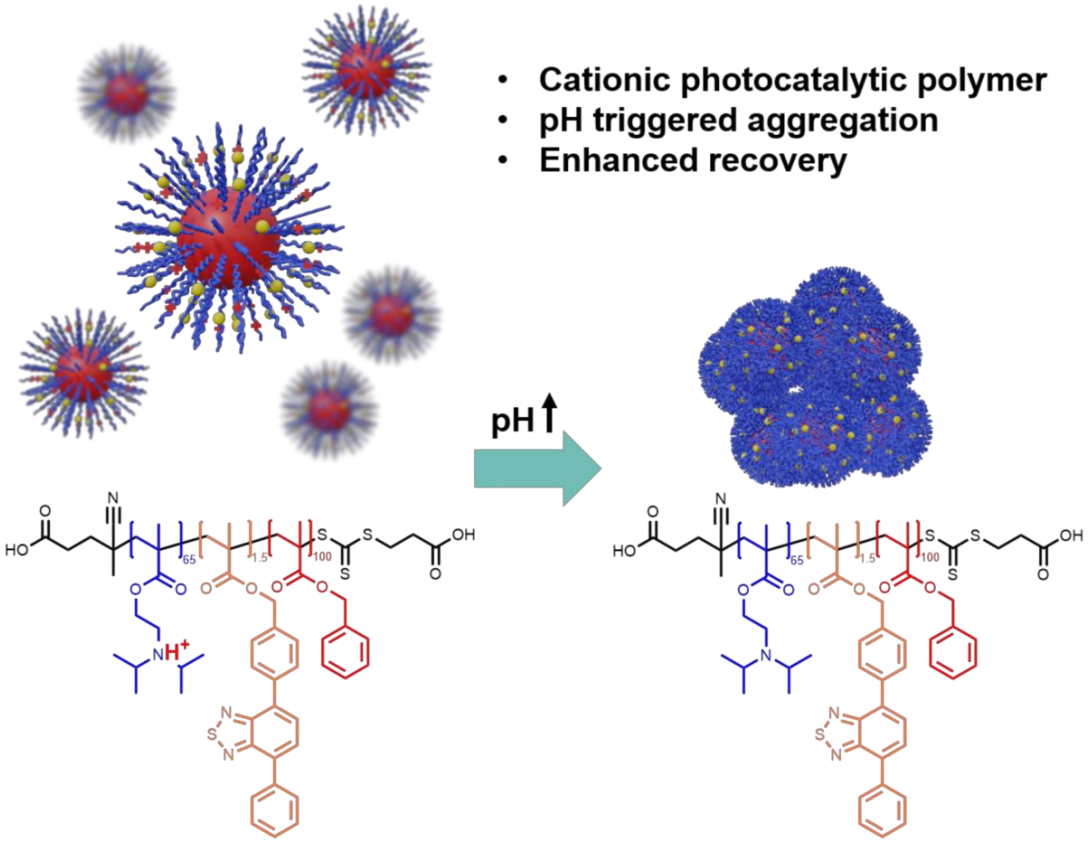

Figure 17. Schematic illustration of the switchable hydrophilicity of the pH-responsive polymer photocatalyst nanoparticles by adjusting the pH of the solvent.

pH-responsive photocatalytic polymer nanoparticles were synthesized using as aforementioned reversible addition-fragmentation chain transfer mediated polymerization induced self-assembly (RAFT-PISA) technique similar to reported in the literature[163], where a pH-responsive photocatalytic macro-chain transfer agent (CTA) poly(diisopropylamino ethylmethacrylate-*co*-*N*-(4-(7-phenylbenzo [*c*] [1,2,5] thiadiazol-4-yl)phenyl)methyl methacrylate) (P(DPA-*co*-Ph_2BTMA)) was synthesized

prior to its chain extension with hydrophobic benzyl methacrylate (BzMA) monomers. This creates a highly hydrophobic PBzMA core stabilized by protonated P(DPA-*co*-Ph_2BTMA) chains that tether from the surface of the core in acidic buffer conditions (Figure 18a). Transmission electron microscopy (TEM) was applied to confirm the spherical morphology of the nanoparticles (Figure 18b).

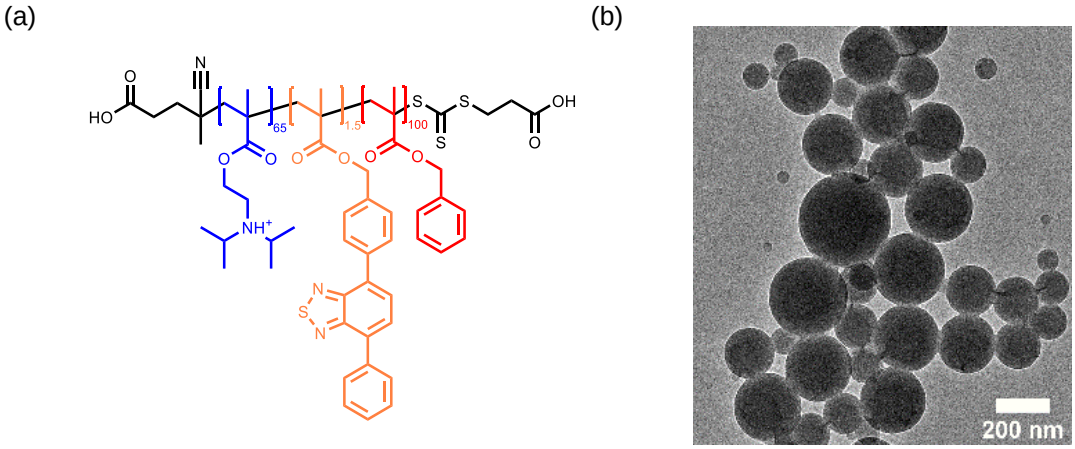

Figure 18. pH-responsive photocatalytic nanoparticles. (a) Molecular structure of designed photocatalytic NP-BT-PDPAH$^+$ nanoparticles. (b) TEM image of the nanoparticle dispersion.

^{1}H NMR (Figure 19), and FTIR (Figure 20) spectroscopy were used to examine the chemical compositions of photocatalytic polymer nanoparticles. The NMR spectrum illustrated the chemical structure of purified polymers, where no signals of monomers were observed. The aromatic proton peaks from the photocatalytic monomers were clearly visible at around 8 ppm, despite an extremely small amount of the photocatalytic monomer (0.9 mol%) was loaded.

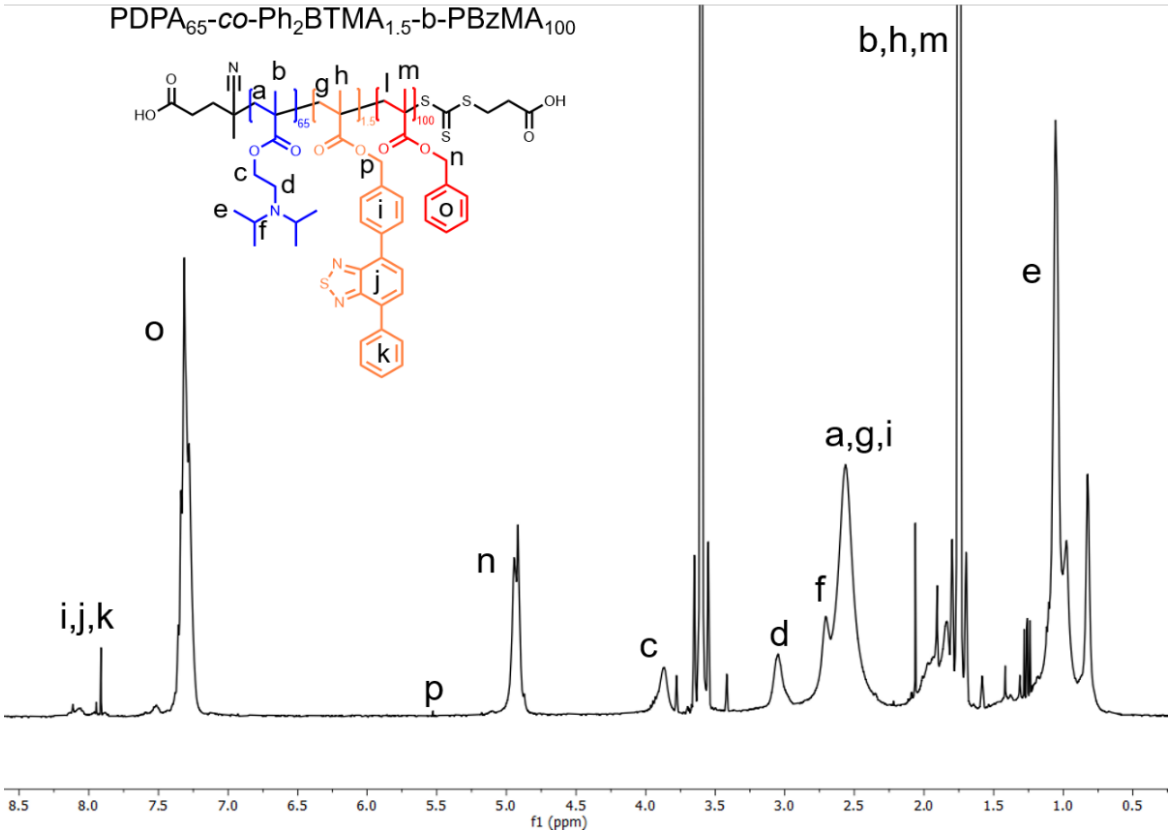

Figure 19. 1H NMR spectrum of NP-BT-PDPA in THF-d8 (400 MHz, at 298 K).

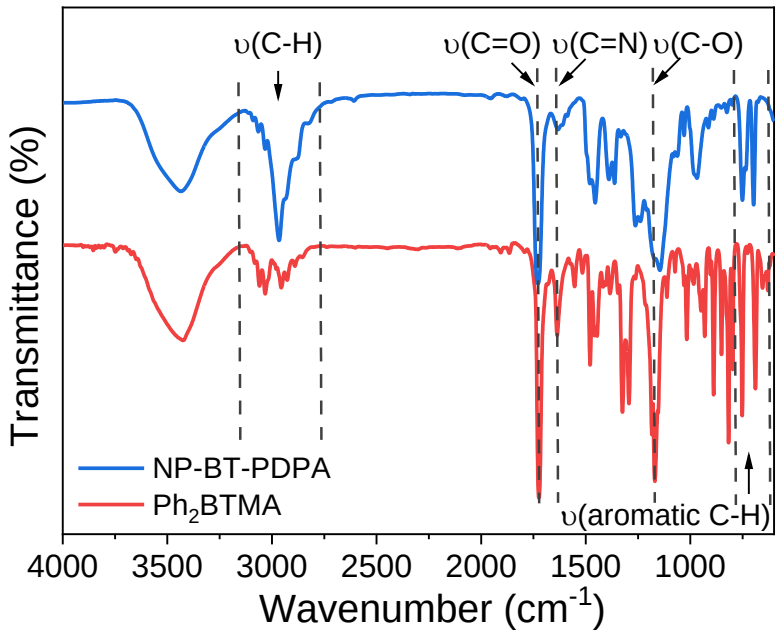

Figure 20. FTIR spectra of photocatalytic monomer Ph_2BTMA (red) and NP-BT-PDPA (blue).

The FTIR spectrum displayed aliphatic backbone (-CH_2- and -CH_3) stretch vibration from 2700 to 3100 cm^{-1}. In addition, typical signals at 1720, 1640, and 1170 cm^{-1} are attributed to carbonyl C=O stretching, C=N stretching, and C-O stretching, respectively. The signal at 610-710 cm^{-1} resulted from the aromatic CH stretch in the PBzMA cores and photocatalytic Ph_2BTMA moieties. The effect of the photocatalytic units on the FTIR spectrum is limited, because only 0.9 mol% of photocatalytic unit has been incorporated.

GPC (Figure 21) has been utilized to examine the molecular weight (M_n =10.4 kDa) of the polymer photocatalyst. The polymer photocatalytic nanoparticles were dissolved in THF-d_8 for GPC measurement and the dispersity of the polymer was determined to be 1.52. The high dispersity could result from the exit effect caused by the hydrophilic carboxylic acid end-group of the CTA.[164]

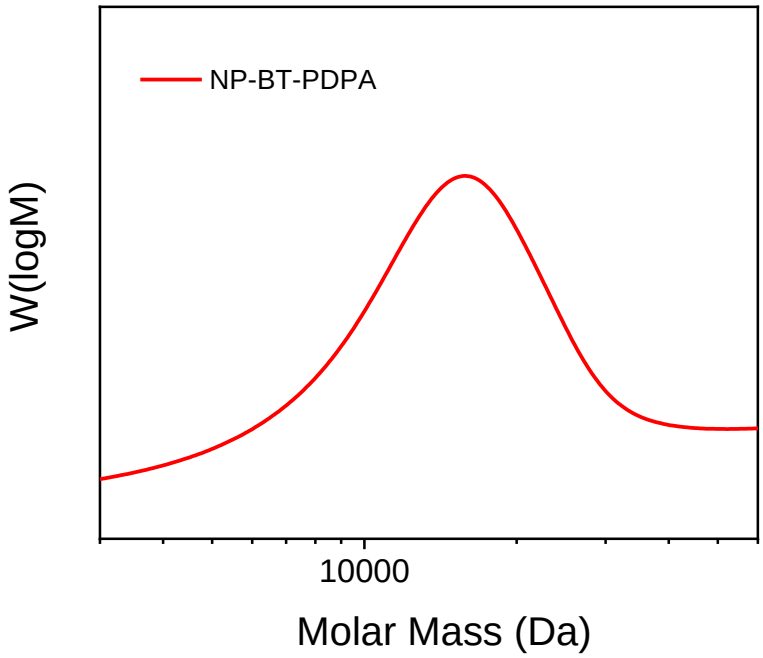

Figure 21. Molecular weight distribution of PDPA-*co*-PPh_2BTMA-*b*-PBzMA block copolymer (UV signal, *M*n = 10359 Da, *Đ* = 1.52, standard: polystyrene).

The hydrodynamic diameter of the photocatalytic material dispersed in acetate buffer (pH 4.0) was determined by DLS, displaying a size distribution centered at around 250 nm with a polydispersity of 0.214 (Figure 22).

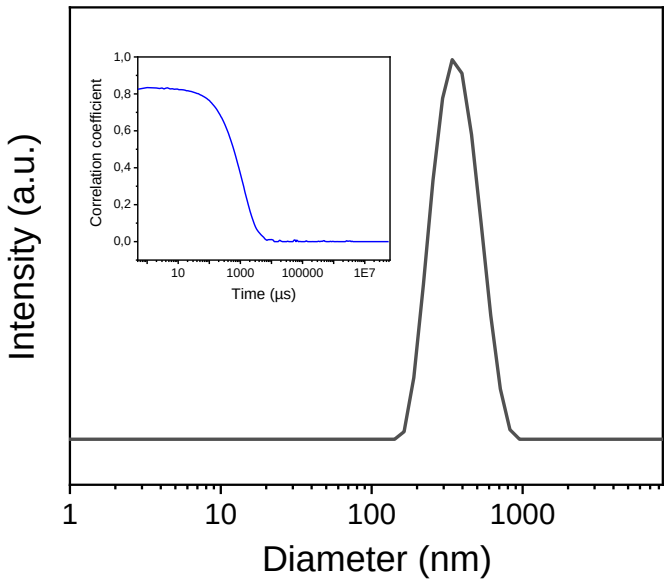

Figure 22. DLS measurement of NP-BT-PDPAH$^+$ dispersion in acetate buffer solution (pH 4.0, 0.1 mM) with a hydrodynamic diameter peaking at 340 nm and PDI = 0.214.

PDPA is a common and inexpensive polymer that can reversibly alter its solubility in water by responding to pH changes. The protonation of hydrophobic PDPA chains was simply generated through tuning the water pH below the pKa (pH 6.3, Figure 23) of the tertiary amine.

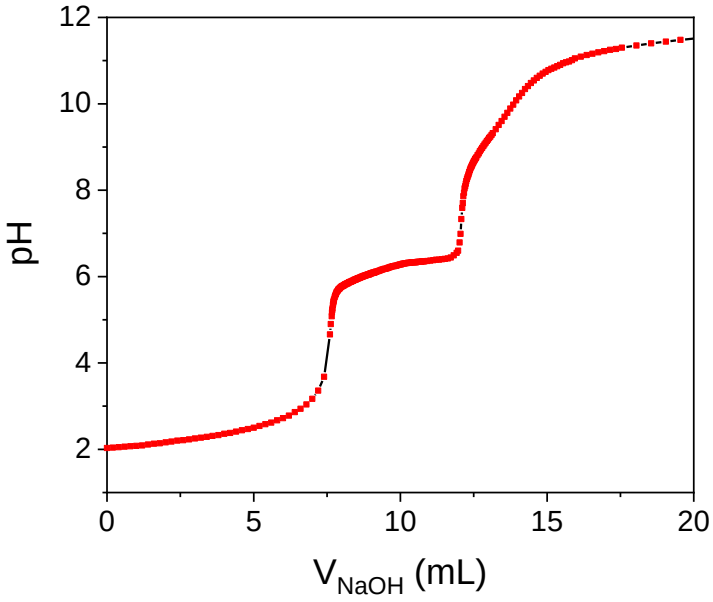

Figure 23. Titration curve of P(DPA-*co*-Ph$_2$BTMA) macroCTA.

In addition, the pH-triggered protonation/deprotonation was further investigated by zeta potential (Figure 24). NP-BT-PDPAH$^+$ exhibited a ca. +32 mV of zeta potential at pH 4.0, suggesting a stable positively charged colloid. Upon increasing the solvent pH, zeta potential decreased accordingly. At pH 7.0, a ca. +2 mV of zeta potential was observed, indicating an unstable neutral colloid with a rapid flocculation behavior, which agreed well with the pKa value of PDPA (ca. pH 6.3). With further increasing the pH, a negative ca. -36 mV zeta potential was obtained at pH 10.0 possibly due to the interaction between OH^- from buffer solution and the neighboring α-CH groups of tertiary amines acting as Brønsted-Lowry acids.

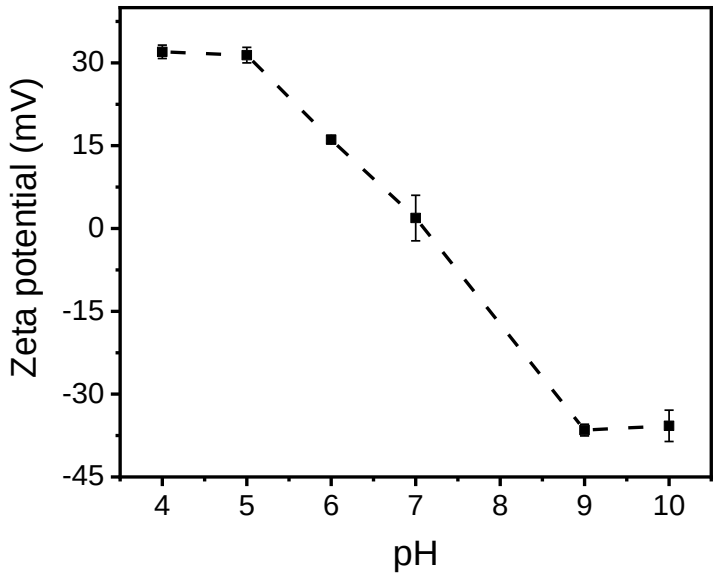

Figure 24. Zeta potential of NP-BT-PDPA dispersion as a function of pH value.

Moreover, the reversibility of the protonation/deprotonation process triggered by pH change was also confirmed by zeta potential (Figure 25), where the zeta potential reversibly switched from ca. +33 mV to -38 mV for 5 cycles by tuning pH between pH 4.0 and pH 10.0.

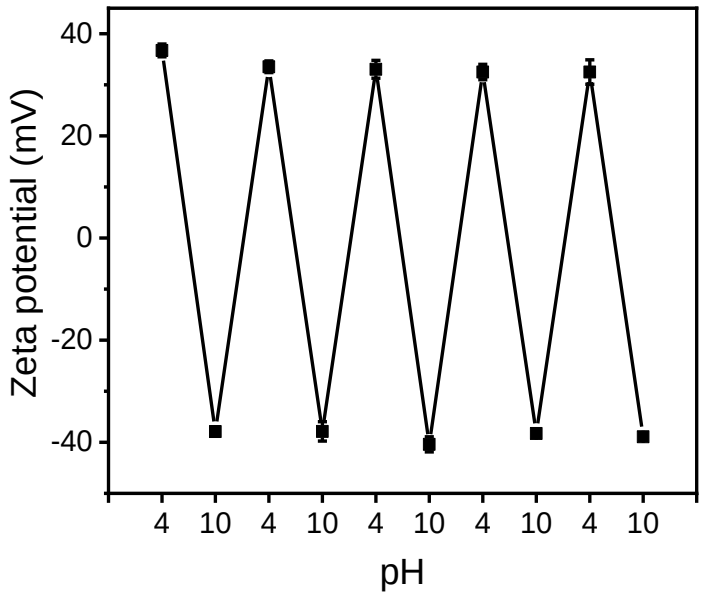

Figure 25. Zeta potential of nanoparticle in response to minute change of pH value for 5 cycles.

Pristine P(DPA-*co*-Ph_2BTMA)-*b*-PBzMA nanoparticles (marked as NP-BT-PDPA) are hydrophobic in neutral water, but upon treating with acid, the tertiary amine end groups of PDPA chains are protonated, leading to a full solvation of PDPA chains and a homogeneous dispersion of nanoparticles (marked as NP-BT-PDPAH^+). The proton cations on the tertiary amine can be reversibly removed by adjusting the pH value above the pKa and these photocatalytic nanoparticles can be simply recycled by centrifugation or sedimentation (Figure 26).

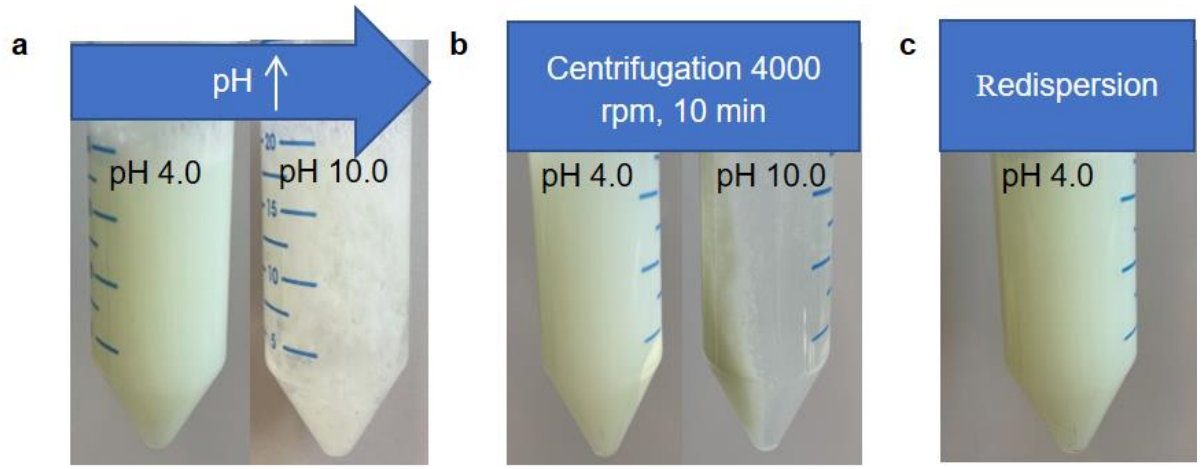

Figure 26. Photographs of (a) NP-BT-PDPAH^+ dispersion at pH 4.0 and after tuning the pH of NP-BT-PDPAH^+ dispersion to pH 10.0, (c) NP-BT-PDPAH^+ dispersion (pH 4.0) and NP-BT-PDPA dispersion (pH 10.0) centrifuged at 4000 rpm for 10 min, (c) redispersion of isolate NP-BT-PDPA nanoparticles to acetate buffer solution (pH 4.0).

The pH-dependent wettability change of NP-BT-PDPA has been monitored by the UV/Vis transmittance change of nanoparticle dispersion as a function of solvent pH value. As shown in Figure 27, the transmittance of the dispersion increased with the elevation of pH, where aggregations have been formed under basic conditions.

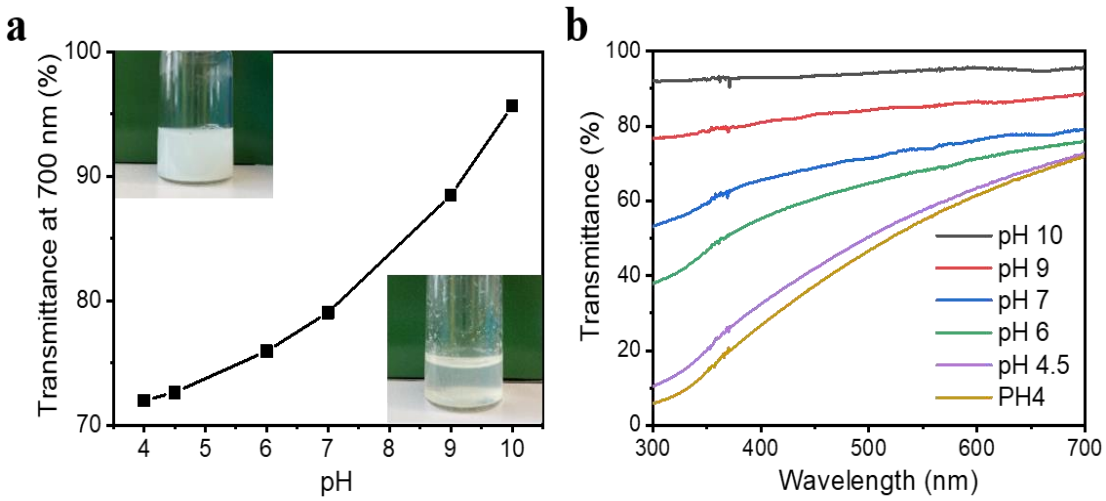

Figure 27. UV/Vis transmittance of NP-BT-PDPA dispersions as a function of pH value (a) Transmittance of NP-BT-PDPA dispersions from pH 4.0 to pH 10.0 at 700 nm. (b) UV/Vis transmittance spectra of NP-BT-PDPA dispersions from pH 4.0 to pH 10.0.

The optical properties of the photocatalytic material were visualized by UV/Vis spectra, displaying a broad absorption peak in the visible light region up to 600 nm and the peak position at around 390 nm is consistent with the literature[84,165] (Figure 28).

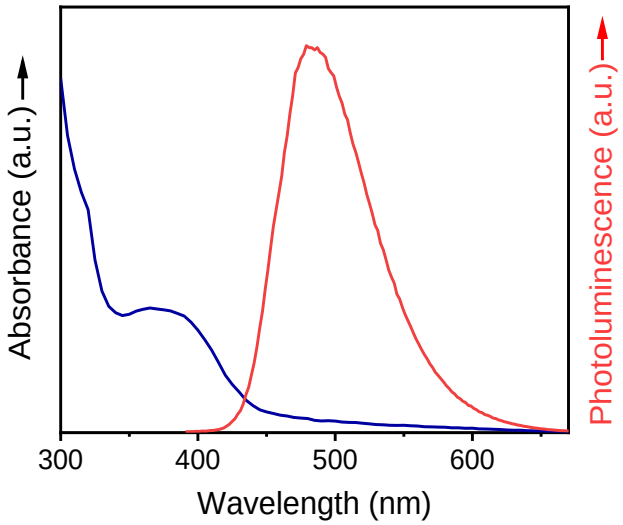

Figure 28. UV/Vis absorbance (blue) and emission (red) spectra.

The onset reduction potential of the photocatalytic unit diphenylbenzothiadiazole was determined to be -1.34 V vs. SEC (Figure 29) via cyclic voltammetry analysis, which agrees well with the value reported previously.[68]

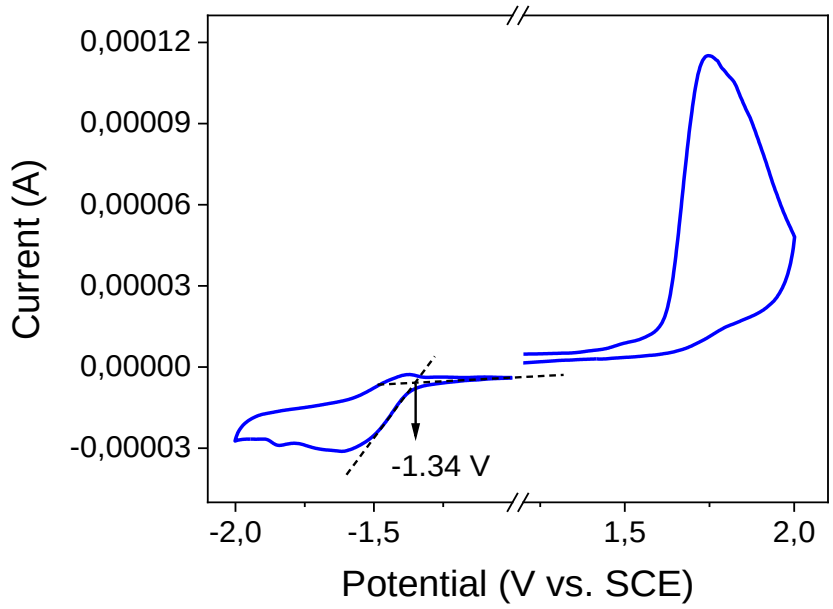

Figure 29. Cyclic voltammogram of Ph2BT with a scan rate of 0.1 V/s of 0.1 M NBu4PF6 in acetonitrile. Due to no smooth film formation on the working electrode and possible oxidation of the PDPA block, the cyclic voltammogram of NP-BT-PDPA polymer could not be measured. However, according to previous studies[68,165] the onset reduction potential of Ph_2BT units before and after incorporation into polymer structures remains at a similar level. Therefore, here we use the onset reduction potential of the Ph_2BT unit to represent the value for the polymer due to the challenges for sample preparation.

These NP-BT-PDPA nanoparticles are confirmed to be photoactive and can respond instantly to pH changes. Therefore, the photocatalytic reactivity of these nanoparticles has been further investigated.

2.2 Photocatalytic Reactions

The switchable hydrophilicity and photocatalytic nature of these newly designed photocatalytic polymer nanoparticles allow the investigation of photocatalysis in acidic aqueous medium.

2.2.1 Photocatalytic $K_2Cr_2O_7$ Reduction

Initially, the photocatalytic activity of NP-BT-PDPAH$^+$ has been demonstrated by photocatalytic reduction of Cr(VI) under visible light irradiation as a model reaction for heavy-metal-contaminated wastewater treatment. In a typical experimental set-up, an aqueous solution of $K_2Cr_2O_7$ was added to pH-responsive NP-BT-PDPAH$^+$ buffer dispersion (pH 4.0) prior to the irradiation of blue LED light. The reduction of Cr(VI) was monitored, in triplicate, by UV/Vis spectroscopy.

As illustrated in Figure 30a, the positively charged NP-BT-PDPAH$^+$ dispersion produced over 90% Cr(VI) reduction after 45 min of light exposure, whereas the control reaction without photocatalyst provided less than 20% conversion. It is worth noting that 55% of Cr(VI) reduction has been achieved using NP-BT-PDPAH$^+$ after 2 min of light irradiation without pre-adsorption, which shows an exceptionally high reduction rate compared to the state-of-the-art cationic conjugated polymer photocatalyst[111] and neutral photocatalytic hydrogels.[165]

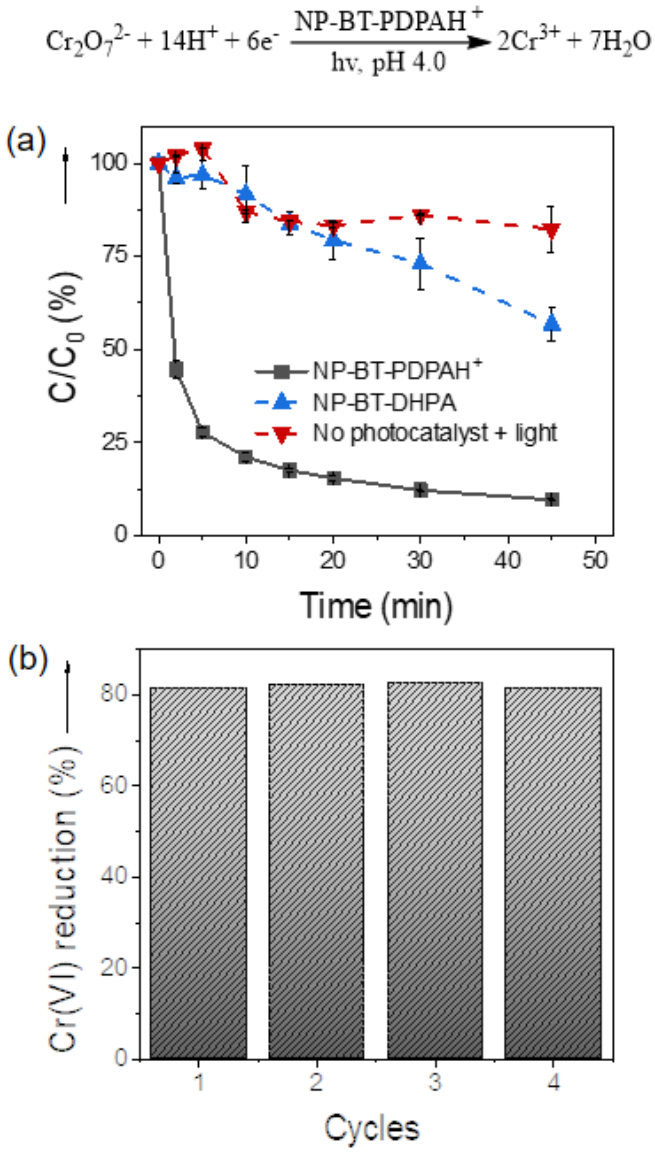

Figure 30. (a) Photocatalytic reduction of Cr(VI) in NP-BT-DHPA dispersion (pH 4.0), NP-BT-PDPAH$^+$ dispersion (pH 4.0), and without photocatalyst (pH 4.0) under blue LED irradiation (power: 17 mW/cm^2, λ=460 nm). C_0 is the initial concentration of Cr(VI) under dark conditions. C is the concentration of Cr(VI) with light irradiation after a certain time intervals. (b) Reusability of NP-BT-PDPAH$^+$ for repeated reduction of Cr(VI).

Furthermore, we have also investigated the Cr(VI) reduction (Figure 30a) using neutral polymer photocatalytic nanoparticles NP-BT-DHPA (poly(2,3-dihydroxypropyl methacrylate-*co*-*N*-(4-(7-phenylbenzo[*c*][1,2,5]thiadiazol-4-yl)phenyl)methyl methacrylate-*b*-benzylmethacrylate, where only 4% and 43% Cr(VI) reduction was facilitated after 2 and 45 min of light exposure, respectively. The turnover frequency[166] of these neutral NP-BT-DHPA nanoparticles at 5 min was calculated to be 20 times lower than that of cationic NP-BT-PDPAH$^+$ nanoparticles. This strongly

suggests that the cationic nature of NP-BT-PDPAH$^+$ has significantly accelerated the conversion rate. Typically, chemical compositions of Cr(VI) species highly depend on their concentrations and the pH value of the solution.[167,168] Under the present reaction condition at pH 4.0, two predominant species $HCrO_4^-$ and $Cr_2O_7^{2-}$ could present in the form of anions that show high affinities to cationic photocatalytic shell of NP-BT-PDPAH$^+$. Indeed, ion-ion interactions are the strongest non-covalent bond in chemistry.[169–171] This attractive nature of the cationic NP-BT-PDPAH$^+$ to the anionic $HCrO_4^-$ and $Cr_2O_7^{2-}$ substrates drives the substrate diffusion and leads to enhanced efficiency. Moreover, NP-BT-PDPAH$^+$ nanoparticles were subjected to repeated cycles of Cr(VI) reduction. No noticeable loss in Cr(VI) photoreduction efficiency was observed up to 4 cycles (Figure 30b and Figure 31d), demonstrating efficient and reusable photocatalytic nanoparticles.

Additionally, we have also investigated how the concentration of the photocatalytic materials and degassing process could affect the reduction efficiency, respectively. Here we have performed the kinetic study of Cr(VI) reduction using three different concentrations of the nanoparticles (0.5 mg/mL, 1 mg/mL, and 2 mg/mL) (Figure 31a). Interestingly the degassing process improved the Cr(VI) reduction efficiency using a lower concentration of nanoparticles (0.5 mg/mL). This is probably as the energy transfer to triplet oxygen generating singlet oxygen is more favorable at lower nanoparticle concentrations.

Cr(VI) photocatalytic reduction has been effectively achieved using charged photocatalytic nanoparticles with concentrations from 0.5 mg/mL to 2 mg/mL. A slightly more rapid reaction rate has been observed when using higher concentrations of nanoparticles. However, after degassing all reduction reactions were completed after 30 min at all concentrations. Therefore, the particle concentration at 1 mg/mL has been selected for photoreduction of Cr(VI) (Figure 31c).

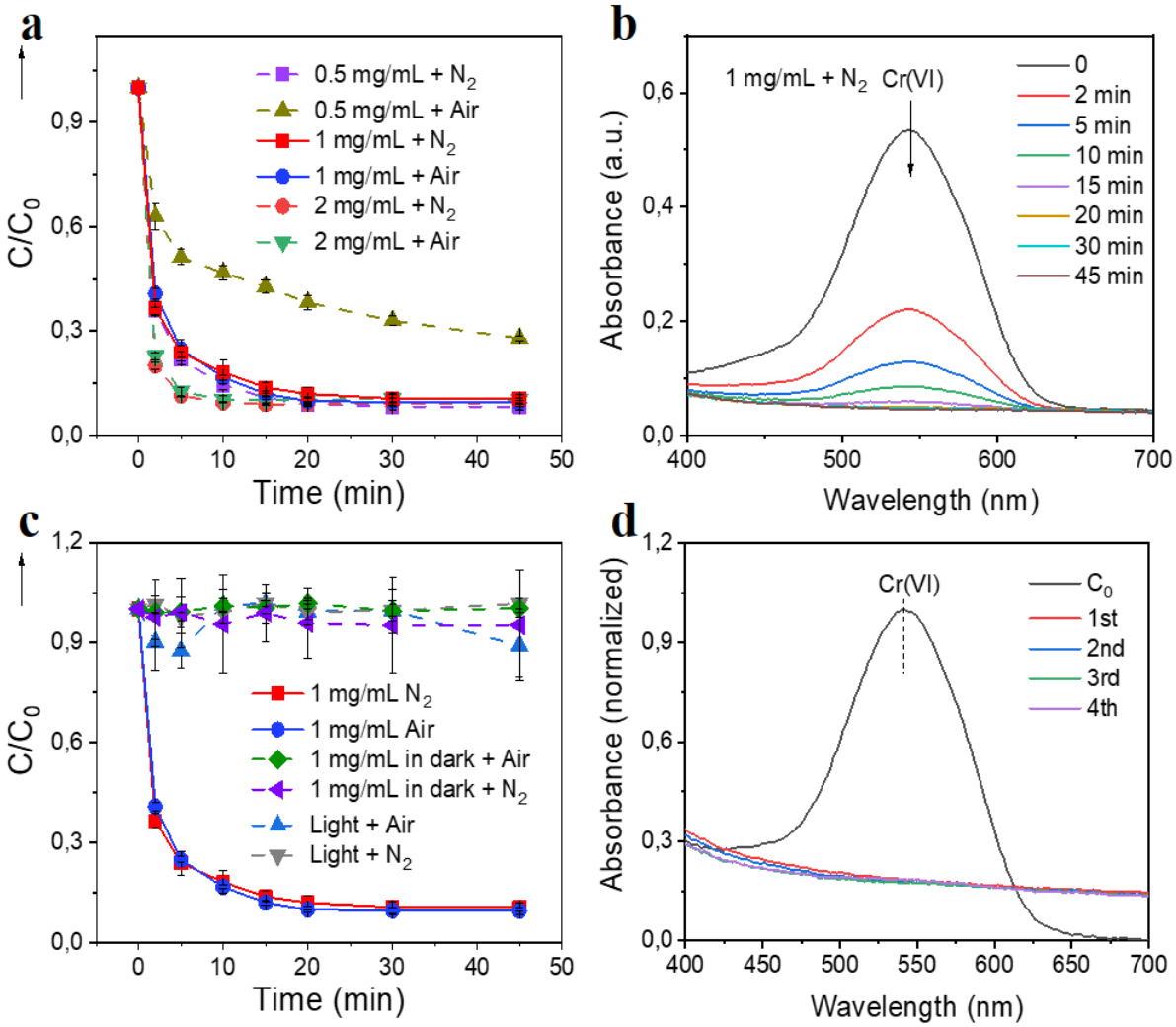

Figure 31. Detailed kinetic profiles of Cr(VI) reduction : (a) concentration dependence of NP-BT-PDPAH$^+$ on the conversion of the Cr(VI) reduction over time, as well as the effect of atmosphere (N_2 and air). (b) The UV/Vis spectrum of kinetic study at NP-BT-PDPAH$^+$ concentration of 1 mg/mL after degassing as an example. (c) Control experiments without photocatalyst and without light irradiation, (d) Recycling experiment UV/Vis spectra.

2.2.2 Photocatalytic Sulfide Oxidation

In addition to inorganic heavy metal reduction, the switchable polymer photocatalytic nanoparticles were further applied for various organic transformations. Oxidation reactions, as a fundamental class of organic transformations, have been intensively investigated. Particularly, the sulfoxidation of sulfides is of great importance in many fields, including the pharmaceutical industry,[172] wastewater treatment,[165] as well as crude oil desulfurization.[173] Several different photocatalysts[74,165,174,175] have been utilized for sulfide oxidation, where monoxide products has been produced.

Here, we have utilized the well-dispersed NP-BT-PDPAH$^+$ photocatalyst to induce the oxidation of methyl phenyl sulfide in water. The effect of the concentration of photocatalytic material on the oxidation efficiency has been revealed by applying three different concentrations at 1 mg/mL, 2.5 mg/mL, and 4 mg/mL for sulfide oxidation as shown in Figure 32a. The concentration of 2.5 mg/mL has been selected as the standard reaction parameter because of the better balance between material quantity and reaction conversion rate.

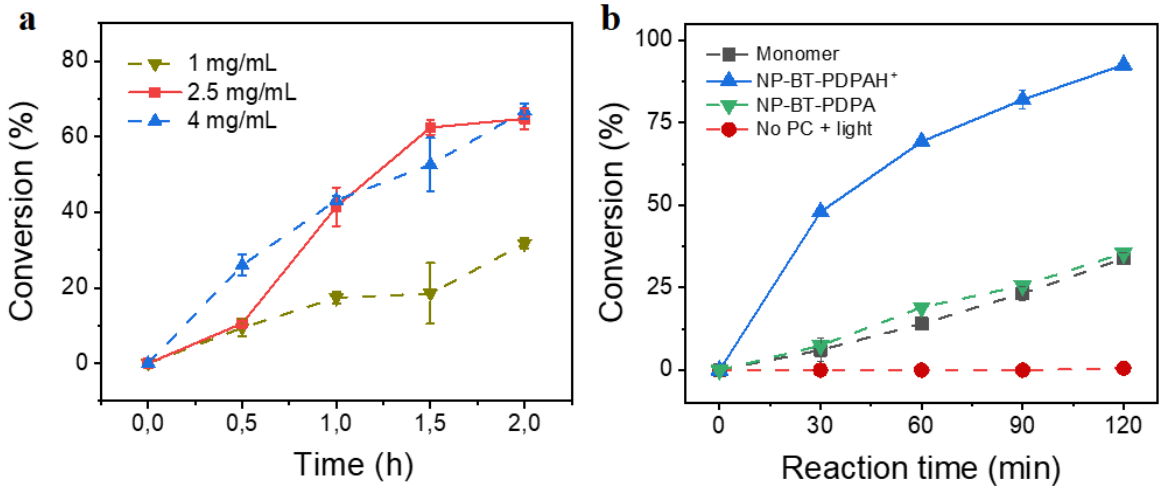

Figure 32. Sulfide oxidation (a) kinetic profiles of the photocatalytic sulfide oxidation (80 mM) reaction including NP-BT-PDPAH$^+$ as photocatalyst at concentrations of 1, 2.5, and 4 mg/mL. (b) Kinetic study of sulfide (50 mM) oxidation using NP-BT-PDPAH$^+$ (2.5 mg/mL, blue), Ph_2BTMA photocatalyst monomer (dark grey), NP-BT-PDPAH (green) with an identical concentration of photocatalytic units (45 µg/mL), as well as control reaction without photocatalyst (red). Yield determined by GCMS in triplicate.

A high yield of 93% and selectivity of over 99% monoxide product was observed after a 2 h reaction (Table 1 entry 1), which significantly shortens the reaction time compared to the state-of-art photocatalyst (e.g. 18 h, 99% conversion, 93% selectivity[74]). Control reactions without photocatalyst or in the dark did not result in conversion (Table 1 entries 2 & 3). Furthermore, the activation/deactivation of photocatalytic moieties as a function of the pH of the reaction medium has also been investigated by comparing the sulfoxidation using hydrophobic NP-BT-PDPA dispersion as photocatalyst. A reduced yield (< 36%) was obtained using NP-BT-PDPA dispersion (Table 1 entry 4) after 2 h of light irradiation. Interestingly, a similar yield (34%) and reaction kinetics (Figure 32b) of sulfoxidation was obtained applying

hydrophobic photocatalytic monomers (Table 1 entry 5) at an identical photocatalyst content compared to NP-BT-PDPA nanoparticles. NP-BT-PDPA nanoparticles and photocatalytic monomers are highly hydrophobic, acting as heterogeneous photocatalysts in aqueous solution. Conversely, the greater yield of the sulfoxidation obtained using NP-BT-PDPAH$^+$ dispersion suggests that the pseudo-homogeneous state of photocatalytic sites significantly promotes the reactivity.

Table 1. Photocatalytic sulfoxidation using NP-BT-PDPA in either pH 4.0 or pH 9.0 buffer medium. Reactions were undertaken under blue LED light irradiation (power: 17 mW/cm^2, λ = 460 nm).

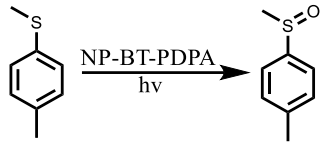

Entry	Catalyst	Light	Time/h	Yield
1	NP-BT-PDPAH$^+$	+	2	93%
2	NP-BT-PDPAH$^+$	-	2	0%
3	-	+	2	0.5%
4	NP-BT-PDPAH	+	2	36%
5	Monomer	+	2	34%

Reaction conditions: Methyl p-tolyl sulfide (50 mM), NP-BT-PDPA (2.5 mg/mL, 45 µg/mL photocatalyst), 4 mL buffer solution (Entry 1, 2, 3, and 5: acetate buffer pH 4.0; Entry 4: carbonate-bicarbonate buffer pH 9.0), RT, 2 h, yield determined by GC-MS.

Scavenger tests were further performed using sodium azide, potassium iodide, isopropanol, copper chloride, and benzoquinone as $^1O_2$, e^-, $\cdot OH$, h^+ and $\cdot O_2^-$ scavenger, respectively. Control reactions in presence of scavengers revealed that $^1O_2$, h^+ and $\cdot O_2^-$ are crucial for sulfoxidation in the presence of photocatalytic nanoparticles (Table 2 and Figure 33).

Table 2. Control experiments of the photocatalytic sulfoxidation

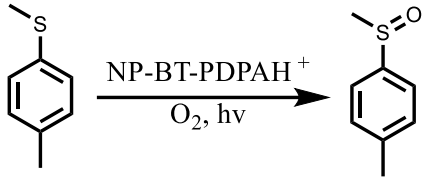

Entry	Changes to standard conditions[a]	Conversion(%)[b]	Yield (%)[b]
1	None	99.37	93.02
2	No light	0	0
3	No NP-BT-PDPAH$^+$	5.5	5.5
4	No oxygen	96.45	95.55
5	NaN_3	98.97	98
6	Isopropanol	99.32	97.64
7	KI	27.49	27.49
8	$CuCl_2$	9.06	8.8
9	1,4-benzoquinone	52.75	38

[a] Standard conditions: 2.5 mg NP-BT-PDPAH$^+$ nanoparticles in 1 mL acetate buffer (pH 4.0), 0.022 mmol Methyl p-tolyl sulfide, oxygen balloon, blue LED (λ_{max} = 460 nm) at power of 17 mW/cm^2, 4 h, temperature = 18 °C.

[b] Conversion and yield determined by GCMS.

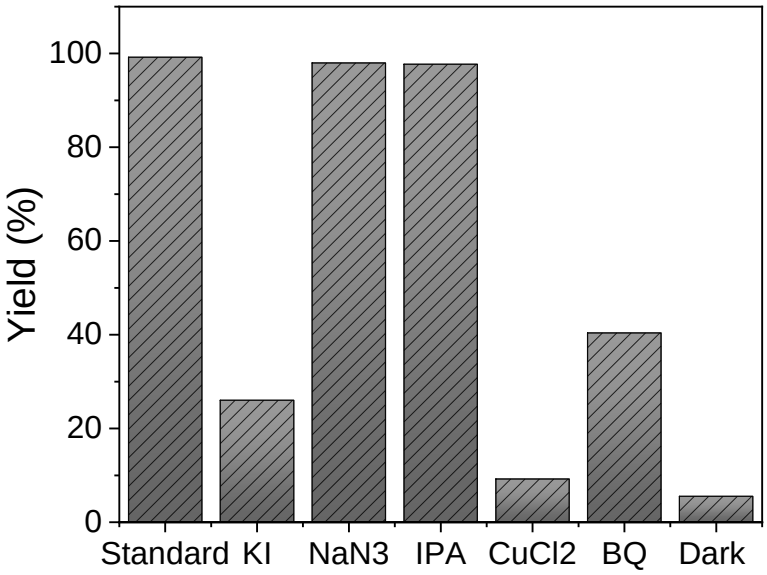

Figure 33. Scavenger tests of sulfoxidation using sodium azide, potassium iodide, isopropanol, copper chloride, and benzoquinone as $^1O_2$, e^-, $\cdot OH$, h^+ and $\cdot O_2^-$ scavenger, respectively. Yield determined by GCMS.

Furthermore, NP-BT-PDPAH$^+$ were subjected to repeated cycles of sulfide oxidation through acidic/basic solvent switching, therefore, nanoparticle precipitation and redispersion. No perceptible loss in sulfide oxidation efficiency was observed after 4 cycles, despite a slight loss of nanoparticles after 2nd run of the recycling experiments (Figure 34c and d). Nevertheless, the chemical structures of nanoparticles after being used for repeated cycles of reactions have been determined by FTIR (Figure 34e) and no obvious change in the structure has been observed. In addition, the photocatalytic nanoparticles remained spherical after the completion of 4 cycles of reaction as characterized by TEM measurement (Figure 34f).

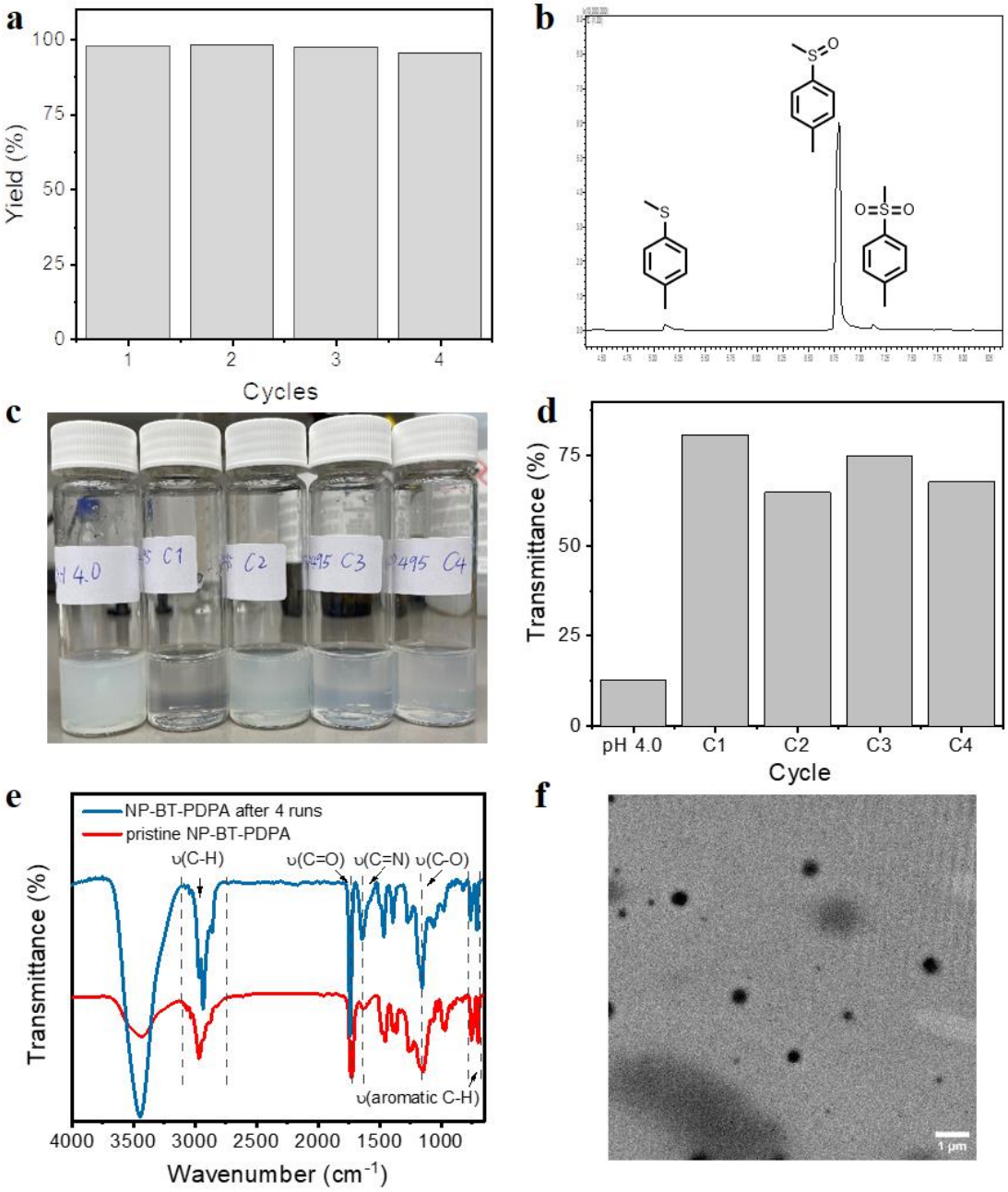

Figure 34. Recycling experiment for sulfoxidation determined by GCMS. (a) The result indicates no noticeable decrease in product yield after 4 cycles of reactions. (b) GCMS spectrum of sulfoxidation product after 4th run of reaction. (c) supernatants were collected after each run of reaction (pH 4.0, cycle 1, and cycle 2: centrifugation 7000 rpm, 10 min; cycle 3-4: centrifugation 10000 rpm, 10 min). (d) Transmittance (at 700 nm) of the supernatants of sulfide oxidation recycling tests corresponding to figure (c). (e) FTIR spectra of nanoparticles before and after 4 cycles of repeat experiments. (f) TEM image of nanoparticles after 4 cycles of repeat experiments.

2.2.3 2-Furoic Acid Oxidation

NP-BT-PDPAH$^+$ is capable of efficiently generating $^1O_2$ (Figure 35) confirmed by EPR measurement, which has been widely used to drive oxidation reactions.

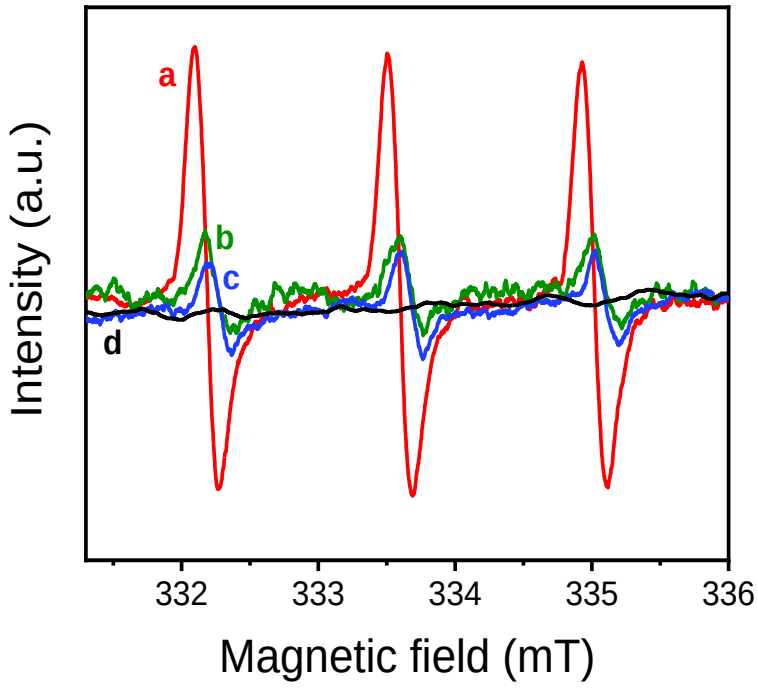

Figure 35. Electron paramagnetic resonance (EPR) spin trapping spectra of TEMP-$^1O_2$ generated under different conditions. (a) NP-BT-PDPAH$^+$ (1 mg/ml), Tetramethylpiperidine (TEMP, 0.1 M), O_2 . (b) NP-BT-PDPA (1 mg/ml), TEMP (0.1 M), O_2. (c) TEMP (0.1 M), O_2. (d) NP-BT-PDPAH$^+$ (1 mg/ml), TEMP (0.1 M), N_2. All the samples were irradiated under blue LED for 1 h before measurement.

2-furoic acid, as a well-known $^1O_2$ trap, was effectively oxidized to 5-hydroxy-2(5H)-furanone in the presence of oxygen with a yield of > 99% after 20 h. Control reactions (Table 3) in the closed air condition, in dark, and without photocatalyst produced 30%, < 1%, and < 1% of yield, respectively, indicating oxygen and photocatalyst with light irradiation are required to facilitate sufficient $^1O_2$ generation.

Table 3. Control experiments of the photocatalytic 2-furoic acid oxidation

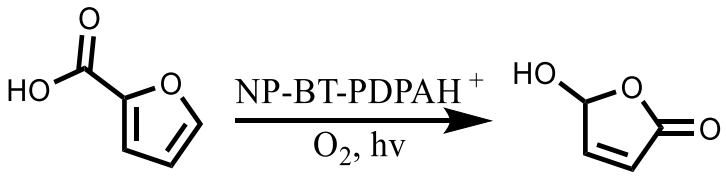

Entry	Changes to standard conditions[a]	Conversion(%)[b]	Yield (%)[b]
1	None	>99	>99
2	No light	<1	<1
3	No NP-BT-PDPAH$^+$	<1	<1
4	No oxygen	30	30

[a] Standard conditions: 2.5 mg NP-BT-PDPAH$^+$ nanoparticles in 1 mL acetate buffer (pH 4.0), 0.134 mmol 2-furoic acid, oxygen balloon, blue LED (λ_{max} = 460 nm) at power of 17 mW/cm^2, 20 h, temperature = 18 °C.

[b] Conversion and yield determined by ^{1}H NMR.

The reaction efficiency has been slightly improved by increasing the dose of photocatalytic nanoparticles from 1 mg/mL to 2.5 mg/L and 4 mg/mL, however, only negligible difference has been observed for concentrations at 2.5 mg/mL and 4 mg/mL (Figure 36a). In order to have efficient photocatalytic performance as well as no high cost of the photocatalytic material, we have applied the photocatalytic nanoparticles for 2-furoic acid oxidation at a concentration of 2.5 mg/mL. NP-BT-PDPAH$^+$ nanoparticles have facilitated over 95% conversion of 2-furoic acid up to five 24 h-cycles without losing the conversion efficiency (Figure 36b and c), suggesting a stable and efficient photocatalytic material for photooxidation reaction.

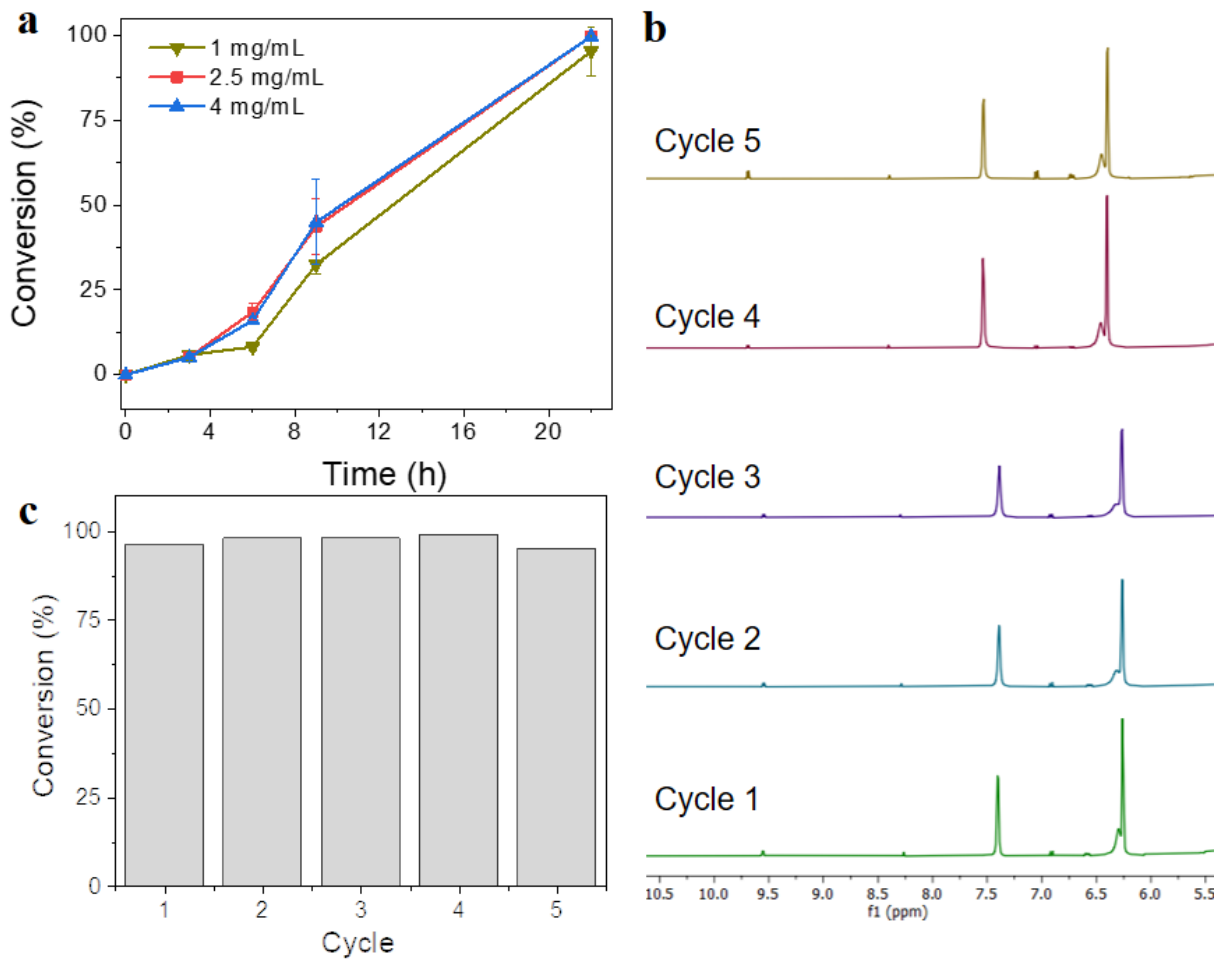

Figure 36. 2-Furoic acid oxidation (a) kinetic profiles of the photocatalytic 2-furoic acid oxidation reaction including NP-BT-PDPA H^+ as photocatalyst at concentrations of 1, 2.5, and 4 mg/mL. (b) ^1H NMR spectra of the recycling experiments, showing high conversion of 2-furoic acid oxidation. (c) Recycling experiment for 2-furoic acid oxidation determined by ^1H NMR spectroscopy (700 MHz, at 298 K). The result illustrates no noticeable decrease in product yield after 5 cycles of 24 h reactions.

Moreover, extremely high material recovery was maintained throughout the recycling tests (Figure 37), suggesting the high recyclability and stability of NP-BT-PDPAH^+ photocatalyst. Additionally, no obvious alternation in the chemical structure of the photocatalytic nanoparticles has been detected with FTIR measurement after the completion of the recycling experiment. The spherical morphology of the photocatalytic nanoparticles has not been changed after 5 cycles of recycling experiments. It is worth noting that consideration of substrate choice is required for the proper recycling of these photocatalytic nanoparticles.

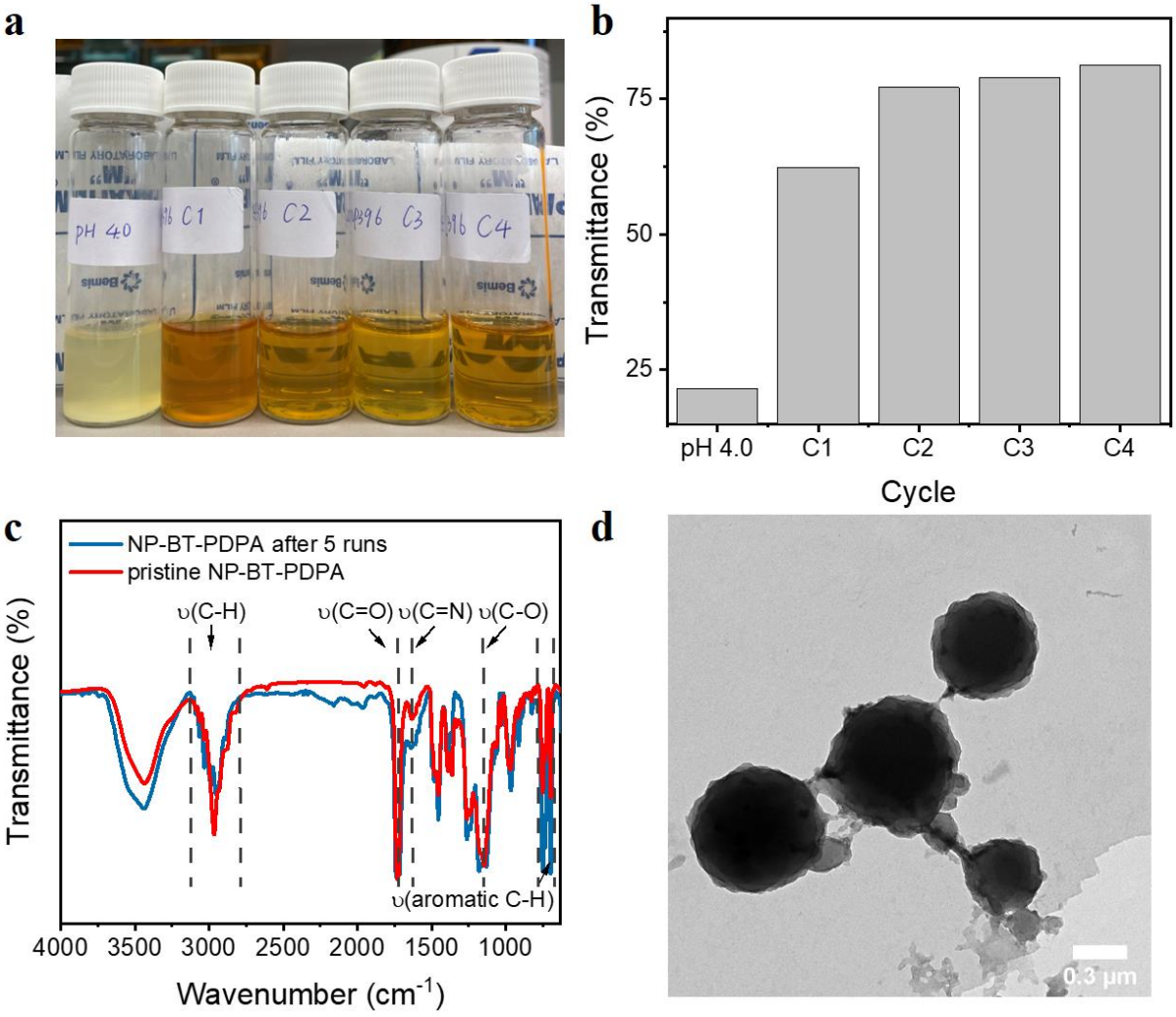

Figure 37. 2-furoic acid oxidation (a) Supernatants collected after each run of reaction (pH 4.0, cycle 1-4: centrifugation 7000 rpm, 10 min. (b) Transmittance (at 700 nm) of the supernatants of 2-furoic acid oxidation recycling tests corresponding to figure (a). (c) FTIR spectra of nanoparticles before and after 5 cycles of 24 h repeating photocatalysis experiments. (d) TEM image of nanoparticles after 5 cycles of repeat experiments.

2.2.4 Photocatalytic Alkylation of 3-Methylindole and β-Nitrostyrene

The promising performance of NP-BT-PDPAH$^+$ in the photocatalytic reductive and oxidative transformations has encouraged us to examine its potential in performing redox reactions. Indole has been widely used as an important building block for the production of biologically active compounds.[176,177] The N-1, C-2 to C-6, or C-7 positions of indole can be substituted to produce versatile indole derivatives, demonstrating a diverse scaffold for drug design.[178–181] Recently, a new strategy for the photocatalytic production of Friedel-Crafts alkylation at the C-3 position of indoles through the reaction of indoles and nitroalkenes has been reported, where water has

been used as a green solvent.[182] However, a relatively high temperature (60 °C) was required to accelerate these reactions. Therefore, we have investigated the radical-mediated Friedel-Crafts alkylation at room temperature to further verify the versatility of NP-BT-PDPAH$^+$. Surprisingly, our attempts showed that the coupling at the C-3 position of indole derivatives proceeded under blue light irradiation without photocatalyst at ambient temperature. The high yield in the absence of NP-BT-PDPAH$^+$ may proceed through a free radical pathway proposed by a previous investigation, where the 1,3 H shift of indole was activated by blue light irradiation followed by the generation of an indole radical to initiate the coupling reaction.[183] However, no products with substituent at the C-2 position of indole molecule have been reported in previous studies, possibly because of the low reactivity of the C-2 position of indole.[182–184]

Indole derivatives substituted at the indole C-2 and C-3 positions have been widely applied as target-based anti-cancer inhibitors and some of these therapeutics have been approved by FDA.[181] In particular, indole-based tubulin inhibitors are of great importance that inhibit the polymerization of tubulin, thereafter suppress mitosis, and induce apoptosis of cancer cells.[179–181] In our investigation, 3-methyl indole has been selected as a simple C-3 substituted model indole derivative, where additionally the aforementioned 1,3 H shift process initiated by light may be suppressed. Here, the alkylation of 3-methyl indole and β-nitrostyrene proceeded to afford a 70% yield by adding NP-BT-PDPAH$^+$ (Table 4), where the control reaction proceeded with a 19% yield without photocatalyst. Without light illumination, no coupling product was formed after 20 h. Although oxidation byproducts of 3-methyl indole and direct [2+2] addition of β-nitrostyrene were observed, photoredox-induced alkylation was still dominant.

Table 4. Control experiments of the photocatalytic Friedel-Crafts alkylation

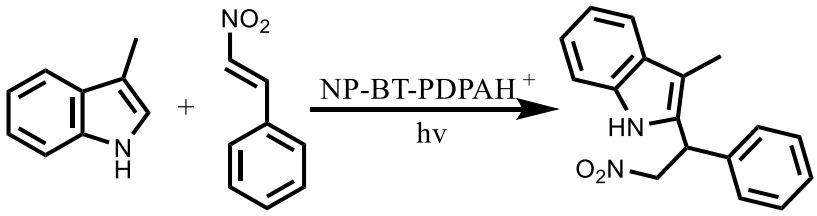

Entry	Changes to standard conditions[a]	Conversion(%)[b]	Yield (%)[b]
1	None	80	70
2	No light	0	0
3	No NP-BT-PDPAH$^+$	80	18.7
4	NaN_3	63	30
5	isopropanol	90	74
6	KI	79	41
7	$CuCl_2$	70	43
8	1,4-benzoquinone	50	39

[a] Standard conditions: 2.5 mg NP-BT-PDPAH$^+$ nanoparticles in 1 mL acetate buffer (pH 4.0), 0.02 mmol 3-methyl indole (1 equiv.), 0.02 mmol nitrostyrene (1 equiv.), under nitrogen environment, blue LED (λ_{max} = 460 nm) at power of 17 mW/cm^2, 14 h, temperature = 18 °C.

[b] Conversion and yield determined by GCMS.

A possible mechanism[182] of this C-C coupling is illustrated in Figure 38. Upon visible-light irradiation, the photocatalyst was excited and 3-methyl indole gave an electron to the highest occupied molecular orbital (HOMO) of the photocatalyst, generating a radical. The resultant 3-methylindole radical reacted with the double bond of β-nitrostyrene to produce a radical intermediate. This intermediate was further reduced by the photo-promoted electron in the lowest unoccupied molecular orbital (LUMO) of the photocatalyst giving a negatively charged intermediate. After protonation, the final coupled product was obtained.

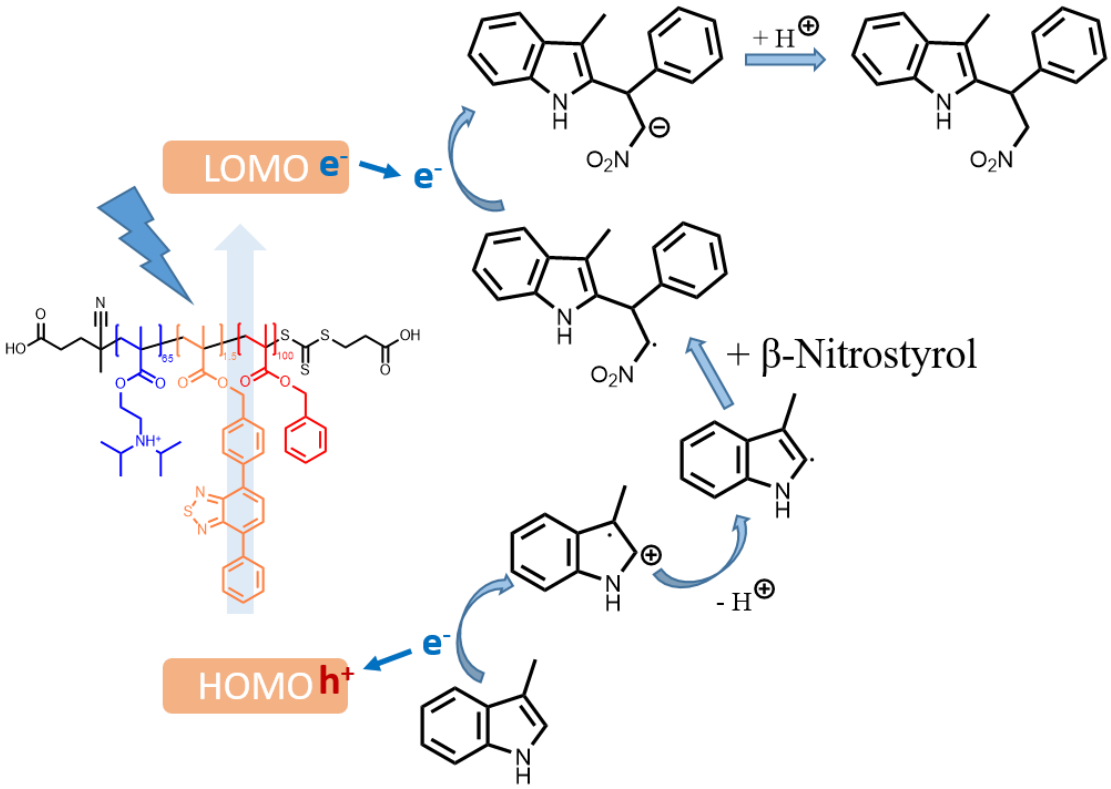

Figure 38. Proposed mechanism in the literature[189] of photocatalyzed alkylation in the absence of oxygen.

2.3 Conclusion

In summary, we have demonstrated novel pH-responsive polymer photocatalytic nanoparticles, containing diisopropylamino moieties as the sensitive functional groups and a small portion of photocatalytic moieties. pH-triggered hydrophobicity change of the stabilizing PDPA block enables controllable photocatalysis in an aqueous environment. In acidic conditions (pH 4.0) below the pKa of the PDPA block, the photocatalytic moieties are in a pseudo-homogeneous state facilitating effective catalytic activity towards both inorganic and organic transformations, including photo-reduction of Cr(VI) and photo-redox Friedel-Crafts alkylation of indole derivative. These reactions exhibited a nanoparticle concentration dependence. Moreover, the charged $PDPAH^+$ block is capable of not only enhancing the dispersibility of the nanoparticles, but also accelerating photocatalytic reactions of anionic substrates owing to charge attraction interactions. Furthermore, by simply tuning the pH value above the pKa of the stabilizing PDPA block, photocatalytic nanoparticles with unaltered morphology and composition have been recycled, allowing a sustainable

performance. This strategy produces highly effective polymeric photocatalytic nanoparticles with great photocatalytic performance, switchability, and recyclability.

2.4 Experimental Section

2.4.1 Materials

All chemicals and solvents were purchased from chemical suppliers and used without further purification unless specifically noted. Benzyl methacrylate (BzMA, 98%) was obtained from TCI. 4-((((2-carboxyethyl)thio)carbonothioyl)thio)-4-cyanopentanoic acid (CCCP, 95%) was purchased from Boron Molecular. 2-(Diisopropylamino)ethyl methacrylate (DPA, 97%), 4,4'-azobis(4-cyanovaleric acid) (ACVA, 98%), potassium dichromate ($K_2Cr_2O_7$, 99%), methyl *p*-tolyl sulfide (99%), 2-furoic acid (98%), 3-methylindole (98%), and β-nitrostyrene (99%) were purchased from Sigma Aldrich. Diphenylcarbazide (DPC), THF-d8 (99.5 atom % D) was acquired from VWR.

2.4.2 Characterization Methods

^{1}H NMR and ^{13}C NMR spectra were measured by Bruker Avance 400 and 700 MHz. UV-Vis transmittance spectra were taken from a Cary 60 UV/Vis spectrometer. UV/Vis absorption and emission were monitored by a plate reader. The hydrodynamic diameter of the photocatalytic nanoparticles was determined by Zetasizer Nano ZS. Gas chromatograms and corresponding mass spectra were taken from GCMS-QP-2010 Ultra. FTIR spectra were measured using a Bruker Tensor II FTIR spectrometer. TEM was conducted using a JEM-1400 Transmission Electron Microscope. Samples were prepared by dispersing the particles in 0.01 mM pH 4.0 buffer solution (0.1 wt%) and applying them to carbon coated copper grids. The particles were stained using uranyl acetate stain allowing us to better visualize the particles. Zeta potential was examined by applying Zetasizer Malvern, Nano Z.

2.4.3 Synthesis of Photocatalytic Monomer

Step 1 (4-bromo-7-phenylbenzo[c][1,2,5]thiadiazole): 4,7-dibromobenzo [c][1,2,5]thiadiazole (553 mg, 4.54 mmol, 1 eq.) and phenylboronic acid (2 g, 6.8 mmol, 1.5 eq.) were charged in a 100 mL Schlenk flask and dissolved in 18 mL of toluene, 8 mL of 2.0 M aqueous Na_2CO_3 solution and 8 mL of ethanol solvent mixture. Catalyst $Pd(PPh_3)_4$ (157 mg, 136 μmol, 0.03 eq.) was added after degassing by argon (Ar) bubbling for 20 min and the solution was vigorously stirred at 90 ˚C for 48 h under Ar ambient. After the completion of the reaction, the mixture was cooled to room temperature and extracted with dichloromethane (4 × 20 mL). The combined organic

phases were washed with brine and dried over anhydrous $MgSO_4$. After filtration the solvent was removed by rotary evaporation and the final green solid product was afforded by column chromatography (silica gel, petroleum ether/dichloromethane 3/1). Step 2 2 (4-(7-phenylbenzo[c][1,2,5]thiadiazol-4-yl)hydroxymethyl): The crude product from step 1 (500 mg), 4-(hydroxymethyl) phenylboronic acid pinacol ester (440 mg, 1.88 mmol, 1.10 eq.) were dissolved in 7.5 mL of 1,4-dioxane and 3 mL of a 2.0 M aqueous Na_2CO_3 solution in a 50 mL Schlenk tube. After degassing by Ar bubbling for 20 min $Pd(PPh_3)_4$ (39.3 mg, 34.3 µmol, 0.02 eq.) was added in an Ar counter stream. The solution was vigorously stirred and refluxed at 100 °C overnight under Ar. After cooling to room temperature, the resulting mixture was then extracted with dichloromethane (3 x 15 ml). The combined organic phases were washed with brine (50 ml) and dried over anhydrous $MgSO_4$. After filtration and rotary evaporation of solvents the residue was purified by column chromatography on silica gel (petroleum ether/dichloromethane 1/1), giving green-yellowish product.

Step 3 (N-(4-(7-phenylbenzo[c][1,2,5]thiadiazol-4-yl)phenyl)acrylate): Under Schlenk condition in a 50 ml Schlenk tube 4-(7-phenyl-benzo[c][1,2,5]thiadiazol-4-yl)hydroxymethyl (200 mg, 659 µmol, 1.00 eq.), trimethylamine (119 µL, 856 µmol, 1.3 eq.) and dichloromethane (5 ml) were stirred for 10 min at room temperature under Ar. Acryloyl chloride (64 µL, 791 µmol, 1.20 eq.) was slowly added to the mixture and cooled with an ice-bath. The reaction was stirred overnight at room temperature. The reaction mixture was diluted with DCM (10 mL) and washed with 2 M NaOH (1 x 10 ml), 2 M HCl (1 x 10 ml) and brine (1 x 20 ml). After drying over $MgSO_4$ and filtration the organic phase was concentrated by rotary evaporation. The residue was purified by column chromatography (ethyl acetate/petroleum ether 1:1). The product was obtained as bright yellow powder.

^{1}H NMR (300 MHz, CDCl3) δ = 7,97 (s, 1H), 7,94 (s, H), 7,84 (d, 2H), 7,73 (q, 2H), 7,55 (t, 2H), 7,46 (t, 1H), 6,85 (d, 2H) and 3,86 (s, 2H) ppm. ^{13}C NMR (75 MHz, CDCl3) δ = 154.35, 154.34, 146.97, 137.80, 133.56, 132.27, 130.48, 129.32, 128.73, 128.48, 128.28, 127.74, 126.78, 115.21 ppm.

2.4.4 Synthesis of non-pH-responsive Polymer Photocatalytic Nanoparticles

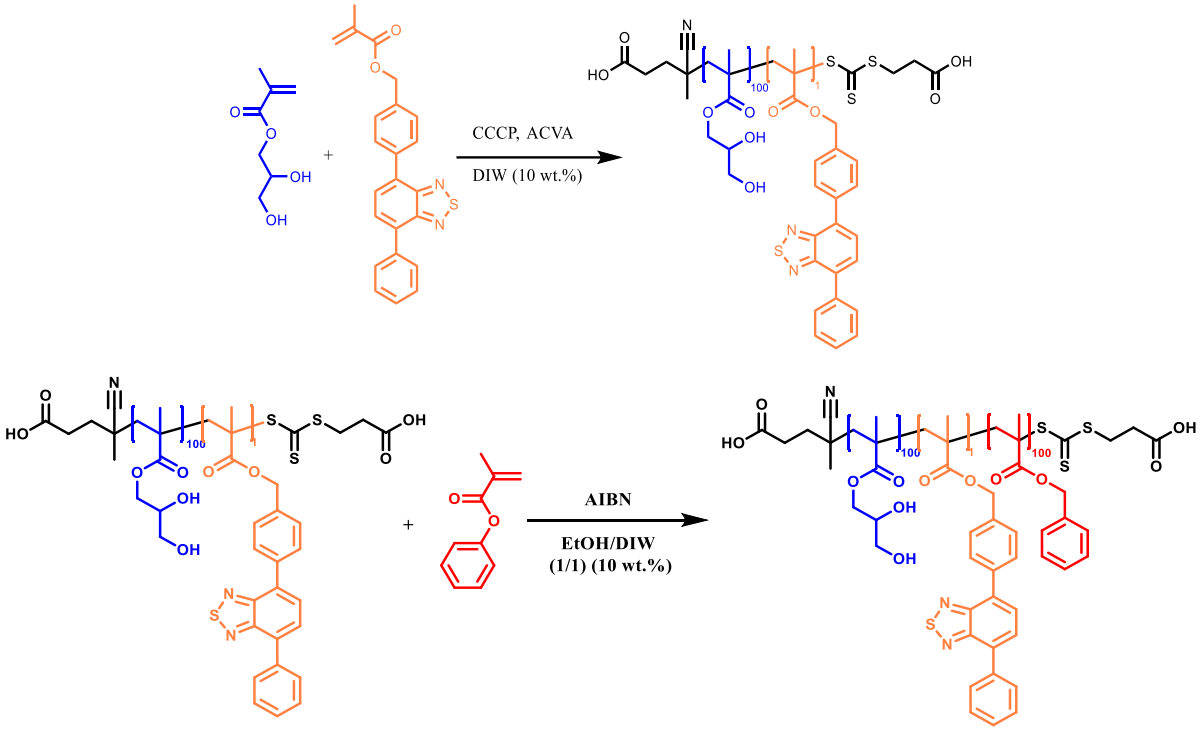

Non-pH-responsive polymer photocatalytic nanoparticles (NP-BT-DHPA (poly(2,3-dihydroxypropylmethacrylate-*co*-*N*-(4-(7-phenylbenzo[*c*][1,2,5]thiadiazol-4yl)phenyl)methyl methacrylate-*b*-benzylmethacrylate) were synthesized by RAFT-mediated polymerization induced self-assembly (RAFT-PISA). Initially, The CCCP CTA (43.2 mg, 0.014 mmol, 1.0 equiv.), DHPMA (1.1 g, 1.4 mmol, 100 equiv.), Ph_2BTMA (10.5 mg, 0.028 mmol, 2 equiv.), and ACVA (0.8 mg, 0.0028 mmol, 0.2 equiv.) were dissolved in 5 mL DIW to a concentration of 10 wt.% in a 20 mL glass vial equipped with a magnetic stirrer and septum. The solution was mixed vigorously and degassed with Ar for 15 min. Subsequently, the reaction mixture was heated to 70 °C for 3 h while stirring at 500 rpm. The resulting P(DHPMA-co-Ph_2BTMA) macroCTA was purified by dialysis against water/THF (1/1) mixture for 3 days and dried by lyophilization. Nanoparticles were formed via RAFT-PISA of the second block. The P(DHPMA-co-Ph_2BTMA) macro CTA (500 mg, 0.0305 mmol, 1 equiv.), benzyl methacrylate (537.4 mg, 3.05 mmol, 100 equiv.), and ACVA (1.7 mg, 0.0061 mmol, 0.2 equiv.) were dissolved in 10 mL a mixture of EtOH and DIW (v:v 1:1) to a concentration of 10 wt.% in a glass vial containing a magnetic stirrer and septum. After degassing with Ar for 15 min, the reaction was undertaken at 70 °C for 5 h. The resultant nanoparticles were purified by dialysis against water/acetone (1/1) mixture

for 3 days and DIW for 1 day before drying by lyophilization, obtaining a fluorescent yellow powder.

2.4.5 Synthesis of pH-responsive Polymer Photocatalytic Nanoparticles

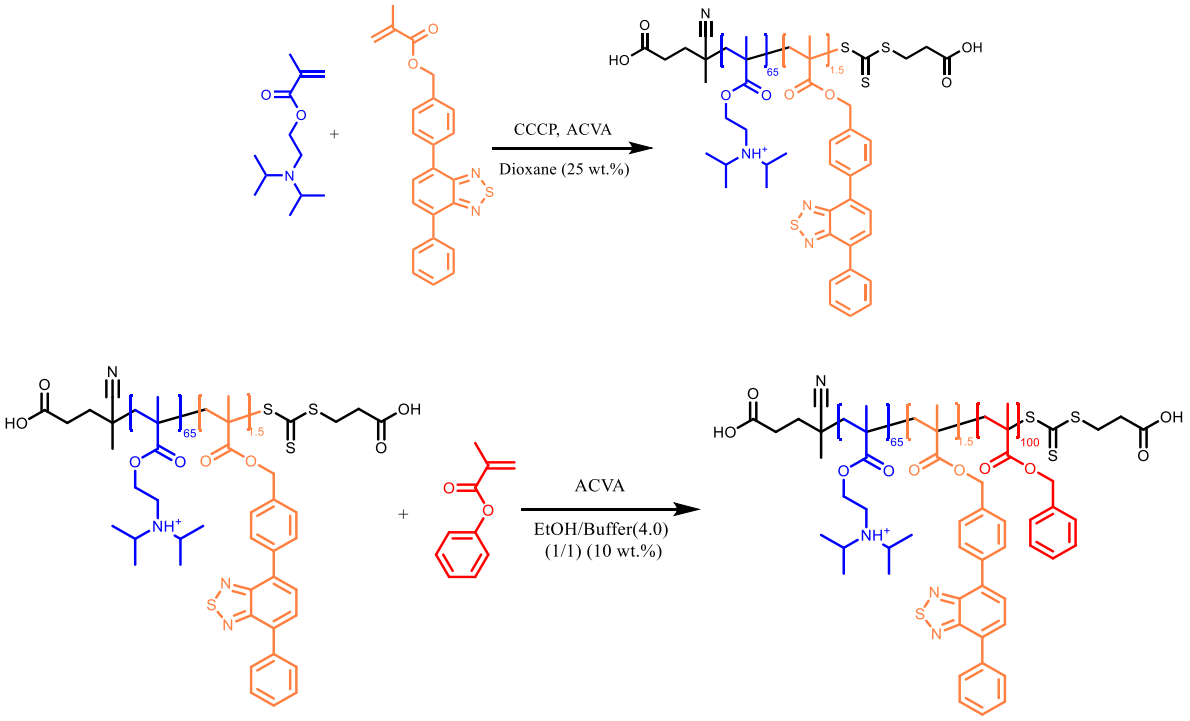

pH-responsive polymer photocatalytic nanoparticles (NP-BT-DHPA poly(diisopropylamino ethylmethacrylate-*co*-*N*-(4-(7-phenylbenzo [*c*] [1,2,5] thiadiazol-4-yl)phenyl)methyl methacrylate-*b*-benzylmetharylate) (P(DPA-*co*-Ph_2BTMA-*b*-PBzMA)) were synthesized by RAFT-mediated polymerization induced self-assembly. The CCCP CTA (14.4 mg, 0.047 mmol, 1.0 equiv.), DPA (1 g, 4.7 mmol, 100 equiv.), Ph_2BTMA (87.3 mg, 0.23 mmol, 5 equiv.), and ACVA (2.6 mg, 0.009 mmol, 0.2 equiv.) were dissolved in 3 mL of anhydrous dioxane to a concentration of 25 wt.% in a 20 mL glass vial equipped with a magnetic stirrer and septum. The solution was mixed vigorously and degassed with Ar for 15 min. Subsequently, the reaction mixture was heated to 70 °C for 5 h while stirring at 500 rpm. The resulting P(DPA-co-Ph_2BTMA) macroCTA was purified by dialysis against water/acetone (1/1) mixture for 3 days and 1 day in DIW before drying by lyophilization. Nanoparticles were formed via RAFT-PISA of the second block. The P(DPA-*co*-Ph_2BTMA) macroCTA (434 mg, 0.0063 mmol, 1 equiv.), benzyl methacrylate (481.7 mg, 2.7 mmol, 100 equiv.), and ACVA (1.5 mg, 0.0055 mmol, 0.2 equiv.) were dissolved in 8.6 mL a mixture of EtOH and acetate buffer (pH 4.0) to a concentration of 10 wt.% in a glass vial containing a magnetic stirrer and septum. After degassing with Ar for 15 min, the reaction was

undertaken at 70 °C for 5 h. The resultant nanoparticles were purified by dialysis against water/acetone (1/1) mixture for 3 days and 1 day in DIW before drying by lyophilization, obtaining a fluorescent yellow powder.

2.4.6 Photocatalytic $K_2Cr_2O_7$ Reduction

$$Cr_2O_7^{2-} + 14H^+ + 6e^- \xrightarrow[hv,\ pH\ 4.0]{NP\text{-}BT\text{-}PDPAH^+} 2Cr^{3+} + 7H_2O$$

Photocatalytic nanoparticles 2 mg NP-BT-PDPAH$^+$ (1 mg/mL, photocatalytic unit 18 μg/mL) and 4.4 mg NP-BT-DHPA (2.2 mg/mL, photocatalytic unit 18 μg/mL) were suspended in 2 mL acetate buffer solution (pH 4.0) in 4 mL open-top screw cap vials, respectively. 0.2 mL $K_2Cr_2O_7$ aqueous stock solution (2.5 mg/mL) was added to nanoparticle dispersions, respectively. The reaction mixtures were degassed by N_2 before being subjected to blue LED irradiation (power: 17 mW/cm^2, λ = 460 nm). All reactions were carried out in triplicate. The Cr(III) concentration was determined by UV/Vis absorbance at 542 nm by titration with a DPC solution in acetone (0.25 wt.%). In detail, 20 μL of solution after photocatalytic reduction of Cr(VI) was mixed with 0.96 mL of 0.2 M H_2SO_4, followed by the addition of 20 μL of freshly prepared DPC solution. The mixture was allowed to stand for 15 min to develop the purple color before UV/Vis absorbance measurement.

The reusability of these photocatalytic nanoparticles has been further investigated to justify the stability and sustainability of this designed material. A 4 mL open-top screw cap vial charged with a stirring bar was added 5 mg NP-BT-PDPAH$^+$ and 2 mL acetate buffer solution (pH 4.0). 0.5 mL $K_2Cr_2O_7$ aqueous stock solution (2.5 mg/mL) was added to the nanoparticle dispersion. The reaction medium was degassed by N_2 before subjected to blue LED irradiation (power: 17 mW/cm^2, λ = 460 nm) for 1 h. 10 μL of reaction mixture was taken for conversion measurement by UV/Vis spectroscopy. Another 0.5 mL $K_2Cr_2O_7$ aqueous stock solution (2.5 mg/mL) was added to the aforementioned reaction medium for repeating the experiment, which was proceeded for 4 cycles. After each cycle of reaction completion, 10 μL of solution after photocatalytic reduction of Cr(VI) was mixed with 0.97 mL of 0.2 M H_2SO_4, followed by the addition of 20 μL of freshly prepared DPC solution. The mixture was allowed to stand for 15 min to develop the purple color before UV/Vis absorbance measurement.

2.4.7 Photocatalytic Sulfide Oxidation

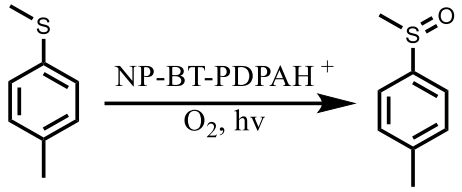

Photocatalytic nanoparticles 10 mg NP-BT-PDPAH$^+$ (2.5 mg/mL, 45 μg/mL) were suspended in 4 mL acetate buffer solution (pH 4.0) and carbonate buffer (pH 9.0) in a 20 mL open-top screw cap vial, respectively. Methyl p-tolyl sulfide (28 μL, 50 mM) was added to the dispersed nanoparticles and the reaction medium was purged with oxygen. The vial was then irradiated with blue LED light (power: 17 mW/cm^2, λ=460 nm) for 2 h, with aliquots taken to monitor conversion over time. The sample aliquots (0.4 mL) were mixed with DCM (2.5 mL) to extract reagents and products. The DCM solutions were further dried over $MgSO_4$ before GCMS measurements. The yield and products were monitored by GC-MS in triplicate. The crude product after a 2 h reaction was extracted by Chloroform-d and measured with NMR. ^{1}H NMR (400 MHz, $CDCl_3$) δ 7.54 (d, *J* = 8.1 Hz, 2H), 7.37 – 7.29 (m, 2H), 2.70 (s, 3H), 2.41 (s, 3H). ^{13}C NMR (101 MHz, $CDCl_3$) δ 142.61, 141.67, 130.18, 123.69, 44.11, 21.53.

2.4.8 Photocatalytic Alkylation of 3-Methylindole and β-Nitrostyrene

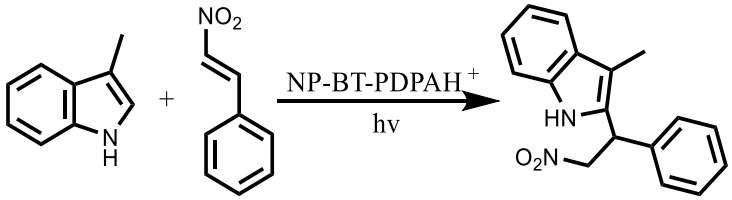

Photocatalytic nanoparticles (2.5 mg/mL, 45 μg/mL) were suspended in 10 mL acetate buffer solution (pH 4.0) in a 20 mL open-top screw cap vial. 3-methyl indole (25 mg, 19 M) and β-nitrostyrene (30 mg, 20 M) were added to the dispersed nanoparticles and the reaction medium was purged with N_2. The vial was then irradiated with blue LED light (power: 17 mW/cm^2, *λ* = 460 nm) for 14 h. The sample aliquot was extracted with DCM (4 mL) and dried over $MgSO_4$, and the conversion and products were determined by GC-MS. The crude product was purified by preparative liquid chromatography PLC (ethyl acetate/hexane 1/10) to afford the final product as white crystals. ^{1}H NMR (400 MHz, $CDCl_3$) *δ* 7.58 – 7.54 (m, 1H), 7.35 (d, *J* = 7.7 Hz, 4H),

7.24 – 7.11 (m, 4H), 6.94 (d, *J* = 1.2 Hz, 1H), 6.38 (dd, *J* = 9.1, 6.2 Hz, 1H), 5.25 – 5.09 (m, 2H), 2.31 (d, *J* = 1.1 Hz, 3H). ^{13}C NMR (101 MHz, $CDCl_3$) *δ* 136.49, 136.05, 129.44, 129.07, 126.60, 125.67, 122.50, 121.88, 119.87, 119.49, 113.00, 109.45, 77.48, 77.16, 76.84, 56.95, 30.47, 9.87.

3 Magnetically Recyclable Polymer Photocatalytic Materials for Sustainable Photocatalysis

In the previous chapter, the recycling of photocatalytic nanoparticles has been efficiently triggered by pH, making use of the reversible protonation-deprotonation of the tertiary amino groups presented in the polymers. However, an extra centrifugation process is still required for the recycling of the photocatalytic material. In this following project, we have investigated recyclable photocatalytic materials with no external energy input required for the material separation process. This chapter is based on the submitted article 'Magnetically recyclable polymer photocatalytic materials for sustainable photocatalysis'.

The production of easily separable and recoverable photocatalytic materials remains a critical challenge in achieving sustainable photocatalysis. Here, we have created a hybrid material consisting of photocatalytic polymers encapsulated magnetite nanoparticles. These nanoparticles exhibit excellent performance in oxidative hydroxylation of both boronic acid and boronic acid pinacol ester-containing substrates. Moreover, these nanoparticles can be easily recovered and regenerated from the reaction medium via a simple magnetic separation technique. Extremely high efficiency has been maintained over multiple cycles, by recycling the magnetic photocatalyst.

3.1 Motivation

Visible light-facilitated photoredox processes have been widely applied in organic synthesis, which allows reactions to occur under mild conditions compared to thermal-mediated reactions. In recent years, organic dyes have been targeted as tunable and efficient alternatives to traditional metal-based photocatalysts. Moreover, organic dyes are often less toxic and even outperform metal complex photocatalysts.[21,25] Among these materials, eosin Y is particularly attractive and has been intensively investigated as an organo-photocatalyst in chemical transformations, including reduction reactions (e.g. reduction of phenacyl sulfonium salts,[22] reduction of nitrobenzene,[23] and desulfonylation[24]), oxidation reactions (e.g. oxidative iminium ion formation,[185] hydroxylation,[27] desulfurization,[29] and oxidation of silyl enol ethers[31]) and redox reactions (e.g. arylation reactions[186–188]). However, there is a trade-off between efficient photocatalysis and the ability to recycle homogeneous photocatalysts.

One strategy to produce recoverable organic dye-based photocatalytic materials with enhanced solvent compatibility is to merge molecular photocatalysts with polymer matrices, which can be either applied as heterogeneous or pseudo-homogeneous photocatalysts.[68,74,5,189,84,190,165] Moreover, the incorporation of organic dyes into stimuli-responsive polymers has facilitated the switchable wettability of the photocatalytic moieties to obtain a rapid phase separation and/or controllable reactivity.[191] Recently, our group has illustrated pH-responsive photocatalytic nanoparticles, where the recycling of photocatalytic materials can be triggered by a simple pH alternation.[190] Although these photocatalytic nanoparticles can be easily and efficiently recovered by changing the pH value of the medium, the pH value is not a completely orthogonal stimulus. Besides, there is still an external energy input (centrifugation) required to facilitate the recycling of nano-scaled photocatalytic materials. Therefore, the creation of recoverable photocatalytic materials responding to an orthogonal stimulus, such as magnetism, requiring no external energy input is highly desired.

The implantation of magnetic materials into conjugated polymer photocatalysts has allowed the production of recoverable photocatalysts with enhanced photocatalytic efficiency, such as hybrid structures of graphitic carbon nitrides with $ZnFe_2O_4$, Fe_3O_4, and $BaFe_{12}O_{19}$, and conjugated polyelectrolytes with Fe_3O_4.[116–120] However, the merger of polymer-based photocatalysts and magnetic materials has not yet been maximized. Ideally, the photocatalytic units are solvated and easily accessible by both light and substrates, enabling efficient photocatalysis. In addition, the implantation of magnetite nanoparticles offers the opportunity to facilitate the recycling of photocatalytic materials simply by the application of a magnet without additional centrifugation steps, demonstrating a more sustainable approach.

Here, we have produced magnetic-responsive polymeric photocatalysts comprising photocatalytic polymers and magnetic nanoparticles. An amphiphilic diblock copolymer construction has been selected to encapsulate hydrophobic magnetite nanoparticles, where the hydrophobic segments can deposit on the surface of the magnetite nanoparticles and the hydrophilic block with photocatalytic moieties can stabilize the nanoparticles by tethering on the surface of nanoparticles after the encapsulation process. Therefore, these nanoparticles were expected to facilitate photocatalytic reactions efficiently in aqueous conditions and after the completion of

reactions photocatalytic nanoparticles can be easily recovered by applying a magnet (Figure 39).

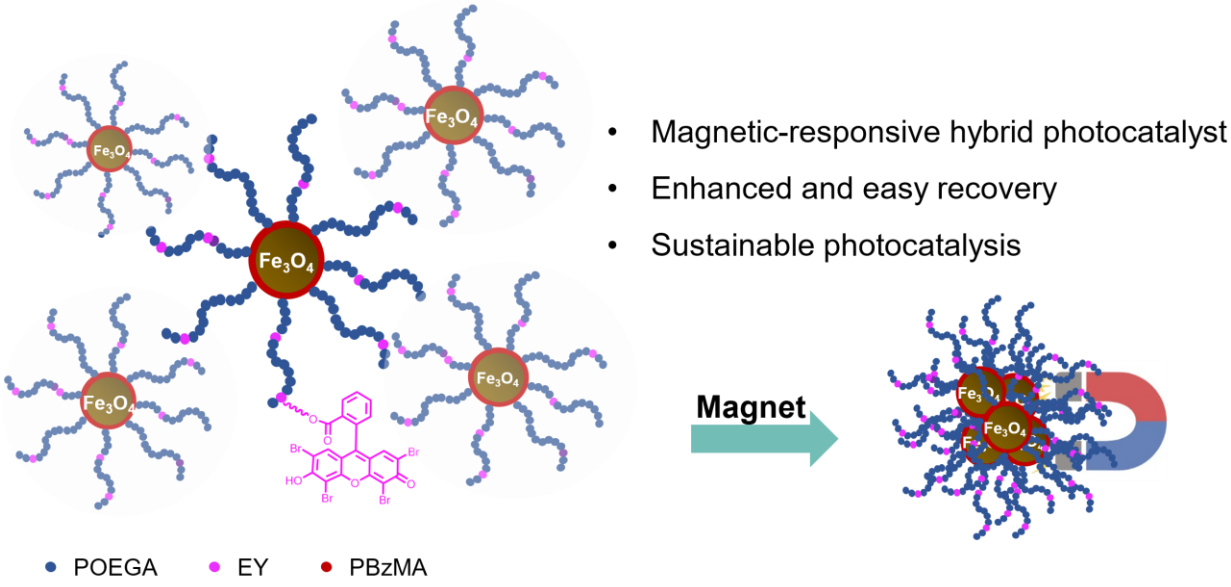

Figure 39. Scheme of the magnetic-responsive photocatalytic hybrid materials and their easy recycling.

3.2 Synthesis and Characterization of Magnetic Photocatalytic Polymer Nanoparticles

Photocatalytic macroCTA poly(oligoethylene glycol acrylate)-*s*-2-(methacryloyloxy)ethyl 2-(2,4,5,7-tetrabromo-6-hydroxy-3-oxo-3H-xanthen-9-yl)benzoate (POEGA-*s*-EY) was synthesized via reversible addition-fragmentation chain transfer (RAFT) polymerization, prior to the chain extension of a ligand block using 2-carboxyethyl acrylate (CEA) as monomers. The resulting diblock copolymer was confirmed by ^{1}H NMR spectroscopy (Figure 40), where the aromatic peaks (6.7-8.1 ppm) attributed to the eosin Y photocatalytic units were clearly visible from the ^{1}H NMR spectrum. The molar mass of the polymer was determined by GPC (Figure 41) with a number average molar mass of 14.6 kDa.

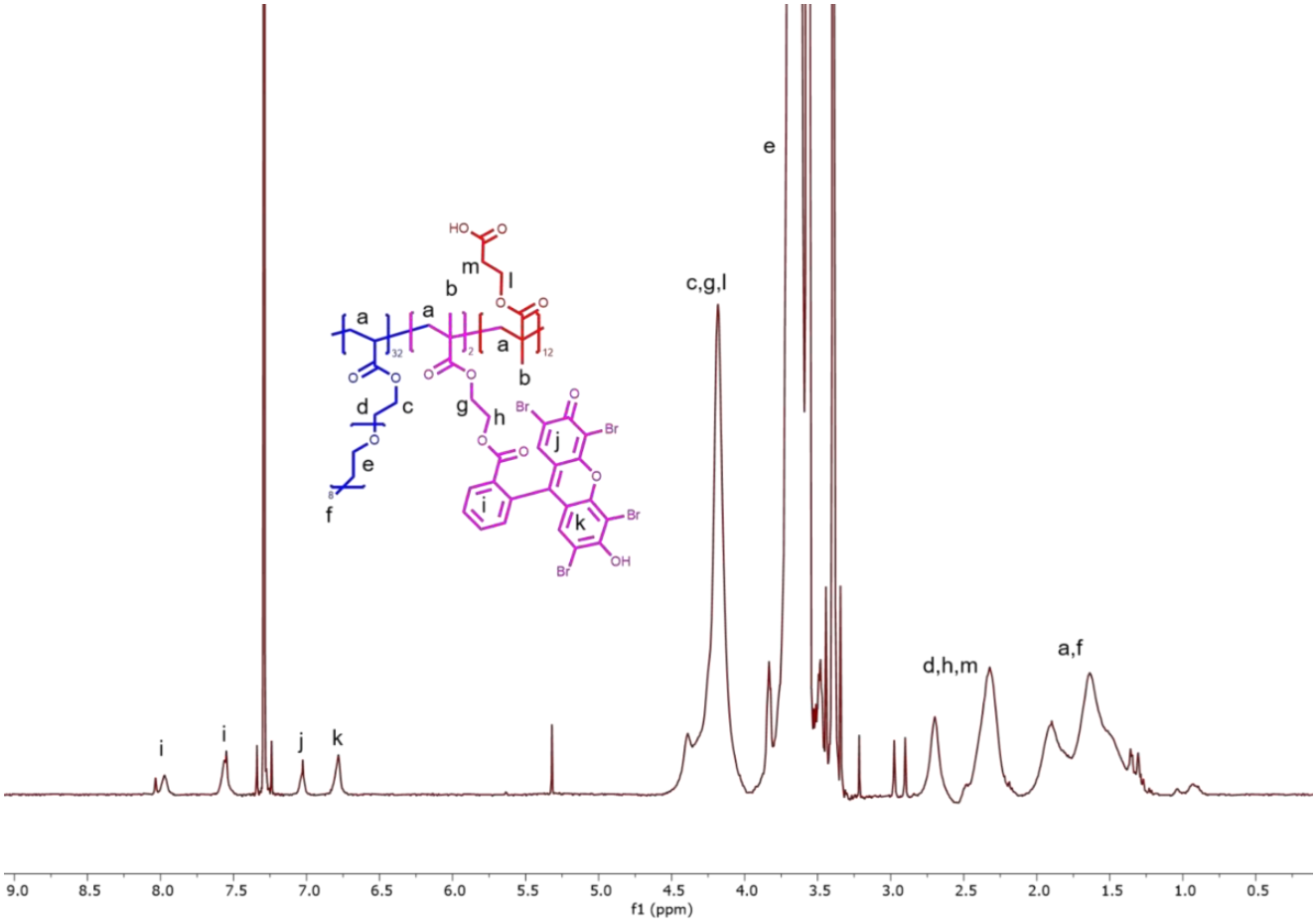

Figure 40. ^{1}H NMR spectrum of the POEGA-*s*-EY-*b*-PCEA diblock copolymer.

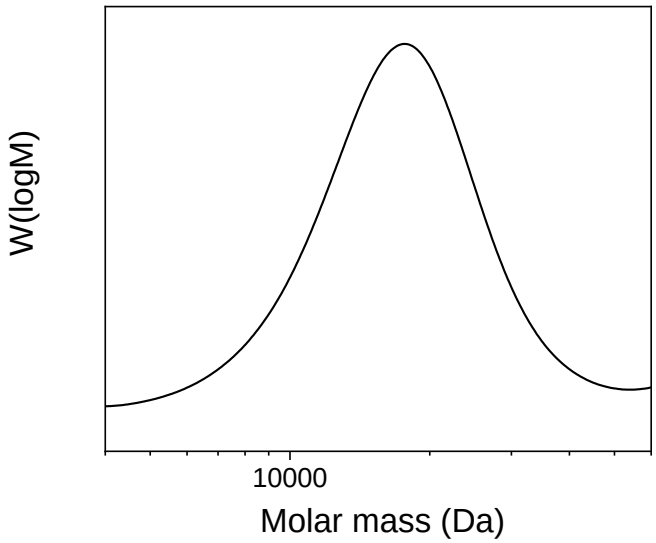

Figure 41. GPC measurement of the POEGA-*s*-EY-*b*-PCEA diblock copolymer (solvent: DMF and standard: PMMA).

These diblock copolymers were further applied as stabilizing ligands for the *in situ* co-precipitation of polymer coated iron oxide nanoparticles. Ferrous and ferric salts (1/2 molar ratio of Fe^{2+}/Fe^{3+}) were dissolved in DIW with the addition of POEGA-*s*-EY-*b*-CEA at various weight percentages from 1:1 to 1:4. These solutions were preheated at 70 °C for 0.5 h with vigorous agitation prior to the addition of NaOH (1 M) aqueous solution, enabling *in situ* co-precipitation of Fe_3O_4. The nanoparticle dispersion prepared with a polymer to nanoparticle weight ratio at 1:1 was not stable, where particles were precipitated on the bottom of the glassware. Therefore, this sample was excluded from further characterizations. The rest of the as-obtained nanoparticle dispersions were separated from the reaction medium by a magnet. The dispersion with a [polymer] : [Fe_3O_4] weight ratio at 2:1 was selected for further investigations, since samples with higher polymer ligand loading ([polymer] : [Fe_3O_4] ratio at 3:1 and 4:1) did not respond to the magnet effectively. The chemical composition of these as-obtained Fe_3O_4 coated with polymers were characterized by XRD (Figure 42) and FTIR (Figure 43).

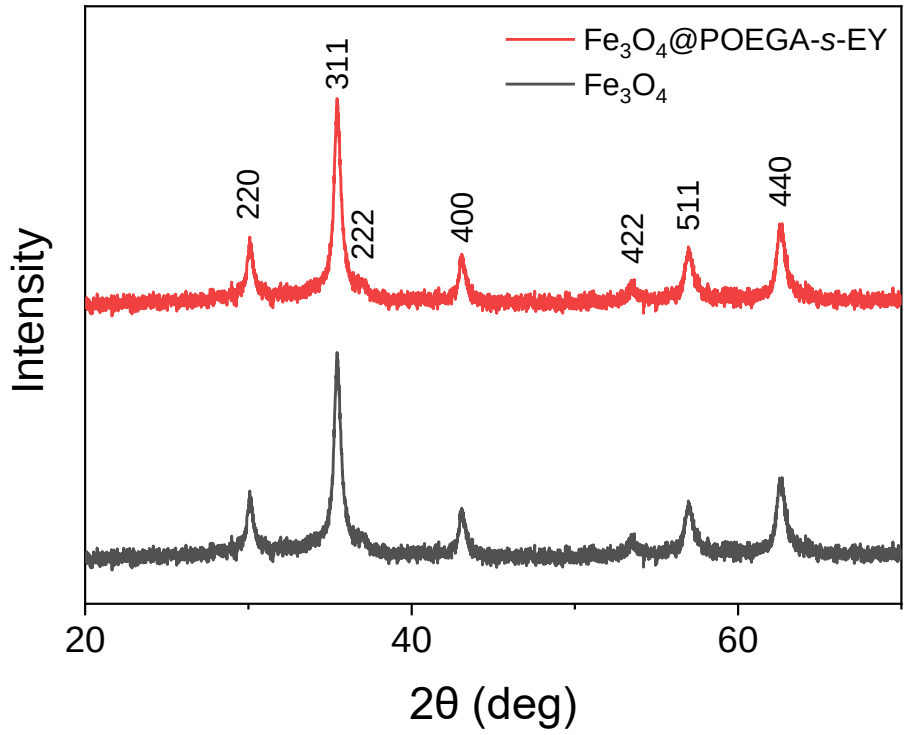

Figure 42. XRD spectra of polymer coated Fe_3O_4 nanoparticles at [polymer] : [Fe_3O_4] weight ratio of 2 and bare Fe_3O_4 nanoparticles.

Fe_3O_4 nanoparticles coated with polymers yielded the same XRD pattern as the pristine Fe_3O_4 nanoparticles, where diffraction peaks at [220], [331], [222], [400], [422], [511], and [440] were clearly visible.

To validate the coating of photocatalytic polymers on Fe_3O_4 nanoparticles, FTIR was utilized to monitor the changes in the surface structure with and without the polymer chain as a stabilizer. The aliphatic -CH_2- in backbones were observed at 2750 -3050 cm^{-1} for particles coated with polymer chains. In addition, the band peaked at 1720 cm^{-1} and was attributed to the C=O groups in the polymers. This result demonstrated the successful coating of the polymers on Fe_3O_4 nanoparticles.

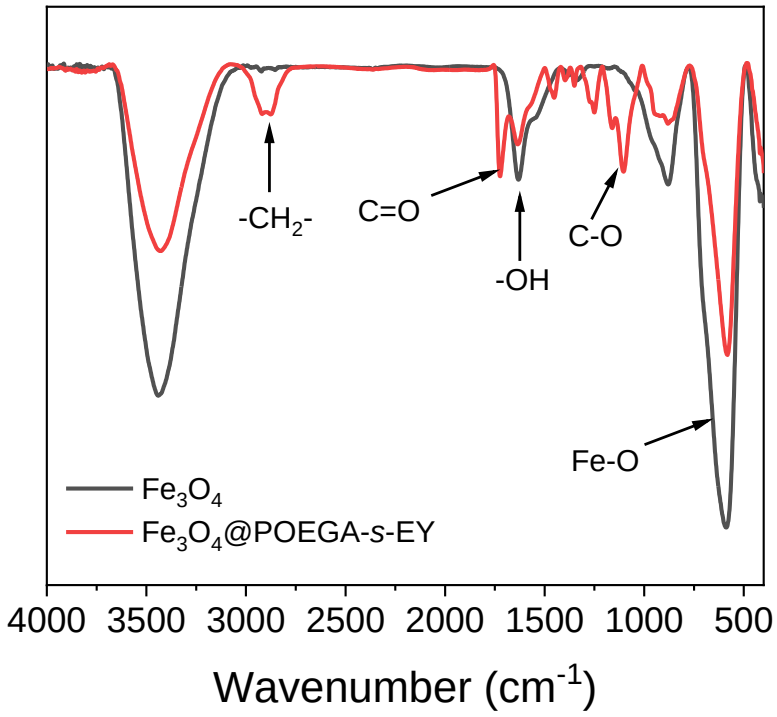

Figure 43. FTIR spectra of Fe_3O_4 nanoparticles with (red) and without (black) photocatalytic polymer coatings.

The morphology of Fe_3O_4 nanoparticles has been characterized by TEM. As shown in the Figure 44, magnetite nanoparticles with irregular shapes were synthesized. However, the organic polymer content was not visible from TEM images, probably because of the extremely small size of Fe_3O_4 nanoparticles and the thin layer of polymer shells could be burned by the electron beam while measurement.

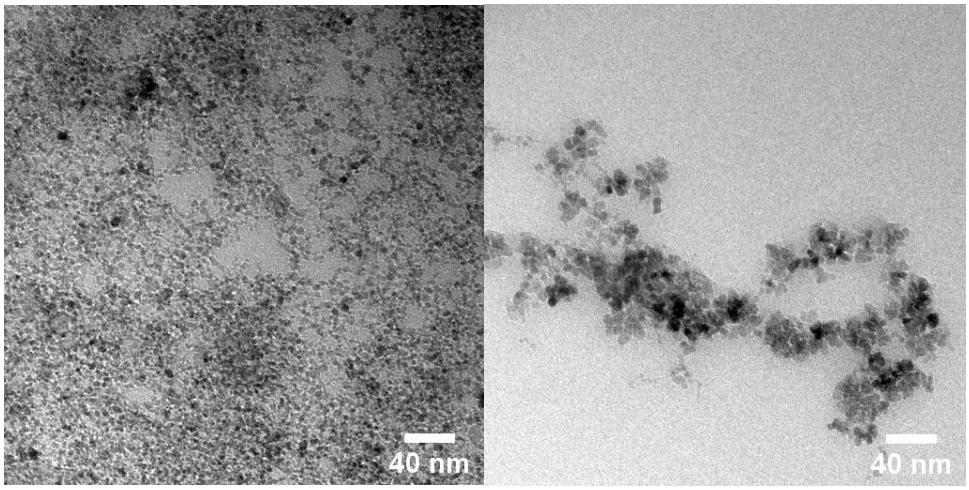

Figure 44. TEM images of photocatalytic polymer stabilized Fe_3O_4 nanoparticles.

To ensure the amount of photocatalyst incorporated in the hybrid materials, the Fe_3O_4 anchored with photocatalytic diblock copolymers have been subjected to thermogravimetric analysis. A relatively high polymer content (25 wt.%) was obtained, suggesting an efficient approach to preparing hybrid materials with high content of soft matter (Figure 45).

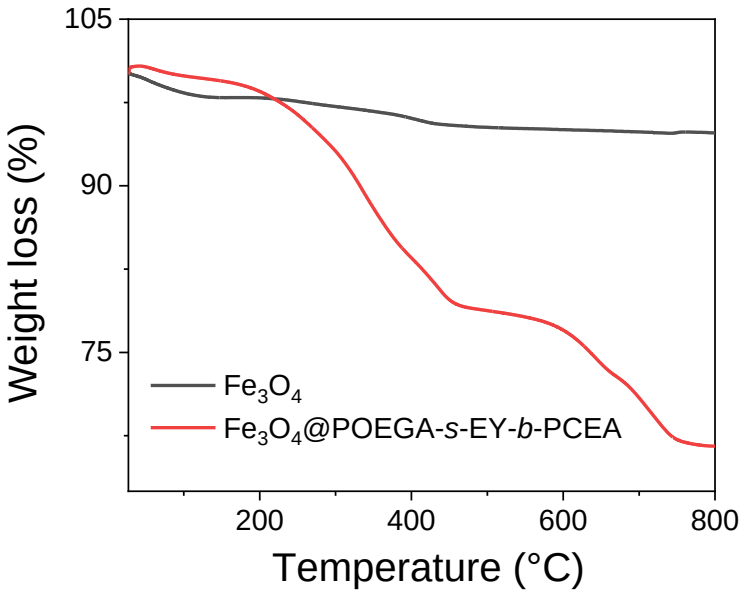

Figure 45. Thermo-grams for heating the pristine Fe_3O_4 nanoparticles and Fe_3O_4 nanoparticles coated with polymer chains (Fe_3O_4@POEGA-*s*-EY) from 25 °C to 800 °C.

The hydrophilic nature of POEGA polymers allows pseudo-homogeneous photocatalysis by applying these photocatalytic nanoparticles (Fe_3O_4@POEGA-*s*-EY)

in aqueous medium. Initially, the photocatalytic activity of Fe_3O_4@POEGA-*s*-EY has been demonstrated by photocatalytic oxidation of methyl phenyl sulfide. However, there was no conversion obtained using these Fe_3O_4@ POEGA-*s*-EY nanoparticles measured by GCMS (Figure 46).

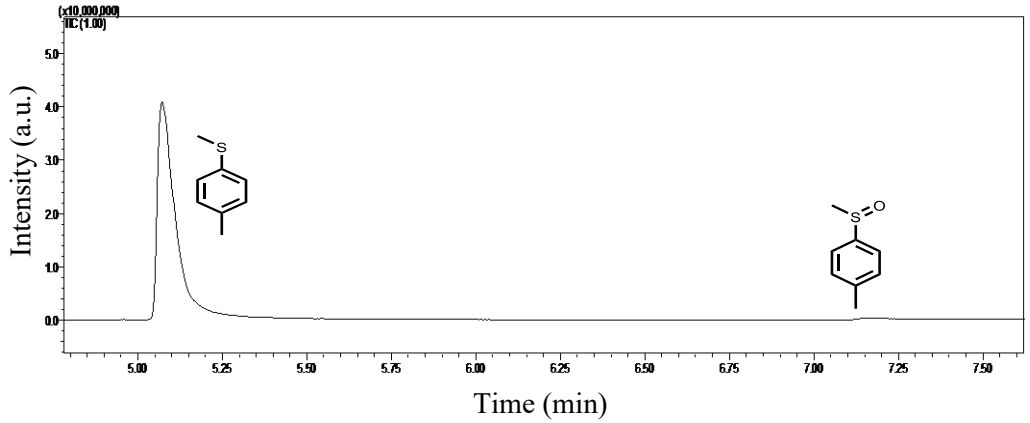

Figure 46. GCMS analysis of the methyl phenyl sulfide oxidation using photocatalytic polymer stabilized Fe_3O_4 nanoparticles Fe_3O_4@POEGA-*s*-EY.

To confirm the photocatalytic reactivity of the polymeric photocatalyst, free polymer chains were mixed with pristine Fe_3O_4 and used for sulfide oxidation, where 15% conversion was obtained after 2 h of reaction measured by GCMS (Figure 47). This suggests that the anchoring of photocatalytic polymer chains could have facilitated the electron transfer from the photocatalytic moieties to the Fe_3O_4 nanoparticles, due to the spatial proximity, leading to the reduction of Fe^{3+} to Fe^{2+} instead of oxidation of methyl phenyl sulfide.

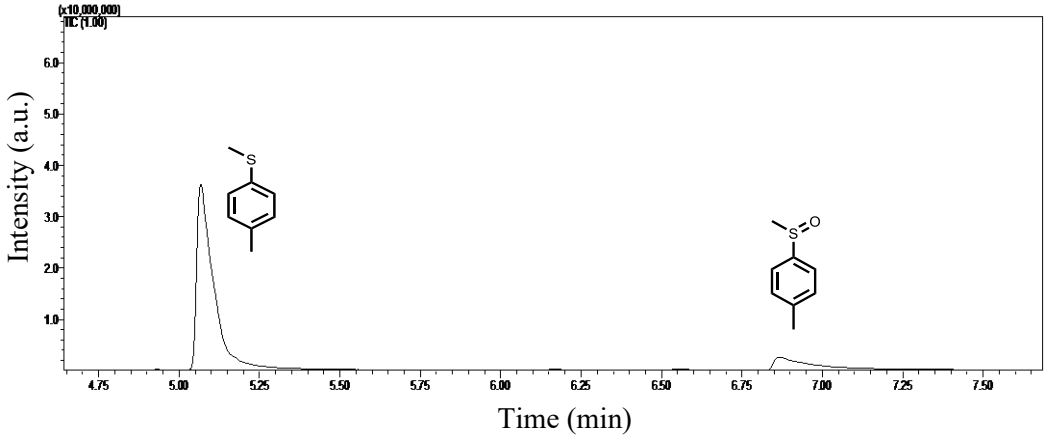

Figure 47. GCMS analysis of the methyl phenyl sulfide oxidation using free photocatalytic polymer and Fe_3O_4 nanoparticles mixture.

To avoid the electron transfer from photocatalytic polymer to magnetite nanoparticles, we adapted the strategy to encapsulate iron nanoparticles with amphiphilic photocatalytic polymers. Here, the marcoCTA POEGA-*s*-EY was extended with a second hydrophobic benzyl methacrylate (BzMA) block instead of the aforementioned PCEA anchoring block. The chemical composition of POEGA-*s*-EY-*b*-PBzMA photocatalytic polymers was characterized by NMR spectroscopy (Figure 48). The molecular weight (12.3 kDa) and dispersity (1.34) of the polymer chains were examined by GPC as displayed in Figure 49.

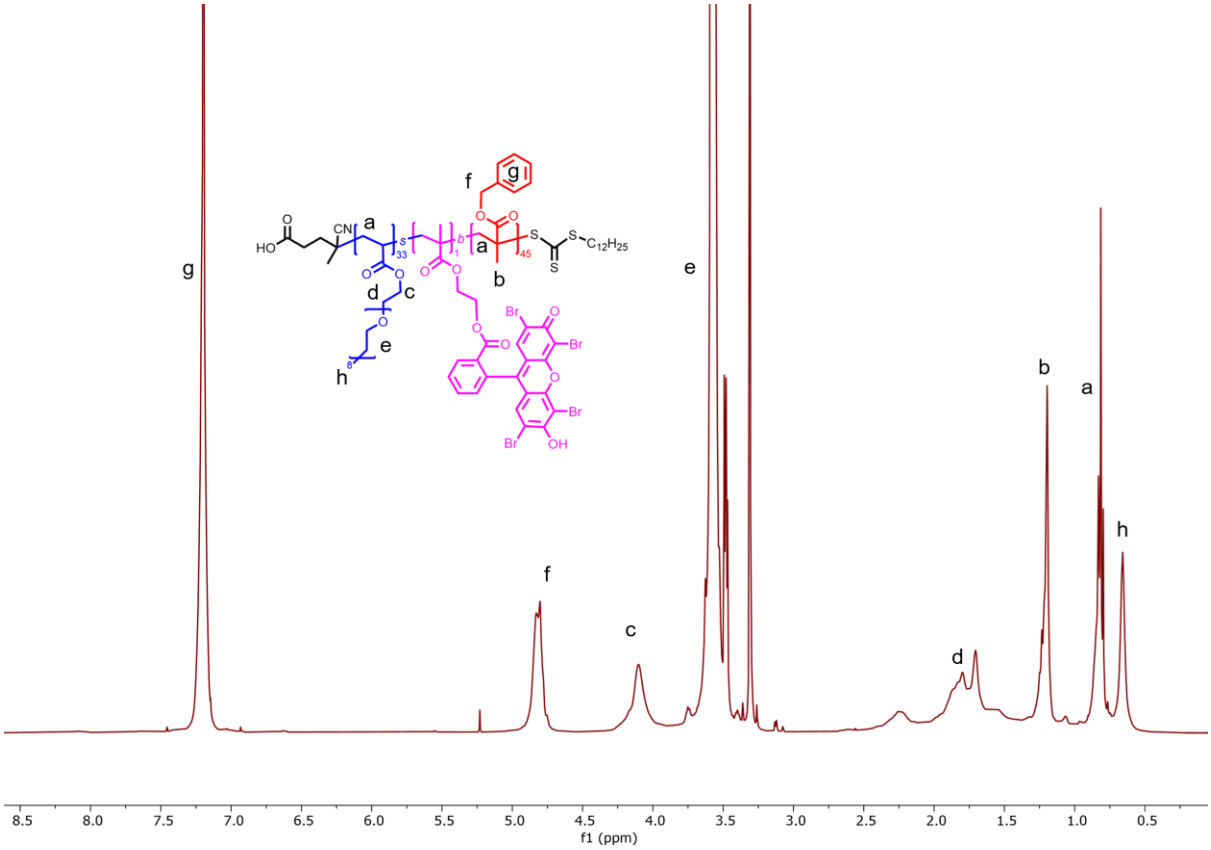

Figure 48. ^{1}H NMR spectrum of the POEGA-*s*-EY-*b*-PBzMA diblock copolymer.

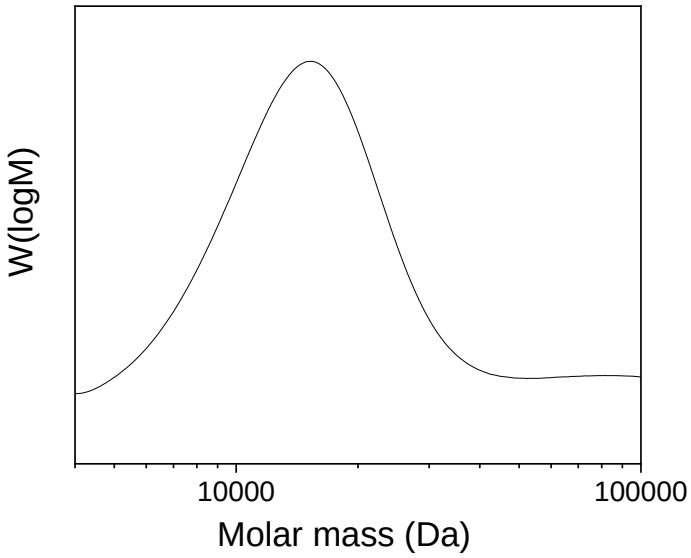

Figure 49. GPC measurement of the POEGA-*s*-EY-*b*-PBzMA diblock copolymer.

The optical properties of the photocatalytic polymer POEGA-*s*-EY-*b*-PBzMA were visualized by UV-Vis spectroscopy (see Figure 50), displaying strong absorptions in the green light region and emitting red light, which agrees well with the literature.[192]

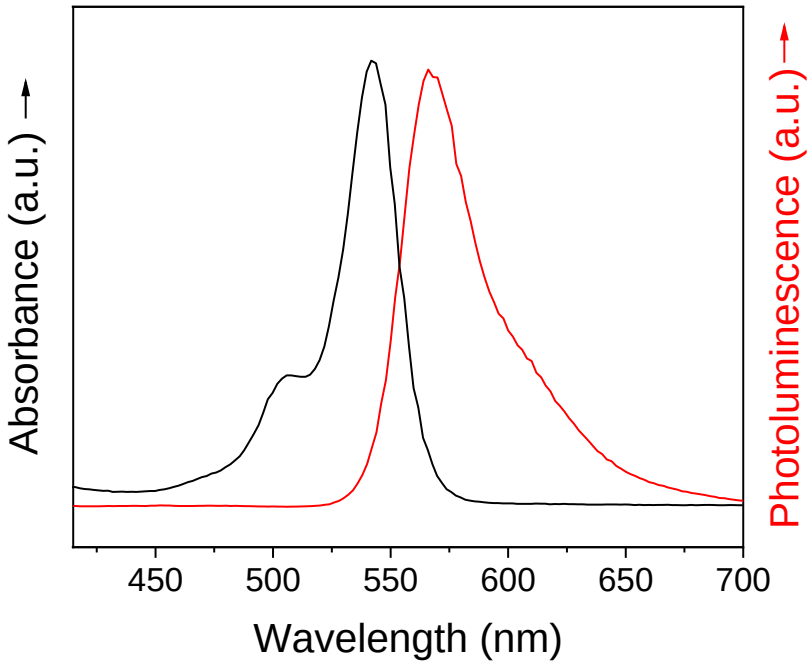

Figure 50. UV-Vis absorbance (black) and emission (red) spectra of POEGA-*s*-EY-*b*-PBzMA in DMSO.

The encapsulation of iron nanoparticles was achieved in three steps as illustrated in Figure 51. Firstly, iron nanoparticles were modified with hydrophobic trichlorododecylsilane molecules, generating a hydrophobic iron nanoparticle dispersion. The hydrophobic silane acted as a seed for the following micelle formation of the amphiphilic photocatalytic polymer. Amphiphilic photocatalytic polymers and iron nanoparticles modified with silanes were dissolved in chloroform before the addition of DIW. This mixture was subjected to ultrasonication tip at 20% amplitude for 3 min (pulse: 20 s on and 10 s off) and cooled with an ice bath. During this process, the amphiphilic photocatalytic polymers served as emulsifying agents. The mixture was sonicated in a sonication bath to evaporate the organic chloroform solvent. These as-obtained polymer encapsulated iron nanoparticles were separated by a magnet to remove empty micelles and washed three times with DIW.

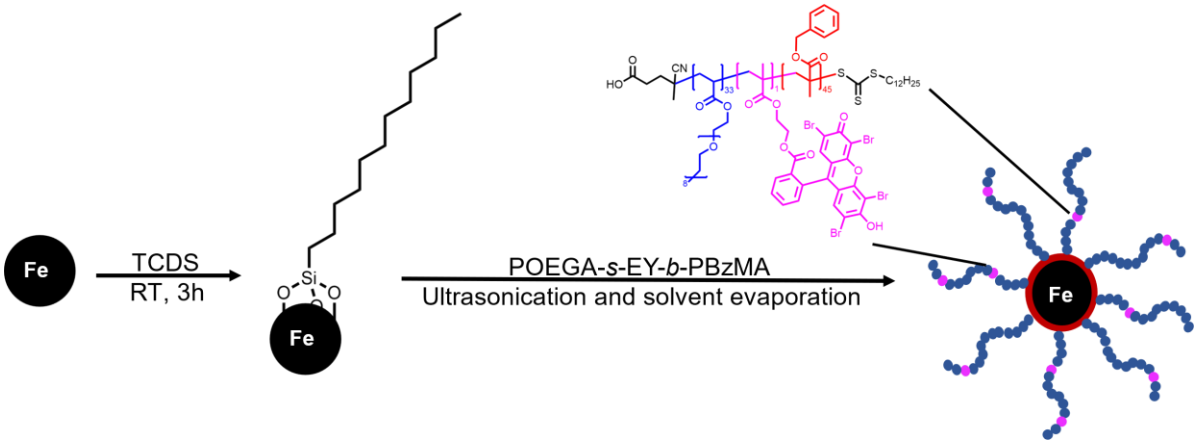

Figure 51. Illustration of surface modification process for iron nanoparticles. Initially, the pristine Fe nanoparticles were immobilized with hydrophobic TCDS molecules. Secondly, these hydrophobic Fe nanoparticles namely Fe@TCDS were encapsulated in photocatalytic polymers by ultrasonication tip and solvent evaporation procedure, generating a hybrid material with photocatalytic polymer coating on the surface of the magnetic Fe nanoparticles.

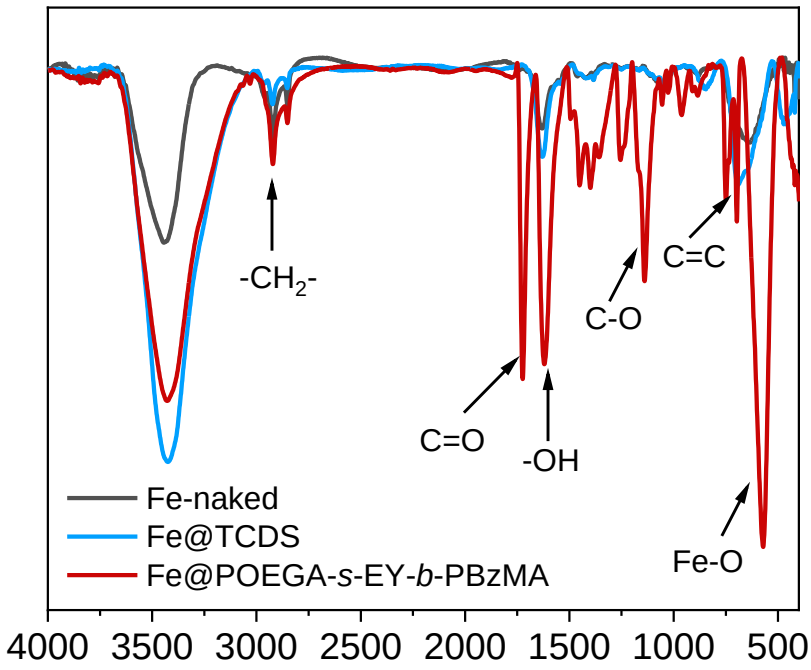

Figure 52. FTIR spectra of pristine iron nanoparticles (black), iron nanoparticles with silane ligands Fe@TCDS (blue), and iron nanoparticles encapsulated in photocatalytic polymer chains (red).

To ensure the encapsulation of iron nanoparticles with photocatalytic polymer chains, FTIR was utilized to monitor the changes in the chemical compositions. As shown in Figure 52, peaks at 2750 -3050 cm^{-1} were owing to the -CH_2- groups presenting in the silane and polymer chains. Especially, the band peaked at 1720 cm^{-1} attributing to C=O groups, and the peak at 760 cm^{-1} resulting from the C=C groups (aromatic units) was only observed in the polymer encapsulated samples, demonstrating the formation of polymer-iron hybrid nanoparticles.

To further visualize the encapsulation of iron nanoparticles with polymer chains, TEM was employed to acquire the image of the hybrid materials as shown in Figure 53. Polymeric soft matters were coated around the iron nanoparticles forming a hybrid complex, where photocatalytic moieties were introduced accordingly to the surface of the iron nanoparticles and the hybrid particles can be stabilized by the hydrophilic POEGA polymers.

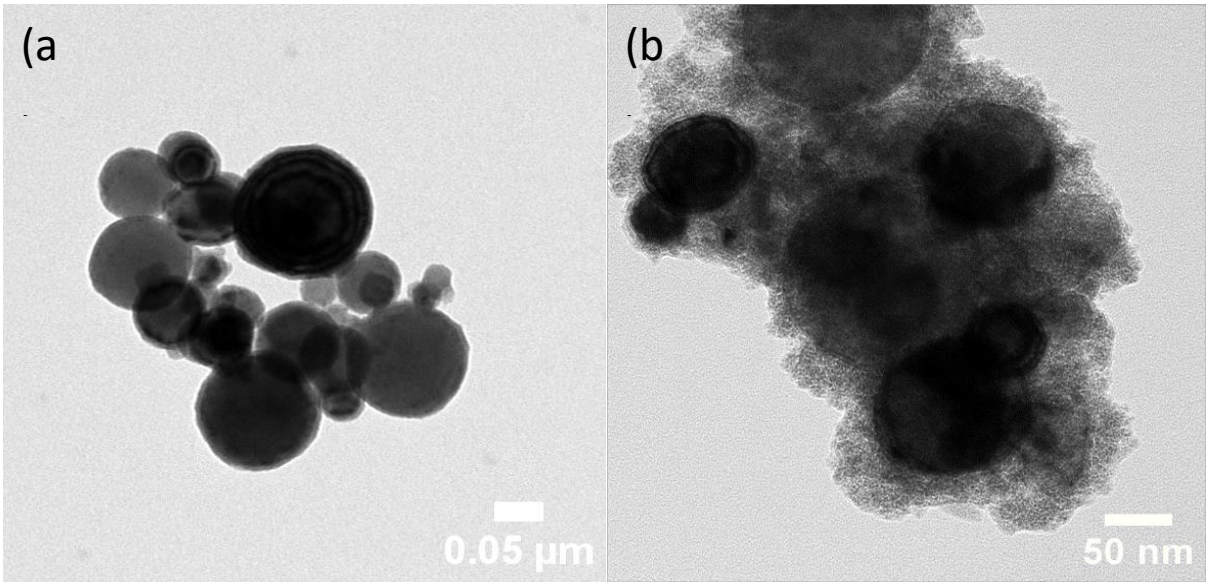

Figure 53. TEM images of (a) pristine iron nanoparticles and (b) encapsulated in polymer chains.

TGA was applied to measure the polymer content of the hybrid material and, thereafter, calculate the photocatalyst loading for photocatalytic reactions (Figure 54). The weight percentage of the TCDS molecules on the surface of the iron nanoparticles was calculated to be 4.3 wt.%. After encapsulated into photocatalytic polymers the weight of the organic matter on the surface increased to 10.6 wt.%, therefore there was only 6.3 wt.% of the polymeric photocatalyst presenting on the iron nanoparticles.

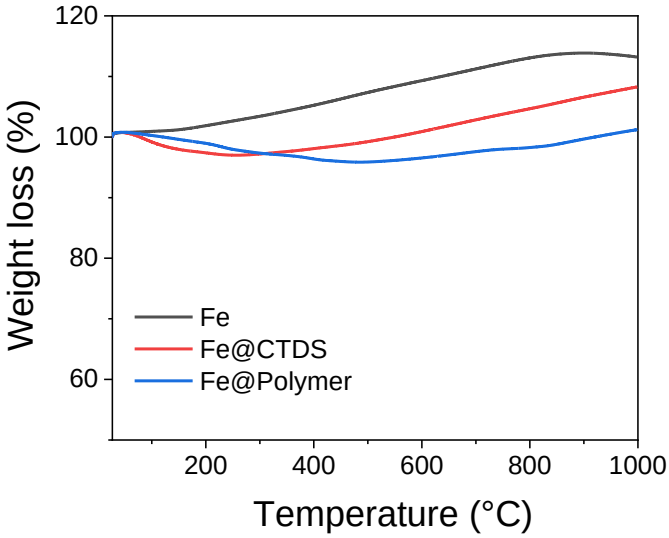

Figure 54. Thermo-grams for heating the pristine Fe nanoparticles and Fe nanoparticles coated with photocatalytic polymer chains (Fe@POEGA-*s*-EY-*b*-PBzMA) from 25 °C to 1000 °C.

Nevertheless, these particles can be easily dispersed in aqueous solution, forming a homogeneous and stable dispersion. Therefore, we have applied this particle dispersion for photocatalytic oxidation of sulfide substrate as a model reaction. As shown in the GCMS spectrum, 91% conversion of oxidation product has been achieved, demonstrating a photocatalytically active hybrid material (Figure 55).

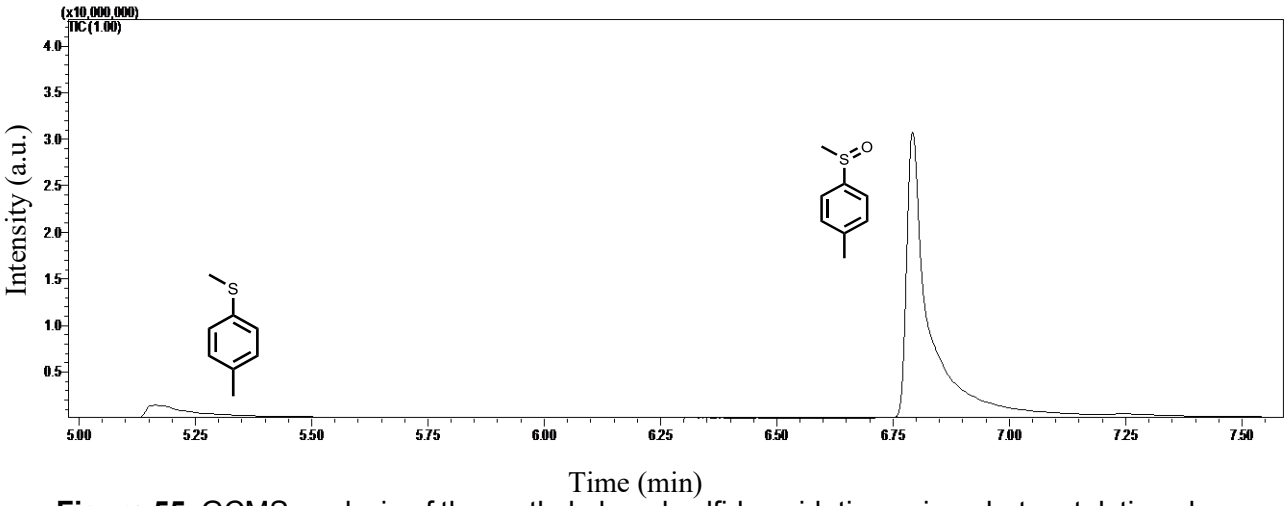

Figure 55. GCMS analysis of the methyl phenyl sulfide oxidation using photocatalytic polymer encapsulated Fe nanoparticles Fe@POEGA-*s*-EY-*b*-PBzMA.

However, the reaction takes 14 h to reach 90% conversion, which is 7 times longer compared to the pH-responsive nanoparticles we have synthesized.[190] This slow reaction rate possibly resulted from the low photocatalytic polymer content in the hybrid material. Therefore, a higher polymer loading is highly desired to enhance the efficiency of the hybrid photocatalytic materials.

To increase the photocatalytic polymer content of the hybrid materials, we have further improved the encapsulation method by using smaller magnetite nanoparticles (purchased) with a diameter of 18-28 nm, which is one third to half of the size of the iron nanoparticles. The electron transfer between the photocatalyst to magnetite is expected to be inhibited by the hydrophobic PBzMA core. Here, a very similar approach to the preparation of iron nanoparticle encapsulation has been applied to prepare photocatalytic polymer coated magnetite hybrid nanoparticles. Initially, pristine magnetite Fe_3O_4 nanoparticles were functionalized with hydrophobic trichlorododecylsilane molecules, which were further mixed with amphiphilic photocatalytic polymers (POEGA-*s*-EY-*b*-PBzMA) in DCM with a magnetite to polymer ratio of 1:2 and 1:3 respectively. To the mixture, DIW was added to form emulsions by magnetic stirring. The organic solvent DCM was allowed to evaporate overnight,

resulting in photocatalytic polymer encapsulated magnetite nanoparticles. These particles were washed with DIW under sonication, where the free polymer chains and empty micelles were removed by particle separation using a magnet. The color of the magnetic nanoparticles turned from brownish to reddish after the encapsulation. Besides, these as-obtained magnetic nanoparticles can be easily dispersed in DIW that differ from the hydrophobic magnetite nanoparticles, indicating the incorporation of photocatalytic polymers on the surface of the magnetite nanoparticles.

The soft matter coating on the surface of the magnetite nanoparticles was confirmed by FTIR spectroscopy as shown in Figure 56, where typical peaks at 1720 cm^{-1} and 1150 cm^{-1} attributing to C=O and aromatic C=C peaks of the polymer, respectively, were only observed in samples coated with polymer chains. No specific peaks of the eosin Y unit could be identified due to the low material loading of eosin Y (1.28 mol%).

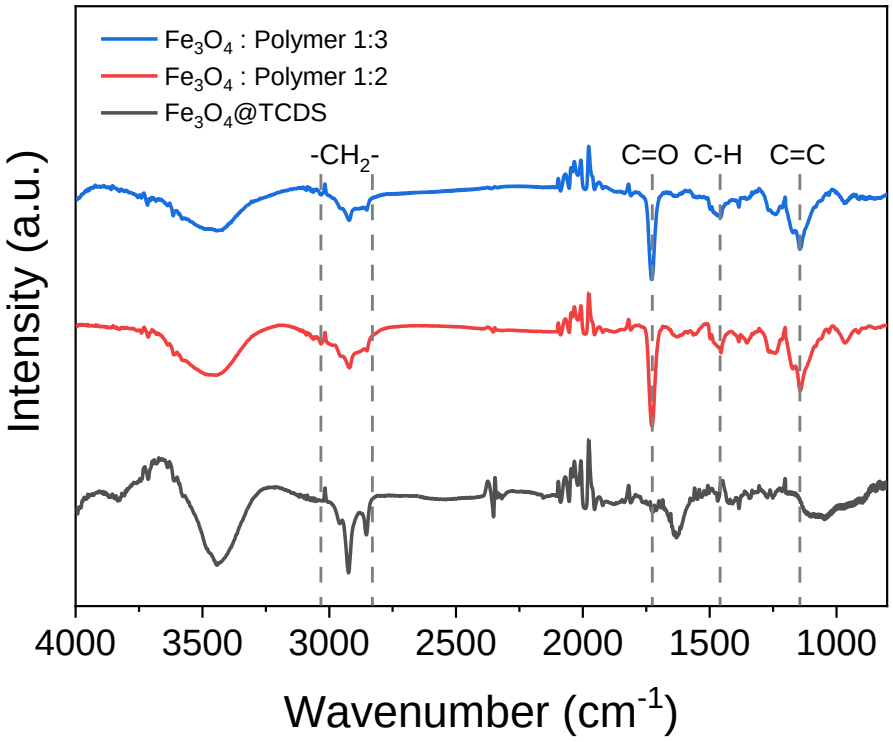

Figure 56. FTIR spectra of magnetite nanoparticles with silane ligands Fe_3O_4@TCDS (black), and magnetite nanoparticles encapsulated in photocatalytic polymer chains (magnetite : polymer ratio = 1:2 in red, magnetite : polymer ratio = 1:3 in blue).

Furthermore, TGA (Figure 57) was carried out to examine the polymer content on these hybrid nanoparticles, thereafter the photocatalytic units applied in the

photocatalytic reactions can be calculated. The weight percentage of the hydrophobic TCDS anchored on the surface of the Fe_3O_4 nanoparticles was determined to be 1.5 wt.%. We have observed the weight percentage increased only slightly from 50 wt.% to 52.5 wt.% when the polymer loading was increased from 1:2 to 1:3 (magnetite : polymer), suggesting the surface of magnetite nanoparticles was saturated. To optimize the use of photocatalytic polymer, the polymer-to-magnetite ratio of 1:2 was selected to prepare the magnetic-responsive photocatalyst hybrid materials.

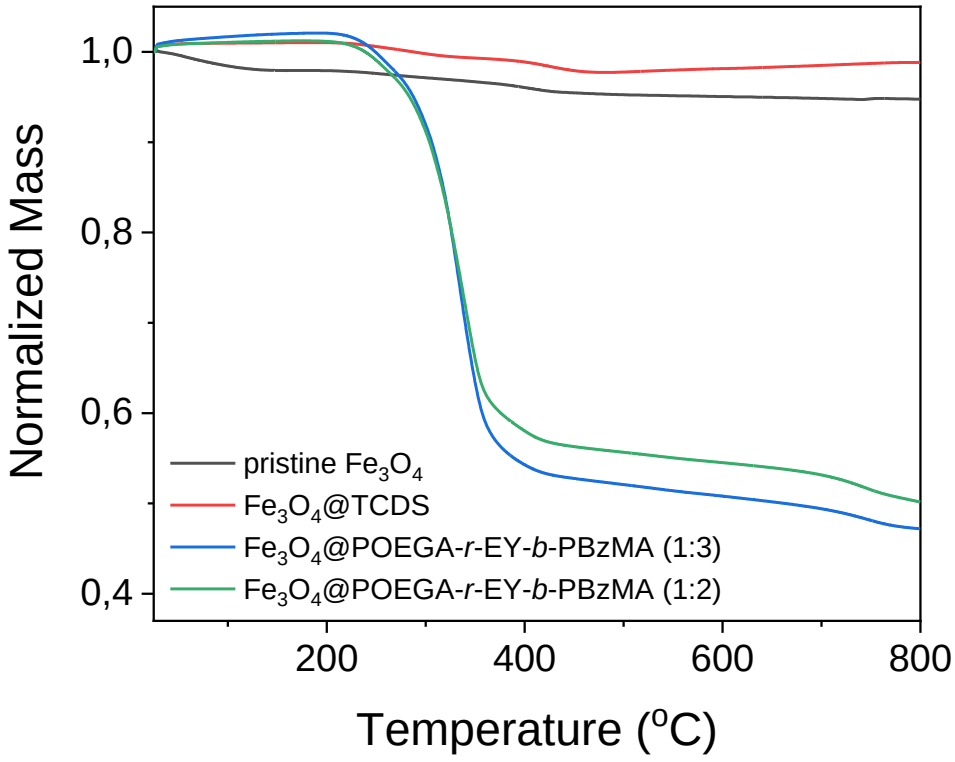

Figure 57. Thermo-grams for heating the pristine Fe_3O_4 nanoparticles and Fe_3O_4 nanoparticles coated with photocatalytic polymer chains (Fe_3O_4 @POEGA-*r*-EY-*b*-PBzMA) from 25 °C to 800 °C.

TEM images further visualized the surface modification process of magnetite nanoparticles. The as-purchased magnetite nanoparticles were spherical nanoparticles with a diameter of around 20 nm (Figure 58 (a-c)). As illustrated in Figure 58(d-f), no obvious change observed after modifying the magnetite nanoparticles with TCDS molecules. It was obvious that clusters of magnetite nanoparticles with polymer chains were formed after incubated with photocatalytic polymers, forming irregular and bigger particles with diameters above 200 nm (Figure 58(g-i)).

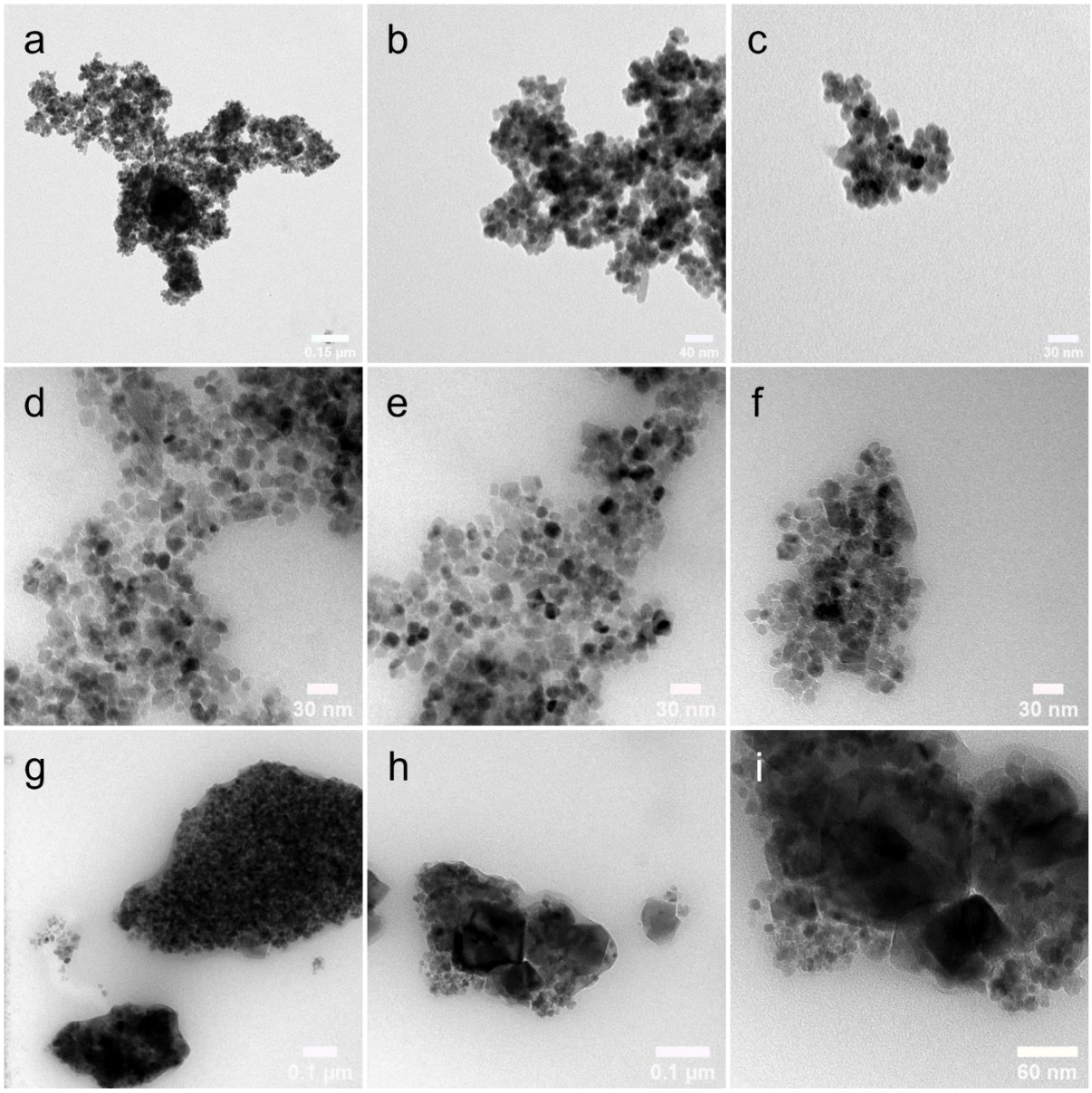

Figure 58. TEM images of magnetite nanoparticles with different surface treatments. (a-c) pristine magnetite nanoparticles dispersed in DIW; (d-f) magnetite nanoparticles modified with hydrophobic trichlorododecyl silane (dispersed in DCM); (g-i) magnetite nanoparticles encapsulated in photocatalytic polymers (dispersed in DIW).

As displayed in Figure 59 (right), some precipitation at the bottom of the vial was observed when dispersing the pristine magnetite nanoparticles in water. After being modified with TCDS, the magnetite nanoparticles were well dispersed in DCM, resulting in a light brownish dispersion. After the photocatalytic polymer encapsulation process, the brownish dispersion turned reddish which was consistent with the reddish color of the photocatalytic polymers, suggesting the formation of a photocatalytic and magnetic hybrid material.

Figure 59. Image of magnetite dispersions before and after the modifications: pristine magnetite nanoparticle dispersion in DIW (right), magnetite nanoparticles modified with TCDS Fe_3O_4@TCDS (middle), and magnetite nanoparticles encapsulated with photocatalytic polymers (left).

In addition, we have investigated the recycling of the photocatalytic polymer encapsulated magnetite nanoparticles as shown in Figure 60, where magnetic photocatalyst nanoparticles can be easily separated from the solvent by a magnet. Moreover, by simply shaking the glass vial the magnetic photocatalyst nanoparticles can be redispersed in DIW, demonstrating sustainable photocatalytic materials with an easy recovery and reuse process.

Figure 60. Images of the recycling process of magnetic-responsive photocatalytic hybrid materials.

The promising potential of as-obtained magnetic photocatalytic hybrid materials has encouraged us to investigate their photocatalytic reactivity. Initially, we applied the materials to catalyze the methyl phenyl sulfide oxidation as a model reaction. As displayed in the GCMS analysis (Figure 61), over 95% of the sulfide substrate was oxidized within 4 h of light irradiation, demonstrating an efficient photocatalytic material.

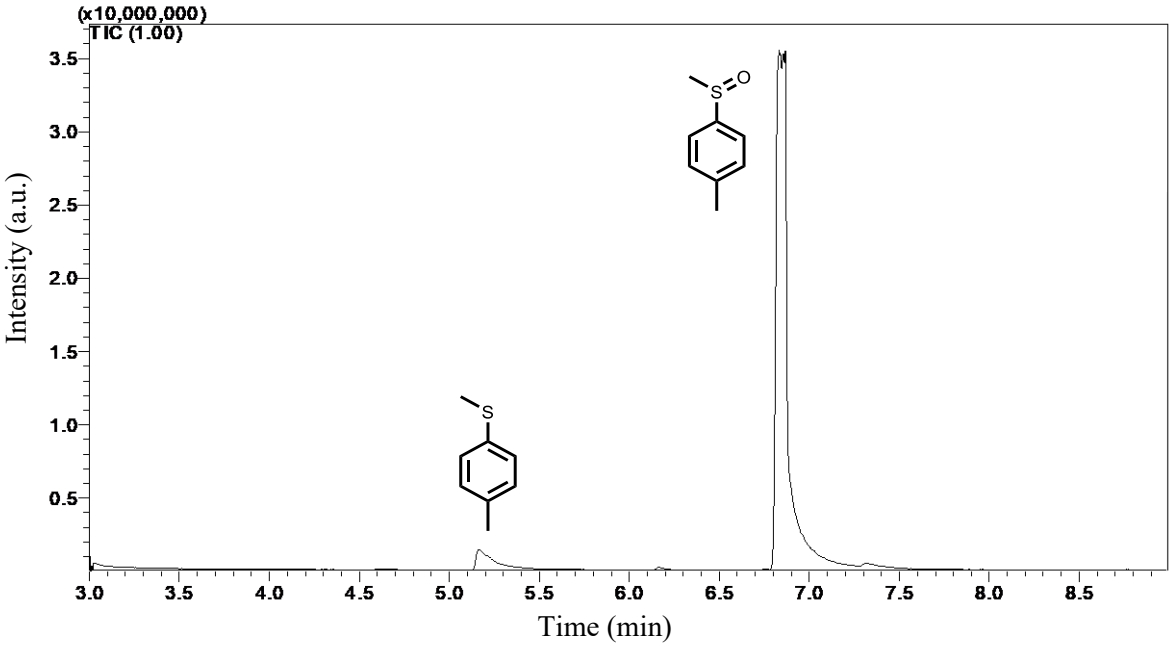

Figure 61. A representative GCMS spectrum of the methyl phenyl sulfide oxidation using photocatalytic polymer encapsulated Fe_3O_4 nanoparticles Fe_3O_4@POEGA-*s*-EY-*b*-PBzMA.

In addition to sulfide oxidation, photocatalytic hydroxylation of boronic acids has been intensively investigated in the past decade, providing a green entry to produce various phenols and aliphatic alcohols with extremely high yields.[193] The mechanism[27,194–196] of this reaction has been well explained, showing that superoxide radical anion was generated by a single electron transfer from the excited reductive photocatalyst to molecular oxygen. This resultant superoxide radical anion is further coupled to the boron atom and subsequently rearranged to form a boronic ester. Eventually, a phenol or an aliphatic alcohol is produced after hydrolysis.

With our interest in photocatalytic hydroxylation reactions, we have applied magnetic-responsive photocatalytic hybrid materials with eosin Y as an active photocatalyst for this transformation. Initially, we have selected (4-methoxyphenyl)boronic acid (Table 5, Entry 1) as a model substrate. The reaction was carried out at room temperature in the presence of oxygen as the oxidant, sodium ascorbate as the sacrificial electron

donor, and DIW as the solvent. Over 99% GCMS yield of the desired 4-methoxyphenol has been obtained after 3 h of blue light irradiation. A control experiment in the absence of a photocatalyst (Table 5, Entry 2) has resulted in a very low yield (5%). Further investigation of the reaction under dark conditions (Table 5, Entry 3) failed to produce the desired product with less than 2% yield. The replacement of the oxygen atmosphere with an air atmosphere hindered this transformation, yielding only 65% of the final product (Table 5, Entry 4). These results demonstrated that Entry 1 gave the optimal result and the necessity of continuous light irradiation, oxygen, and photocatalyst to deliver the desired product.

The scope of this hydroxylation reaction has been expanded with alkylboronic acids with different functional groups employing the optimal conditions. Substrate with an electron-donating phenyl group showed slightly diminished reactivity giving 86% yield (Table 5, Entry 5). However, it could also be a result from the extremely limited water compatibility of the highly hydrophobic substrate. Electron-withdrawing groups, such as methoxycarbonyl (Table 5, Entry 6) and trifluoromethyl groups (Table 5, Entry 7) were also investigated, exhibiting excellent yields with 97% and more than 99%, respectively. The oxidative hydroxylation of boronic acid substrates has been efficiently facilitated using magnetic-responsive photocatalytic hybrid nanoparticles and a great tolerance of functional groups has been observed.

Table 5. The oxidative hydroxylation of alkylboronic acids with various substitutes under different conditions.

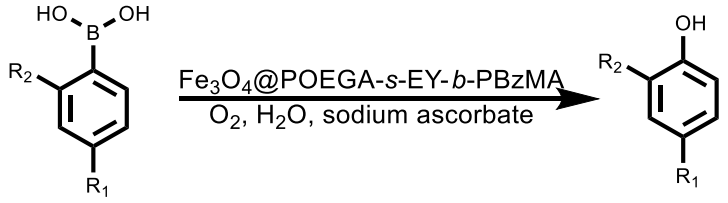

Entry	Condition	Yield
1	R_1 = -OMe, R_2 = -H	> 99%[a]
2	No photocatalyst	5%
3	No light	< 2%
4	No oxygen	65%
5	R_1 = -Phenyl, R_2 = -H	86%[a]
6	R_1 = -CO_2Me, R_2 = -H	97%[a]
7	R_1 = -CF_3, R_2 = -CF_3	>99%[a]

[a]Standard reaction conditions: boronic acid substrates (10 mM), Fe_3O_4@POEGA-*s*-EY-*b*-PBzMA (5 mg/mL, with a photocatalytic polymer content of 2.5 mg/mL), 1 mL DIW, RT, 3 h, yield determined by GCMS.

Further to boronic acids, arylboronic acid pinacol ester was investigated as a suitable substrate for this reaction. Here, the simplest phenylboronic acid pinacol ester has been selected as a model compound. The kinetic profile of hydroxylation was monitored, in triplicate, by GCMS. As illustrated in Figure 62, the magnetic photocatalytic nanoparticles efficiently produced 90% yield of the hydroxylation after 3 h of light irradiation, whereas no conversion was observed in control reaction conditions. Moreover, these nanoparticles were subjected to repeated cycles of hydroxylation reaction. No obvious loss in hydroxylation efficiency after being used 4 times, demonstrating efficient and easily recoverable photocatalytic nanoparticles.

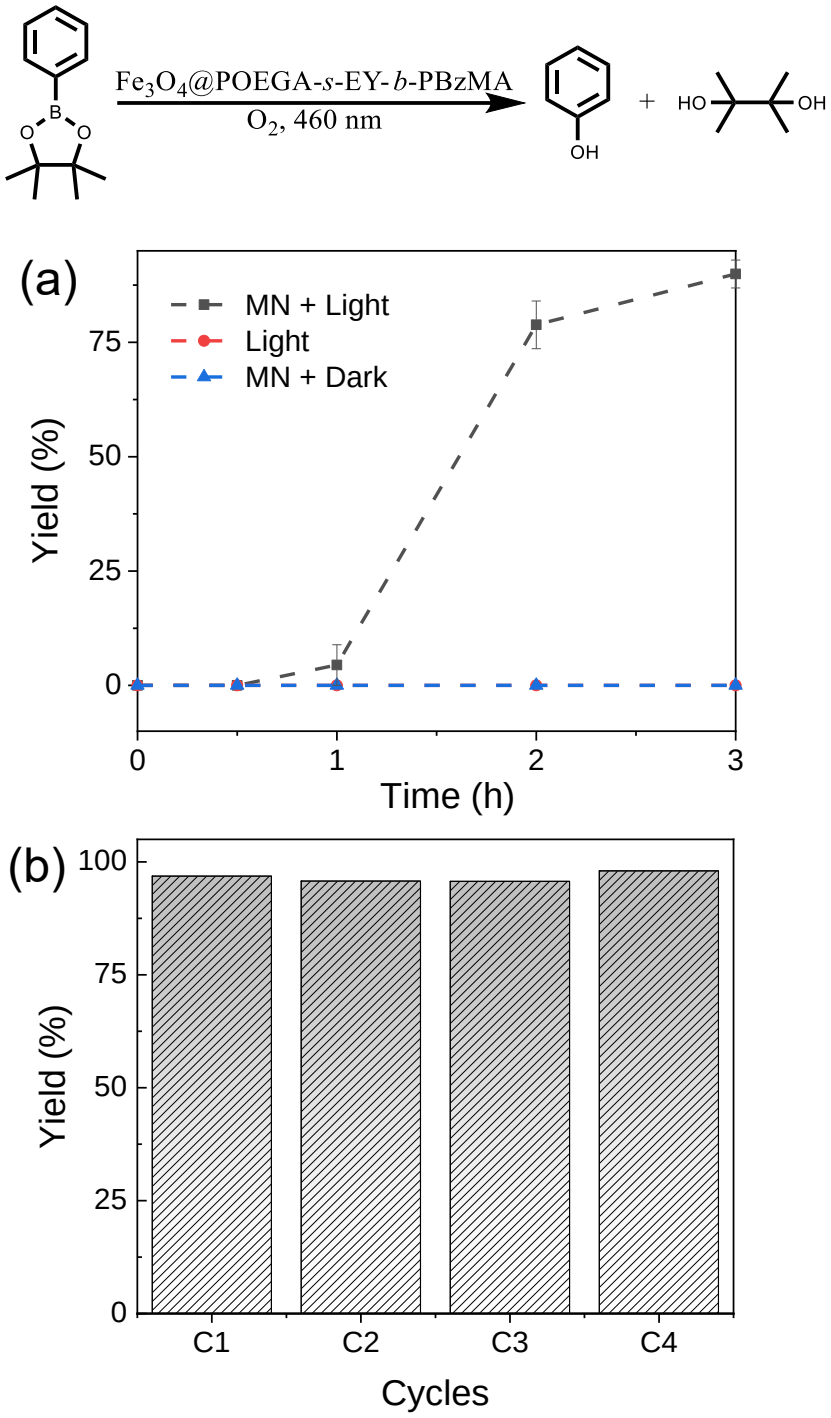

Figure 62. Fe_3O_4@POEGA-*s*-EY-*b*-PBzMA catalyzed hydroxylation of phenylboronic acid pinacol ester. (a) Kinetic profiles of the phenylboronic acid pinacol ester hydroxylation in the presence of magnetic photocatalytic nanoparticles and control reactions (without photocatalyst in light and with photocatalyst in dark). (b) Repeated cycles of hydroxylation reactions using Fe_3O_4@POEGA-*s*-EY-*b*-PBzMA as a recyclable photocatalyst and the recycling test was carried out with 6 h of blue light irradiation for each cycle.

A possible mechanism of this oxidative hydroxylation is illustrated in Figure 63. Upon visible-light irradiation, the photocatalyst was excited and it donated an electron to the oxygen generating a superoxide radical anion. This anion further reacted with the

boronic acid pinacol ester forming an intermediate that subsequently rearranged and hydrolysed to produce the final phenol. Moreover, sodium ascorbate gave an electron to the highest occupied molecular orbital (HOMO) of the photocatalyst, leading to the regeneration of ground state photocatalyst.

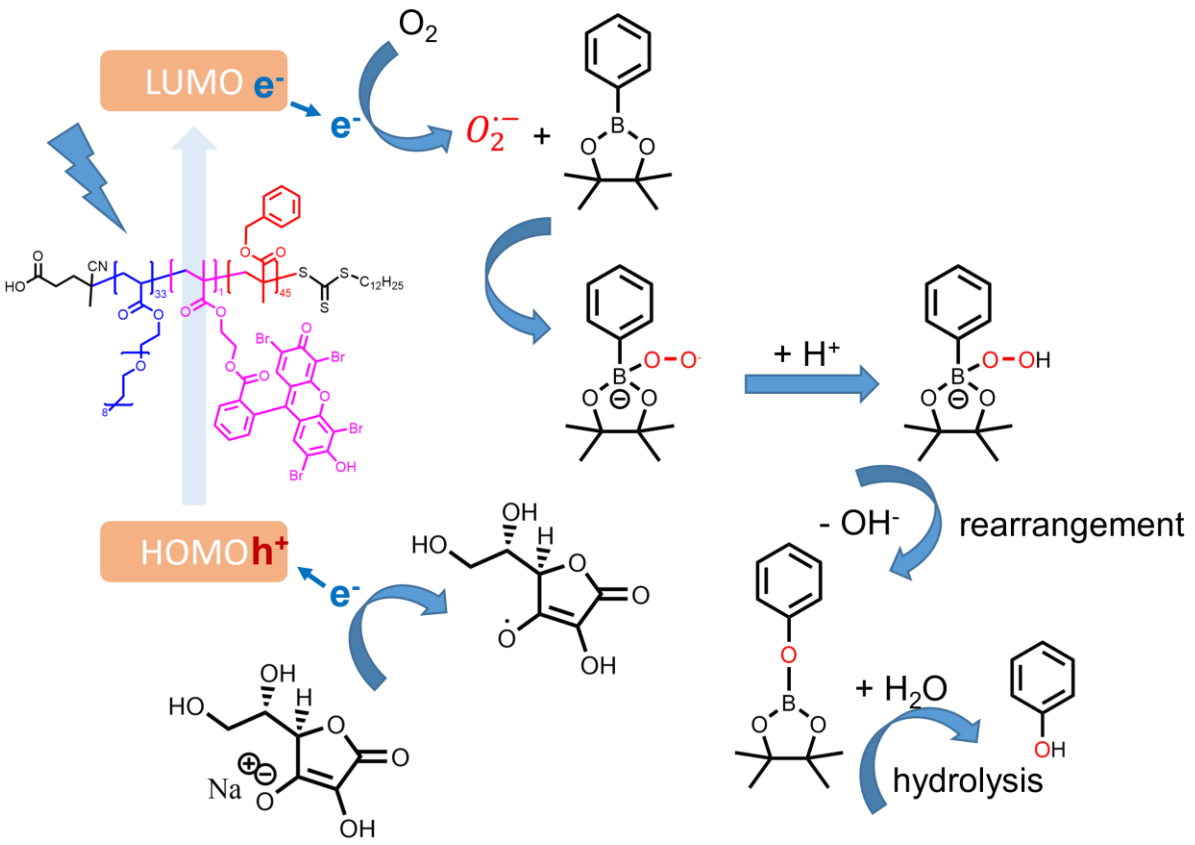

Figure 63. Proposed mechanism in the literature[194] of photocatalyzed hydroxylation in the presence of oxygen.

3.3 Conclusion

In summary, we have produced magnetically recyclable photocatalytic nanoparticles that exhibit extremely excellent performance for boronic acid and boronic acid pinacol ester hydroxylation. This approach involved eosin Y as the effective photocatalytic moiety and water as the sustainable solvent. Excellent yields have been obtained using the magnetic-responsive photocatalytic nanoparticles and broad substrate tolerance has been confirmed. Moreover, these nanoparticles can be easily recovered from the reaction medium by applying a magnet, which can be further used for repeated cycles of the reactions with no loss of efficiency.

3.4 Experimental section

3.4.1 Materials

All chemicals and solvents were purchased from chemical suppliers and used without further purification, unless specifically noted. Poly(ethylene glycol) methyl ether acrylate (M_n = 480), 4,4'-azobis(4-cyanovaleric acid) (ACVA, 98%), 2,2'-azobis(2-methylpropionitrile) (AIBN, 98%), eosin Y (EY, 75%), 2-hydroxyethyl methacrylate (HEMA, 99%), carboxyethyl acrylate (CEA, 97%), 1-hydroxybenzotriazole hydrate (HOBt, 97%), 2,4-bis(trifluoromethyl)phenylboronic acid (95%), iron nanoparticles (99%), DMSO-d_6 (99.9 atom % D), and $CDCl_3$ (99.8 atom % D) were purchased from Sigma Aldrich. Triethylamine (TEA, 99%) was acquired from VWR. 1-Ethyl-3-(3-dimethylaminopropyl) carbodiimide hydrochlorides (EDC·HCl, 98%), 4-methoylphenylboronic acid (95%), 4-methoxycarbonyl phenylboronic acid (95%), biphenylboronic acid (97%), phenylboronic acid pinacol ester (97%), and benzyl methacrylate (BzMA, 98%) were purchased from CDI. 4-((((2-Carboxyethyl)thio)carbonothioyl)thio)-4-cyanopentanoic acid (CCCP, 95%) was purchased from Boron Molecular. Fe3O4 nanoparticles (size 18-28 nm, 98.45+%) were purchased from Nanografi Nano Technology.

3.4.2 Characterization Techniques

^{1}H NMR spectra were measured by Bruker Avance 400, to determine the chemical structures of polymers. UV/Vis absorption and emission were monitored by a plate reader. Gas chromatograms and corresponding mass spectra were taken from GCMS-QP-2010 Ultra. FTIR spectra were measured using a Bruker Tensor II FTIR spectrometer to characterize the chemical structures and compositions of the polymers and hybrid materials (magnetite nanoparticles and photocatalytic polymers, iron nanoparticles and photocatalytic polymers, magnetite nanoparticles with TCDS, and iron nanoparticles with TCDS). TEM was conducted using a JEM-1400 Transmission Electron Microscope. Samples were prepared by dispersing the particles in DIW (0.1 wt%) and applying them to carbon coated copper grids.

3.4.3 Preparation of Diblock Copolymer POEGA-*r*-EY-*b*-PCEA and Amphiphilic Diblock Copolymer POEGA-*r*-EY-*b*-PBzMA

POEGA-*s*-EY-*b*-PCEA and POEGA-*s*-EY-*b*-PBzMA were synthesized by RAFT polymerization, respectively. Briefly, CCCP (0.048 g, 0.15 mmol), POEGA (3 g, 6.25 mmol), EYHEMA (0.19 g, 0.25 mmol), and AIBN (5 mg, 3.1 µmol) were dissolved in

anhydrous DMF (3.2 mL). After degassing, the mixture was stirred at 70 °C for 2 h followed by dialysis against DIW/acetone (1/1) for 3 days and DIW for 1 day. The sample was dried by lyophilization. The final product was obtained as a reddish viscous liquid. The degree of polymerization of the POEGA block was determined as 32 according to the ^{1}H NMR spectrum. The dispersity and molecular weight were determined by GPC using DMF as solvent. The obtained POEGA-*s*-EY was further used as macroCTA for the chain extension of the ligand block PCEA or hydrophobic PBzMA block. More in detail, POEGA-*s*-EY (500 mg, 26 μmol), CEA (76.1 mg, 0.53 mmol), and ACVA (1.8 mg, 5.3 μmol) were dissolved in anhydrous DMF (2 mL) and degassed with Ar. The reaction mixture was heated up to 70 °C overnight followed by dialysis in acetone/DIW (1/1) for 3 days and DIW for 1 day. The final product was dried by lyophilization, obtaining a fluorescent red sticky polymer.

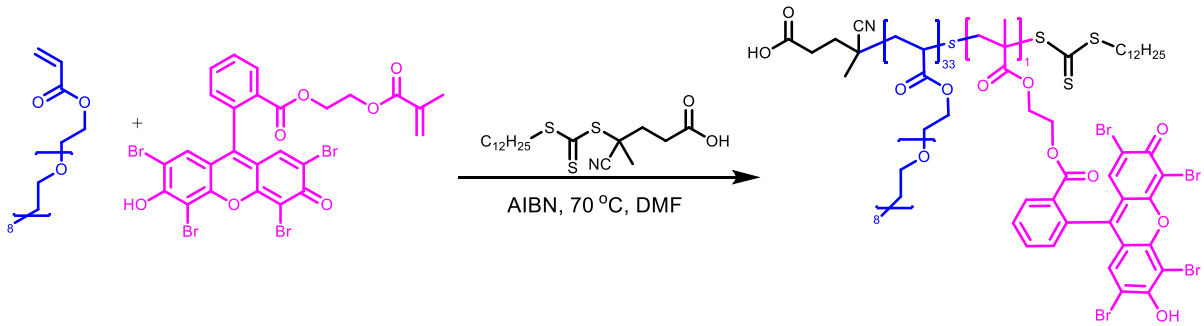

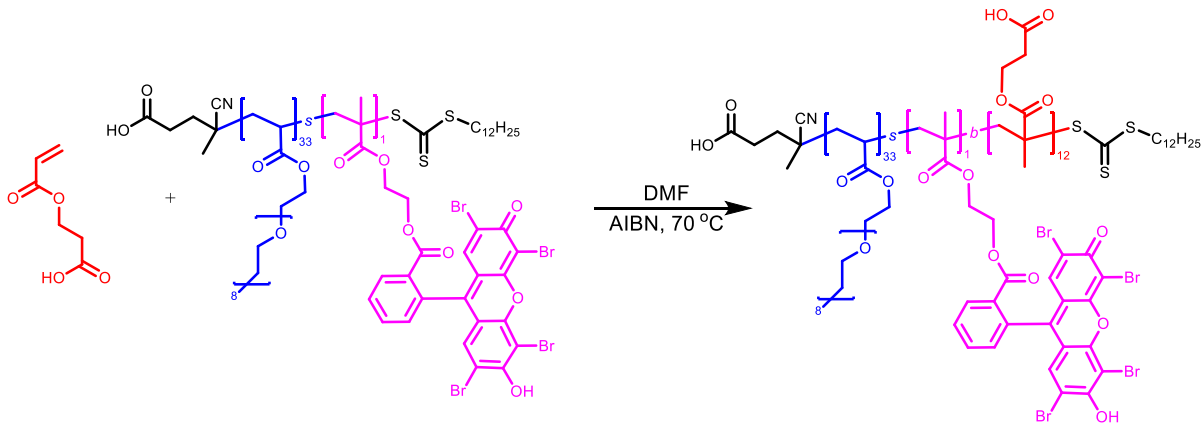

Regarding amphiphilic block copolymer POEGA-*s*-EY-*b*-PBzMA, POEGA-*s*-EY (1.1 g, 59 μmol), BzMA (566 mg, 3.2 mmol), and AIBN (2.0 mg, 11.9 μmol) were dissolved in anhydrous dioxane (2.6 mL) and degassed with Ar. The reaction mixture was heated up to 70 °C overnight followed by dialysis in acetone/DIW (1/1) for 3 days and DIW for 1 day. The final product was dried by lyophilization, obtaining a fluorescent red sticky polymer.

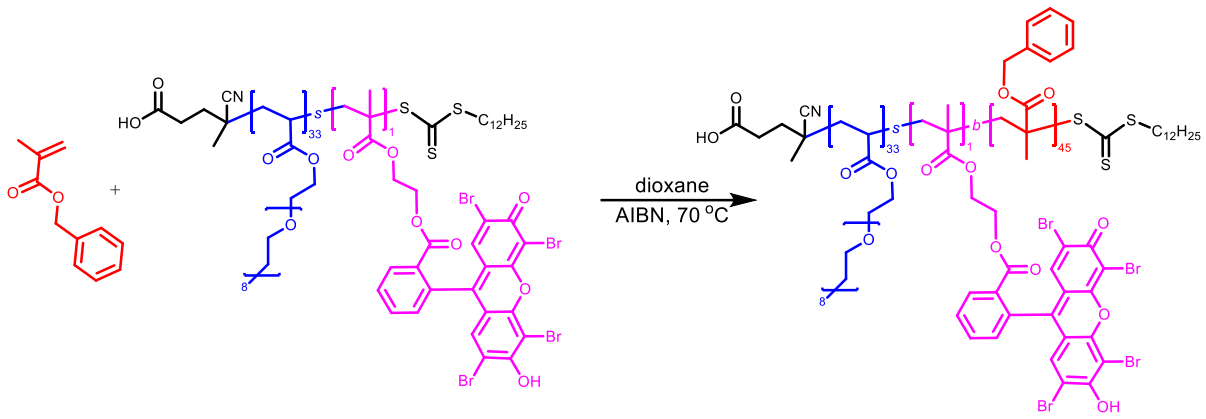

3.4.4 Synthesis of Diblock Copolymer POEGA-*s*-EY-*b*-PDHMA Stabilized Fe_3O_4 Nanoparticles

The synthesis procedure was adapted from the literature.[197] In brief, 0.233 g (0.86 mmol) of iron (III) chloride hexahydrate (270.3 g/mol) and 0.086 g (0.43 mmol) of iron (II) chloride tetrahydrate (198.81 g/mol) were mixed in 20 mL of de-ionized water to give a concentration of 0.065 M or 9.75 mg/mL of $FeCl_3$ and $FeCl_2$. The solution was purged with N_2. 2 mL of the iron salt stock solution (19.5 mg of $FeCl_3$ and $FeCl_2$) was mixed with 2 mL of an aqueous solution of diblock copolymer at different weights (40 mg and 60 mg), which were degassed with N_2 before pre-heated half an hour at 70 °C. The color of the solution turned dark from blood red after 2 mL of NaOH solution (1 M) was added to each vial, respectively. The reaction was carried out at 70 ° C for 2 h with vigorous stirring.

3.4.5 Surface Modification of Fe Nanoparticles

Fe nanoparticles (50 mg, from Sigma Aldrich) were dispersed in anhydrous toluene (15 mL) and sonicated for 15 min. To the nanoparticle dispersion, 0.15 mL TCDS was added dropwise. The mixture was sonicated for 3 h at room temperature. The nanoparticles were separated from the solution by a magnet and washed with chloroform three times. The nanoparticles were sonicated in chloroform for 15 min for each cycle of washing. After the washing step was completed, the iron nanoparticles were stored in chloroform for further encapsulation. These iron nanoparticles were marked as Fe@TCDS.

3.4.6 Encapsulation of Fe Nanoparticles with Photocatalytic Amphiphilic Polymers

Fe@TCDS (50 mg Fe) nanoparticles dispersed in chloroform (2 mL) were mixed with 100 mg POEGA-*s*-EY-*b*-PBzMA prior to the addition of 10 mL DIW. The mixture was subsequently subjected to ultrasonication tip with an amplitude of 20%, 3 min pulse

sonication (20 s on and 10 s off), cooled with an ice-bath. The as-obtained emulsion was further sonicated with a sonication bath to evaporate the chloroform. After the organic solvent was evaporated, the magnetic nanoparticles coated with photocatalytic polymers can be easily dispersed in DIW, demonstrating the successful incorporation of the photocatalytic polymers. These hybrid particles were washed with DIW to remove empty micelles (micelles without Fe nanoparticles). Although the magnetic particles were coated with photocatalytic polymers, the efficiency of the encapsulation was very low since only 6.3 wt% of the polymer content was coated on the surface and majority of the polymers were self-assembled into empty micelles.

3.4.7 Surface Modification of Fe_3O_4 Nanoparticles

Purchased Fe_3O_4 nanoparticles (50 mg, from Nanografi Nano Technology) were dispersed in anhydrous toluene (15 mL) and sonicated for 15 min. To the nanoparticle dispersion, 0.15 mL TCDS was added dropwise. The mixture was sonicated for 3 h at room temperature. The nanoparticles were separated from the solution by a magnet and washed with DCM three times. The nanoparticles were sonicated in DCM for 15 min for each cycle of washing. After the washing step was completed, the magnetite nanoparticles were stored in DCM for further encapsulation. These magnetite nanoparticles were marked as Fe_3O_4@TCDS.

3.4.8 Encapsulation of Fe_3O_4 Nanoparticles with Photocatalytic Amphiphilic Polymers

Fe_3O_4@TCDS (50 mg Fe_3O_4) nanoparticles dispersed in DCM (2 mL) were mixed with 100 mg or 150 mg POEGA-*s*-EY-*b*-PBzMA to have a magnetite nanoparticle to polymer ratio at 1:2 or 1:3, respectively, prior to the addition of 10 mL DIW. The mixture was subsequently subjected to magnetic stirring overnight to evaporate the DCM solvent. After the organic solvent was evaporated, the magnetic nanoparticles coated with photocatalytic polymers can be easily dispersed in DIW, demonstrating the successful incorporation of the photocatalytic polymers. These hybrid particles were washed with DIW to remove empty micelles (micelles without Fe nanoparticles) or free polymers. These particles were coated with photocatalytic polymers, the efficiency of the encapsulation was very high.

3.4.9 Photocatalytic Reactions

Boronic Acid Hydroxylation

Photocatalytic nanoparticles Fe_3O_4@POEGA-*s*-EY-*b*-PBzMA 5 mg (photocatalytic polymer 2.5 mg/mL) were suspended in 1 mL DIW in 4 mL open-top screw cap vials.

Boronic acid substrates (10 mM) including 4-methoylphenylboronic acid, 4-methoxycarbonyl phenylboronic acid, biphenylboronic acid, and 2,4-bis(trifluoromethyl)phenylboronic acid and sodium ascorbate (50 mM) were added to nanoparticle dispersions, respectively. The reaction mixtures were supplied with oxygen before being subjected to blue LED irradiation (power: 21 mW/cm^2, λ = 460 nm) for 3 h. The samples were mixed with DCM (4 mL) to extract reagents and products. The DCM solutions were further dried over $MgSO_4$ before GCMS measurements. The yield and products were monitored by GC-MS.

Boronic Acid Pinacol Ester Hydroxylation

Photocatalytic nanoparticles Fe_3O_4@POEGA-*s*-EY-*b*-PBzMA 10 mg (photocatalytic polymer 2.5 mg/mL) were suspended in 2 mL DIW in 4 mL open-top screw cap vials. Phenylboronic acid pinacol ester (14 mM) and sodium ascorbate (50 mM) were added to nanoparticle dispersion. The reaction mixture was supplied with oxygen before subjected to blue LED irradiation (power: 21 mW/cm^2, λ = 460 nm) for kinetic study. The sample aliquots (0.4 mL) were mixed with DCM (2.5 mL) to extract reagents and products. The DCM solutions were further dried over $MgSO_4$ before GCMS measurements. The yield and products were monitored by GC-MS in triplicate.

Boronic Acid Pinacol Ester Hydroxylation Recycling Experiments

A 4 mL vial containing a stir bar was charged with 10 mg of Fe_3O_4@POEGA-*s*-EY-*b*-PBzMA (5 mg/mL, fresh or used) and 2 mL of DIW. To the suspension, phenylboronic acid pinacol ester (14 mM) and sodium ascorbate (50 mM) were added, and the vial was sealed with a septum screw cap. The reaction mixture was connected to an oxygen-filled balloon. The vial was then subjected to the liquid-cooled photoreactor, where it was irradiated by 21 mW/cm^2 of blue light (λ_{max} = 460 nm) for 6 h. After completion, 0.5 mL of the reaction mixture was extracted with 2.5 mL DCM for GCMS analysis. Product yield was determined as described above.

4 Therapeutic Applications of Responsive Organic Photocatalytic Polymers, Enabling *in situ* Prodrug Activation

In the previous chapters, the recycling of photocatalytic nanoparticles has been efficiently obtained by tuning the pH value or via a magnetic separation technique, which greatly enhanced the sustainability of the photocatalytic materials. Further to improving the recyclability of photocatalytic materials using external stimuli, we are also interested in modulating photocatalytic reactivity by an external stimulus. In this following project, we have investigated targeted prodrug activation using pH-responsive photocatalytic systems. This chapter is based on the submitted article 'Therapeutic applications of responsive organic photocatalytic polymers, enabling *in situ* prodrug activation'.

A general strategy for activating prodrugs was developed utilizing the acidic tumor microenvironment and reactive oxygen species (ROS) generation. Here, pH-responsive polymers consisting of photocatalytic units can form deactivated nanoparticles in the blood due to the limited accessibility of the reactive centers in the core of the nanoparticles, whereas these nanoparticles can disassemble in response to the acidic tumor extracellular microenvironment, exposing the photocatalytic centers that subsequently activate the prodrug by ROS generation under light irradiation.

4.1 Motivation

The emergence of photodynamic therapy (PDT) has facilitated minimally invasive treatment for various diseases (e.g. cancers) with well-understood fundamental mechanisms of operation. Upon light irradiation, a photocatalyst absorbs a photon generating a short-lived excited singlet state (S1) that can undergo intersystem crossing and populate the more stable excited triplet state (T_1). The energy of this excited triplet state can be further transferred to the molecular oxygen (O_2), generating reactive singlet oxygen $^1O_2$. Additionally, other reactive oxygen species (ROS) such as superoxide $O_2^{\cdot}$ can be produced via an electron transfer process, which can further interact with water as a solvent generating hydroxyl radicals $OH^{\cdot}$. These ROS can induce oxidative damage and ultimately kill cancer cells.[198–200] However, the performance of many currently developed photocatalytic molecules have significant

limitations such as the intrinsic hydrophobicity[201] and the lack of targeting selectivity towards tumor cells.[202–205] Therefore, the development of a novel tumor-specific PDT system is still highly desired.

To develop a general strategy to selectively target the tumor tissue, ubiquitous features of tumor microenvironment (for instance low pH value, high interstitial pressure, or hypoxia) have been frequently selected as an alternative to endogenous biomarkers.[206] Typical systems have been designed by incorporating stimuli-responsive moieties to modulate their functionalities in response to either external (e.g. UV light[207,208])) or endogenous stimuli (e.g. enzyme,[209,210] low pH,[211–213] redox,[214] and hypoxia[215,216]). Solid tumors are ubiquitously characterized by the dysregulated pH value, where the extracellular microenvironment (pH_e 6.5-6.9) is slightly lower in comparison to normal tissues (pH 7.2-7.4). To this consideration, developing a pH-sensitive polymer system may achieve the targeted activation of the photocatalyst in the tumor microenvironment. Polymer chains can form particles through self-assembly, where the photocatalytic segments are captured in the core and remain inactive in the bloodstream. However, upon exposure to the acidic extracellular microenvironment, photocatalytic moieties are revealed and activated due to the disassembly of nanoparticles, during which the aqueous compatibility of the photocatalyst is also enhanced. Therefore, we propose that a pH-responsive polymer system containing photocatalytic moieties may modulate the tumor-specific production of ROS for cancer therapy.

ROS can act as not only an active therapeutic agent to kill cancer cells directly but also as a trigger to control the activation of other treatment processes (e.g., prodrug activation or drug release from nanocarriers), inducing additive or even synergistic efficacies. For example, conjugating ROS-sensitive linkers[200,217] such as aminoacrylate bond,[218,219] thioketal bond,[220,221] phenylboronic ester[222–225] in the chemical structures of nanocarriers and/or prodrugs have been explored for cascade reactions-driven anti-cancer drug release. Among these, polyprodrugs have emerged as an alternative to nanomedicine encapsulation, avoiding the inevitable drug leakage of nanocarriers. Typically, therapeutic drugs are conjugated to the polymer backbones using a ROS-sensitive linker, allowing tunable drug-loading and controllable drug release.[199,212,226] Therefore, the combination of pH-responsive polymeric photocatalysts and ROS-responsive polyprodrug-based micelles enabling ROS

generation in the tumor microenvironment and subsequently ROS trigger the drug release *in situ*, which may provide a promising strategy to enhance anti-tumor efficacy through PDT/chemo combination therapy.

Here, we have developed a pH-responsive photocatalytic system that can selectively generate ROS at tumor tissue and further activate prodrugs through a cascade reaction. To demonstrate the versatility of this photocatalytic system, the activation of four ROS-sensitive linkages, including aminoacrylate bond, thioketal bond, phenylboronic ester and oxalate, have been examined. Moreover, by combining these pH-responsive photocatalytic polymers with pH/ROS-responsive prodrug polymers we can produce a system consisting of both photocatalysts and prodrugs in one spherical nanoparticle structure, enabling the delivery of functional species at once. As illustrated in Scheme 1, two series of amphiphilic polymers, pH-responsive poly(ethylene glycol)-*b*-poly(2-azepane ethylmethacrylate)-*b*-2-(methacryloyloxy)ethyl 2-(2,4,5,7-tetrabromo-3,6-dihydroxy-9H-xanthen-9-yl)benzoate (PEG_{113}-*b*-$PAEMA_{50}$-*b*-$EYHEMA_1$) and pH/ROS-responsive poly(ethylene glycol)-*b*-poly(2-azepane ethylmethacrylate)-*b*-4-ethyl-3,14-dioxo-3,4,12,14-tetrahydro-1H-pyrano[3',4':6,7]indolizino[1,2-b]quinolin-4-yl (2-(methacryloyloxy)ethyl) oxalate (PEG-*b*-PAEMA-*s*-PCPT) have been synthesized to prepare particles. These amphiphilic polymer chains can self-assemble at pH 7.4 to form particles with extended circulation time in blood stream. Once accumulated in the acidic tumor intracellular environment (pH 6.5), the hydrophobic PAEMA block of the particles is protonated, leading to the disassembly of the particles and exposure of the photocatalyst eosin Y. Upon light irradiation, ROS are generated by the active eosin Y and subsequently allow the activation of prodrugs through the ROS-induced cleavage (Figure 64).

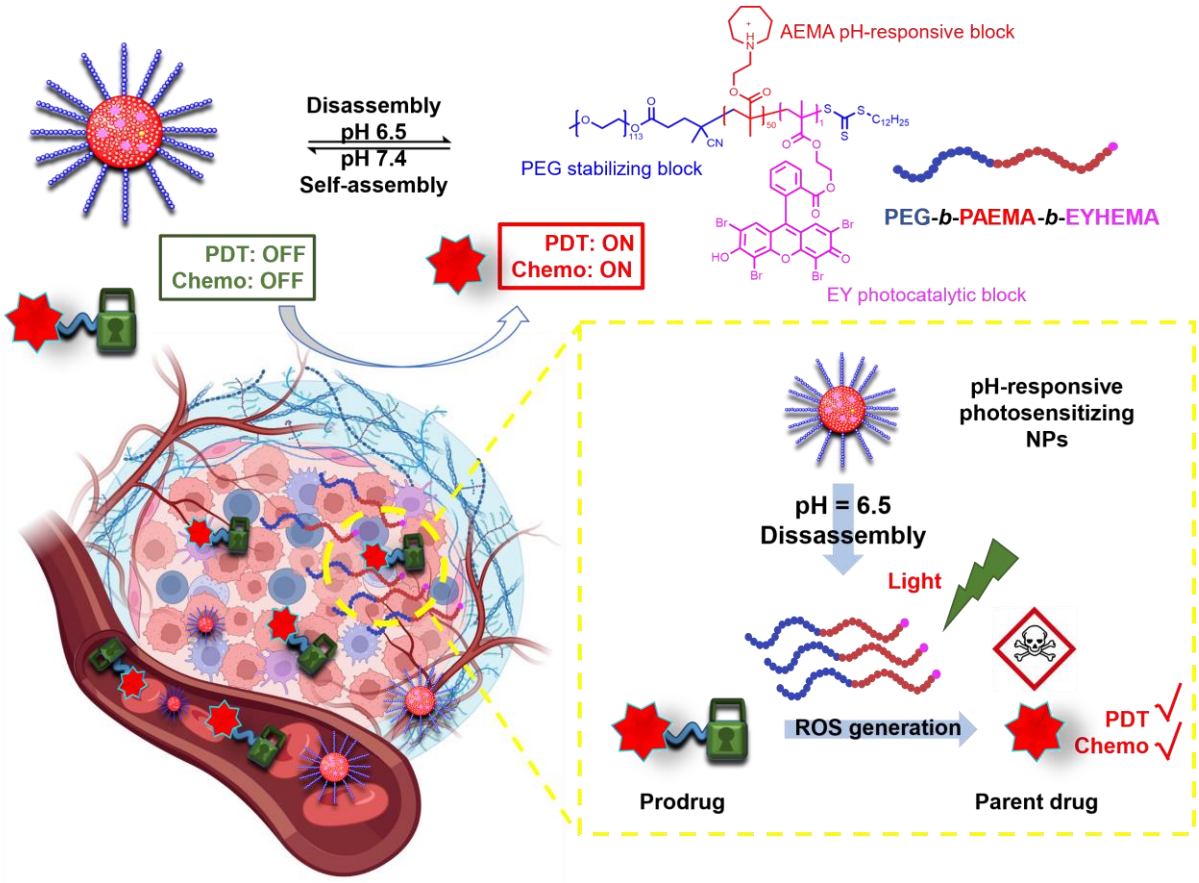

Figure 64. Schematic illustration of the switchable hydrophilicity of the pH-responsive polymer photocatalyst nanoparticles responding to the subtle pH change from the bloodstream (pH 7.4) to the tumor extracellular microenvironment (pH 6.5). The activated photocatalytic polymer chains after disassembly can further activate the prodrug into active therapeutics, leading to targeted cancer treatment.

4.2 Synthesis and Characterization of pH-responsive Photocatalytic Polymer Nanoparticles for Therapeutic Applications

Eosin Y was selected as the photocatalyst for the activation of prodrug model compounds due to its high singlet oxygen quantum yield.[227] In order to incorporate the molecular eosin Y into polymeric structures, we have coupled eosin Y molecules with two polymerizable functional groups 2-aminoethylmethacrylate (AMA) and 2-hydroxylethylmethacrylate (HEMA), respectively, resulting in 2-(2-(2,4,5,7-tetrabromo-6-hydroxy-3-oxo-3H-xanthen-9-yl) benzamido) ethyl methacrylate (EYAMA) and 4-methyl-3-oxopent-4-en-1-yl 2-(2,4,5,7-tetrabromo-6-hydroxy-3-oxo-3H-xanthen-9-yl)benzoate (EYHEMA) as two sets of photocatalytic monomers. Thereafter, two series of pH-responsive triblock copolymers PEG_{113}-*b*-$PAEMA_{50}$-*b*-$EYAMA_1$ and PEG_{113}-*b*-$PAEMA_{50}$-*b*-$EYHEMA_1$ (Figure 65) based on these two photocatalytic

monomers were synthesized by reversible addition-fragmentation chain transfer (RAFT) polymerization using poly(ethylene glycol) methyl ether (4-cyano-4-pentanoate dodecyl trithiocarbonate) ($mPEG_{113}$-CPDTC) as the macro-chain transfer agent (macro-CTA), 2-azepane ethylmethacrylate (AEMA) as pH-responsive monomers. Initially, pH-responsive diblock copolymer PEG_{113}-*b*-$PAEMA_{50}$ was synthesized using $mPEG_{113}$-CPDTC as macroCTA and AEMA as monomers. To incorporate the photocatalytic EY moieties, we have tried the direct copolymerization of AEMA monomers and EYAMA monomers as the second block (statistic copolymer). However, only EYAMA monomers were blocked off from the PEG macroCTA, which could have resulted from the different polymerization rates of both monomers and/or the radical trapping effect of the EYAMA monomers. When EYHEMA was copolymerized with AEMA monomers, the polymerization proceeded however with a very low conversion (25%). Therefore, the EY moieties were implanted by blocking off from the PEG_{113}-*b*-$PAEMA_{50}$ diblock copolymer, producing triblock copolymers (Figure 65(a)) PEG_{113}-*b*-$PAEMA_{50}$-*b*-$EYAMA_1$ and ((Figure 65(b)) PEG_{113}-*b*-$PAEMA_{50}$-*b*-$EYHEMA_1$, respectively.

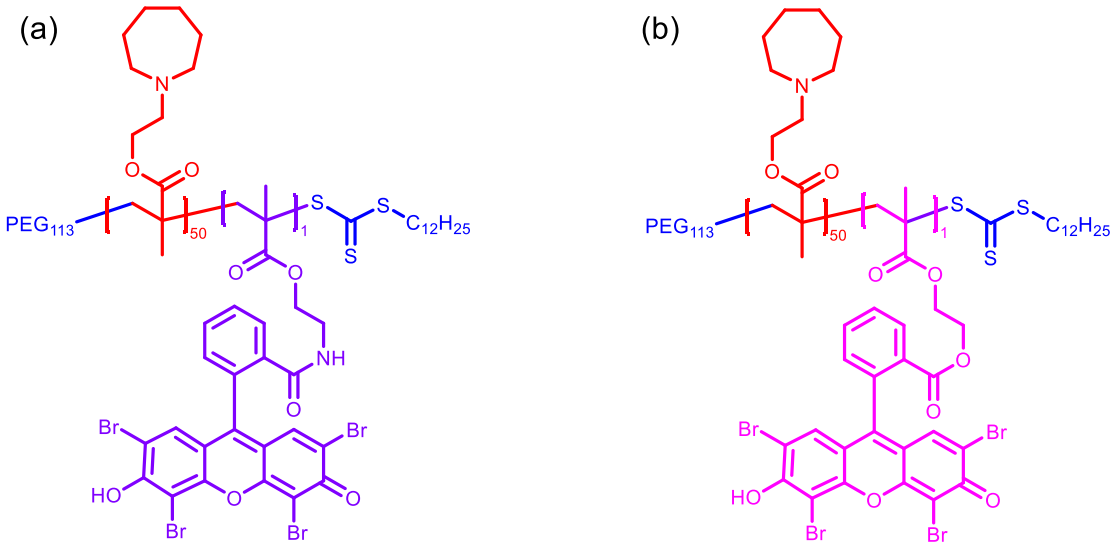

Figure 65. Chemical structure of the pH-responsive triblock photocatalytic copolymers: (a) PEG_{113}-*b*-$PAEMA_{50}$-*b*-$EYAMA_1$ and (b) PEG_{113}-*b*-$PAEMA_{50}$-*b*-$EYHEMA_1$

The resulting polymers were confirmed by ^1H NMR spectroscopy (see Figure 66 and 67) and GPC (see Figure 68).

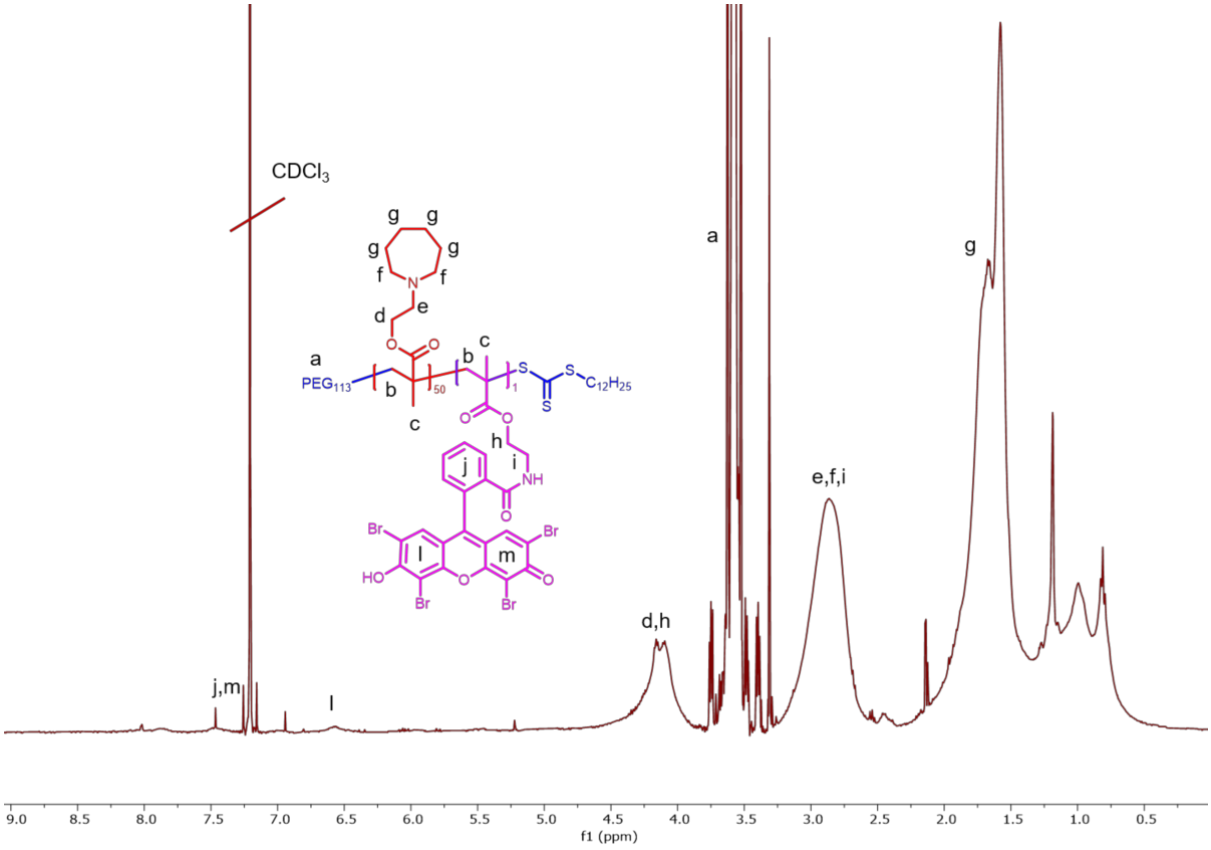

Figure 66. ^{1}H NMR spectrum of the PEG_{113}-*b*-$PAEMA_{50}$-*b*-$EYAMA_{1}$ triblock copolymer.

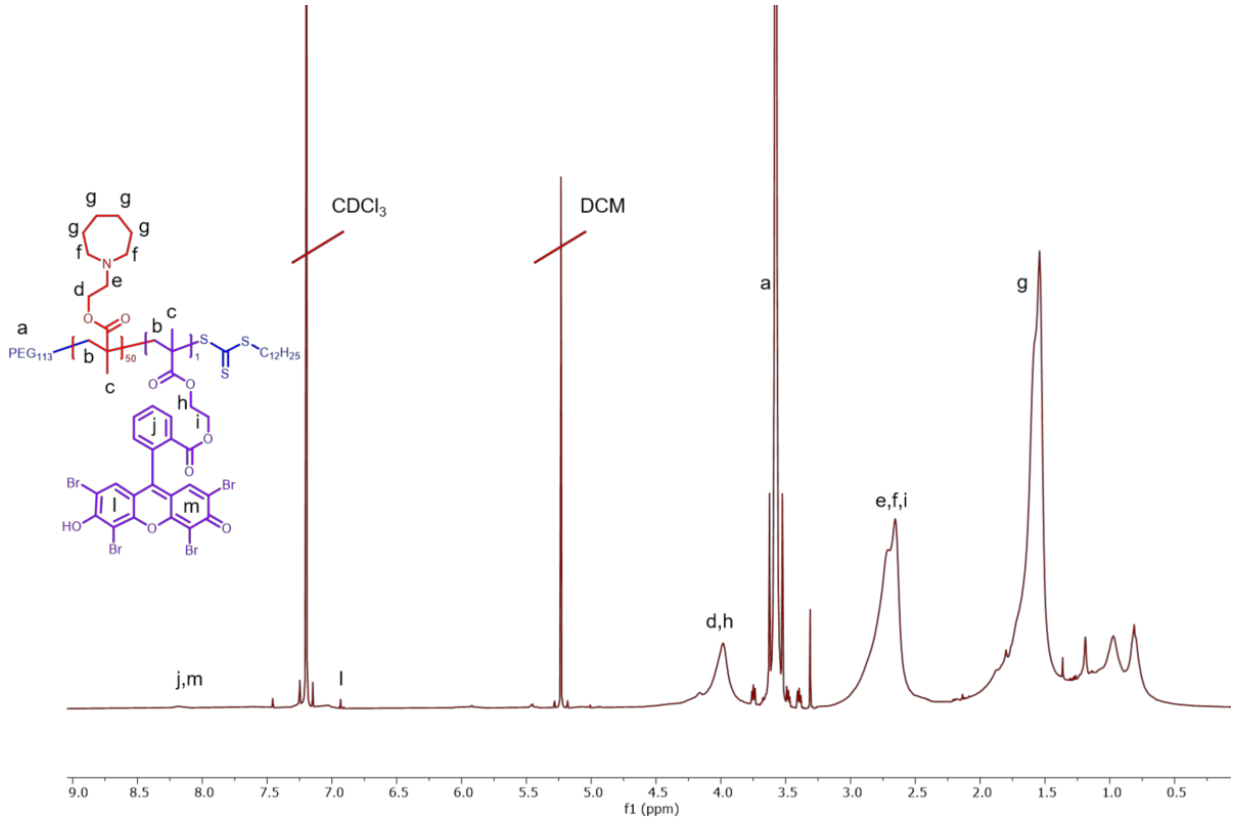

Figure 67. ^{1}H NMR spectrum of the PEG_{113}-*b*-$PAEMA_{50}$-*b*-$EYHEMA_{1}$ triblock copolymer.

GPC has been applied to examine the molecular weight of the photocatalytic triblock copolymers, where DMF was used as solvent and PMMA acted as standard (Figure 68). The molecular weight and dispersity of PEG_{113}-*b*-$PAEMA_{50}$-*b*-$EYAMA_1$ polymer chains were determined to be 21.9 kDa and 1.88, respectively. The molecular weight and dispersity of PEG_{113}-*b*-$PAEMA_{50}$-*b*-$EYHEMA_1$ polymer chains were determined to be 13.9 kDa and 1.24, respectively.

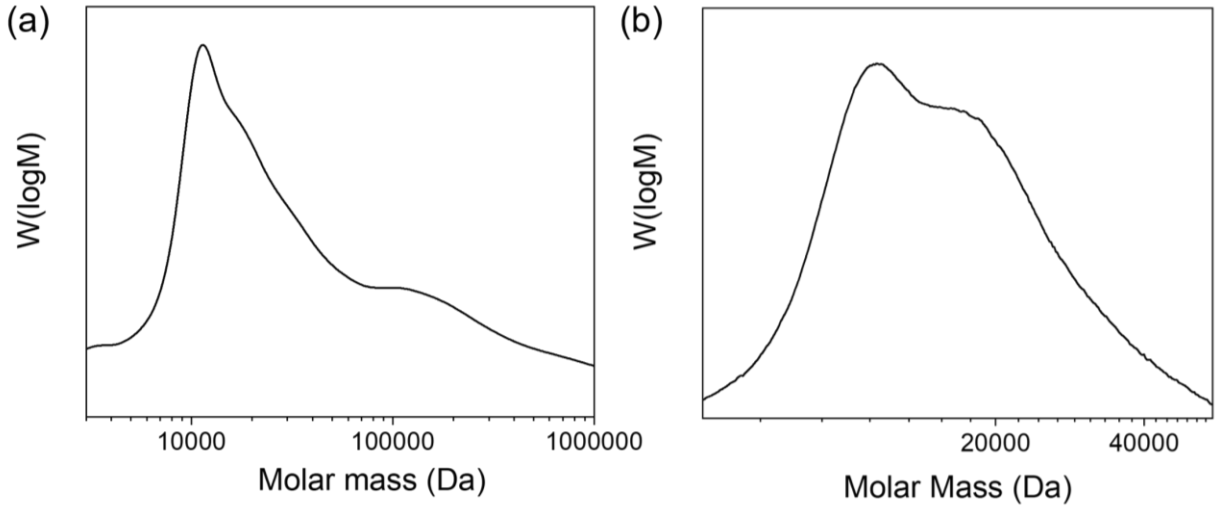

Figure 68. GPC analysis of the (a) PEG_{113}-*b*-$PAEMA_{50}$-*b*-$EYAMA_1$ and (b) PEG_{113}-*b*-$PAEMA_{50}$-*b*-$EYHEMA_1$ triblock copolymers.

Besides, FTIR (Figure 69) has been utilized to examine the chemical compositions of PEG_{113}-*b*-$PAEMA_{50}$, PEG_{113}-*b*-$PAEMA_{50}$-*b*-$EYAMA_1$ and PEG_{113}-*b*-$PAEMA_{50}$-*b*-$EYHEMA_1$ polymer chains. The FTIR spectrum illustrated the aliphatic backbone (-CH_2- and -CH_3) stretch vibration from 3100 to 2700 cm^{-1}. The fingerprint functional groups of the polymer chains, including C=O, C-O, and C-N, were observed peaking in 1720, 1640, and 1170 cm^{-1}, respectively. However, the effect of the photocatalytic moiety was not observed on the FTIR spectrum due to the extremely low loading (0.49 mol%) of the photocatalytic monomer.

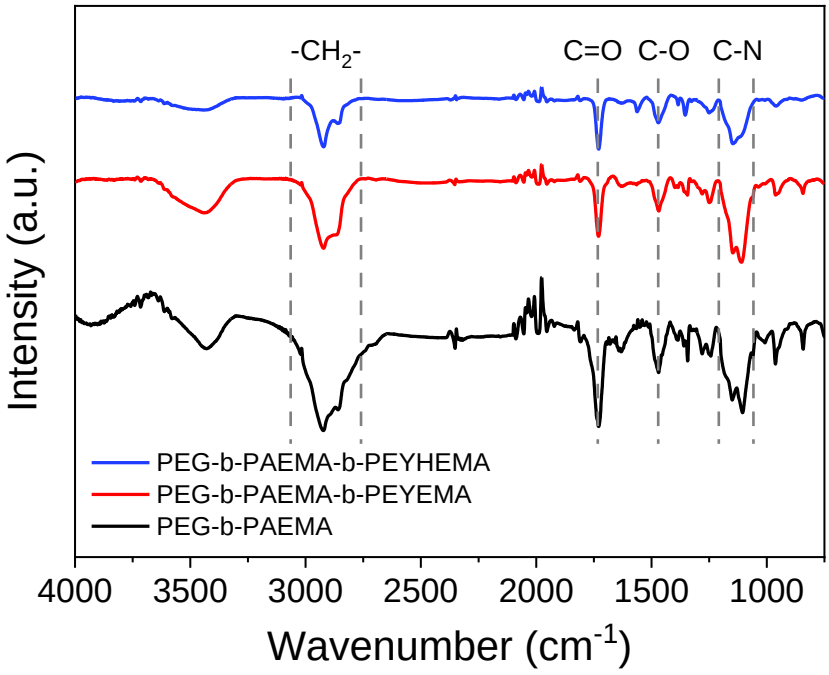

Figure 69. FTIR spectrum of the PEG_{113}-*b*-$PAEMA_{50}$-*b*-$EYAMA_1$ and PEG_{113}-*b*-$PAEMA_{50}$-*b*-$EYHEMA_1$ triblock copolymers.

The optical property of the dual-responsive polymers was visualized by the UV/Vis spectrum, displaying strong absorption in the green light region and emitting red light (Figure 70), which agrees well with the literature.[192]

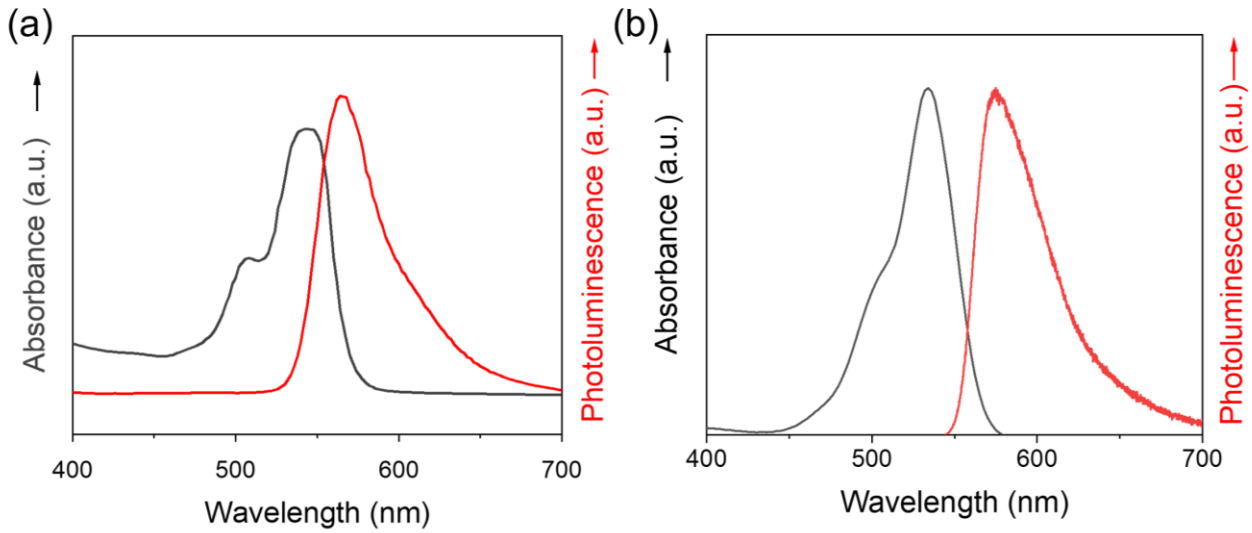

Figure 70. UV/Vis absorbance and emission spectra of the (a) PEG_{113}-*b*-$PAEMA_{50}$-*b*-$EYAMA_1$ and (b) PEG_{113}-*b*-$PAEMAH^+_{50}$-*b*-$EYHEMA_1$ in DMSO (1 mg/mL) triblock copolymers in phosphate buffer (pH 6.5, 1 mg/mL).

PAEMA has been specifically developed as an ultra-pH-sensitive polymer that can exceptionally respond to around 0.3 pH increment[211,213,228], aligning perfectly with the pH difference of the extracellular microenvironment (pH_e 6.5-6.9) compared to normal tissues (pH 7.2-7.4).[229] Taking advantage of this ultrasensitive pH-responsiveness of PAEMA, PEG_{113}-*b*-$PAEMA_{50}$ can be protonated at pH 6.5 leading to the solvation of the polymer chains, while deprotonated at pH 7.4 resulting in an amphiphilic diblock copolymer. Therefore, pH-sensitive nanoparticles were prepared by self-assemble of photocatalytically active PEG_{113}-*b*-$PAEMA_{50}$-*b*-$EYAMA_1$ (NP-PAEMA-EYAMA) and PEG_{113}-*b*-$PAEMA_{50}$-*b*-$EYHEMA_1$ (NP-PAEMA-EYHEMA) or photocatalytically inactive PEG_{113}-*b*-$PAEMA_{50}$ (NP-PAEMA) copolymers, respectively. Due to the light absorbance of the photocatalytic EY moiety, the hydrodynamic diameter of the photocatalytically inactive nanoparticles was determined by dynamic light scatting (DLS) that the diameter of the nanoparticles was approximately 164 nm at pH 7.4, which decreased to 13 nm at pH 6.5 (Figure 71).

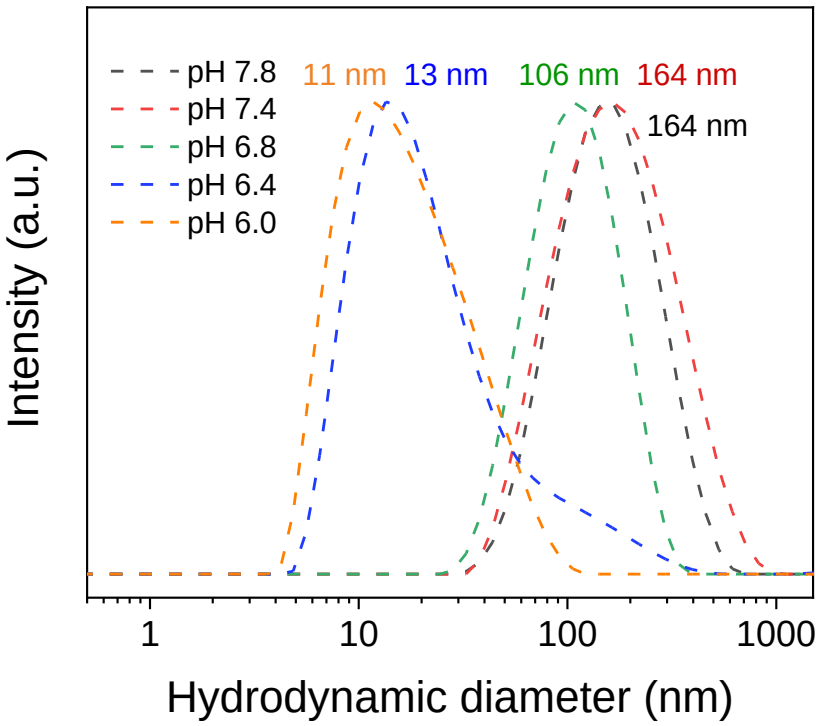

Figure 71. The hydrodynamic diameter of NP-PAEMA changes as a function of pH value measured by DLS.

Additionally, UV-Vis transmittance (Figure 72) measurement of NP-PAEMA nanoparticle dispersions showed increased turbidity when increasing the pH value of the buffer solution, further demonstrating the pH responsiveness of these NPs.

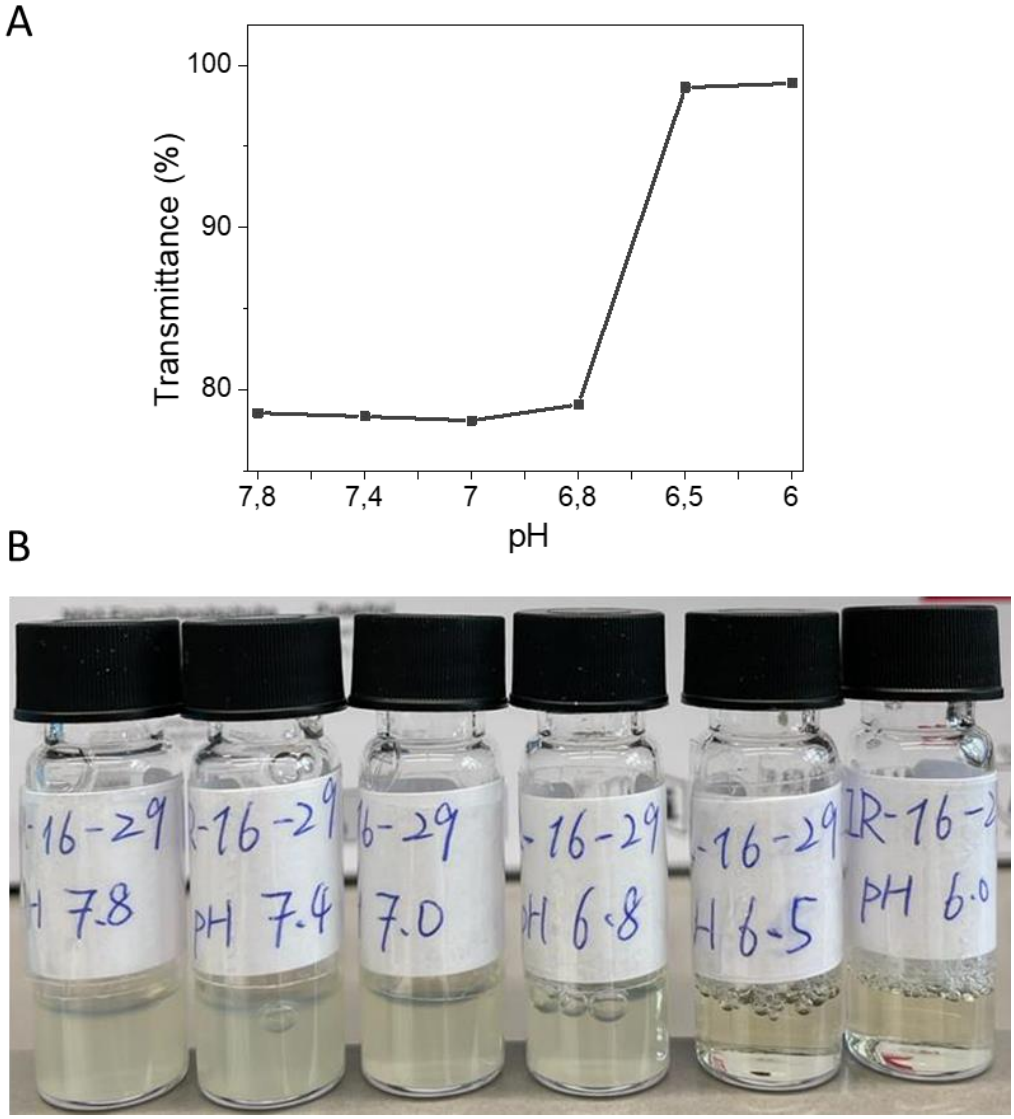

Figure 72. (A) UV/Vis transmittance of NP-PAEMA dispersions as a function of pH value from pH 6.0 to pH 7.8 at 700 nm. (B) Image of the corresponding NP-PAEMA dispersions in phosphate buffer solutions with pH values varying from pH 6.0 to pH 7.8.

This sharp size change of the nanoparticles in response to pH values monitored by DLS together with the nanoparticle dispersions at different pH values displayed in the digital image indicates the disassembly of the nanoparticles under slightly acidic

conditions, which agrees well with the p*K*a value (~7.2) of the block copolymer (Figure 73).

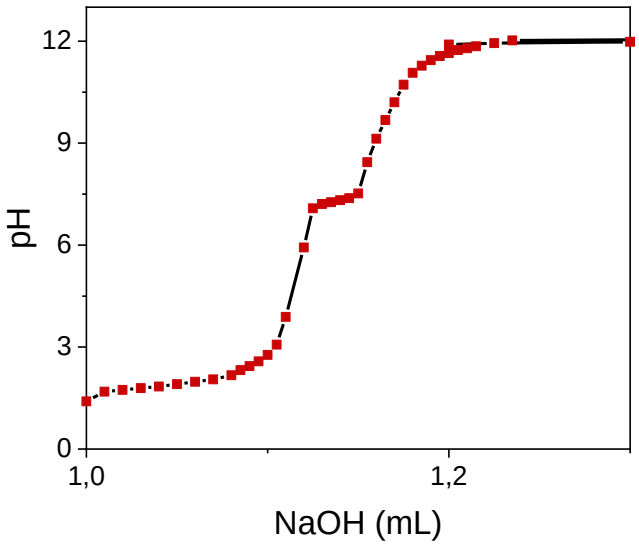

Figure 73. Titration curve of PEG_{113}-*b*-$PAEMA_{50}$ polymer chains in DIW (PEG_{113}-*b*-$PAEMA_{50}$ concentration 5 mg/mL and NaOH concentration 0.1 M).

Furthermore, TEM has confirmed at pH 7.4 that the polymer chains were self-assembled into spherical nanoparticles. Additionally, TEM images of particle dispersions at different pH values revealed the size and morphology changes of pH-responsive photocatalytic nanoparticles (NP-PAEMA-EYHEMA) from pH 7.4 to pH 6.5 (Figure 74), demonstrating the disassembly of the nanoparticles at pH 6.5 that agrees well with the DLS results.

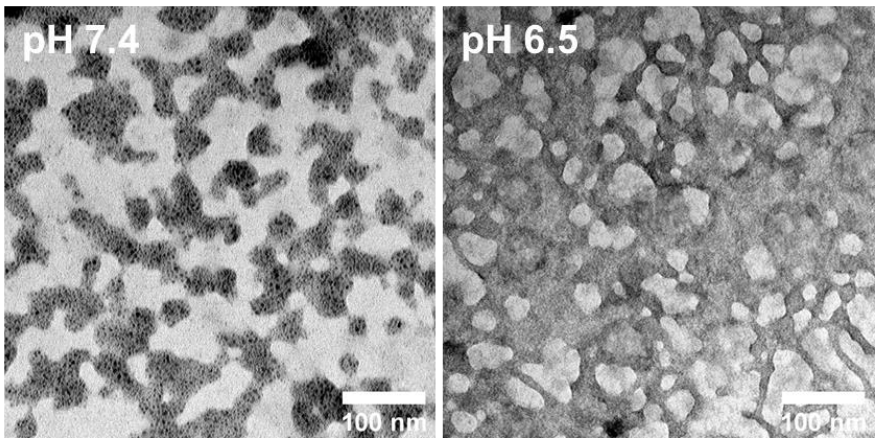

Figure 74. TEM images of NP-PAEMA-EYHEMA dispersion in phosphate buffer (0.1 mM) at pH 7.4 and pH 6.5.

4.3 Photocatalytic Reactions

The photocatalyst eosin Y is an inexpensive and biocompatible material that has been used extensively in biological applications.[230] Eosin Y is capable of efficiently generating singlet oxygen that was confirmed by EPR measurement (Figure 75), which has been widely used for PDT.[231]

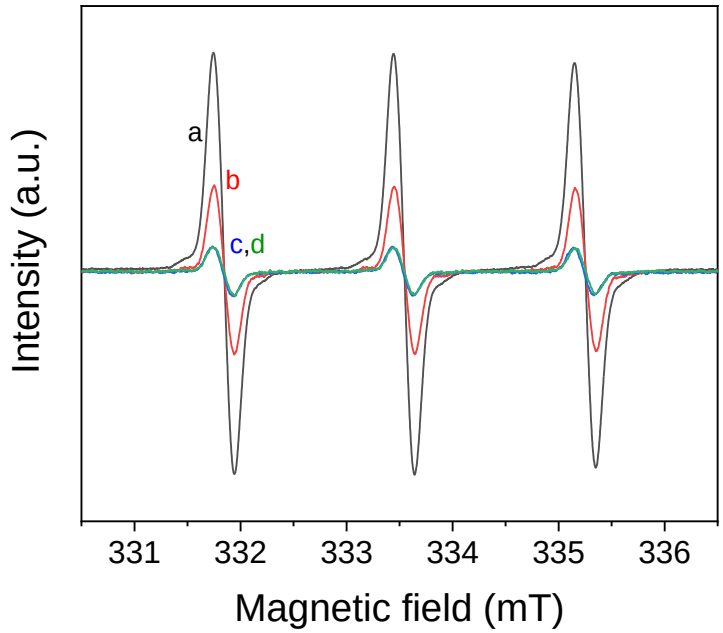

Figure 75. Electron paramagnetic resonance (EPR) spin trapping spectra of TEMP $^1O_2$ generated under different conditions. (a) Eosin Y disodium salt (1 mg/mL), tetramethylpiperidine (TEMP, 0.1 M), O_2. (b) Eosin Y disodium salt (1 mg/mL), TEMP (0.1 M), air. (c) TEMP (0.1 M), O_2. (d) Eosin Y disodium salt (1 mg/mL), TEMP (0.1 M), O_2, dark. All the samples were irradiated under blue LED for 30 min before measurement.

In our preliminary study, with blue light irradiation molecular eosin Y (eosin Y disodium salt) can efficiently activate prodrug model compounds containing various ROS-sensitive linkers/cap, including thiol ketal, aminoacrylate, boronic acid pinacol ester, and oxalate (Figure 76, Table 6). After 2 to 4 h of light irradiation, the prodrug model compounds were activated with over 70% yield, suggesting that the eosin Y photocatalyst is effective in activating a broad range of ROS-sensitive linkages.

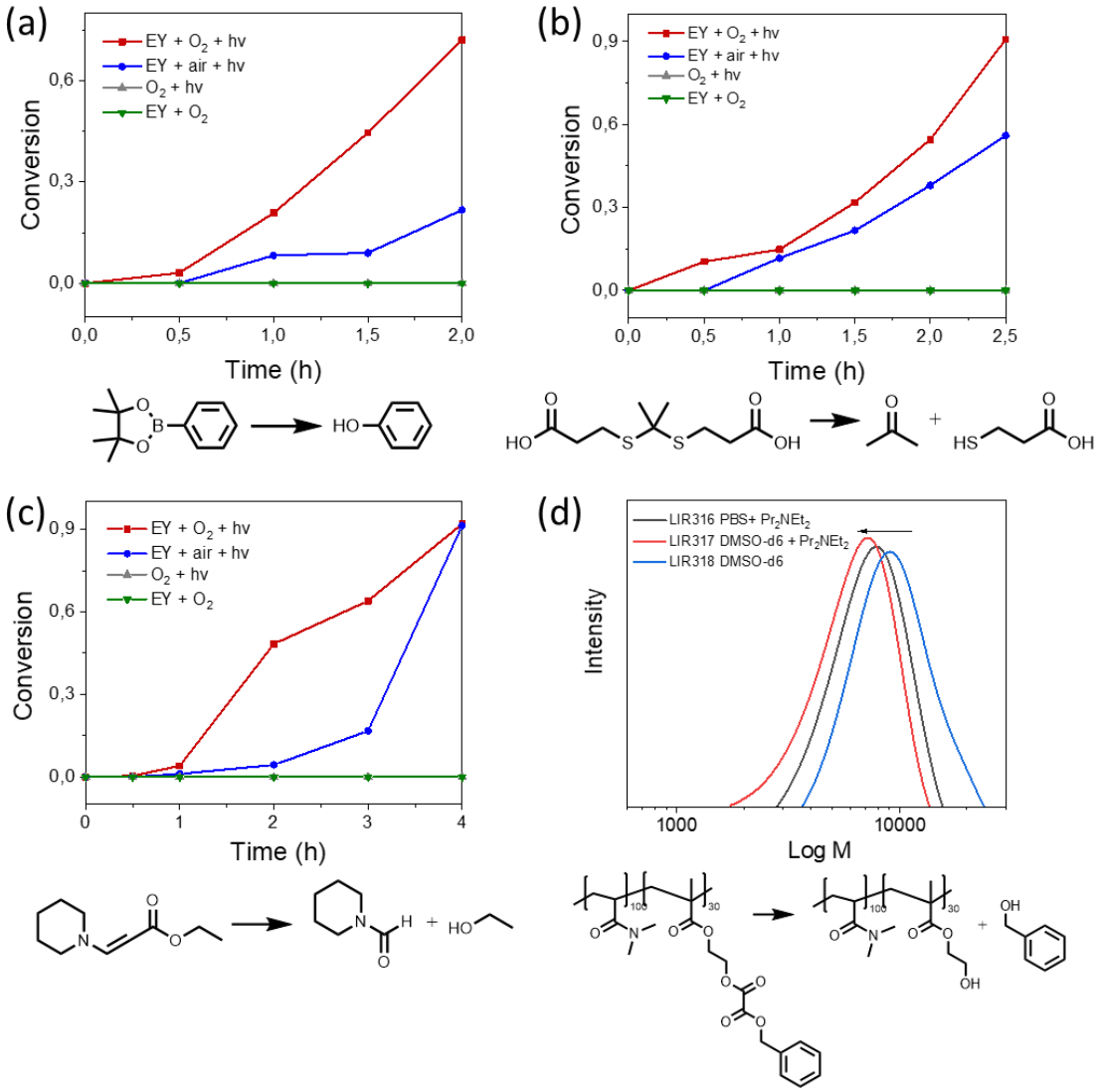

Figure 76. Prodrug model compounds activation using eosin Y disodium salt (5 mol%) loading for all reactions. (a) Kinetic profile of boronic acid pinacol ester activation, using sodium ascorbate as sacrificing agent. Conversion determined by GCMS. (b) Kinetic profile of thiol ketal activation without additive. Conversion determined by ^{1}H NMR spectroscopy. (c) Kinetic profile of aminoacrylate activation without additive. Conversion determined by GCMS. (d) GPC monitored the degradation of oxalate-based model polymer using either PBS or DMSO-d_6 as solvent, as well as Pr_2NEt_2 as sacrificing agent.

Table 6. Summary of the activation of ROS-sensitive prodrug model molecules by molecular eosin Y disodium salt.

Entry	Linkage	Oxygen	Time/h	Yield/%
1	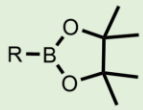	+	2	72[a]
2		-	2	22[a]
3		+	2.5	91[a]
4		-	2.5	56[a]
5	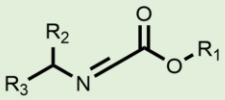	+	4	92[a]
6		-	4	91[a]
7	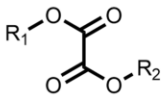	+	2.5	94[b]
8		-	2.5	>99[c]

[a]Standard conditions: prodrug model molecules (50 mM), eosin Y disodium salt (5 mol%), PBS buffer (3 mL), under either oxygen or ambient environment. [b]Condition: prodrug model polymer (50 mM of the ROS sensitive linkage), eosin Y disodium salt (5 mol%), PBS buffer (1 mL), with oxygen. [c]Condition: prodrug model polymer (50 mM of the ROS sensitive linkage), eosin Y disodium salt (5 mol%), DMSO-d_6 (1 mL), with oxygen. Blue LED (λ_{max} = 460 nm) at the power of 17 mW/cm^2, temperature = 18 °C. Yield of Entry 1,2,5, and 6 were determined by GCMS. The yield of Entry 3 and 4 was measured by ^{1}H NMR spectroscopy. The yield of Entry 7 and 8 was calculated based on data collected by GPC.

The promising performance of the molecular EY photocatalyst in activating the prodrug model molecules has encouraged us to further examine EY-based pH-responsive photocatalytic nanoparticles (NP-PAEMA-EYAMA and NP-PAEMA-EYHEMA) for the controlled activation of prodrug model compounds. Surprisingly, we observed intense photobleaching of both polymeric photocatalyst dissolved in phosphate buffer solution (pH 6.5) PEG_{113}-*b*-$PAEMAH^+_{50}$-*b*-$EYAMA_1$ and NP-PAEMA-EYAMA dispersed in PBS (pH 7.4), where the reddish color of the solution and dispersion turned colorless within 10 min of light irradiation, respectively. This photobleaching of the photocatalyst possibly resulted from the five-membered lactam formation of the eosin Y photocatalyst, leading to an unexpected degradation of the photocatalyst. Nevertheless, the analogue PEG_{113}-*b*-$PAEMA_{50}$-*b*-$EYHEMA_1$ photocatalytic polymer displayed higher stability against photobleaching after 5 h of light irradiation, where lactone formation is prohibited. Therefore, this PEG_{113}-*b*-$PAEMA_{50}$-*b*-$EYHEMA_1$

polymer photocatalyst has been selected for further investigations of the photocatalytic prodrug activation.

Initially, the photocatalytic activation of a prodrug model compound containing a boronic acid pinacol ester moiety was carried out using PEG$_{113}$-*b*-PAEMAH$^{+}_{50}$-*b*-EYHEMA$_1$ polymer as photocatalyst. In a typical experiment set-up, PEG$_{113}$-*b*-PAEMA$_{50}$-*b*-EYHEMA$_1$ was dissolved in phosphate buffer at pH 6.5 and combined with prodrug model compound in a glass vial prior to the light irradiation. The prodrug activation kinetic profiles were monitored by GCMS in triplicate. As illustrated in Figure 77, over 90% of the yield of activation was obtained using PEG$_{113}$-*b*-PAEMA$_{50}$-*b*-EYHEMA$_1$ polymer as photocatalyst (2.5 mol% eosin Y moiety) after 1 h of light irradiation. When the oxygen atmosphere was replaced with air, the hydroxylation reaction progressed with a slower reaction rate compared to the reaction in the presence of oxygen. Only 16% yield was delivered after 1 h under ambient condition, suggesting the presence of oxygen is crucial for photocatalytic hydroxylation to occur efficiently. No conversion was detected for controlled reactions without a photocatalyst in light and with photocatalyst in the dark, respectively.

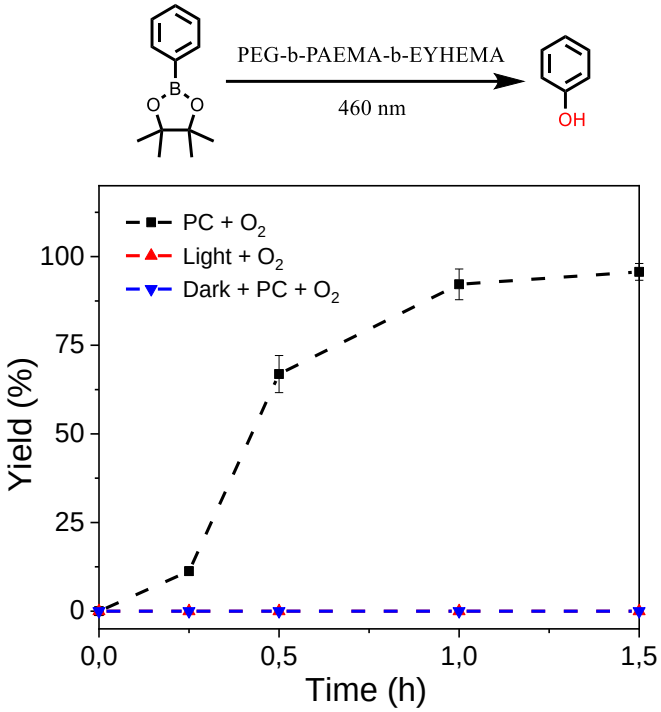

Figure 77. Prodrug model compound activation kinetic profile using PEG$_{113}$-*b*-PAEMAH$^{+}_{50}$-*b*-EYHEMA$_1$ polymeric photocatalyst (2.5 mol%) solution in phosphate buffer solution at pH 6.5 (black). Control reactions: without photocatalyst in light (green) and with photocatalyst in dark (blue).

Furthermore, we have also investigated the controlled activation of a prodrug model compound that contains a singlet oxygen sensitive aminoacrylate linker applying pH-responsive photocatalytic nanoparticle NP-PAEMA-EYHEMA dispersions at pH 7.4 and PEG$_{113}$-*b*-PAEMAH$^{+}_{50}$-*b*-EYHEMA$_{1}$ dissolved in phosphate buffer at pH 6.5, respectively. In a typical experiment set-up, NP-PAEMA-EYHEMA dispersed in PBS buffer or PEG$_{113}$-*b*-PAEMAH$^{+}_{50}$-*b*-EYHEMA$_{1}$ dissolved in phosphate buffer at pH 6.5 and prodrug were combined in a glass vial prior to the irradiation of blue LED light, respectively. The prodrug activation kinetic profiles were monitored by GCMS in triplicate. As we can see from Figure 78, 68% of the prodrug model compound was activated by solvated PEG$_{113}$-*b*-PAEMAH$^{+}_{50}$-*b*-EYHEMA$_{1}$ polymeric photocatalyst at pH 6.5 after 1.5 h of light irradiation, whereas only 2.7% yield of activation was obtained by using NP-PAEMA-EYHEMA nanoparticle dispersion at pH 7.4. This strongly suggests that the photocatalytic eosin Y moieties were more accessible when the polymer chains were fully solvated at mild acidic conditions, therefore, leading to a targeted activation of prodrug model compound at the tumor tissue.

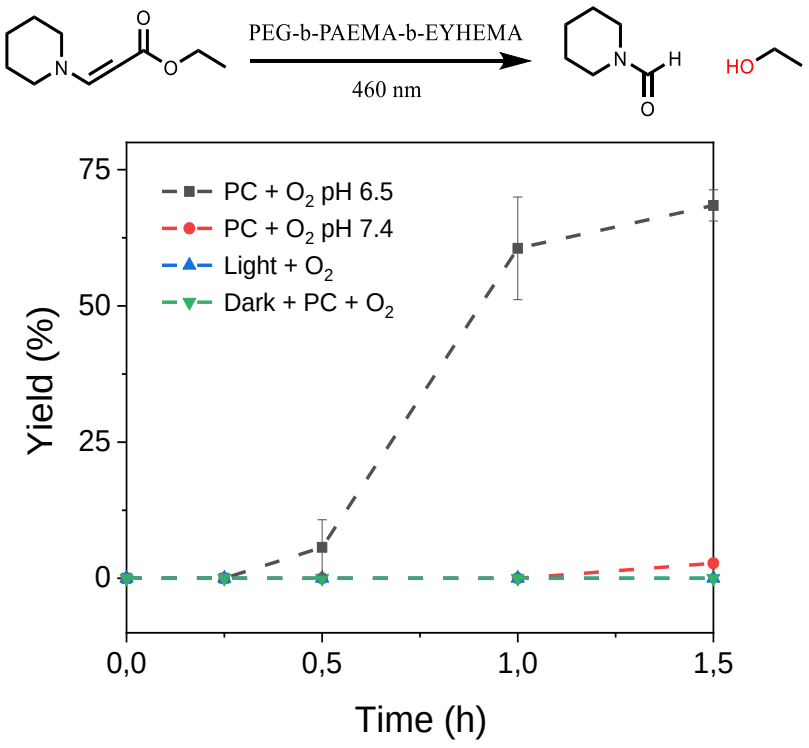

Figure 78. The controlled activation kinetic profile of prodrug model compound using PEG$_{113}$-*b*-PAEMAH$^{+}_{50}$-*b*-EYHEMA$_{1}$ polymeric photocatalyst (2.5 mol%) solution in phosphate buffer solution at pH 6.5 (black) and NP-PAEMA-EYHEMA in PBS buffer at pH 7.4 (red). Control reactions: without photocatalyst in light (green) and with photocatalyst in dark (blue).

The excellent performance of the polymeric photocatalyst in activating ROS-sensitive caping groups in a controlled manner has boosted our interest in investigating the activation of an anticancer drug molecule. 5-Fluorouracial (5FU) is an FDA-approved chemotherapy drug that has been widely prescribed alone or in combination with other chemotherapeutics for various of solid tumor treatment (e.g. breast cancer, pancreatic cancer, colorectal cancer, stomach cancer, cervical cancer, and skin cancer). Over the past decades, mechanisms of the action of 5FU in human body has been intensively studied and clearly demonstrated.[232–234] Briefly, 5FU molecules can inhibit the activity of the nucleotide synthesis enzyme thymidylate synthase (TS), which is crucial to catalyze the reductive methylation of deoxyuridine monophosphate to deoxythymidine monophosphate. As a result of blocking the function of TS, the DNA replication and repair is interrupted.[232,234] Despite the excellent anticancer activity, major side effects of 5FU including central neurotoxicity, gastrointestinal toxicity, and myelosuppression, as well as being metabolically unstable still significantly limit its clinical use.[235] Therefore, prodrug strategies have been actively investigated to overcome these limitations, where several 5FU-prodrugs among many analogues have been successfully applied in clinic use.[236]

Here, 5FU was selected as an example of anticancer drug and we are interested in the creation of a ROS-sensitive 5FU-prodrug that can be selectively activated by the pH-responsive photocatalyst at the tumor site. As we have demonstrated the remarkable performance of the pH-responsive photocatalyst in activating the boronic acid pinacol ester group, an arylboronate-based prodrug of 5FU has been synthesized by introducing a ROS-sensitive *p*-boronate-benzyl group to the N1 position of the 5FU according to the literature.[237] Similar to aforementioned procedures of prodrug model compound activation, the 5FU prodrug was mixed with PEG_{113}-*b*-$PAEMAH^{+}_{50}$-*b*-$EYHEMA_{1}$ solution in phosphate buffer at pH 6.5 before being subjected to light irradiation. The conversion of 5FU prodrug was monitored by ^{19}F-NMR spectroscopy, where > 99% conversion of 5FU prodrug into an intermediate was obtained after half an hour light irradiation (Figure 79). As reported in the literature,[237] this intermediate is subsequently activated in cell culture condition spontaneously, leading to the release of active 5FU and the death of cancerous tissue.

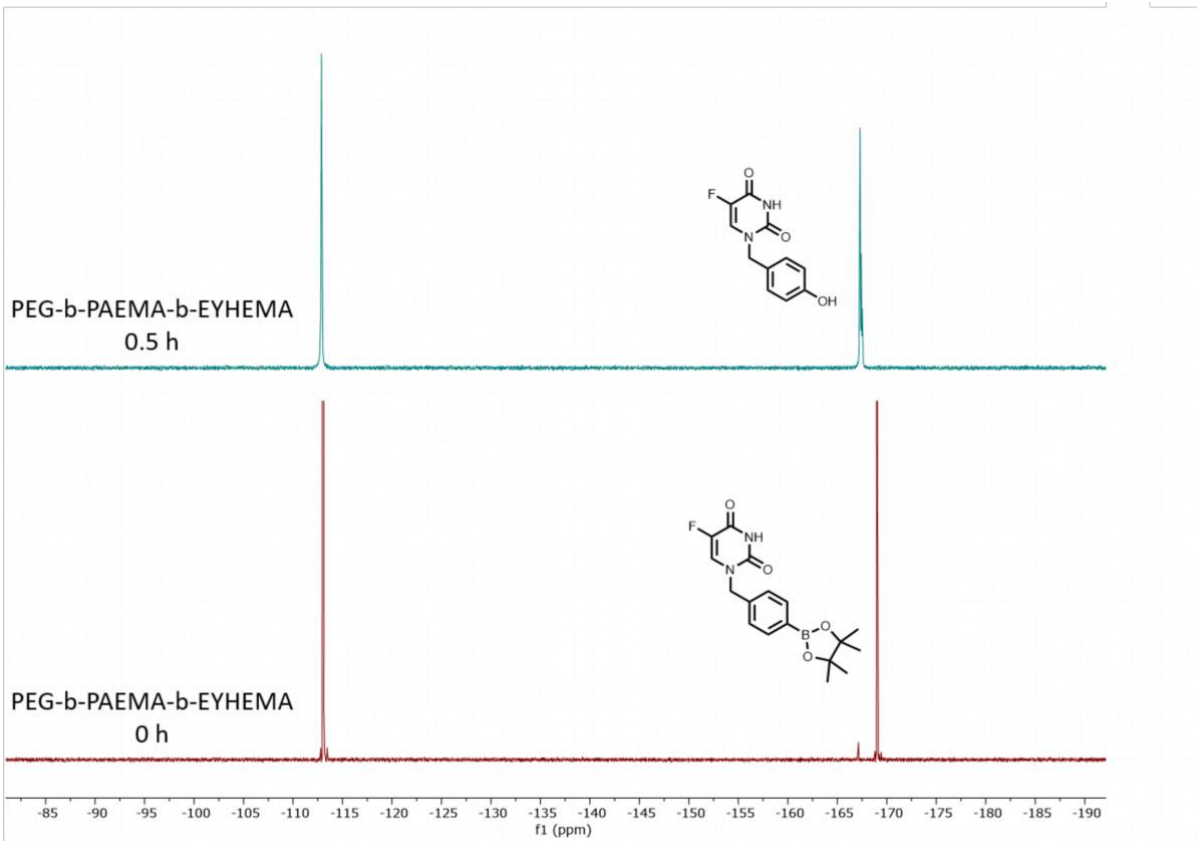

Figure 79. ^{19}F-NMR spectrum of the activation of 5FU prodrug (40 mM) using PEG_{113}-*b*-$PAEMAH^{+}_{50}$-*b*-$EYHEMA_1$ polymeric photocatalyst (2.5 mol%) solution in phosphate buffer solution at pH 6.5 (the reference peak at -113 ppm was from fluorobenzene).

A cell viability study was undertaken to verify that the photocatalytically activated 5FU prodrug intermediate could subsequently be converted to 5FU and induce cell death (see Figure 80). Here, the prodrug and photocatalyst were either irradiated or kept in dark prior to incubation with cancer cells. Additionally, control experiments of just the photocatalyst and the prodrug separately were performed. The cell viability results showed that only the combination of prodrug, photocatalyst and light induced cell death. This suggests that the photoactivated prodrug intermediate undergoes further activation and forms 5FU as expected, leading to cell death. As the concentration of the activated prodrug loading increased, cell viability of the group treated with combination of prodrug and photocatalytic polymer PEG_{113}-*b*-$PAEMAH^{+}_{50}$-*b*-$EYHEMA_1$ after blue light LED irradiation significantly decreased, indicating prominent antitumor efficacy through 5FU chemotherapy. Meanwhile, the individual components of prodrug, photocatalytic polymer PEG_{113}-*b*-$PAEMAH^{+}_{50}$-*b*-$EYHEMA_1$, as well as prodrug and photocatalytic polymer PEG_{113}-*b*-$PAEMAH^{+}_{50}$-*b*-$EYHEMA_1$ mixture in the

absence of light irradiation (dark) treatments, showed negligible toxicity until high concentrations (100 uM) were applied.

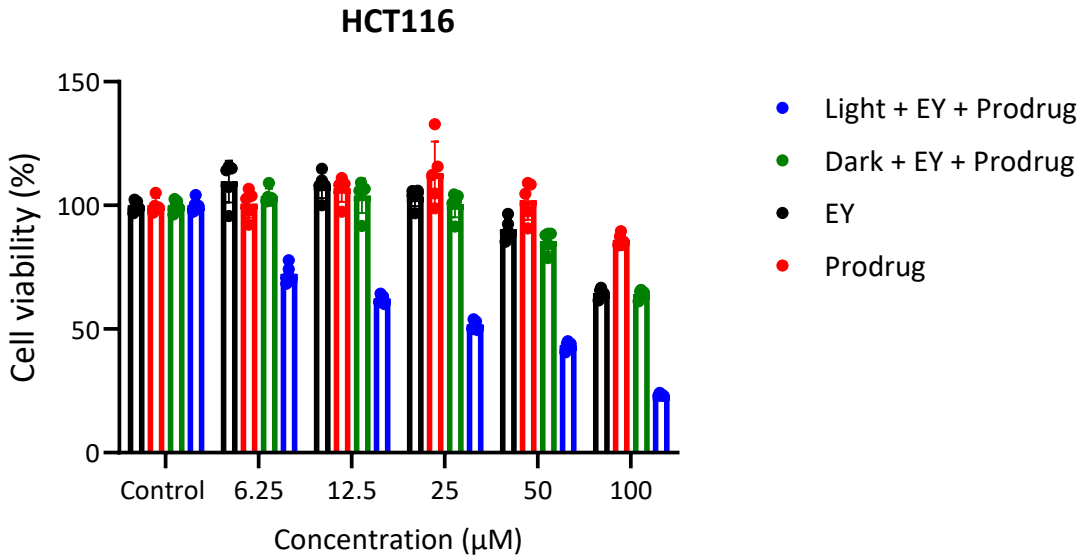

Figure 80. The viability of HCT116 cancer cells treated with varying concentrations of prodrug, PEG_{113}-*b*-$PAEMAH^{+}_{50}$-*b*-$EYHEMA_1$ (shortened as EY), the combination of prodrug and PEG_{113}-*b*- $PAEMAH^{+}_{50}$-*b*-$EYHEMA_1$ before and after blue light LED irradiation. The cells were treated for 72 h with the indicated concentrations of the compounds. Data are presented as mean ± S.D, n = 5.

In addition to small molecule prodrug model compounds, therapeutic drugs can also be conjugated to the polymer backbones using a ROS-sensitive linker, allowing tunable drug-loading and controllable drug release. Therefore, we have conjugated an anticancer drug camptothecin to a polymerizable functional group through a ROS-sensitive oxalate linker, producing a polymerizable prodrug monomer. Here, these ROS-sensitive prodrug monomers pro-camptothecin (PCPT) were copolymerized with the pH-responsive AMEA monomers using PEG as macro-CTA. The resulting pH/ROS-responsive prodrug polymers PEG-*b*-PAEMA-*s*-PCPT were further combined with pH-responsive polymeric photocatalyst PEG_{113}-*b*-$PAEMA_{50}$-*b*-$EYHEMA_1$, generating pH/light/ROS-responsive polyprodrug-based particles. Here, we have studied the ROS-triggered drug release from polyprodrugs. In order to monitor the drug activation easily, we carried out the experiment in deuterated solvent $CDCl_3$ and the reaction was monitored by NMR spectroscopy.

As shown in the NMR spectra (Figure 81), typical peaks of the polymer mixture disappeared after 3 h of light irradiation, including peaks at 7-8.7 ppm attributed to the aromatic peaks of the PCPT units, peaks at 4.25 ppm attributed to the -CH_2- groups adjacent to the acrylate groups of AEMA and PCPT moieties, as well as the peaks from 0.5 to 3.2 ppm assigned to both AEMA and PEG blocks. This result indicates that the mixture of two polymers PEG-*b*-PAEMA-*s*-PCPT and PEG_{113}-*b*-$PAEMA_{50}$-*b*-$EYHEMA_1$ have precipitated out of the solution. Crosslinking of the unsaturated bonds of the polymers in solution with a high concentration (20 mg/mL polymer concentration) could be initiated by the radicals generated by the photocatalytic units while light irradiation, which possibly led to the formation of crosslinked matrix and thereafter the precipitation of the polymer mixture. Unfortunately, no clear bond cleavage was monitored by NMR in this experiment. Due to the complexity of mixing two polymeric components, selecting proper characterization techniques to monitor the activation of the prodrug polymer is very challenging. Besides, side reactions (e.g. crosslinking or degradation) can dominate under conditions with a high polymer concentration. Therefore, high-performance liquid chromatography (HPLC) and matrix assisted laser desorption/ionization-mass spectrometry (MALDI-MS) can be applied in future investigations to characterize the activated CPT drug molecules and the molar mass changes of the polymers, respectively. However, specific HPLC and MALDI-MS methods should be developed for this complex condition, which exceeded the scope of this thesis but should be further explored in the future. Here, the focus of the investigation lies on the proof of concept, where tumor microenvironment responsive photocatalytic materials developed in this thesis can effectively activate prodrug model molecules with various ROS-sensitive caps.

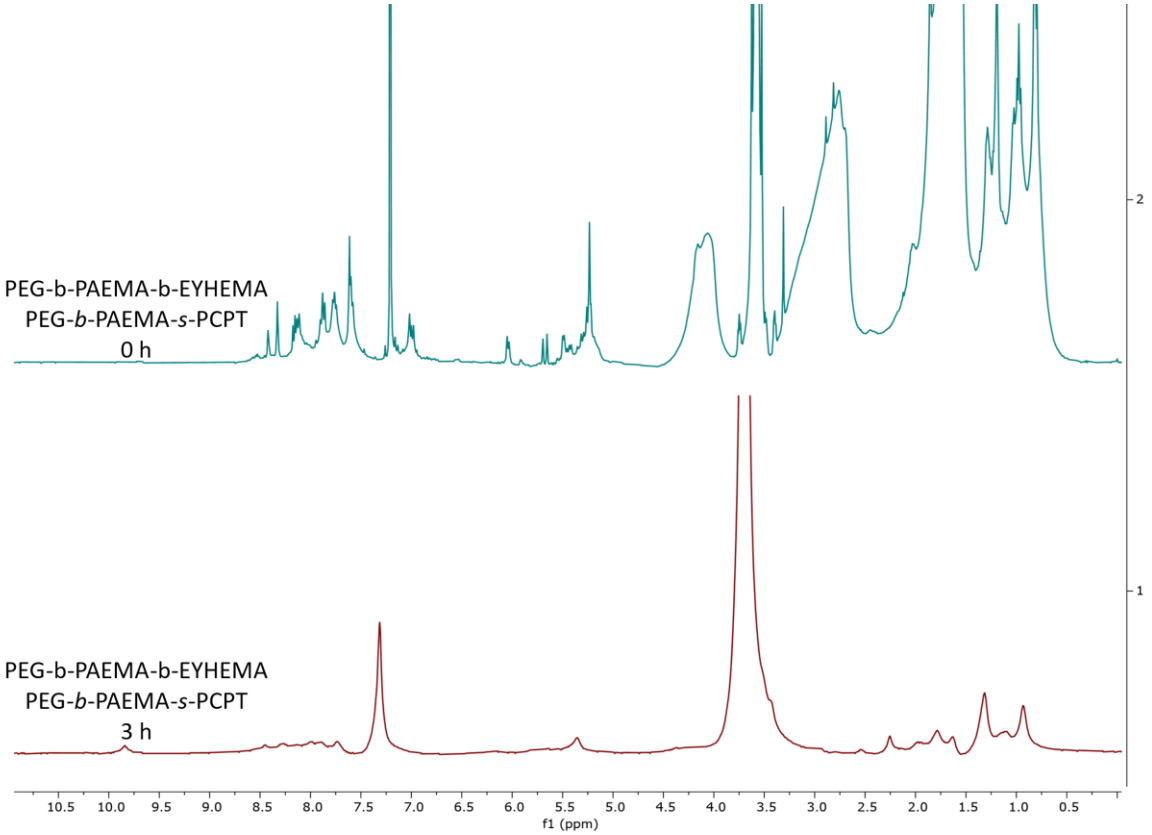

Figure 81. ^{1}H NMR spectra of the activation of polyprodrug PEG-*b*-PAEMA-*s*-PCPT using PEG_{113}-*b*-$PAEMA_{50}$-*b*-$EYHEMA_{1}$ polymeric photocatalyst solution in $CDCl_3$ before and after 3 hours of light irradiation, respectively.

4.4 Conclusion

In summary, we have designed and synthesized a novel pH-responsive polymeric photocatalyst, consisting of azepane moieties as pH-responsive functional groups and a small loading of eosin Y as photocatalyst. This polymeric photocatalytic material exhibited an excellent reactivity in the activation of prodrug model compounds with different ROS-sensitive protecting groups at mild acidic conditions (pH 6.5). Moreover, the controlled activation of prodrug model compound has been achieved taking advantage of the ultra pH-sensitive nature (0.3 pH increment) of the polymeric photocatalyst, where 25 times high yield of release has been obtained at pH 6.5 compared to the reaction at pH 7.4. Furthermore, this polymeric photocatalyst has efficiently activated the 5FU prodrug into an intermediate, which can be spontaneously activated into the active parent 5FU in cell cultivation. These findings demonstrate that the pH-responsive polymeric photocatalyst provides an effective approach to selectively activate prodrugs with various ROS-sensitive linkers/caps at the tumor site, which can potentially enhance the antitumor efficacy through PDT/chemo combination

therapy. The combination of photocatalytic polymers and prodrug polymers can enhance the activation of the prodrug in theory due to the spatial approximation of the photocatalytic units and prodrug moieties. However, this combined micellar system also increased the difficulty of monitoring the release of the drug molecules due to the mixture of two polymers. Therefore, further development of proper methods for the characterization of this complex system needs to be investigated in the future.

4.5 Experimental Section

4.5.1 Materials

All chemicals and solvents were purchased from chemical suppliers and used without further purification, unless specifically noted. 2-(Azepan-1-yl)ethan-1-ol (95%) was obtained from Thermo Fisher Scientific. Poly(ethylene glycol) methyl ether (4-cyano-4-pentanoate dodecyl trithiocarbonate) ($mPEG_{113}$-CPDTC), methacryloyl chloride (97%), 4,4'-azobis(4-cyanovaleric acid) (ACVA, 98%), eosin Y (EY, 75%), titanium(VI) chloride ($TiCl_4$, 99.9%), anhydrous acetone, 4,4,5,5-tetramethyl-2-phenyl-1,3,2-dioxaborolane (97%), 2-Hydroxyethyl methacrylate (HEMA, 99%), 1-hydroxybenzotriazole hydrate (HOBt, 97%), DMSO-d_6 (99.9 atom % D), and $CDCl_3$ (99.8 atom % D) were purchased from Sigma Aldrich. Triethylamine (TEA, 99%) was acquired from VWR. 3-Mercaptopropanoic acid (98%), (S)-(+)-Camptothecin (CPT, 97%), ethyl propiolate (98%), 1-ethyl-3-(3-dimethylaminopropyl) carbodiimide hydrochlorides (EDC·HCl, 98%), 4-(Dimethylamino)pyridine (DMAP, 99%), and piperidine (99%) were purchased from CDI.

4.5.2 Characterization Techniques

^1H NMR and ^{13}C NMR spectra were measured by Bruker Avance 400 to confirm the chemical structures and compositions of polymers and small molecules. UV-Vis transmittance spectra were taken from a Cary 60 UV/Vis spectrometer to determine the turbidity of the nanoparticle (without photocatalyst) dispersions in buffer solutions (pH 6-7.8), monitoring the disassembly of the polymer nanoparticles as a function of pH from 6-7.8. UV/Vis absorption and emission were monitored by a plate reader. The hydrodynamic diameter of the photocatalytic nanoparticles was determined by Zetasizer Nano ZS. Gas chromatograms and corresponding mass spectra were taken from GCMS-QP-2010 Ultra. FTIR spectra were measured using a Bruker Tensor II FTIR spectrometer. TEM was conducted using a JEM-1400 Transmission Electron Microscope. Samples were prepared by dispersing the particles in PBS 0.1 mM pH

6.4 buffer solution (0.1 wt%) and applying them to carbon coated copper grids. The particles were stained using uranyl acetate stain allowing us to better visualize the particles. Zeta potential was examined by applying Zetasizer Malvern, Nano Z.

4.5.3 Synthesis of Aminoethyl Methacrylate (AMA)

Tert-butyl (2-hydroxyethyl)carbamate (5 g, 31 mmol) was added to a flame-dried Schlenk flask and dissolved in anhydrous DCM 50 mL. Triethylamine (4.1 g, 40.3 mmol) was injected into the solution and the mixture was cooled in an ice bath. After 15 min, methacryloyl chloride was added dropwise. The mixture was allowed to warm up to room temperature and stirred overnight. The solvent was removed, and the final product was recrystallized in hexane. The product 2-((tert-butoxycarbonyl)amino)ethyl methacrylate was further subjected to the de-Boc process to obtain the final AMA monomer. In detail, 2-((tert-butoxycarbonyl)amino)ethyl methacrylate (4 g, 17.45 mmol) and anhydrous 4N HCl in dioxane (54 mL) were combined in a flame-dried Schlenk flask and stirred for 4 h. After the completion of the reaction, the solvent was removed under reduced pressure to afford the final product AMA.

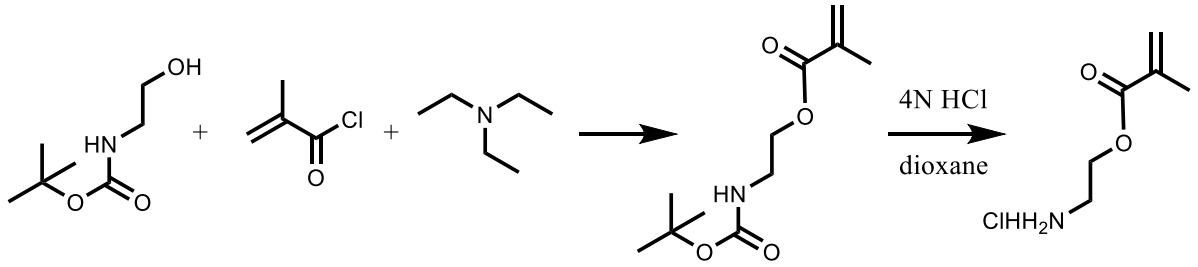

4.5.4 Synthesis of Photocatalytic Methacrylamide Monomer 2-(2-(2,4,5,7-tetrabromo-6-hydroxy-3-oxo-3H-xanthen-9-yl)benzamido)ethyl Methacrylamide (EYAEMA)

EY (2 g, 3.09 mmol), aminoethylmethacylate (511.2 mg, 3.09 mmol), and HOBt (500.6 mg, 3.7 mmol) were combined in a flame-dried round bottom Schlenk flask under Ar and dissolved in 30 mL of anhydrous DMF. The reaction mixture was cooled in an ice-bath at 0 °C. After 10 min, *N*,*N*-diisopropylethylamine (1.38 mL, 7.72 mmol) was added to the mixture. 15 min later, EDC·HCl (710.1 mg, 3.7 mmol) in 10 mL of DMF was added to the reaction mixture above at 0 °C dropwise. The mixture was stirred overnight and warmed up to room temperature under Ar atmosphere. The product was diluted with DCM and washed with HCl (1 M), $NaHCO_3$ (saturated), water and brine. The extracted organic phase was dried over $MgSO_4$ and the solvent was evaporated using a rotary evaporator.

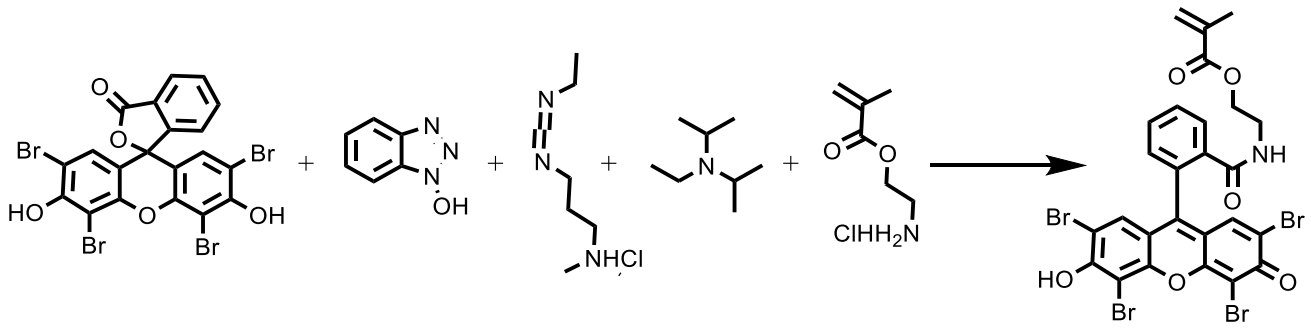

4.5.5 Synthesis of Photocatalytic Methacrylamide Monomer 2-(2-(2,4,5,7-tetrabromo-6-hydroxy-3-oxo-3H-xanthen-9-yl)benzamido)ethyl Methacrylate (EYAEMA)

EY (2 g, 3.09 mmol), hydroxylethylmethacylate (401.7 mg, 3.09 mmol), and DMAP (377 mg, 3.1 mmol) were combined in a flame-dried round bottom Schlenk flask under Ar and dissolved in 30 mL of anhydrous DCM. The reaction mixture was cooled in an ice-bath at 0 °C. After 10 min, EDC·HCl (887.7 mg, 4.6 mmol) in 10 mL of DCM was added to the reaction mixture above at 0 °C dropwise. The mixture was stirred overnight and warmed up to room temperature under Ar atmosphere. The product was diluted with DCM and washed with HCl (1 M), $NaHCO_3$ (saturated), water and brine. The extracted organic phase was dried over $MgSO_4$ and the solvent was evaporated using a rotary evaporator.

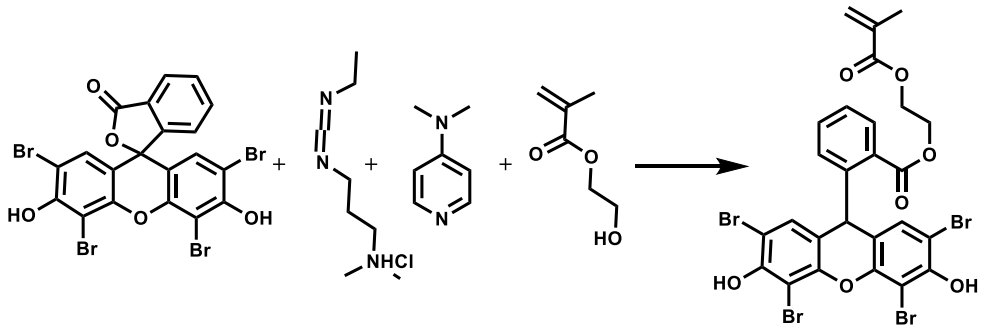

4.5.6 Synthesis of pH-responsive Monomer 2-(Azepan-1-yl)ethyl Methacrylate (AEMA)

2-(azepan-1-yl)ethan-1-ol (1 g, 6.98 mmol) was added to a flame-dried Schlenk tube (100 mL) with 30 mL of anhydrous DCM under Ar, followed by the addition of TEA (1.27 mL, 9.08 mmol). The reaction mixture was cooled in an ice-bath. After 15 min, methacryloyl chloride (818.5 µL, 8.38 mmol) was added dropwise. The reaction mixture was stirred overnight and warmed up to room temperature. The solvent and unreacted starting materials were evaporated.

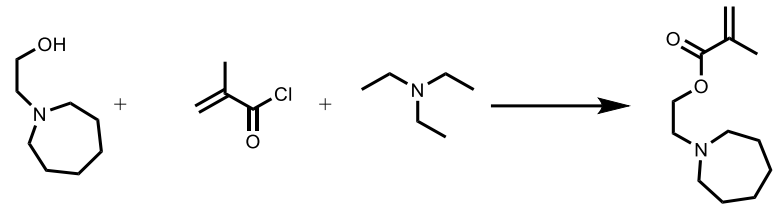

4.5.7 Synthesis of Thiol Ketal (TK)

Mercaptopropionic acid (2 g, 18.84 mmol) and anhydrous acetone (1.4 mL, 18.84 mmol) were combined in a flame-dried Schlenk flask before the addition of anhydrous DCM (40 mL). The reaction mixture was cooled to -10 °C for 15 min before the addition of $TiCl_4$ (1.07 g, 5.65 mmol) dropwise. The color of the solution turned reddish while adding $TiCl_4$ and some white precipitates were formed around the flask wall as the reaction proceeded. The mixture was allowed to warm up to room temperature and stirred overnight. The crude product was washed with aqueous HCl solution (0.2 N), DIW, and brine. The organic phase was dried over $MgSO_4$ and the solvent was evaporated by a rotary evaporator. The final product was obtained as a white powder after recrystallization in ethyl acetate/hexane.

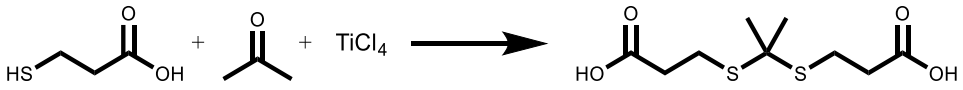

4.5.8 Synthesis of Ethyl 3-(piperidin-1-yl)acrylate

Ethyl propiolate (200 mg, 2.04 mmol) and piperidine (173.6 mg, 2.04 mmol) were dissolved in 25 mL of anhydrous THF in a flame-dried Schlenk tube. The solution was stirred at room temperature for 15 min. The solvent was removed under reduced pressure. The crude product was further purified by column chromatography (ethyl acetate/hexane 7/3), giving the final product as a yellowish liquid.

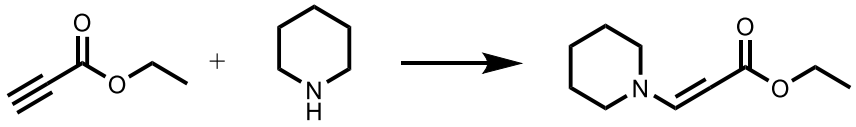

4.5.9 Synthesis of 2-(2-Chloro-2-oxoacetoxy)ethyl Methacrylate

To activate the hydroxyl group of 2-hydroxyl methacrylate by oxalyl dichloride, 2-hydroxyl methacrylate (1.5 g, 11.53 mmol) in anhydrous DCM (30 mL) was charged in a flame-dried Schlenk flask. The solution was cooled in an ice bath prior to the addition of oxalyl dichloride (2.93 g, 23 mmol) in 10 mL anhydrous DCM dropwise. The mixture was stirred for 1 h at room temperature. The excess oxalyl dichloride and solvent were

removed under reduced pressure to afford the final product that was further used for prodrug synthesis.

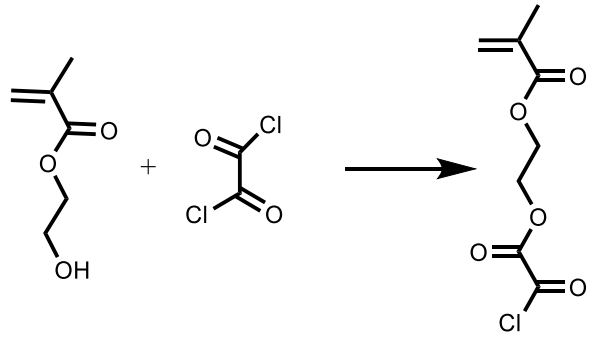

4.5.10 Synthesis of 4-Ethyl-3,14-dioxo-3,4,12,14-tetrahydro-1H-pyrano[3',4':6,7] indolizino [1,2-b]quinolin-4-yl (2-(methacryloyloxy)ethyl) Oxalate (pro-CPT)

Camptothecin (CPT, 658 mg, 1.9 mmol) was added to a flame-dried Schlenk flask and dispersed in anhydrous DCM (30 mL). Triethylamine (248.5 mg, 2.46 mmol) was added to the dispersion and the mixture was cooled in an ice bath. After 15 min, 2-(2-chloro-2-oxoacetoxy)ethyl methacrylate was added dropwise. The reaction mixture was allowed to warm up to room temperature and stirred overnight. A clear yellow-brownish solution was obtained after the completion of the reaction. The solvent was removed under reduced pressure to obtain the final product.

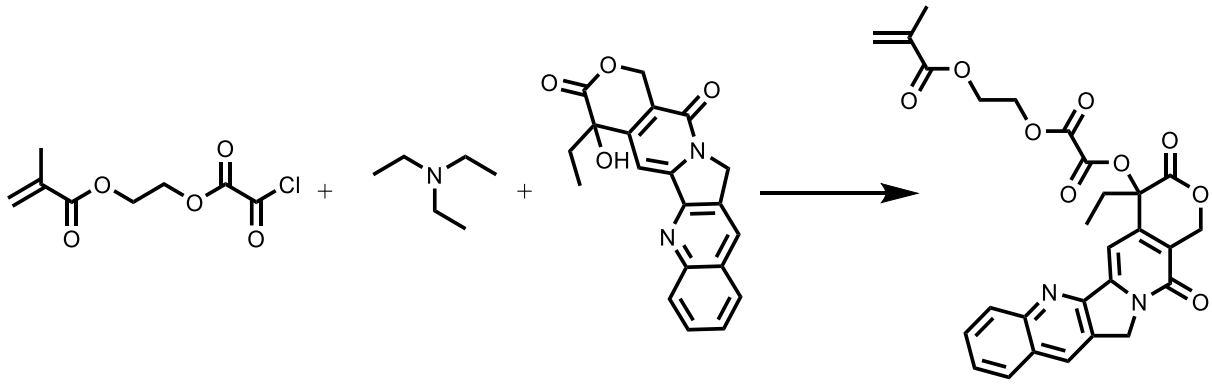

4.5.11 Synthesis of 5-Fluoro-1-(4-(4,4,5,5-tetramethyl-1,3,2-dioxaborolan-2-yl)benzyl)pyrimidine-2,4(1H,3H)-dione

Fluorouracil (FU, 500 mg, 3.84 mmol) and diazabicycloundecene (DBU 585 mg, 3.84 mmol) were added to a flame dried Schlenk flask and disolved in anhydrous DMF (20 mL). The mixture was cooled in an ice-bath. After 15 min, 2-(4-(bromomethyl)phenyl)-4,4,5,5-tetramethyl-1,3,2-dioxaborolane (1.14 g, 3.84 mmol) in DMF (10 mL) was added dropwise. The reaction mixture was allowed to warm up to room temperature

and stirred overnight. The solvent was removed under reduced pressure and the final product was afforded through a silica column (EtAc/hexane 1/1).

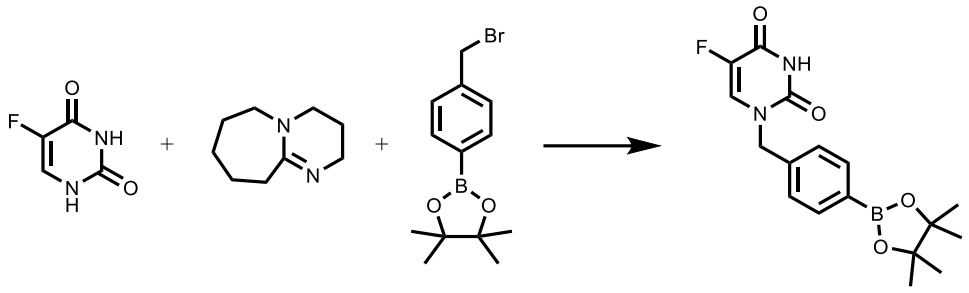

4.5.12 Preparation of pH-responsive Polymer PEG-*b*-PAEMA, Dual-responsive Polymers PEG-*b*-PAEMA-*b*-EYAEMA and PEG-*b*-PAEMA-*b*-EYHEMA

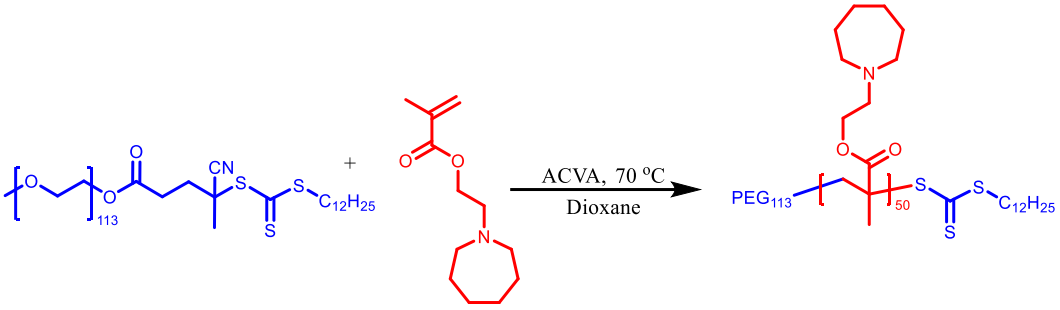

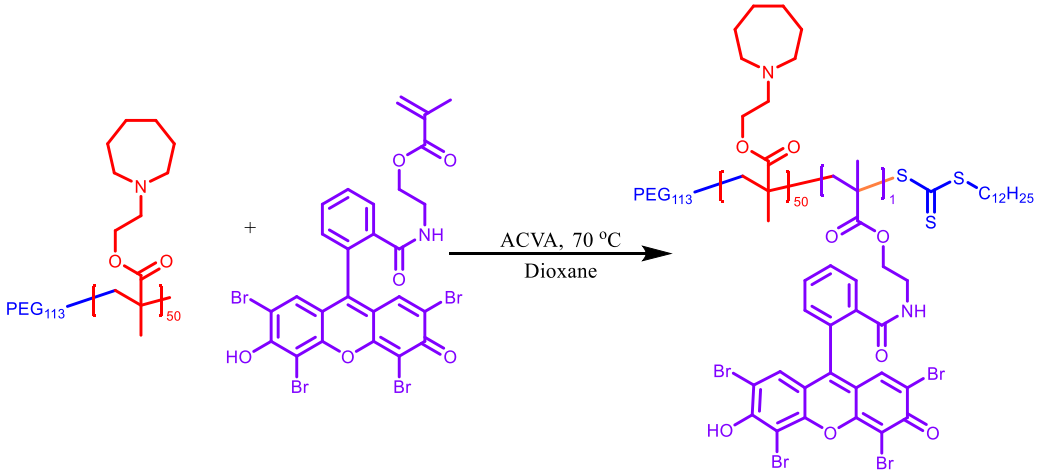

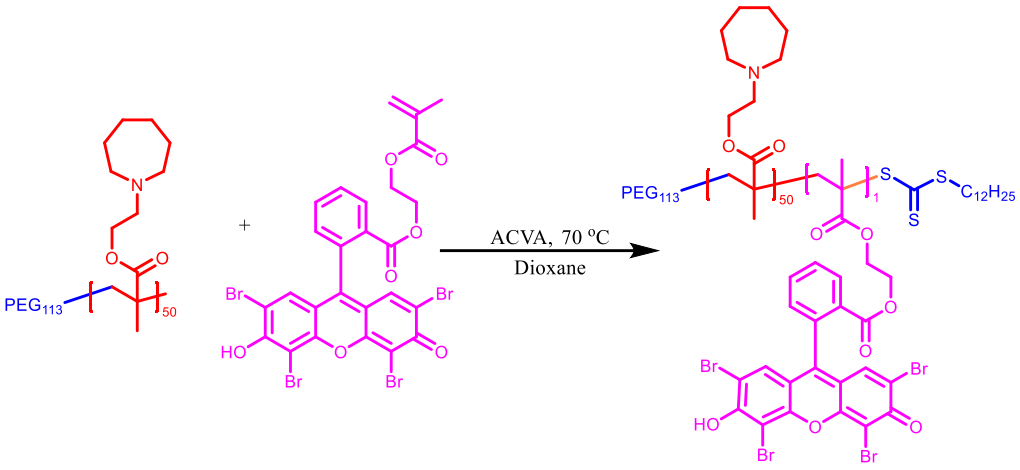

PEG-*b*-PAEMA, PEG-*b*-PAEMA-*b*-EYAMA, and PEG-*b*-PAEMA-*b*-EYHEMA were synthesized by RAFT polymerization. Briefly, mPEG$_{113}$-CPDTC (0.564 g, 0.105 mmol), AEMA (3 g, 12.5 mmol), and ACVA (5.9 mg, 21 μmol) were dissolved in anhydrous dioxane (5 mL). After degassing, the mixture was stirred at 70 °C for 1 day followed by precipitating in cold hexane. The precipitate was collected by filtration and dried in a vacuum overnight. The final product was obtained as a yellow solid. The degree of polymerization of the PAEMA block was determined as 52 according to the ^{1}H NMR spectrum. The dispersity was determined by GPC. The as obtained PEG-*b*-PAEMA was further used as macroCTA for the chain extension of photocatalytic moiety EYAMA. More in detail, PEG-*b*-PAEMA (608.5 mg, 37 μmol), EYAMA (56.4 mg, 74 μmol), and ACVA (2.1 mg, 7.4 μmol) were dissolved in anhydrous DMF (2 mL) and degassed with Ar. The reaction mixture was heated up to 70 °C overnight followed by dialysis in acetone/DIW (1/1) for 6 days and DIW for 1 day. The final product was dried by lyophilization, obtaining a fluorescent red powder. PEG-*b*-PAEMA-*b*-EYHEMA was synthesized using the same procedure described for PEG-*b*-PAEMA-*b*-EYAMA synthesis, only by exchanging the photocatalytic monomer EYAMA with EYHEMA.

Regarding pH-responsive photocatalytic nanoparticle preparation, PEG-*b*-PAEMA-*b*-EYAMA or PEG-*b*-PAEMA-*b*-EYAMA polymers were dissolved in DCM prior to the addition of PBS buffer solution (pH 7.4, 0.1 mM), respectively. The mixture was allowed to stir overnight to evaporate the DCM organic solvent, leading to the self-assembly of the amphiphilic photocatalytic polymers, generating NP-PAEMA-EYAMA and NP-PAEMA-EYHEMA dispersions at a concentration of 10 mg/mL.

4.5.13 Preparation of pH-responsive Prodrug Polymer PEG-*b*-PAEMA-*s*-PCPT

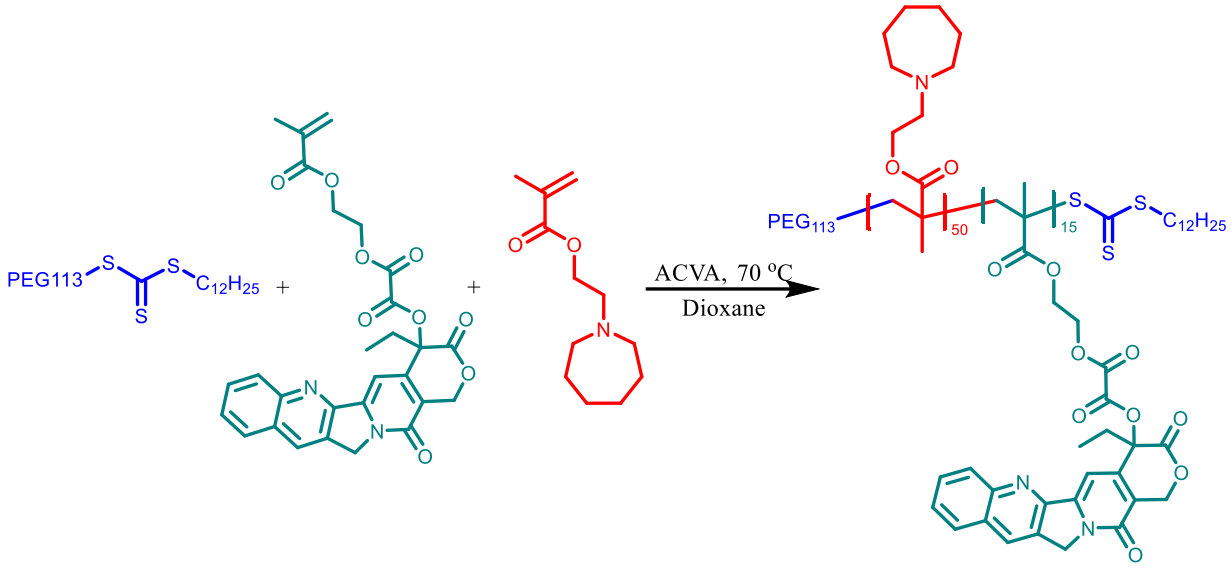

PEG-*b*-PAEMA-*s*-PCPT was synthesized by RAFT polymerization. Briefly, $mPEG_{113}$-CPDTC (0.064 g, 0.0118 mmol), AEMA (0.25 g, 1.18 mmol), Pro-CPT (0.126 g, 0.237 mmol), and ACVA (0.7 mg, 2.3 μmol) were dissolved in anhydrous dioxane (1 mL). After degassing, the mixture was stirred at 70 °C for 1 day followed by precipitating in cold hexane 3 times. The precipitate was collected by filtration and dried in a vacuum overnight. The final product was obtained as a brown-yellowish solid.

4.5.14 Photocatalytic Activation of Prodrug Model Compounds Using EY Disodium Salt

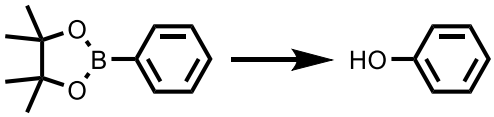

EY disodium salt (5 mol%), 4,4,5,5-tetramethyl-2-phenyl-1,3,2-dioxaborolane (30 mg, 50 mM), sodium ascorbate (150 mg, 5 eq.) was combined in an open-top screw cap vial with 3 mL PBS buffer solution (pH 7.4, 0.1 mM). The reaction mixture was supplied with oxygen through an oxygen balloon connected to the vial. The reaction mixture was irradiated with blue LED light (power: 17 mW/cm^2, λ = 460 nm) for 2 h, with aliquots taken to monitor conversion over time. The sample aliquots (0.4 mL) were mixed with DCM (2.5 mL) to extract reagents and products. The DCM solutions were dried over $MgSO_4$ before submitting to GCMS measurements. The yield and product were obtained by GCMS measurements.

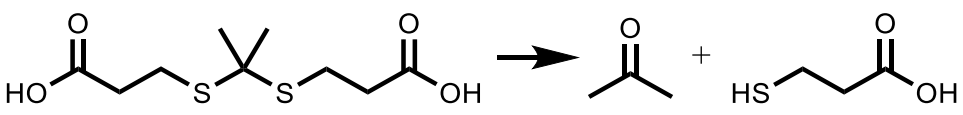

EY disodium salt (5 mol%) and 3,3'-(propane-2,2-diylbis(sulfanediyl))dipropionic acid (37.5 mg, 50 mM) were combined in an open-top screw cap vial with 3 mL PBS buffer solution (pH 7.4, 0.1 mM). The reaction mixture was supplied with oxygen through an oxygen balloon connected to the vial. The reaction mixture was then irradiated with blue LED light (power: 17 mW/cm^2, λ = 460 nm) for 2.5 h, with aliquots taken to monitor conversion over time. The sample aliquots (0.4 mL) were mixed with $CDCl_3$ (2 mL) to extract reagents and products for NMR measurements. The yield was calculated based on NMR measurements.

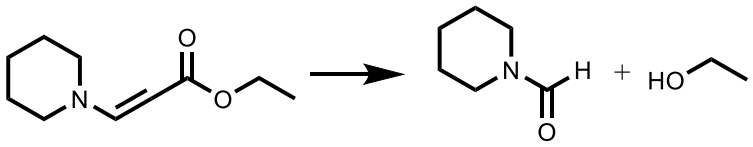

EY disodium salt (5 mol%) and ethyl 3-(piperidin-1-yl)acrylate (30 mg, 50 mM) were combined in an open-top screw cap vial with 3 mL PBS buffer solution (pH 7.4, 0.1 mM). The reaction mixture was supplied with oxygen through an oxygen balloon connected to the vial. The reaction mixture was irradiated with blue LED light (power: 17 mW/cm^2, λ = 460 nm) for 4 h, with aliquots taken to monitor conversion over time. The sample aliquots (0.4 mL) were mixed with DCM (2.5 mL) to extract reagents and products. The DCM solutions were dried over $MgSO_4$ before submitting to GCMS measurements. The yield and product were obtained by GCMS measurements.

4.5.15 Photocatalytic Activation of Prodrug Model Compounds Using Polymeric Photocatalyst

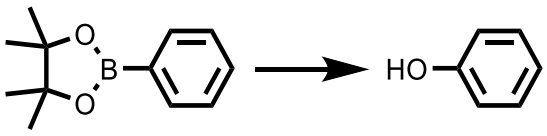

PEG-*b*-PAEMA-*b*-EYHEMA (2.5 mol%), 4,4,5,5-tetramethyl-2-phenyl-1,3,2-dioxaborolane (6 mg, 15 mM), sodium ascorbate (30 mg, 5 eq.) was combined in an open-top screw cap vial with 2 mL phosphate buffer solution (pH 6.5, 0.1 mM). The reaction mixture was supplied with oxygen through an oxygen balloon connected to the vial. The reaction mixture was irradiated with blue LED light (power: 11.9 mW/cm^2, λ = 460 nm) for 1.5 h, with aliquots taken to monitor conversion over time. The sample aliquots (0.4 mL) were mixed with DCM (2.5 mL) to extract reagents and products.

The DCM solutions were dried over $MgSO_4$ before submitting to GCMS measurements. The yield and product were obtained, in triplicate, by GCMS measurements.

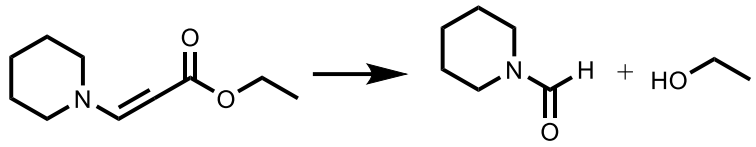

PEG-*b*-PAEMA-*b*-EYHEMA (2.5 mol% photocatalytic unit) and ethyl 3-(piperidin-1-yl)acrylate (20 mg, 50 mM) were combined in an open-top screw cap vial with 2 mL phosphate buffer solution (pH 6.5, 0.1 mM). NP-PAEMA-EY-PAEMA (2.5 mol% photocatalytic units) and ethyl 3-(piperidin-1-yl)acrylate (20 mg, 50 mM) were combined in an open-top screw cap vial with 2 mL PBS buffer solution (pH 7.4, 0.1 mM). The reaction mixtures were supplied with oxygen through an oxygen balloon connected to the vial. The reaction mixtures were irradiated with blue LED light (power: 11.9 mW/cm^2, λ = 460 nm) for 1.5 h, with aliquots taken to monitor conversion over time. The sample aliquots (0.4 mL) were mixed with DCM (2.5 mL) to extract reagents and products. The DCM solutions were dried over $MgSO_4$ before submitting to GCMS measurements. The yield and product were obtained, in triplicate, by GCMS measurements.

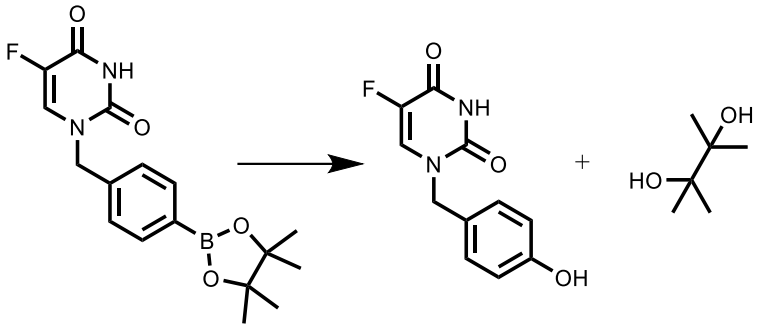

PEG-*b*-PAEMA-*b*-EYHEMA (2.5 mol% photocatalytic unit) and 5-fluoro-1-(4-(4,4,5,5-tetramethyl-1,3,2-dioxaborolan-2-yl)benzyl)pyrimidine-2,4(1H,3H)-dione (20 mg, 40 mM) were combined in an open-top screw cap vial with 1.5 mL phosphate buffer solution (pH 6.5, 0.1 mM). The reaction mixtures were supplied with oxygen through an oxygen balloon connected to the vial. The reaction mixtures were irradiated with blue LED light (power: 11.9 mW/cm^2, λ = 460 nm) for 1.5 h, with aliquots taken to monitor conversion over time. The sample aliquots (0.3 mL) were mixed with DMSO-d6 (0.3 mL) for the ^{19}F-NMR measurements.

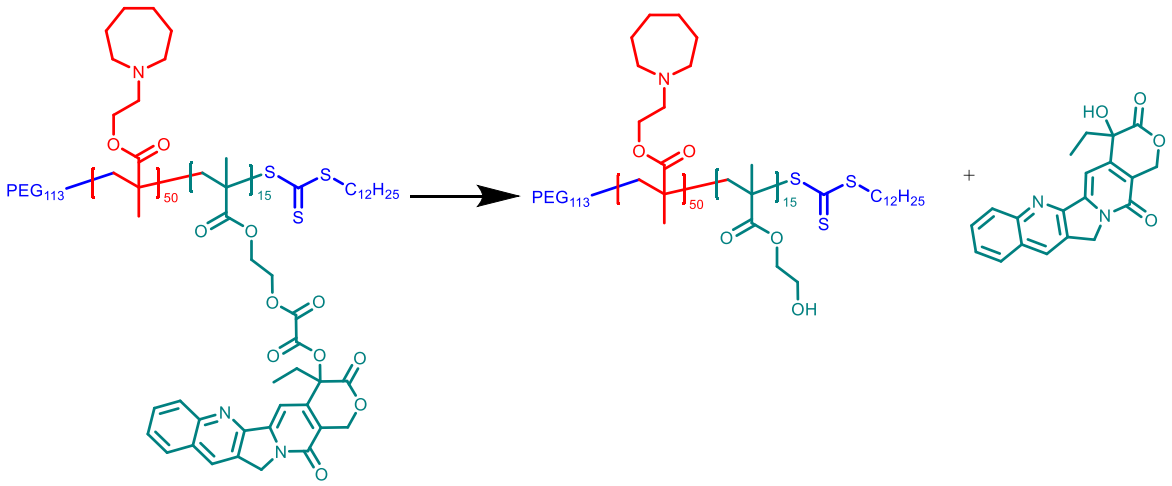

PEG-*b*-PAEMA-*b*-EYHEMA (5 mg) and PEG-*b*-APEMA-*s*-PCPT (15 mg) were combined in an open-top screw cap vial with 1 mL $CDCl_3$. The reaction mixtures were supplied with oxygen through an oxygen balloon connected to the vial. The reaction mixture was irradiated with blue LED light (power: 11.9 mW/cm^2, λ = 460 nm) for 3 h. The samples before and after light irradiation were subjected to NMR measurements.

4.5.16 Cytotoxicity Assay

The standard sample preparation for the cytotoxicity assay: PEG-*b*-PAEMA-*b*-EYHEMA (2.5 mol% photocatalytic unit), 5-fluoro-1-(4-(4,4,5,5-tetramethyl-1,3,2-dioxaborolan-2-yl)benzyl)pyrimidine-2,4(1H,3H)-dione (3.5 mg, 10 mM), and sodium ascorbate (10 mg, 5 eq.) were combined in an open-top screw cap vial with 1 mL phosphate buffer solution (pH 6.5, 0.1 mM). This mixture was supplied with oxygen through an oxygen balloon connected to the vial and irradiated with blue LED light (power: 11.9 mW/cm^2, λ =460 nm) for 2 h. Control conditions: (1) PEG-*b*-PAEMA-*b*-EYHEMA (2.5 mol% photocatalytic unit), 5-fluoro-1-(4-(4,4,5,5-tetramethyl-1,3,2-dioxaborolan-2-yl)benzyl)pyrimidine-2,4(1H,3H)-dione (3.5 mg, 10 mM), and sodium ascorbate (10 mg, 5 eq.) were combined in an open-top screw cap vial with 1 mL phosphate buffer solution (pH 6.5, 0.1 mM). This mixture was supplied with oxygen through an oxygen balloon connected to the vial and kept in dark for 2 h. (2) PEG-*b*-PAEMA-*b*-EYHEMA (2.5 mol% photocatalytic unit) was dissolved in 1 mL phosphate buffer solution (pH 6.5, 0.1 mM). (3) 5-fluoro-1-(4-(4,4,5,5-tetramethyl-1,3,2-dioxaborolan-2-yl)benzyl)pyrimidine-2,4(1H,3H)-dione (3.5 mg, 10 mM) was well dispersed in 1 mL phosphate buffer solution (pH 6.5, 0.1 mM).

Regarding the cell cytotoxicity, briefly, cells were seeded at a density of 10 000 cells per well in white bottom 96 well plates and incubated over-night at 37 ˚C and 5% CO_2.

On the next day, the cells were respectively treated with PEG-*b*-PAEMA-*b*-EYHEMA, prodrug, the combination of prodrug and PEG-*b*-PAEMA-*b*-EYHEMA before and after blue light LED irradiation in various concentrations ranging from 6.25 to 100 mM. After 72 h of incubation, a volume of CellTiter-Glo® Reagent (Promega, Germany) equal to the volume of cell culture media present was added to the cells as recommended by the manufacturer. The luminescent signal was recorded with a Tecan Infinite M100 plate reader. The viability was calculated based on the average luminescent signal intensity (n = 5) for the non-treated cells.

4.6 Additional Trail

In addition to the aforespecified eosin Y based pH-responsive photocatalytic polymers, the hydrophilicity of which was modulated by the protonation-deprotonation process responding to pH changes. A class of pH-responsive crosslinkers have also been reported, utilizing pH-liable amine-aldehyde coupling to form pH cleavable imine bonds.[238] We have applied a similar methodology whereby, a diblock copolymer was synthesized by RAFT polymerization with the photocatalytic moiety copolymerized with a primary amine monomer. Therefore, this amine and photocatalytic block will be heavily cross-linked and deactivated in the presence of crosslinkers above the pH of cancerous cells, whereas at pH 6.4 and below the crosslinks are cleaved which leads to the activation of photocatalytic units. Here, diblock copolymer poly(ethylene glycol-*b*-poly(2-aminoethylmethacrylate-*s*-*N*-(4-(7-phenylbenzo [*c*] [1,2,5] thiadiazol-4-yl)phenyl)methyl methacrylate)) PEG_{113}-*b*-P(AMA_{50}-*s*-Ph_2BTMA_1) has been synthesized by chain extension of PEG-macroCTA with 2-aminoethylmethacrylate (AMA) monomers with primary amine groups and Ph_2BTMA monomers as photocatalytic moieties via RAFT polymerization. The chemical composition has been confirmed by 1H NMR (Figure 82). GPC has examined the as-obtained polymer chains with an average molar mass of 8.9 kDa and a dispersity of 1.31 (Figure 83). This photocatalytic polymer displayed a broad absorbance of visible light that is consistent with the literature[165] (Figure 84).

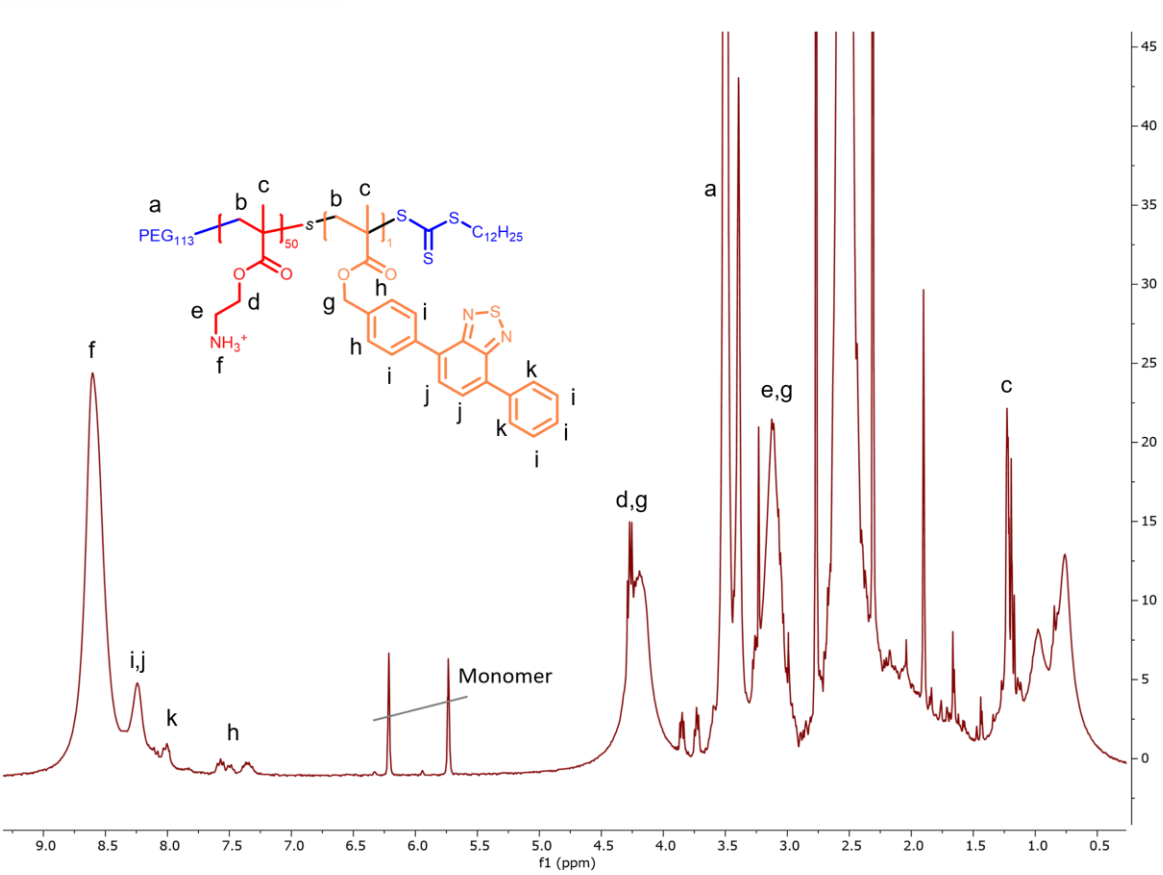

Figure 82. NMR spectrum of PEG_{113}-*b*-P(AMA_{50}-*s*-Ph_2BTMA_1) copolymer (not purified).

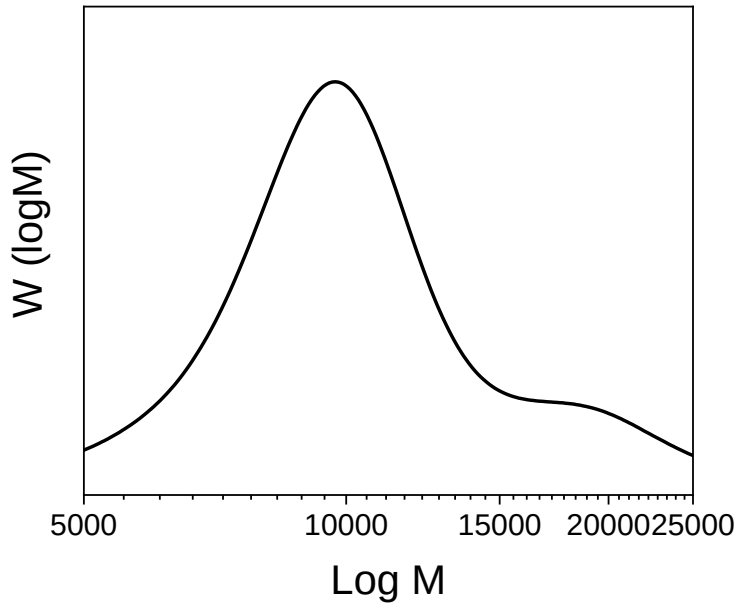

Figure 83. GPC spectrum of PEG_{113}-*b*-P(AMA_{50}-*s*-Ph_2BTMA_1) copolymer.

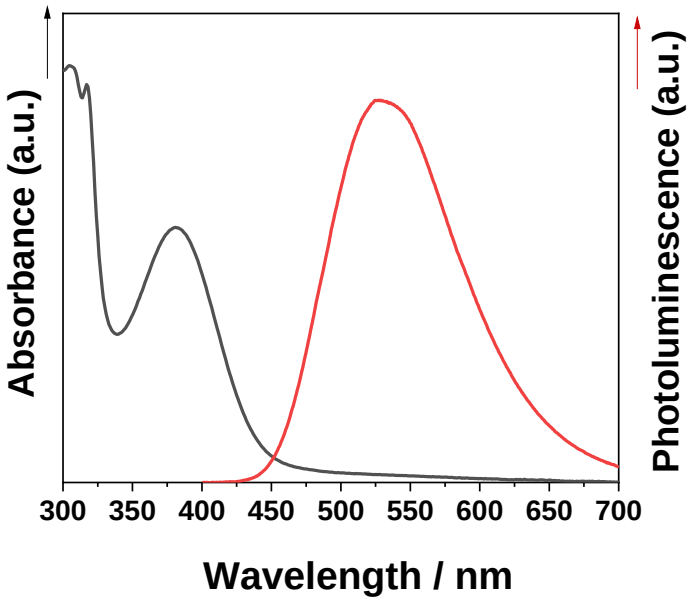

Figure 84. UV/Vis absorbance (black) and photoluminescence (red) spectra of PEG_{113}-*b*-P(AMA_{50}-*s*-Ph_2BTMA_1) copolymer.

These photocatalytic polymer chains containing primary amino groups have been further crosslinked in the presence of terephzhalaldehyde (TPA) as a crosslinker using PBS buffer (pH 7.4) as solvent. The primary amine groups in the photocatalytic polymers react with the aldehyde groups of the TPA crosslinker molecules, forming acid-labile imine bonds at basic conditions (e.g. at pH 7.4). These imine bonds can be reversibly cleaved when subjected to acidic conditions (e.g. at pH 6.4), which overlaps with the pH difference between the tumor tissue and healthy tissue. The crosslinking process of the polymer chains was illustrated in the Figure 85.

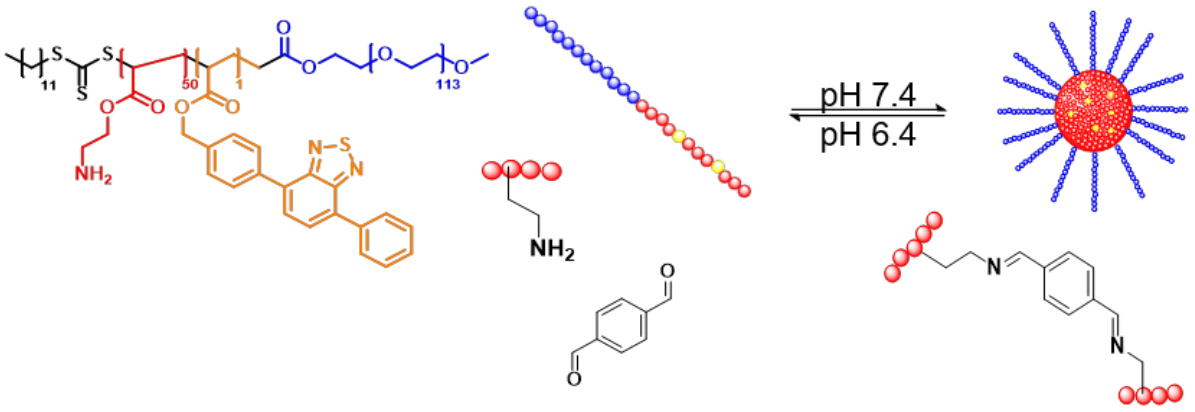

Figure 85. Illustration of the reversible crosslinking-cleavage process that the photocatalytic polymers with primary amine groups are crosslinked with the aldehyde groups in TPA according to the pH conditions.

The morphology of these crosslinked particles was visualized by TEM (Figure 86), where spherical nanoparticles have been observed. Besides, the hydrodynamic diameter of these nanoparticles was also measured by DLS with a hydrodynamic diameter of 176 nm when dispersed in PBS buffer at pH 7.4.

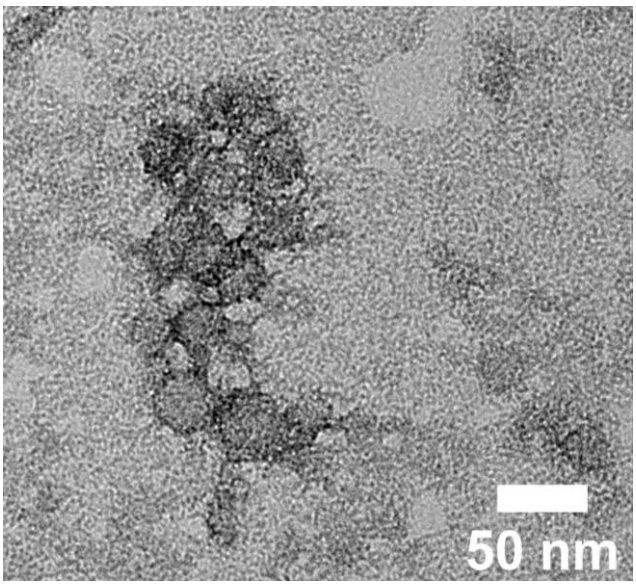

Figure 86. TEM image of the crosslinked photocatalytic nanoparticles dispersed in PBS at pH 7.4.

To verify the pH-responsiveness of these nanoparticles, the crosslinked nanoparticles were dispersed in a series of phosphate buffer solutions ranging from pH 7.4 to 6.4. The hydrodynamic diameter of the particles presented in these dispersions has been monitored by DLS (Figure 87), where a sharp size change from pH 7.0 to 6.8 was observed, which agrees well with the pH difference between the health tissue and cancer cells. The shrunken size of the nanoparticles could be resulted from the dissociation of the crosslinkages in response to the pH change, indicating the revealing/activation of photocatalytic units.

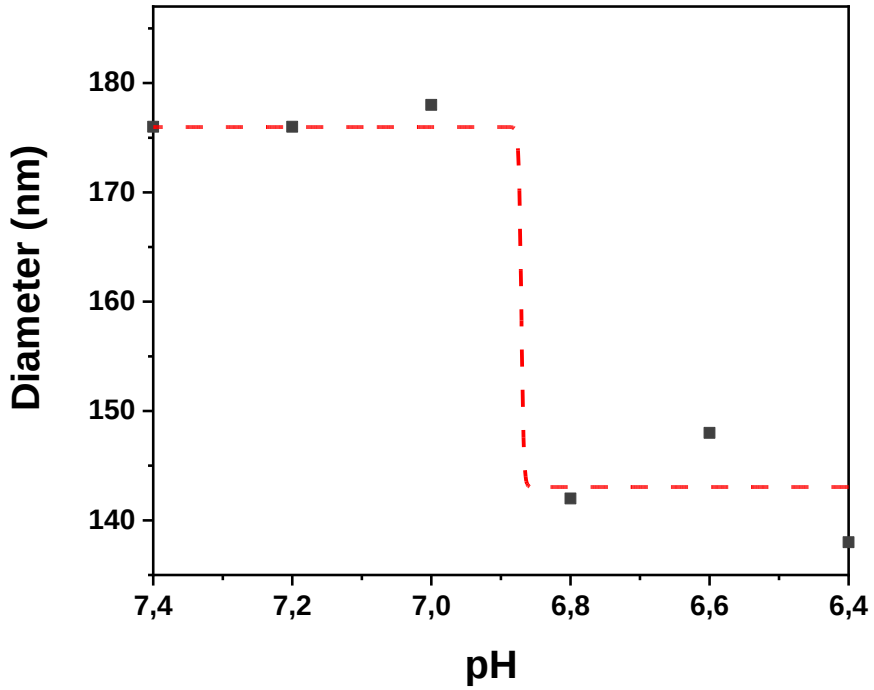

Figure 87. The hydrodynamic diameter of the nanoparticles dispersed in various phosphate buffers from pH 7.4 to 6.4, measured by DLS.

Furthermore, the formation and dissociation of crosslinkages has been characterized by FTIR (Figure 88), where primary amine groups were clearly visible in free PEG_{113}-*b*-P(AMA_{50}-*s*-Ph_2BTMA_1) polymer chains, and a mixture of primary amine groups and imine bonds were presented in nanoparticles before and after subjected to slightly acidic phosphate buffer at pH 6.4. Although the nanoparticles formed at pH 7.4 have shown a sharper peak at 1650 cm^{-1} attributed to the imine bonds, no quantitative conclusion can be drawn based on this FTIR result.

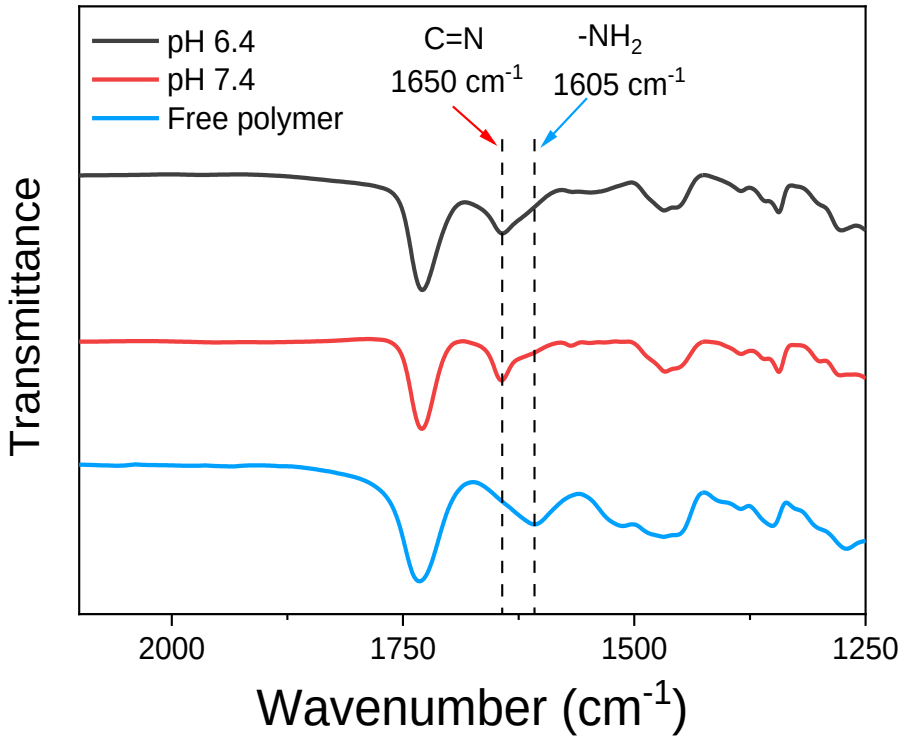

Figure 88. FTIR spectra of the crosslinked photocatalytic nanoparticles at pH 7.4, pH 6.4 and free polymers.

To obtain more quantitative results regarding the crosslink density of these particles, solid-state NMR spectroscopy has been applied to examine the chemical compositions of the particles and free polymers, respectively. As exhibited in Figure 89, no trace of imine bond has been observed in free polymer chains. Regarding nanoparticles before and after the cleavage of the crosslinkages, clear peaks assigned to imines (125-170 ppm) were displayed in the solid-state NMR spectra. Based on the ratio of carbonyl groups (180 ppm) to imine bonds, the crosslink density can be calculated, where the crosslink density decreased from 37% to 9.7% after incubation in an acidic phosphate buffer solution at pH 6.4. This result is consistent with the DLS and FTIR results that further demonstrated the cleavage of the crosslinking and thereby indicated the activation of the photocatalyst. Although the nanoparticles were not completely dissociated after incubation at pH 6.4, the crosslink density dropped around 4 times compared to the pristine nanoparticles, thereby the photocatalytic units were more accessible with lower crosslink density. Therefore, we would expect to control the reactivity of these dispersions by modulating the crosslink density which can be easily achieved via tuning the pH value of the reaction medium.

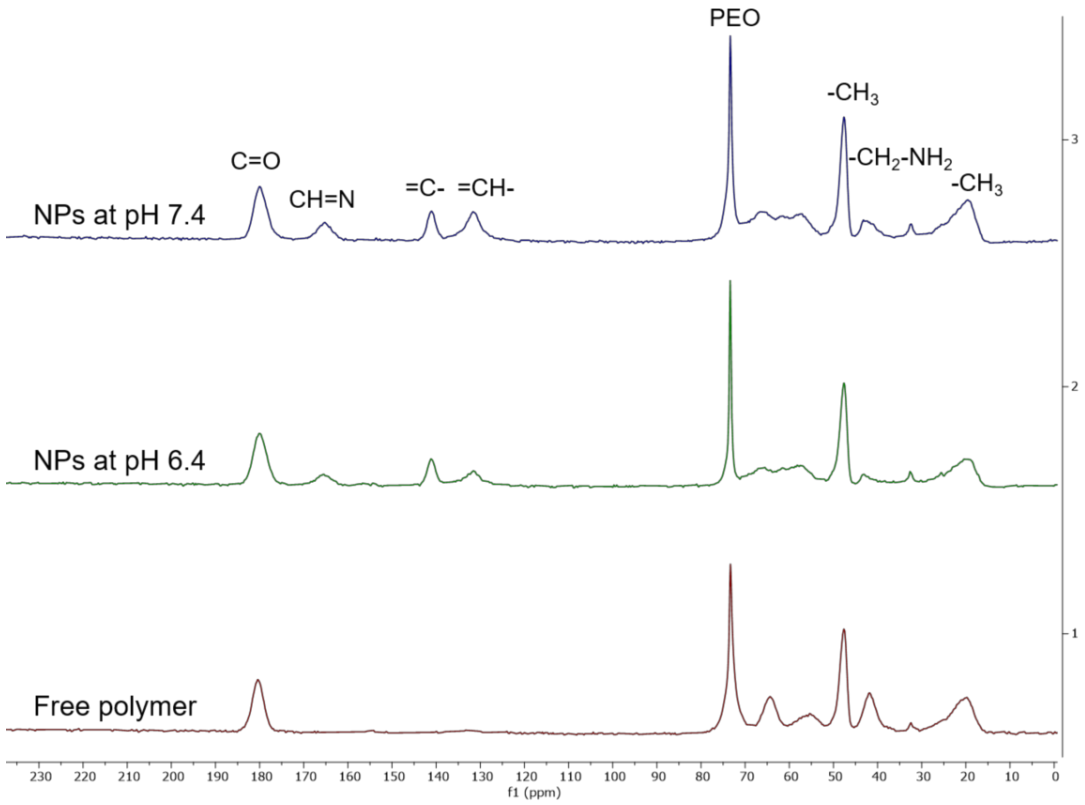

Figure 89. Solid-state NMR spectra of the crosslinked photocatalytic nanoparticles dispersed in PBS at pH 7.4, phosphate buffer at pH 6.4 and free polymers.

Here, we have selected the degradation of rhodamine B as a model reaction to demonstrate the controllable activation of the nanoparticles by controlling the pH of the reaction medium. The degradation reaction was monitored by UV-Vis spectroscopy (Figure 90A). The absorption peak of the reaction medium at pH 6.4 shifted to a short wavelength (peaked at 480 nm) but no obvious change was observed in the absorption peak position (peaked at around 540 nm) of the dispersion at pH 7.4 before and after the reaction. Moreover, the color of the reaction medium remained reddish as the pristine rhodamine B solution after irradiated by light for 15 h in the presence of the photocatalytic nanoparticles. In comparison, the color of the reaction medium turned green at pH 6.4 after being irradiated for 15 h (Figure 90B). These results suggested that the rhodamine B was degraded using the nanoparticle dispersion at pH 6.4, owing to the more accessible photocatalytic units compared to that at pH 7.4.

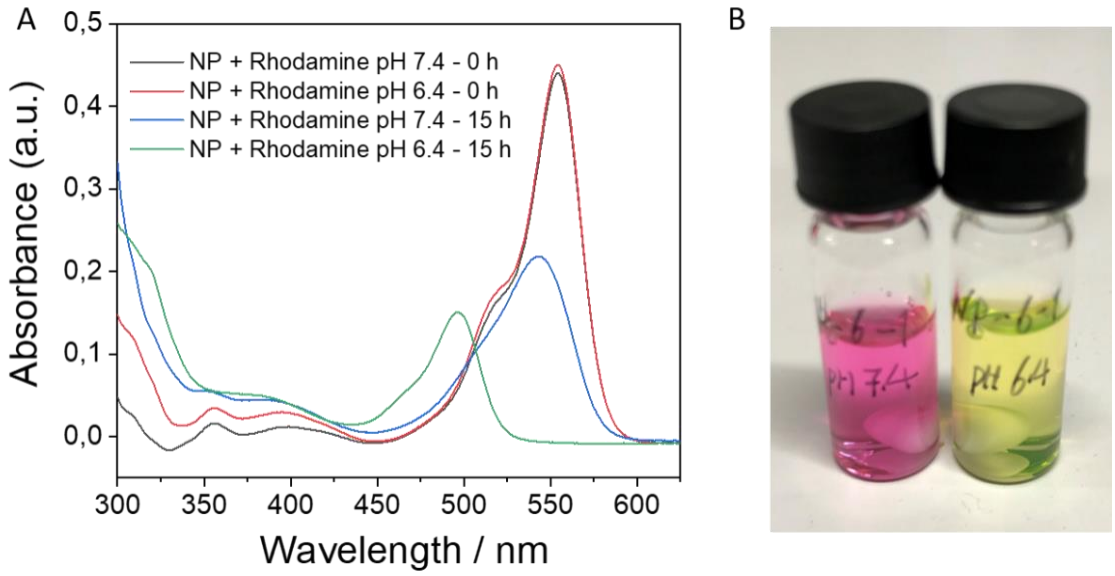

Figure 90. (A) UV-Vis spectra of the crosslinked photocatalytic nanoparticles dispersed in PBS at pH 7.4 and phosphate buffer at pH 6.4 for the degradation of rhodamine B. (B) Digital image of the rhodamine B degradation reaction mixtures after 15 h of light irradiation.

In addition to rhodamine B degradation, we have further compared the reactivity of the photocatalytic nanoparticle dispersions at pH 6.4 and 7.4 for nicotinamide adenine dinucleotide (NADH) oxidation reaction. NADH is an important energy-supplying coenzyme for the generation of ATP. Here, we studied the kinetic profile of the NADH oxidation reaction by 1H NMR using photocatalytic nanoparticles dispersed at pH 7.4 or 6.4 in the presence of oxygen as an external oxidant, respectively. As illustrated in Figure 91, reactions proceeded with an extended time at both pH values. The reaction catalyzed by dispersion at pH 6.4 progressed faster compared to the dispersion at pH 7.4. Eventually, 84% of conversion was obtained after 1 h of light irradiation applying particle dispersion at pH 6.4, which was nearly doubled compared to the conversion delivered by the dispersion at pH 7.4 (45%).

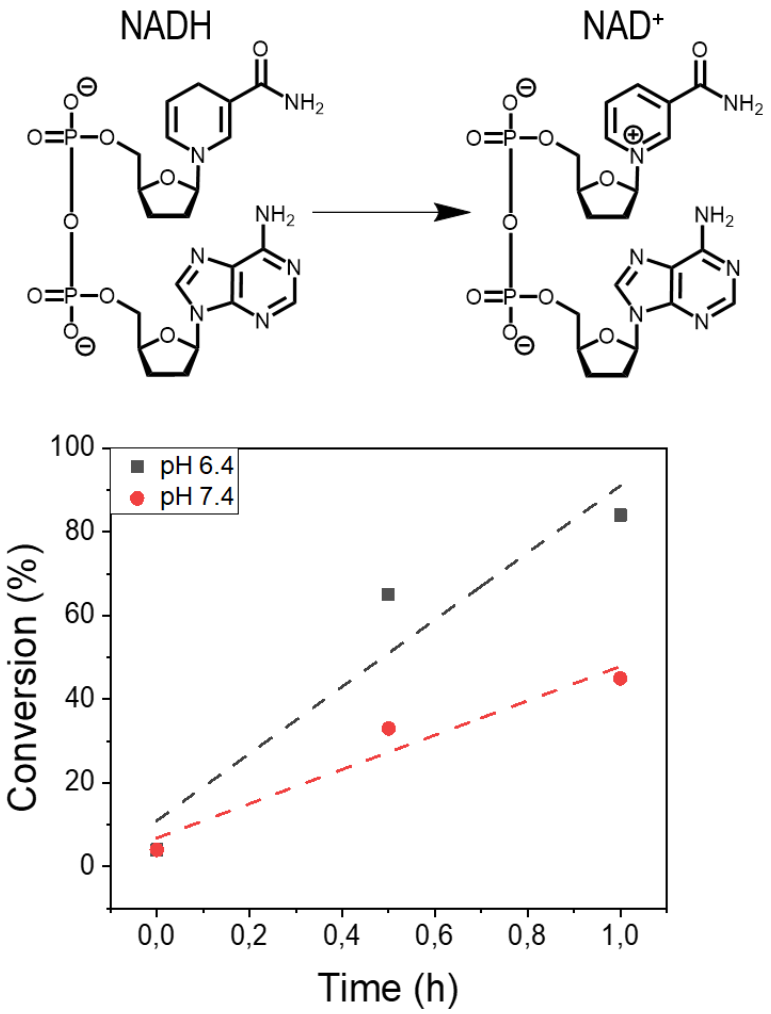

Figure 91. Kinetic profile of the crosslinked photocatalytic nanoparticles dispersed in PBS at pH 7.4 and phosphate buffer at pH 6.4 for the oxidation of NADH.

These results demonstrate that we could control the activation of the photocatalytic nanoparticles by controlling the pH value of the reaction medium. These particles can be deactivated at neutral to basic conditions due to the high crosslink density, which afterward can be activated by cleaving the crosslinkage at acidic conditions. Therefore, these nanoparticles exhibit great potential to be applied as a photocatalytic system to achieve targeted cancer treatment taking advantage of the intrinsic pH difference between the cancer environment and normal tissue.

Considering the limited blue light penetration in human tissue (~ 1 mm),[239] plenty of investigations have been conducted to incorporate luminol as a light source into the PDT design to achieve *in situ* PDT via a bioluminescence resonance energy transfer (BRET) process.[240–244] Luminol as a cheap and efficient emitter has been widely used

in forensic investigations of blood and fingerprints. Its chemiluminescence mechanism has been clearly explained with three basic steps, including 1) initially luminol is oxidized to luminol radical by oxidants (e.g. hydroxyl and associated radicals) in the presence of Fe(II) as a catalyst; 2) the resulting luminol radical is further oxidized to α-hydroxyhydroperoxide; 3) this α-hydroxyhydroperoxide is eventually decomposed to aminophthalate and nitrogen while the emission of chemiluminescence.[245] To our interest, the chemiluminescence generated by luminol is centered at around 420 nm that highly overlaps with the absorption band (350-450 nm) of the developed PEG_{113}-*b*-P(AMA_{50}-*r*-Ph_2BTMA_1) photocatalyst (Figure 84). Here, we examined the BRET of luminol to Ph_2BTMA molecular photocatalyst to catalyze NADH oxidation. A typical reaction setup involves luminol (illuminating), horseradish peroxidase HRP (catalyst for luminol), 4-iodophenol (4-IP, enhancer for luminol), Ph_2BTMA (photocatalyst) and H_2O_2 (oxidant).

To evaluate the oxidizing effect of luminol formulation, luminol, HRP, and H_2O_2 was added to NADH solution, and the NMR spectrum of the mixture was recorded every 3 min. After 18 min, the conversion was increased from 8% to 16% (see Figure 92).

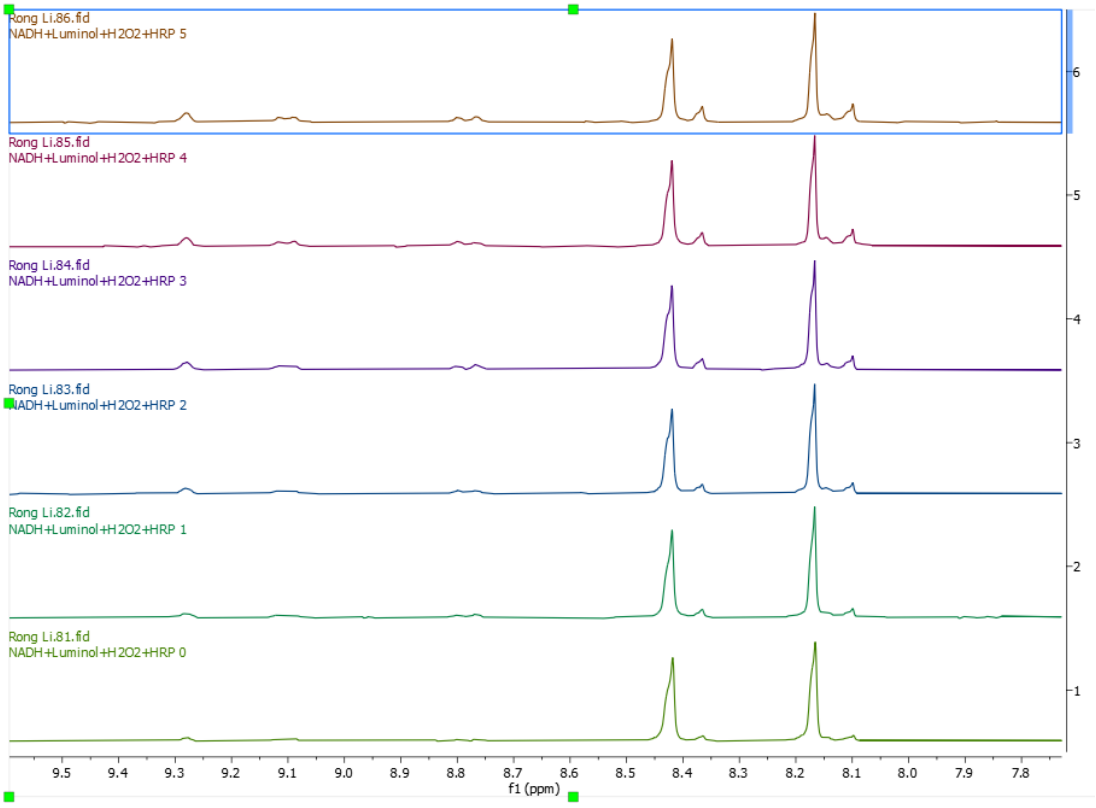

Figure 92. NMR spectra stacking of the kinetic study of NADH + luminol + HRP +H_2O_2 without enhancer.

Thereafter, the enhancer 4-IP was added to the mixture after the oxidation had reached 23% and NMR spectra were recorded accordingly (Figure 93). The conversion remained identical (23%) after 12 min, suggesting no oxidation effect on NADH oxidation.

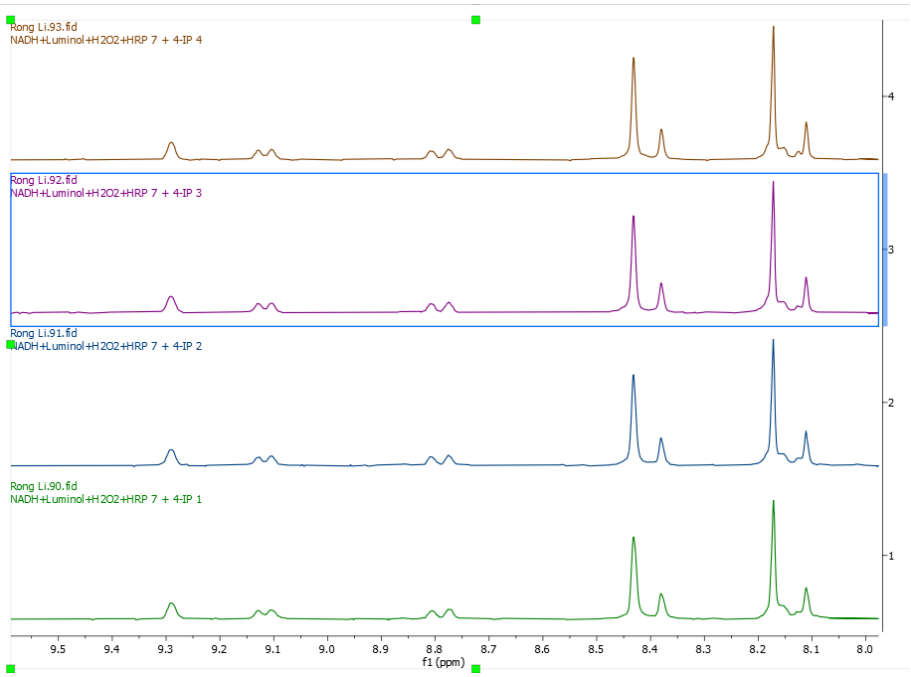

Figure 93. NMR spectrum stacking of the kinetic study of NADH oxidation added with luminol + HRP +H_2O_2 + 4-IP, 4-IP was added to the reaction mixture described previously.

NADH oxidation was then carried out in the presence of both luminol and photocatalyst in dark conditions (see Figure 94). After 9 min, the conversion of NADH increased from 12% to 22%. The reaction rate of NADH oxidation in the presence of a photocatalyst was higher than only in addition to a luminol mixture, which gives promising preliminary results.

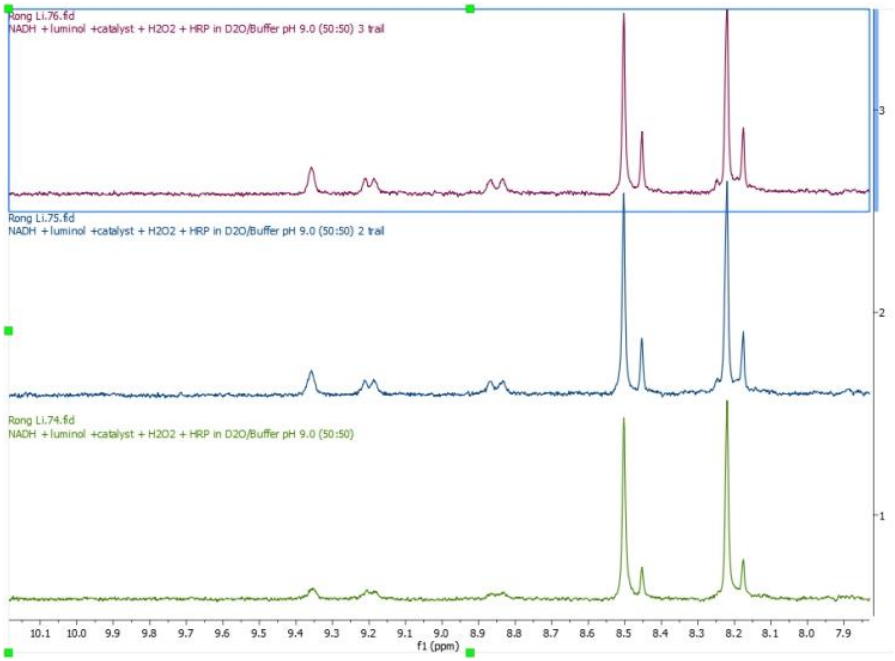

Figure 94. NMR spectrum stacking of the kinetic study of NADH oxidation added with luminol + HRP +H_2O_2 + 4-IP + photocatalyst.

To simply the prodrug activation process and to demonstrate the activity of the photocatalytic polymer towards prodrug activation, we have used the PEG_{113}-*b*-P(AMA_{50}-*s*-Ph_2BTMA_1) polymeric photocatalyst for PFU activation. Briefly, the PEG_{113}-*b*-P(AMA_{50}-*s*-Ph_2BTMA_1) was dissolved in phosphate buffer pH 6.4 at a concentration of 1 mg/mL and to this solution 3 mg of PFU was added with sodium ascorbate (100 mM) as an electron donor. Unfortunately, no conversion of prodrug activation has been monitored by GCMS. Therefore, we have selected another well-established and commercially available photocatalyst eosin Y to facilitate the ROS-sensitive prodrug activation. Since the overlap of the absorption band of eosin Y and luminol luminescence band is too small, we have reshaped the investigation more towards developing photocatalytic systems based on eosin Y as photocatalyst to activation various ROS-sensitive prodrug model compounds as illustrated in Chapter 4. However, it is worth noting that incorporating a light source into the photocatalytic system design is beneficial for *in-situ* prodrug activation. Therefore, in future work, a suitable light emitting unit can be incorporated in the eosin Y based pH-responsive photocatalytic system to achieve efficient targeted prodrug activation *in situ*.

4.6.1 Experimental section

Photocatalytic Polymer Synthesis

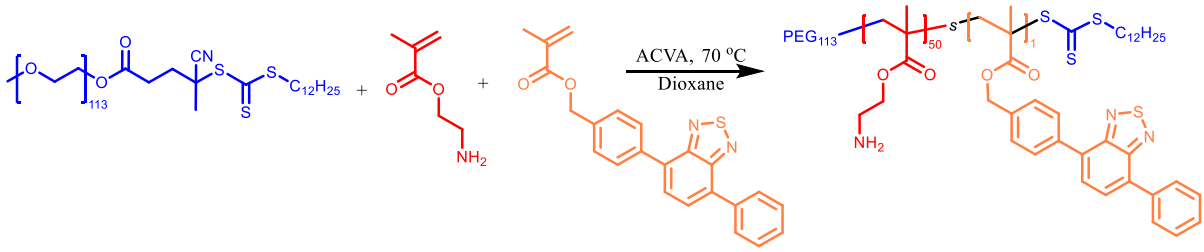

PEG_{113}-*b*-P(AMA_{50}-*s*-Ph_2BTMA_1) was synthesized by RAFT polymerization. Briefly, mPEG_{113}-CPDTC (0.174 g, 32 µmol), AMA (0.288 g, 1.74 mmol), Ph_2BTMA (12 mg, 32 µmol), and AIBN (1 mg, 6.4 µmol) were dissolved in anhydrous DMSO (1.8 mL). After degassing, the mixture was stirred at 70 °C for 4 h followed by dialyzing for 3 days in an acetone/water mixture (1/1 v/v). After purification, the polymer photocatalyst was dried via lyophilization and the final product was obtained as a yellow solid. The degree of polymerization of the PAEMA block was determined as 50 according to the ^{1}H NMR spectrum. The dispersity was determined by GPC.

Photocatalytic Nanoparticle Preparation

Photocatalytic nanoparticles were prepared by crosslinking the linear photocatalyst polymer PEG_{113}-*b*-P(AMA_{50}-*s*-Ph_2BTMA_1) using TPA as a crosslinker. Briefly, the linear polymer was dissolved in PBS buffer at pH 7.4 at a concentration of 5 mg/mL. Crosslinker TPA solution in THF (1 mg/mL) was added to the polymer PBS solution at pH 7.4 dropwise while sonication. The ratio of CHO/NH_2 has been varied from 1.0 to 2.0 and the hydrodynamic diameters of these dispersions were characterized by DLS. The ratio of CHO/NH_2 at 1.4 gave a homogeneous dispersion with a nanoparticle size of 220 nm. Therefore, this ratio has been selected for the nanoparticle preparation.

CHO/NH_2	1.0	1.2	1.4	1.6	1.8	2.0
D_H	171 nm	Precipitation	220 nm	Precipitation	340 nm	295 nm

Rhodamine B Degradation

Crosslinked photocatalytic nanoparticles were dispersed in PBS buffer pH 7.4 and phosphate buffer pH 6.4 at a concentration of 1 mg/mL, respectively. To these photocatalyst nanoparticle dispersions, rhodamine B was added to a concentration of 20 µg/mL. The mixtures were subjected to blue light irradiation under ambient conditions. The absorbance of the samples was monitored by UV-Vis spectrometry before and after being irradiated for 15 h.

NADH Oxidation

In a 4 mL glass vial, 2 mg of crosslinked photocatalytic nanoparticles were dispersed in 2 mL PBS buffer at pH 7.4 and phosphate buffer at pH 6.4, respectively. 35.4 mg of NADH substrate was added to each dispersion and the reaction mixtures were subjected to blue light irradiation under ambient conditions. The kinetic profiles were monitored with 1H NMR using an aliquot of 0.15 mL of the reaction medium at each time interval mixed with 0.35 mL D_2O.

5 Summary and Perspective

In this thesis, novel designs of polymeric photocatalysts consisting of organic dyes as active photocatalytic units were explored in depth to address critical challenges in both sustainable photocatalysis and targeted therapeutic applications.

Initially, core-shell structured pH-responsive polymeric photocatalyst nanoparticles were created to facilitate various chemical transformations in the presence of visible light, including Cr(VI) reduction, sulfide oxidation, 2-furoic acid oxidation, and photoredox Friedel–Crafts alkylation. The stabilizing shell of the nanoparticles was comprised of diisopropylamino moieties as pH-sensitive functional groups as well as a small portion of diphenyl benzothiadiazole (Ph_2BT)-based photoactive centers. These tertiary amine groups can be reversibly protonated and deprotonated in response to the pH changes in the medium. Thereafter, the hydrophilicity of the stabilizing shell with photocatalytic units can be modulated by the pH value of the medium, where the aggregation of photocatalytic nanoparticles can be triggered upon elevating the pH value. These photocatalytic nanoparticles have been efficiently recycled and reapplied to multiple cycles of reactions with no observable loss of efficiency. Moreover, these photocatalytic nanoparticles have outperformed the state-of-art analogues reported in the literature for the Cr(VI) reduction reaction, owing to the accelerated mass diffusion as a result of charge attraction interactions between the positively charged shell and anionic Cr(VI) substrates. This strategy produces highly effective polymeric photocatalyst nanoparticles with great photocatalytic performance and recyclability for sustainable photocatalysis.

Given the possibility of enhancing the recyclability of photocatalytic materials by applying an external stimulus such as pH described in the first project, this approach still requires centrifugation where electricity is consumed to allow efficient recycling of

the materials. To give a more sustainable solution, it is desired to design a photocatalytic system in combination with magnetic nanoparticles, where the photocatalytic material can be easily recovered from the reaction medium via a magnetic separation technique. In the second project, amphiphilic diblock copolymers consisting of a small amount of eosin Y based-photocatalytic units randomly distributed in the oligo(glycidyl ether)-based hydrophilic block and a second poly(benzyl methacrylate) (PBzMA) hydrophobic segment were synthesized to coat on the surface of magnetite nanoparticles. The magnetite nanoparticles were pre-modified with hydrophobic silanes, which acted as the seeds for the deposition of the hydrophobic PBzMA block. The resultant particles were stabilized by the photocatalytic hydrophilic block tethered on the surface. These hybrid photocatalytic nanoparticles exhibited extremely efficient performance in various boronic acids and boronic acid pinacol ester hydroxylation using water as a green solvent with yields ranging from 86% to >99%. Moreover, these photocatalytic particles have been simply recovered via a magnetic separation technique and reused multiple times with no observable loss of efficiency. These results demonstrated a novel and efficient design of photocatalytic materials for sustainable photocatalysis, where the recycling is simply achieved by applying magnetism.

In addition to enhancing the recyclability of photocatalytic materials, incorporating photocatalytic centers into specifically designed stimuli-responsive polymers also allows the modulation of photocatalytic reactivity by external stimuli. In the third project, a pH-responsive photocatalytic system that can specifically respond to the characteristic dysregulated pH of solid tumors has been designed and synthesized to achieve targeted cancer treatment. Block copolymers comprising of a hydrophilic PEG segment, a pH-sensitive tertiary amine-based AEMA switchable block, as well as a small amount of eosin Y based photocatalytic units were synthesized. These block copolymers can be reversibly assembled and disassembled by tuning the pH value of the medium, owing to the protonation-deprotonation process of tertiary amine groups. Consequently, the accessibility of the photocatalytic centers can be modulated by controlling the pH of the medium. This polymeric photocatalyst material exhibited an excellent reactivity in the activation of prodrug model compounds with different ROS-sensitive protecting groups at mild acidic conditions (pH 6.5). Moreover, the controlled activation of the prodrug model compound has been achieved by taking advantage of

the ultra pH-sensitive nature (0.3 pH increment) of the polymeric photocatalyst, where 25 times high yield of release has been obtained at pH 6.5 compared to the reaction at pH 7.4. These findings demonstrated an efficient approach to control the activation of the prodrug model compounds at the targeted tumor site.

In summary, the design of stimuli-responsive photocatalytic materials has been outlined according to their photocatalytic applications. Generally, the combination of stimuli-responsive structures with organic dye-based photocatalysts offers novel solutions to produce recyclable photocatalytic materials for sustainable photocatalysis. Especially, applying magnetism to trigger the recovery of the photocatalytic materials is of great interest, further investigations could be focused on improving the material preparation methods. For example, attaching the polymers through chemical bonds, instead of coating the photocatalytic polymers physically on the magnetite nanoparticles, could potentially enhance the stability of the attachment of photocatalytic polymers to magnetite nanoparticles. In addition, the polymers could be constructed with stimuli-responsive segments, generating multiple-responsive photocatalytic materials. Furthermore, embedding multiple photoactive centers that can be excited by different wavelengths into the polymeric constructions can possibly produce photocatalytic materials for controlled cascade reactions. In addition to improving the recyclability of photocatalytic materials, introducing organic dye-based photoactive centers into pH-responsive polymers has exhibited a great potential to facilitate targeted therapeutic applications. Regarding PDT-related treatment methods, the depth of light penetration is still a limiting factor in the practical application of photocatalytic materials in the human body. The introduction of a light-emitting system (e.g. luminol) into photocatalytic materials appears to be a promising approach to obtaining *in situ* activation of the photoactive centers. Overall, the findings of this thesis lay a foundation for future investigations in the field of stimuli-responsive photocatalysts.

Appendix

A1. List of Figures

Figure 1. Thermodynamics of uphill and downhill photocatalysis: (a) the uphill process; (b) the downhill process. Adapted from Ref. [10] with permission. 16
Figure 2. A typical photocatalytic process of semiconducting photocatalytic materials. Three steps are involved in the photocatalytic process: (1) light absorption and excitation; (2) charge separation and migration; (3) electron transfer between the semiconductors. 17
Figure 3. Selection of important molecular photocatalysts and their simplified functional principles: (a) metal complex. (b) organic dyes. 19
Figure 4. (a) Tri-s-triazine-based structure of g-C_3N_4. Color scheme: gray balls - C atoms, blue ones - N atoms. (b) Band structure of g-C_3N_4. (c) Photocatalysis of g-C_3N_4. Reproduced from Ref. [56] with permission. 23
Figure 5. Chemical structure of the statistical copolymer of styrene, styrene-based B_{12}, and Ru complex photocatalyst. The photocatalytic reaction is facilitated by the polymer photocatalyst. Reproduced from Ref. [63] with permission**.** 26
Figure 6. Illustration of PMMA-based photocatalyst copolymer microgel and its application in photocatalytic [4 + 2] cycloaddition. Reproduced from Ref. [68] with permission from the Royal Society of Chemistry. 29
Figure 7. Structure of poly(NIPAM-co-BP) and changes in the structure of poly(NIPAM-co-BP) in water as a function of temperature. Reproduced with permission from Ref. [86] with permission. 34
Figure 8. Photocatalytic temperature-responsive microgels. (a) structure of cross-linked photocatalytic microgel. (b) Temperature-dependent shrinking of microgel. (c) Controllable optical properties of photocatalytic microgel as a function of temperature. (d) Temperature dependent photocatalytic conversion of the enzyme cofactor NADH to NAD^+. Reproduced with permission from Ref. [84] with permission. 37
Figure 9. PIB coupling to Ir-based photocatalyst. Method developed by Rackl et al.[96] for photocatalysis in a biphasic system with easy separation of products and recyclability of photocatalyst. Figure reproduced from Ref. [96] with permission. 40
Figure 10. Synthetic pathway and modification method for hydrophilic, conjugated, microporous polyazulene networks. Reproduced from Ref. [111] with permission. 43
Figure 11. Schematic illustration of the switchable hydrophilicity of the conjugated polymer photocatalyst through CO_2/N_2 exchange, and its photocatalytic applications in water. Reproduced from Ref. [112] with permission 44

Figure 12. Schematic representation of switchable unimolecular micelles with single Pt atoms. The dispersed UMs are catalytically active, whereas the photocatalytic activity of the aggregated UMs is sharply reduced. Reproduced with permission from Ref. [85]. 47
Figure 13. Illustration of magnetic conjugated polymer (MCP) with controllable wettability via anion exchange and the nanoparticles were used for hydrophilic and hydrophobic substrates. Reproduced with permission from Ref. [117]. 50
Figure 14. Photosensitization processes are illustrated by a modified Jablonski diagram. Light exposure takes a photosensitizer molecule from the ground singlet state (S_0) to an excited singlet state (S_1). The molecule in S_1 may undergo intersystem crossing to an excited triplet state (T_1) and then either form radicals via a type 1 reaction or, more likely, transfers its energy to molecular oxygen ($^3O_2$) and form singlet oxygen ($^1O_2$), which is the major cytotoxic agent involved in PDT. 53
Figure 15. Simplified illustration of the NMR methodology. The nuclear spins found in organic molecules behave similarly to small magnets. While they are statistically oriented in solution, they preferentially align parallel in the external magnetic field. Together they result in a macroscopic magnetization of the spins in the z direction. The spins rotate through targeted excitation of the spins using radio frequency. The macroscopic magnetization is brought horizontal and rotates in the static field after the pulse is switched off. The immediate environment of the nuclear spin (e.g., chemical bonds, electrostatic interactions, solvent matrix, etc.) determines its resonance frequency, which is ultimately reproduced as a signal in the NMR spectrum. Specific molecules can therefore be identified by their characteristic signal patterns.[127] 57
Figure 16. Schematic illustrations of (a) a typical electrochemical cell and (b) a typical voltammogram obtained by CV measurements. Reproduced with permission from Ref.[130] 59
Figure 17. Schematic illustration of the switchable hydrophilicity of the pH-responsive polymer photocatalyst nanoparticles by adjusting the pH of the solvent. 65
Figure 18. pH-responsive photocatalytic nanoparticles. (a) Molecular structure of designed photocatalytic NP-BT-PDPAH$^+$ nanoparticles. (b) TEM image of the nanoparticle dispersion. 66
Figure 19. 1H NMR spectrum of NP-BT-PDPA in THF-d8 (400 MHz, at 298 K). 67
Figure 20. FTIR spectra of photocatalytic monomer Ph_2BTMA (red) and NP-BT-PDPA (blue). 67
Figure 21. Molecular weight distribution of PDPA-co-PPh_2BTMA-b-PBzMA block copolymer (UV signal, Mn = 10359 Da, Đ = 1.52, standard: polystyrene). 68
Figure 22. DLS measurement of NP-BT-PDPAH$^+$ dispersion in acetate buffer solution (pH 4.0, 0.1 mM) with a hydrodynamic diameter peaking at 340 nm and PDI = 0.214. 69
Figure 23. Titration curve of P(DPA-co-Ph_2BTMA) macroCTA. 69

Figure 24. Zeta potential of NP-BT-PDPA dispersion as a function of pH value. 70
Figure 25. Zeta potential of nanoparticle in response to minute change of pH value for 5 cycles. 71
Figure 26. Photographs of (a) NP-BT-PDPAH$^+$ dispersion at pH 4.0 and after tuning the pH of NP-BT-PDPAH$^+$ dispersion to pH 10.0, (c) NP-BT-PDPAH$^+$ dispersion (pH 4.0) and NP-BT-PDPA dispersion (pH 10.0) centrifuged at 4000 rpm for 10 min, (c) redispersion of isolate NP-BT-PDPA nanoparticles to acetate buffer solution (pH 4.0). 71
Figure 27. UV/Vis transmittance of NP-BT-PDPA dispersions as a function of pH value (a) Transmittance of NP-BT-PDPA dispersions from pH 4.0 to pH 10.0 at 700 nm. (b) UV/Vis transmittance spectra of NP-BT-PDPA dispersions from pH 4.0 to pH 10.0. 72
Figure 28. UV/Vis absorbance (blue) and emission (red) spectra. 72
Figure 29. Cyclic voltammogram of Ph2BT with a scan rate of 0.1 V/s of 0.1 M NBu4PF6 in acetonitrile. Due to no smooth film formation on the working electrode and possible oxidation of the PDPA block, the cyclic voltammogram of NP-BT-PDPA polymer could not be measured. However, according to previous studies[68,165] the onset reduction potential of Ph_2BT units before and after incorporation into polymer structures remains at a similar level. Therefore, here we use the onset reduction potential of the Ph_2BT unit to represent the value for the polymer due to the challenges for sample preparation. 73
Figure 30. (a) Photocatalytic reduction of Cr(VI) in NP-BT-DHPA dispersion (pH 4.0), NP-BT-PDPAH$^+$ dispersion (pH 4.0), and without photocatalyst (pH 4.0) under blue LED irradiation (power: 17 mW/cm^2, λ=460 nm). C_0 is the initial concentration of Cr(VI) under dark conditions. C is the concentration of Cr(VI) with light irradiation after a certain time intervals. (b) Reusability of NP-BT-PDPAH$^+$ for repeated reduction of Cr(VI). 75
Figure 31. Detailed kinetic profiles of Cr(VI) reduction : (a) concentration dependence of NP-BT-PDPAH$^+$ on the conversion of the Cr(VI) reduction over time, as well as the effect of atmosphere (N_2 and air). (b) The UV/Vis spectrum of kinetic study at NP-BT-PDPAH$^+$ concentration of 1 mg/mL after degassing as an example. (c) Control experiments without photocatalyst and without light irradiation, (d) Recycling experiment UV/Vis spectra. 77
Figure 32. Sulfide oxidation (a) kinetic profiles of the photocatalytic sulfide oxidation (80 mM) reaction including NP-BT-PDPAH$^+$ as photocatalyst at concentrations of 1, 2.5, and 4 mg/mL. (b) Kinetic study of sulfide (50 mM) oxidation using NP-BT-PDPAH$^+$ (2.5 mg/mL, blue), Ph_2BTMA photocatalyst monomer (dark grey), NP-BT-PDPAH (green) with an identical concentration of photocatalytic units (45 μg/mL), as well as control reaction without photocatalyst (red). Yield determined by GCMS in triplicate. 78
Figure 33. Scavenger tests of sulfoxidation using sodium azide, potassium iodide, isopropanol, copper chloride, and benzoquinone as $^1O_2$, e^-, $\cdot OH$, h^+ and $\cdot O_2^-$ scavenger, respectively. Yield determined by GCMS. 81

Figure 34. Recycling experiment for sulfoxidation determined by GCMS. (a) The result indicates no noticeable decrease in product yield after 4 cycles of reactions. (b) GCMS spectrum of sulfoxidation product after 4th run of reaction. (c) supernatants were collected after each run of reaction (pH 4.0, cycle 1, and cycle 2: centrifugation 7000 rpm, 10 min; cycle 3-4: centrifugation 10000 rpm, 10 min). (d) Transmittance (at 700 nm) of the supernatants of sulfide oxidation recycling tests corresponding to figure (c). (e) FTIR spectra of nanoparticles before and after 4 cycles of repeat experiments. (f) TEM image of nanoparticles after 4 cycles of repeat experiments. 82
Figure 35. Electron paramagnetic resonance (EPR) spin trapping spectra of TEMP-$^1O_2$ generated under different conditions. (a) NP-BT-PDPAH$^+$ (1 mg/ml), Tetramethylpiperidine (TEMP, 0.1 M), O_2 . (b) NP-BT-PDPA (1 mg/ml), TEMP (0.1 M), O_2. (c) TEMP (0.1 M), O_2. (d) NP-BT-PDPAH$^+$ (1 mg/ml), TEMP (0.1 M), N_2. All the samples were irradiated under blue LED for 1 h before measurement. 83
Figure 36. 2-Furoic acid oxidation (a) kinetic profiles of the photocatalytic 2-furoic acid oxidation reaction including NP-BT-PDPA H$^+$ as photocatalyst at concentrations of 1, 2.5, and 4 mg/mL. (b) ^{1}H NMR spectra of the recycling experiments, showing high conversion of 2-furoic acid oxidation. (c) Recycling experiment for 2-furoic acid oxidation determined by ^{1}H NMR spectroscopy (700 MHz, at 298 K). The result illustrates no noticeable decrease in product yield after 5 cycles of 24 h reactions. 85
Figure 37. 2-furoic acid oxidation (a) Supernatants collected after each run of reaction (pH 4.0, cycle 1-4: centrifugation 7000 rpm, 10 min. (b) Transmittance (at 700 nm) of the supernatants of 2-furoic acid oxidation recycling tests corresponding to figure (a). (c) FTIR spectra of nanoparticles before and after 5 cycles of 24 h repeating photocatalysis experiments. (d) TEM image of nanoparticles after 5 cycles of repeat experiments. 86
Figure 38. Proposed mechanism in the literature[189] of photocatalyzed alkylation in the absence of oxygen. 89
Figure 39. Scheme of the magnetic-responsive photocatalytic hybrid materials and their easy recycling. 99
Figure 40. ^{1}H NMR spectrum of the POEGA-s-EY-b-PCEA diblock copolymer. 100
Figure 41. GPC measurement of the POEGA-s-EY-b-PCEA diblock copolymer (solvent: DMF and standard: PMMA). 100
Figure 42. XRD spectra of polymer coated Fe_3O_4 nanoparticles at [polymer] : [Fe_3O_4] weight ratio of 2 and bare Fe_3O_4 nanoparticles. 101
Figure 43. FTIR spectra of Fe_3O_4 nanoparticles with (red) and without (black) photocatalytic polymer coatings. 102
Figure 44. TEM images of photocatalytic polymer stabilized Fe_3O_4 nanoparticles. 103

Figure 45. Thermo-grams for heating the pristine Fe_3O_4 nanoparticles and Fe_3O_4 nanoparticles coated with polymer chains (Fe_3O_4@POEGA-s-EY) from 25 °C to 800 °C.. 103
Figure 46. GCMS analysis of the methyl phenyl sulfide oxidation using photocatalytic polymer stabilized Fe_3O_4 nanoparticles Fe_3O_4@POEGA-s-EY..... 104
Figure 47. GCMS analysis of the methyl phenyl sulfide oxidation using free photocatalytic polymer and Fe_3O_4 nanoparticles mixture. 104
Figure 48. ^{1}H NMR spectrum of the POEGA-s-EY-b-PBzMA diblock copolymer. 105
Figure 49. GPC measurement of the POEGA-s-EY-b-PBzMA diblock copolymer. 106
Figure 50. UV-Vis absorbance (black) and emission (red) spectra of POEGA-s-EY-b-PBzMA in DMSO. 106
Figure 51. Illustration of surface modification process for iron nanoparticles. Initially, the pristine Fe nanoparticles were immobilized with hydrophobic TCDS molecules. Secondly, these hydrophobic Fe nanoparticles namely Fe@TCDS were encapsulated in photocatalytic polymers by ultrasonication tip and solvent evaporation procedure, generating a hybrid material with photocatalytic polymer coating on the surface of the magnetic Fe nanoparticles. 107
Figure 52. FTIR spectra of pristine iron nanoparticles (black), iron nanoparticles with silane ligands Fe@TCDS (blue), and iron nanoparticles encapsulated in photocatalytic polymer chains (red). 108
Figure 53. TEM images of (a) pristine iron nanoparticles and (b) encapsulated in polymer chains. 109
Figure 54. Thermo-grams for heating the pristine Fe nanoparticles and Fe nanoparticles coated with photocatalytic polymer chains (Fe@POEGA-s-EY-b-PBzMA) from 25 °C to 1000 °C..... 109
Figure 55. GCMS analysis of the methyl phenyl sulfide oxidation using photocatalytic polymer encapsulated Fe nanoparticles Fe@POEGA-s-EY-b-PBzMA. 110
Figure 56. FTIR spectra of magnetite nanoparticles with silane ligands Fe_3O_4@TCDS (black), and magnetite nanoparticles encapsulated in photocatalytic polymer chains (magnetite : polymer ratio = 1:2 in red, magnetite : polymer ratio = 1:3 in blue)..... 111
Figure 57. Thermo-grams for heating the pristine Fe_3O_4 nanoparticles and Fe_3O_4 nanoparticles coated with photocatalytic polymer chains (Fe_3O_4 @POEGA-r-EY-b-PBzMA) from 25 °C to 800 °C. 112
Figure 58. TEM images of magnetite nanoparticles with different surface treatments. (a-c) pristine magnetite nanoparticles dispersed in DIW; (d-f) magnetite nanoparticles modified with hydrophobic trichlorododecyl silane (dispersed in DCM); (g-i) magnetite nanoparticles encapsulated in photocatalytic polymers (dispersed in DIW). 113

Figure 59. Image of magnetite dispersions before and after the modifications: pristine magnetite nanoparticle dispersion in DIW (right), magnetite nanoparticles modified with TCDS Fe_3O_4@TCDS (middle), and magnetite nanoparticles encapsulated with photocatalytic polymers (left). 114
Figure 60. Images of the recycling process of magnetic-responsive photocatalytic hybrid materials. 114
Figure 61. A representative GCMS spectrum of the methyl phenyl sulfide oxidation using photocatalytic polymer encapsulated Fe_3O_4 nanoparticles Fe_3O_4@POEGA-s-EY-b-PBzMA. 115
Figure 62. Fe_3O_4@POEGA-s-EY-b-PBzMA catalyzed hydroxylation of phenylboronic acid pinacol ester. (a) Kinetic profiles of the phenylboronic acid pinacol ester hydroxylation in the presence of magnetic photocatalytic nanoparticles and control reactions (without photocatalyst in light and with photocatalyst in dark). (b) Repeated cycles of hydroxylation reactions using Fe_3O_4@POEGA-s-EY-b-PBzMA as a recyclable photocatalyst and the recycling test was carried out with 6 h of blue light irradiation for each cycle. 118
Figure 63. Proposed mechanism in the literature[194] of photocatalyzed hydroxylation in the presence of oxygen. 119
Figure 64. Schematic illustration of the switchable hydrophilicity of the pH-responsive polymer photocatalyst nanoparticles responding to the subtle pH change from the bloodstream (pH 7.4) to the tumor extracellular microenvironment (pH 6.5). The activated photocatalytic polymer chains after disassembly can further activate the prodrug into active therapeutics, leading to targeted cancer treatment. 128
Figure 65. Chemical structure of the pH-responsive triblock photocatalytic copolymers: (a) PEG_{113}-b-$PAEMA_{50}$-b-$EYAMA_1$ and (b) PEG_{113}-b-$PAEMA_{50}$-b-$EYHEMA_1$ 129
Figure 66. ^1H NMR spectrum of the PEG_{113}-b-$PAEMA_{50}$-b-$EYAMA_1$ triblock copolymer. .. 130
Figure 67. ^1H NMR spectrum of the PEG_{113}-b-$PAEMA_{50}$-b-$EYHEMA_1$ triblock copolymer. 130
Figure 68. GPC analysis of the (a) PEG_{113}-b-$PAEMA_{50}$-b-$EYAMA_1$ and (b) PEG_{113}-b-$PAEMA_{50}$-b-$EYHEMA_1$ triblock copolymers. 131
Figure 69. FTIR spectrum of the PEG_{113}-b-$PAEMA_{50}$-b-$EYAMA_1$ and PEG_{113}-b-$PAEMA_{50}$-b-$EYHEMA_1$ triblock copolymers. 132
Figure 70. UV/Vis absorbance and emission spectra of the (a) PEG_{113}-b-$PAEMA_{50}$-b-$EYAMA_1$ and (b) PEG_{113}-b-$PAEMAH^+_{50}$-b-$EYHEMA_1$ in DMSO (1 mg/mL) triblock copolymers in phosphate buffer (pH 6.5, 1 mg/mL). 132
Figure 71. The hydrodynamic diameter of NP-PAEMA changes as a function of pH value measured by DLS. 133

Figure 72. (A) UV/Vis transmittance of NP-PAEMA dispersions as a function of pH value from pH 6.0 to pH 7.8 at 700 nm. (B) Image of the corresponding NP-PAEMA dispersions in phosphate buffer solutions with pH values varying from pH 6.0 to pH 7.8. 134
Figure 73. Titration curve of PEG_{113}-b-$PAEMA_{50}$ polymer chains in DIW (PEG_{113}-b-$PAEMA_{50}$ concentration 5 mg/mL and NaOH concentration 0.1 M). 135
Figure 74. TEM images of NP-PAEMA-EYHEMA dispersion in phosphate buffer (0.1 mM) at pH 7.4 and pH 6.5. 135
Figure 75. Electron paramagnetic resonance (EPR) spin trapping spectra of TEMP $^1O_2$ generated under different conditions. (a) Eosin Y disodium salt (1 mg/mL), tetramethylpiperidine (TEMP, 0.1 M), O_2. (b) Eosin Y disodium salt (1 mg/mL), TEMP (0.1 M), air. (c) TEMP (0.1 M), O_2. (d) Eosin Y disodium salt (1 mg/mL), TEMP (0.1 M), O_2, dark. All the samples were irradiated under blue LED for 30 min before measurement. 136
Figure 76. Prodrug model compounds activation using eosin Y disodium salt (5 mol%) loading for all reactions. (a) Kinetic profile of boronic acid pinacol ester activation, using sodium ascorbate as sacrificing agent. Conversion determined by GCMS. (b) Kinetic profile of thiol ketal activation without additive. Conversion determined by ^{1}H NMR spectroscopy. (c) Kinetic profile of aminoacrylate activation without additive. Conversion determined by GCMS. (d) GPC monitored the degradation of oxalate-based model polymer using either PBS or DMSO-d_6 as solvent, as well as Pr_2NEt_2 as sacrificing agent. 137
Figure 77. Prodrug model compound activation kinetic profile using PEG_{113}-b-$PAEMAH^+_{50}$-b-$EYHEMA_1$ polymeric photocatalyst (2.5 mol%) solution in phosphate buffer solution at pH 6.5 (black). Control reactions: without photocatalyst in light (green) and with photocatalyst in dark (blue). 139
Figure 78. The controlled activation kinetic profile of prodrug model compound using PEG_{113}-b-$PAEMAH^+_{50}$-b-$EYHEMA_1$ polymeric photocatalyst (2.5 mol%) solution in phosphate buffer solution at pH 6.5 (black) and NP-PAEMA-EYHEMA in PBS buffer at pH 7.4 (red). Control reactions: without photocatalyst in light (green) and with photocatalyst in dark (blue). 140
Figure 79. ^{19}F-NMR spectrum of the activation of 5FU prodrug (40 mM) using PEG_{113}-b-$PAEMAH^+_{50}$-b-$EYHEMA_1$ polymeric photocatalyst (2.5 mol%) solution in phosphate buffer solution at pH 6.5 (the reference peak at -113 ppm was from fluorobenzene). 142
Figure 80. The viability of HCT116 cancer cells treated with varying concentrations of prodrug, PEG_{113}-b-$PAEMAH^+_{50}$-b-$EYHEMA_1$ (shortened as EY), the combination of prodrug and PEG_{113}-b- $PAEMAH^+_{50}$-b-$EYHEMA_1$ before and after blue light LED irradiation. The cells were treated for 72 h with the indicated concentrations of the compounds. Data are presented as mean ± S.D, n = 5. 143

Figure 81. ^{1}H NMR spectra of the activation of polyprodrug PEG-b-PAEMA-s-PCPT using PEG_{113}-b-$PAEMA_{50}$-b-$EYHEMA_{1}$ polymeric photocatalyst solution in $CDCl_3$ before and after 3 hours of light irradiation, respectively. 145
Figure 82. NMR spectrum of PEG_{113}-b-P(AMA_{50}-s-Ph_2BTMA_1) copolymer (not purified). . 158
Figure 83. GPC spectrum of PEG_{113}-b-P(AMA_{50}-s-Ph_2BTMA_1) copolymer..... 158
Figure 84. UV/Vis absorbance (black) and photoluminescence (red) spectra of PEG_{113}-b-P(AMA_{50}-s-Ph_2BTMA_1) copolymer..... 159
Figure 85. Illustration of the reversible crosslinking-cleavage process that the photocatalytic polymers with primary amine groups are crosslinked with the aldehyde groups in TPA according to the pH conditions. 159
Figure 86. TEM image of the crosslinked photocatalytic nanoparticles dispersed in PBS at pH 7.4. 160
Figure 87. The hydrodynamic diameter of the nanoparticles dispersed in various phosphate buffers from pH 7.4 to 6.4, measured by DLS. 161
Figure 88. FTIR spectra of the crosslinked photocatalytic nanoparticles at pH 7.4, pH 6.4 and free polymers. 162
Figure 89. Solid-state NMR spectra of the crosslinked photocatalytic nanoparticles dispersed in PBS at pH 7.4, phosphate buffer at pH 6.4 and free polymers. 163
Figure 90. (A) UV-Vis spectra of the crosslinked photocatalytic nanoparticles dispersed in PBS at pH 7.4 and phosphate buffer at pH 6.4 for the degradation of rhodamine B. (B) Digital image of the rhodamine B degradation reaction mixtures after 15 h of light irradiation. 164
Figure 91. Kinetic profile of the crosslinked photocatalytic nanoparticles dispersed in PBS at pH 7.4 and phosphate buffer at pH 6.4 for the oxidation of NADH..... 165
Figure 92. NMR spectra stacking of the kinetic study of NADH + luminol + HRP +H_2O_2 without enhancer..... 166
Figure 93. NMR spectrum stacking of the kinetic study of NADH oxidation added with luminol + HRP +H_2O_2 + 4-IP, 4-IP was added to the reaction mixture described previously. 167
Figure 94. NMR spectrum stacking of the kinetic study of NADH oxidation added with luminol + HRP +H_2O_2 + 4-IP + photocatalyst..... 168

A2. List of Tables

Table 1. Photocatalytic sulfoxidation using NP-BT-PDPA in either pH 4.0 or pH 9.0 buffer medium. Reactions were undertaken under blue LED light irradiation (power: 17 mW/cm2, λ=460 nm). 79
Table 2. Control experiments of the photocatalytic sulfoxidation 80
Table 3. Control experiments of the photocatalytic 2-furoic acid oxidation 84
Table 4. Control experiments of the photocatalytic Friedel-Crafts alkylation 88
Table 5. The oxidative hydroxylation of alkylboronic acids with various substitutes under different conditions. 117
Table 6. Summary of the activation of ROS-sensitive prodrug model molecules by molecular eosin Y disodium salt. 138

A3. ^{1}H and ^{13}C NMR spectra

^{1}H NMR spectrum (400 MHz, THF) of 4-(7-phenylbenzo[1,2,5]thiadiazol-4-yl)benzyl methacrylate

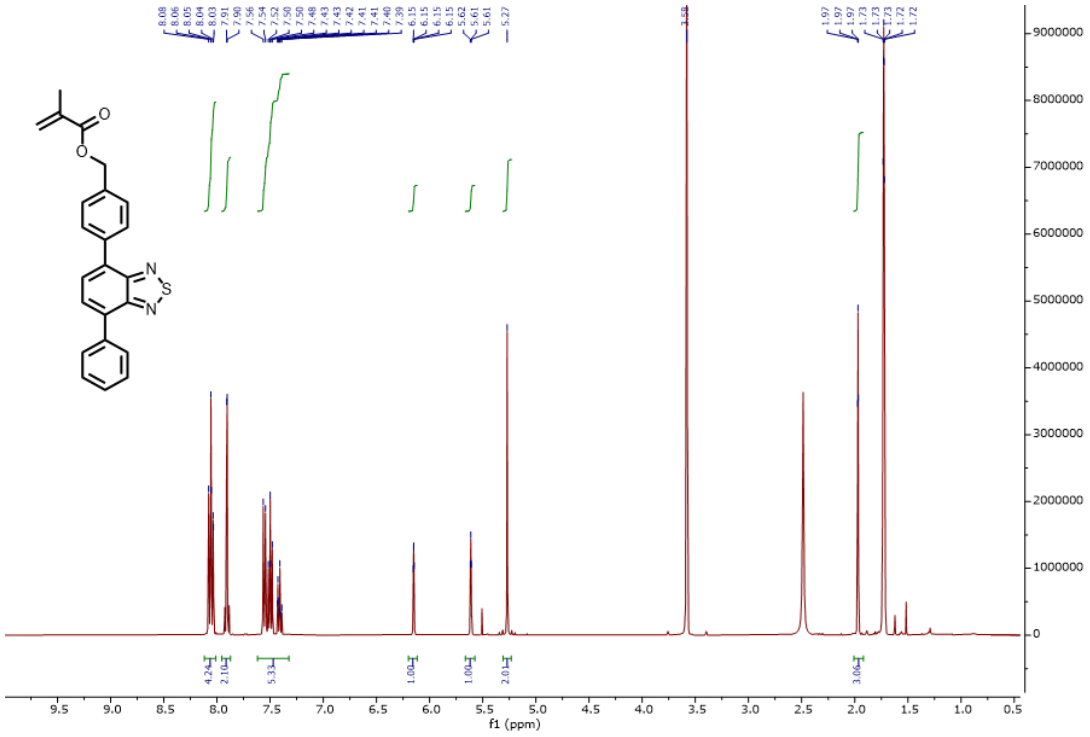

^{13}C-{^{1}H} NMR spectrum (101 MHz, THF) of 4-(7-phenylbenzo[1,2,5]thiadiazol-4-yl)benzyl methacrylate

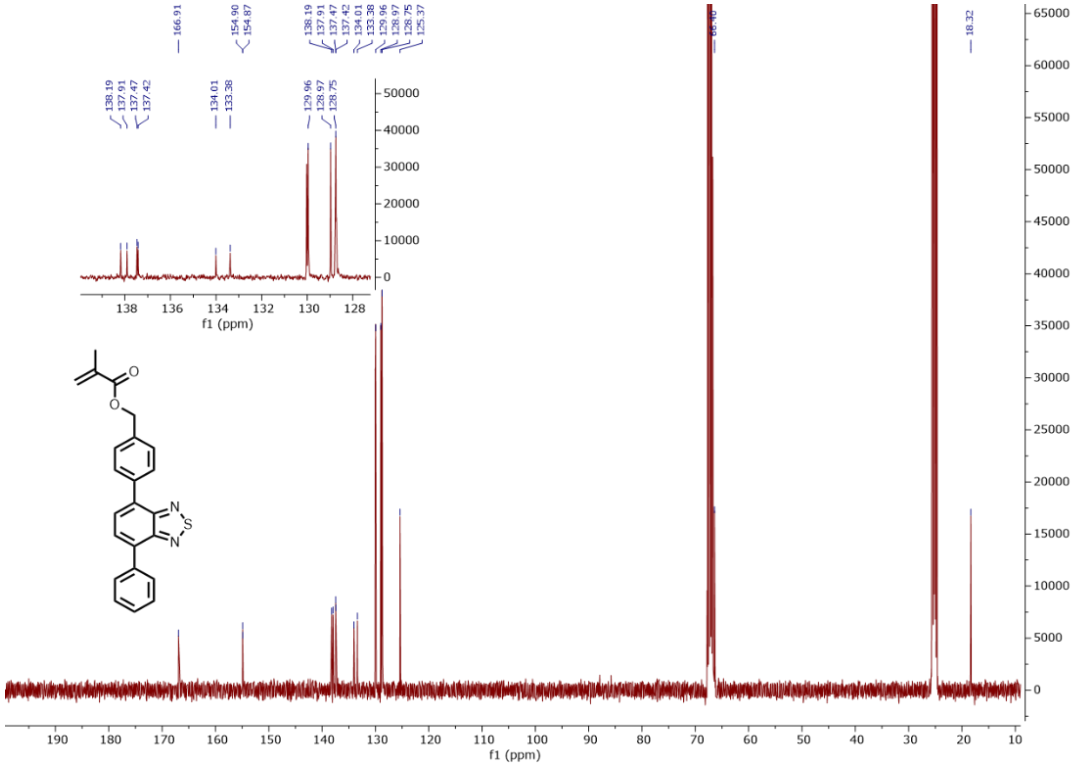

^{1}H NMR spectrum (400 MHz, $CDCl_3$) of 1-methyl-4-(methylsulfonyl)benzene

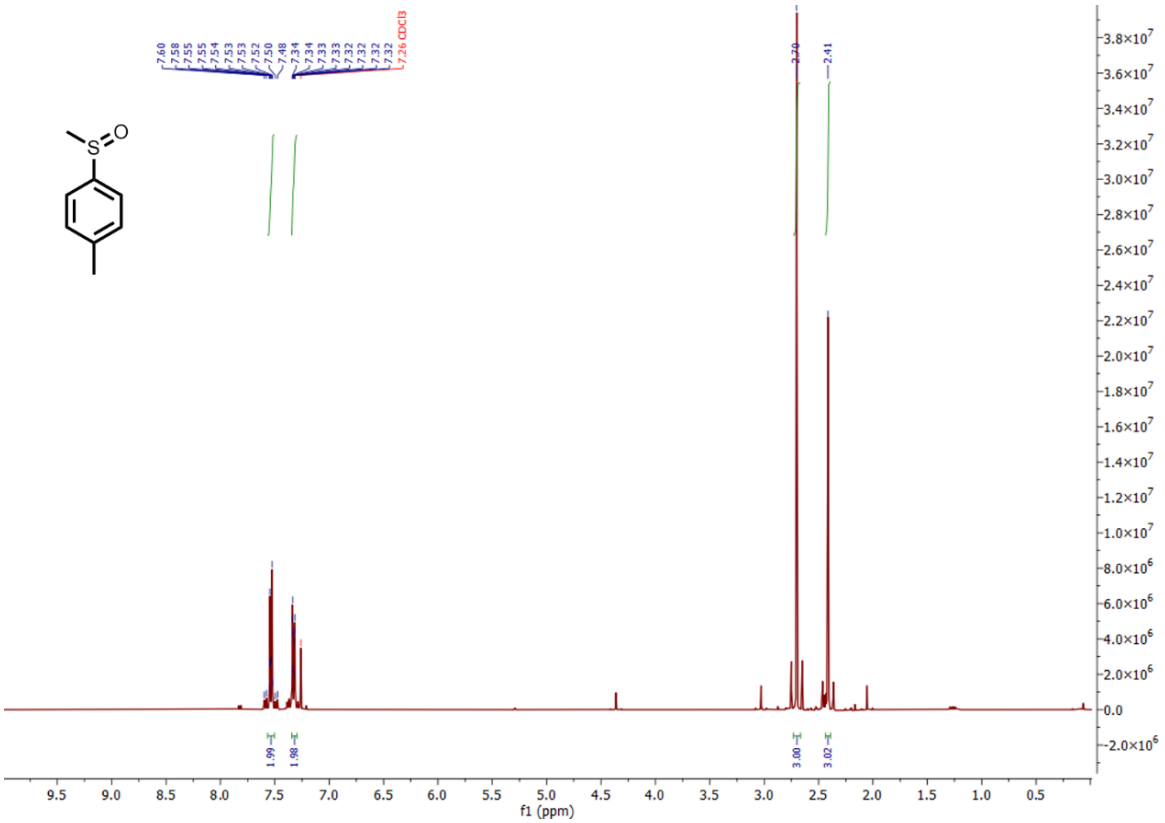

^{13}C-{^{1}H} NMR spectrum (101 MHz, $CDCl_3$) of 1-methyl-4-(methylsulfonyl)benzene

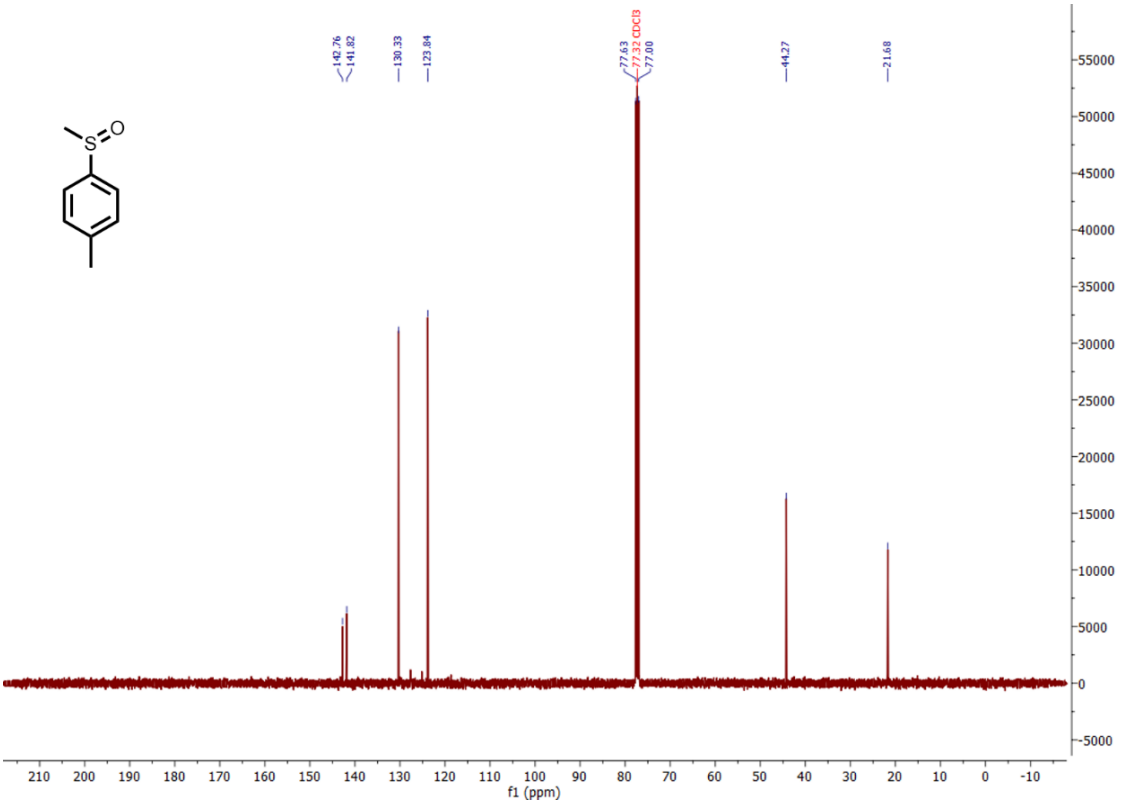

^{1}H NMR spectrum (400 MHz, $CDCl_3$) of 5-hydroxyfuran-2(5H)-one

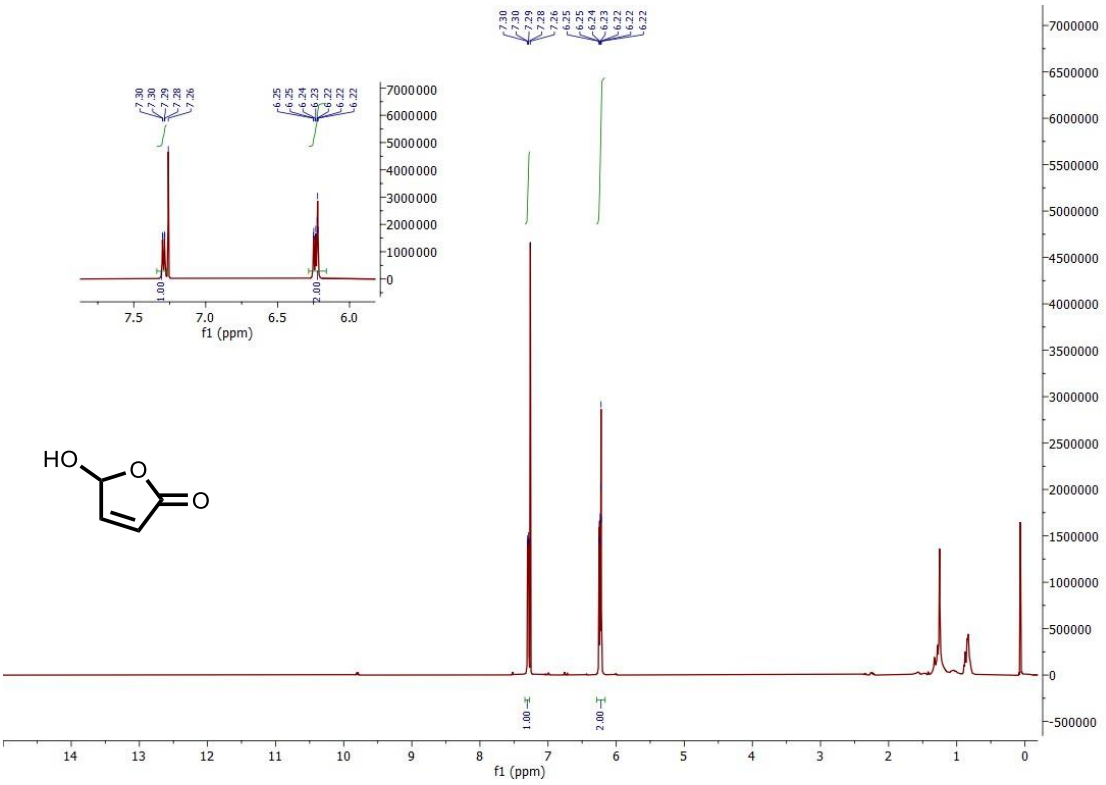

^{13}C-{^{1}H} NMR spectrum (101 MHz, $CDCl_3$) of 5-hydroxyfuran-2(5H)-one

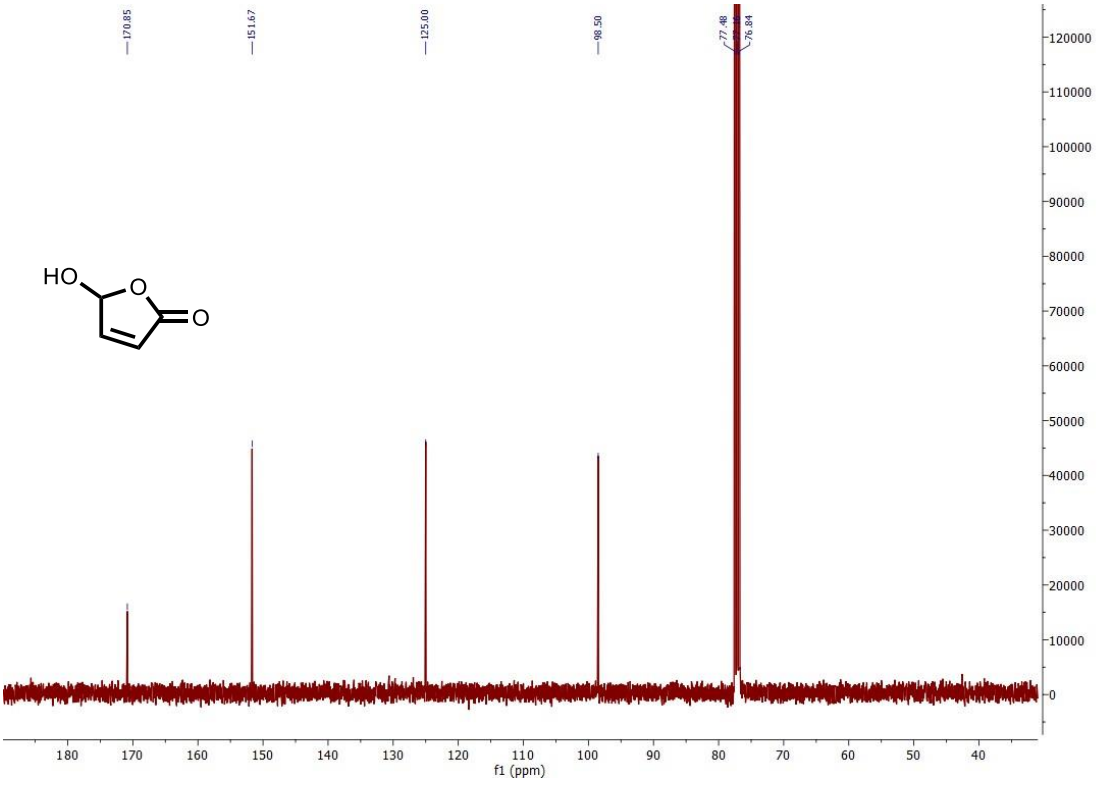

^{1}H NMR spectrum (400 MHz, $CDCl_3$) of 3-methyl-2-(2-nitro-1-phenylethyl)-1H-indole

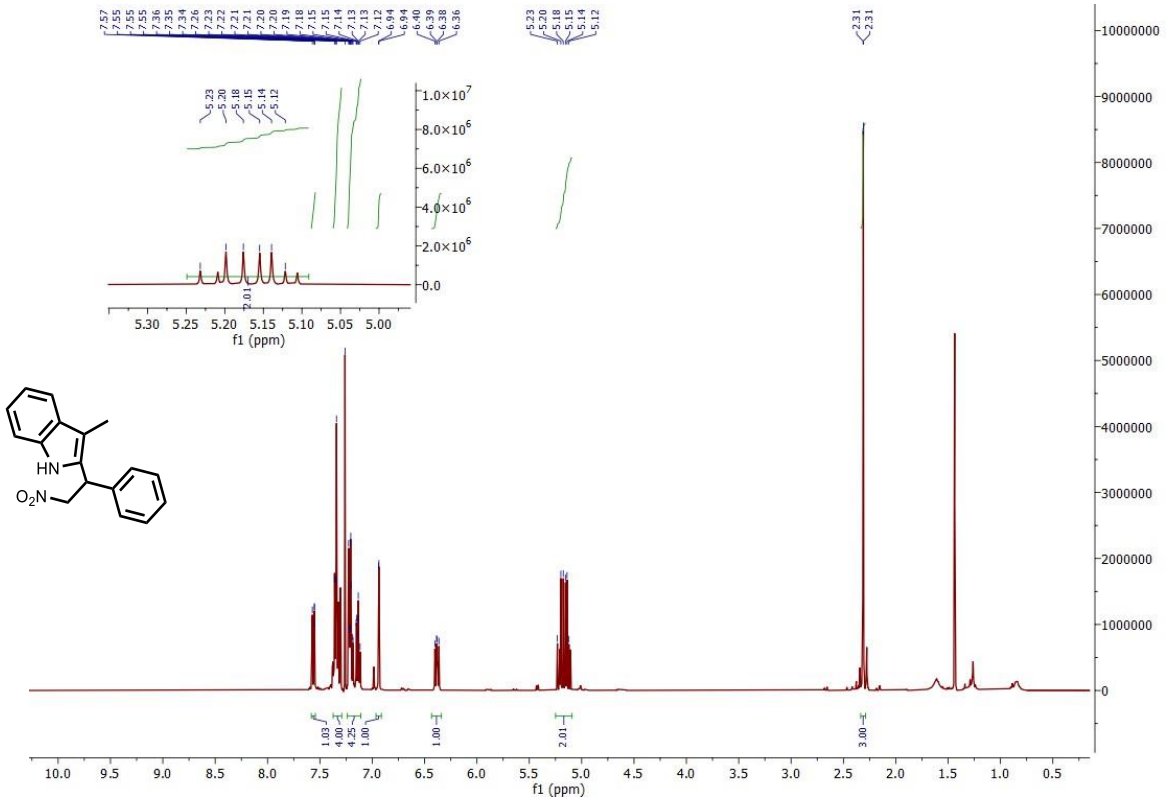

^{13}C-{^{1}H} NMR spectrum (101 MHz, $CDCl_3$) of 3-methyl-2-(2-nitro-1-phenylethyl)-1H-indole

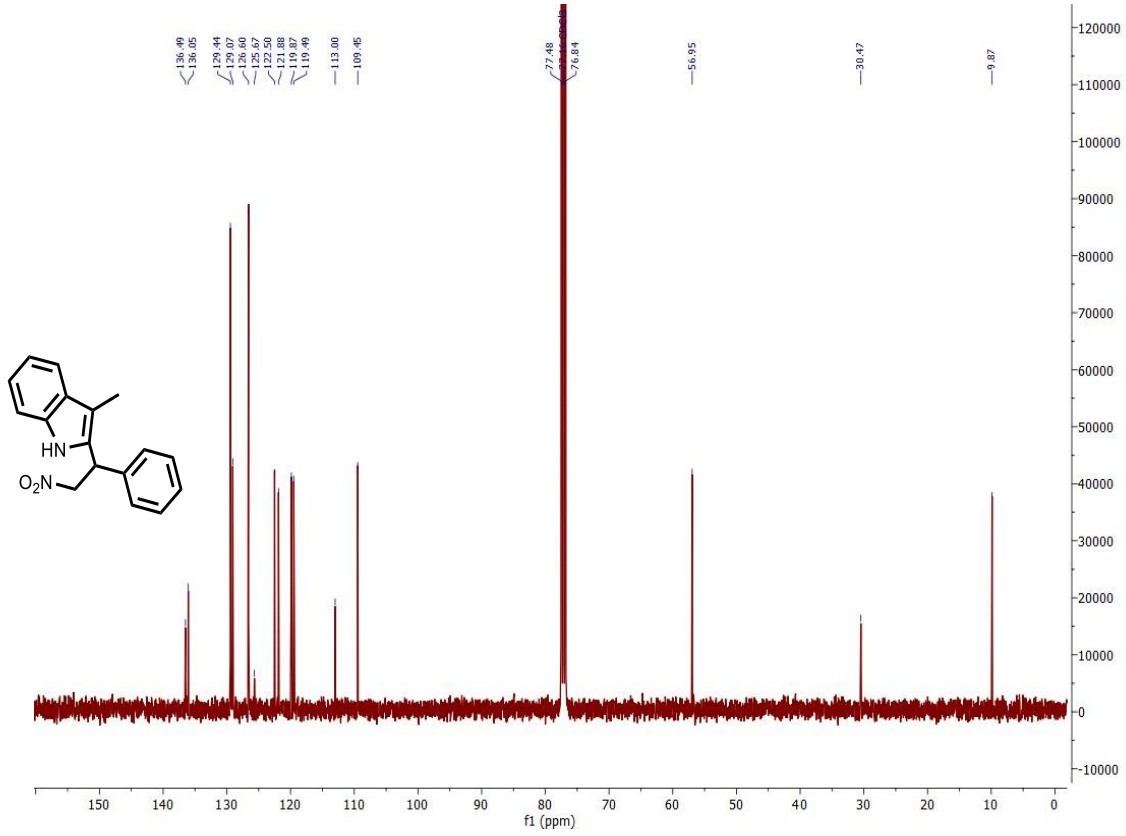

^{1}H NMR spectrum (400 MHz, $CDCl_3$) of 2-(azepan-1-yl)ethyl methacrylate

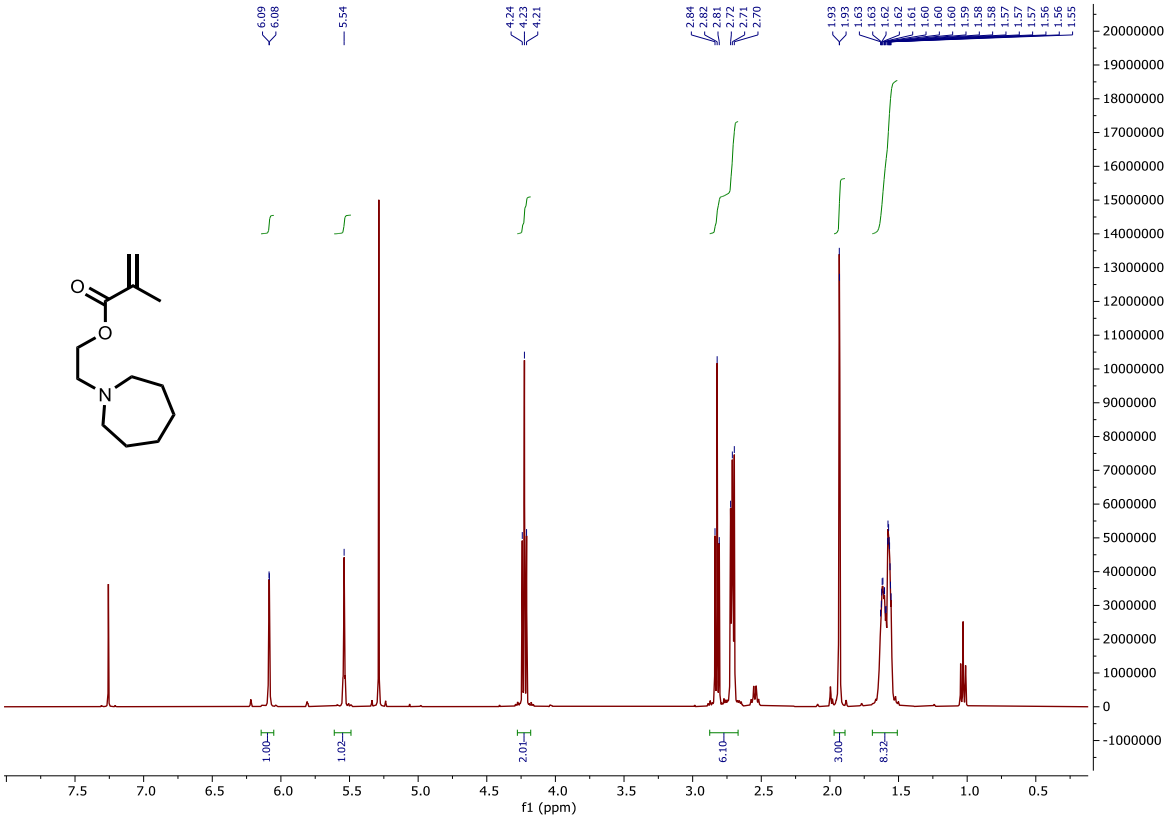

^{13}C-{^{1}H} NMR spectrum (101 MHz, $CDCl_3$) of 2-(azepan-1-yl)ethyl methacrylate

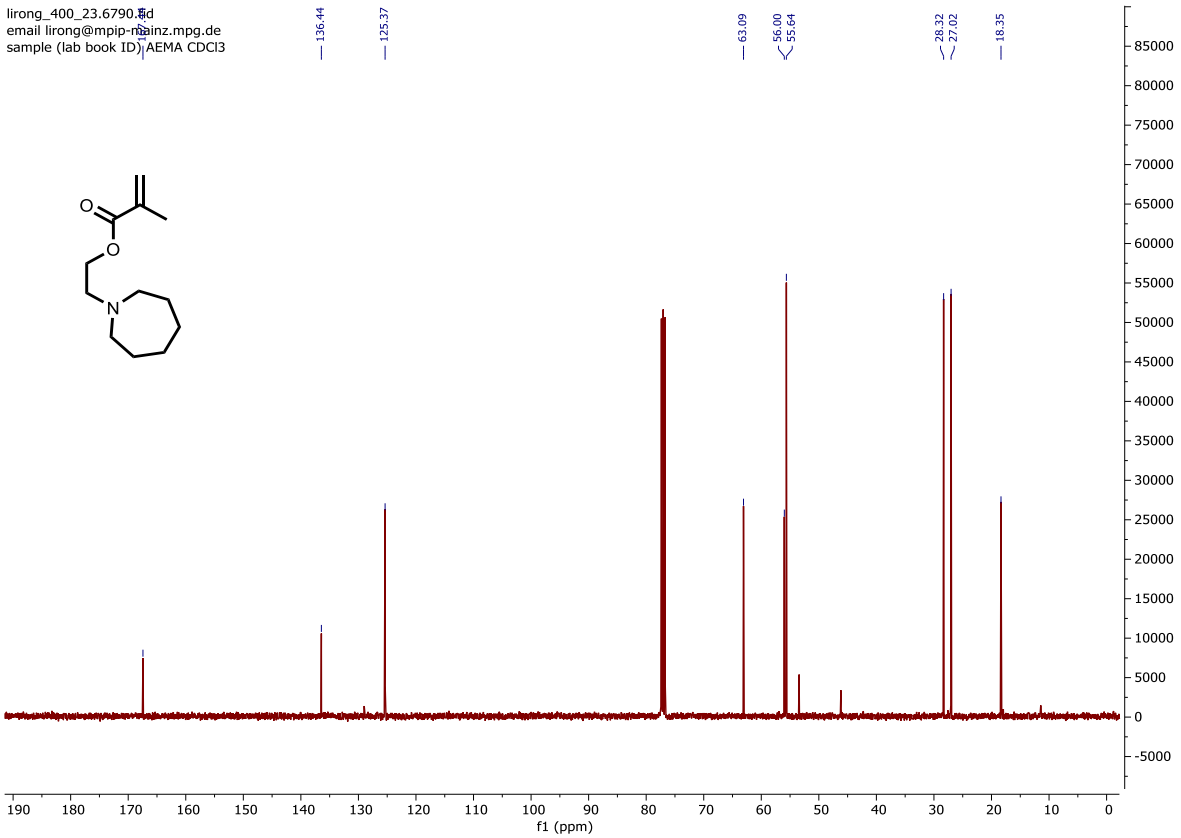

^{1}H NMR spectrum (400 MHz, $CDCl_3$) of thiol ketal

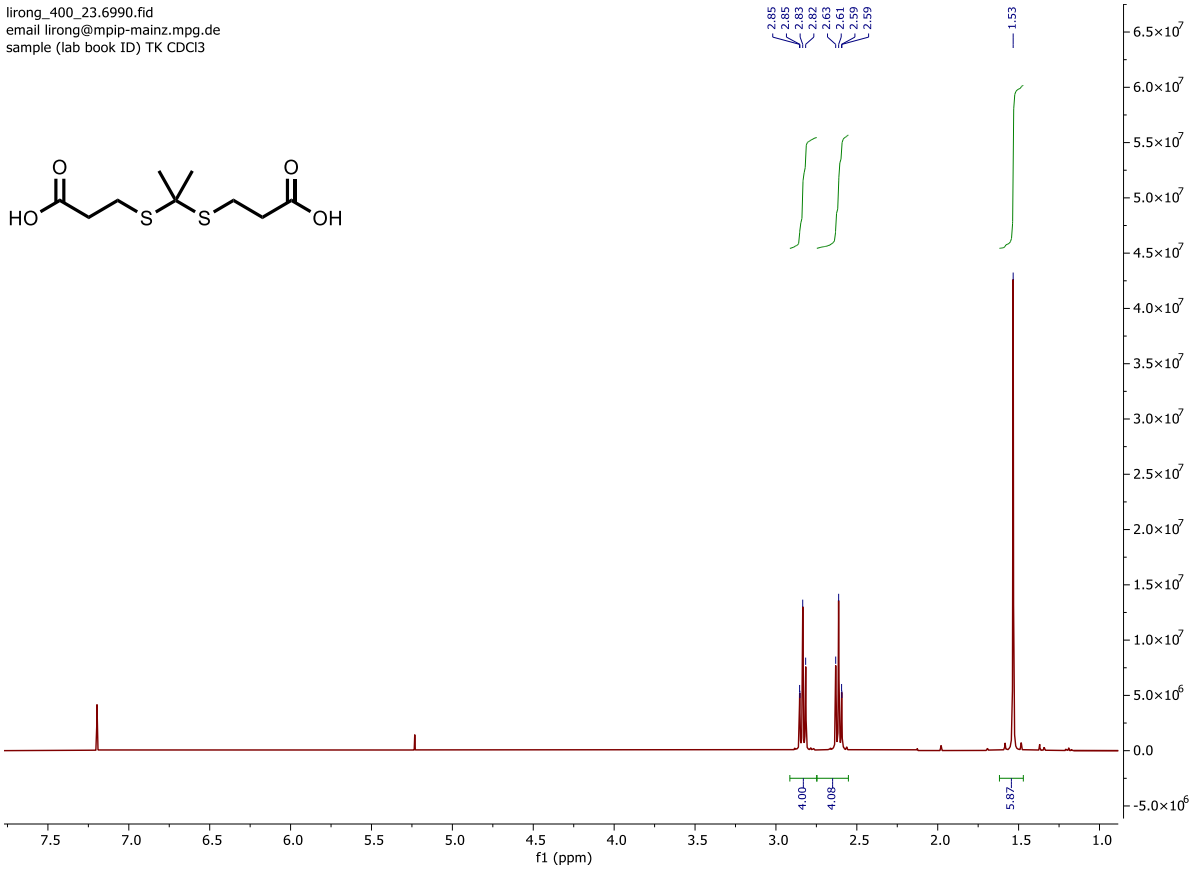

^{13}C-{^{1}H} NMR spectrum (101 MHz, $CDCl_3$) of thiol ketal

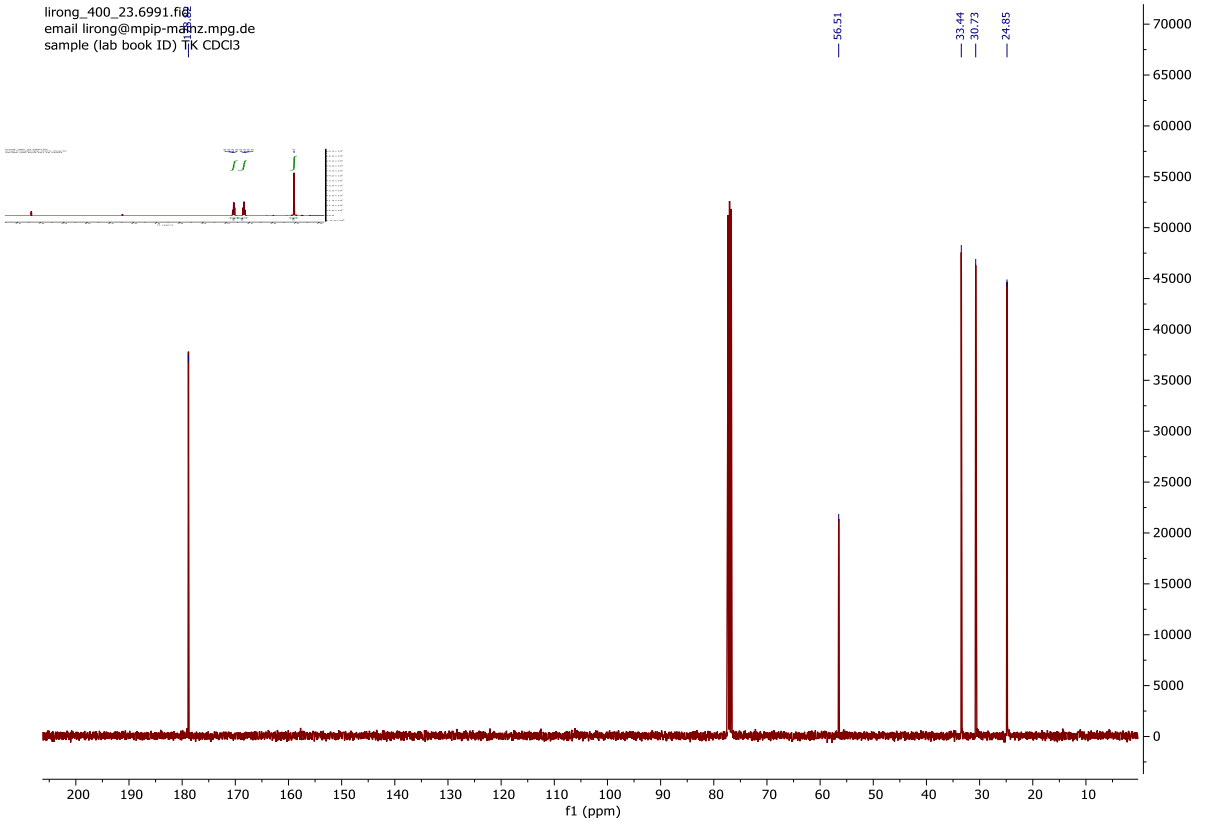

^{1}H NMR spectrum (400 MHz, $CDCl_3$) of ethyl 3-(piperidin-1-yl)acrylate

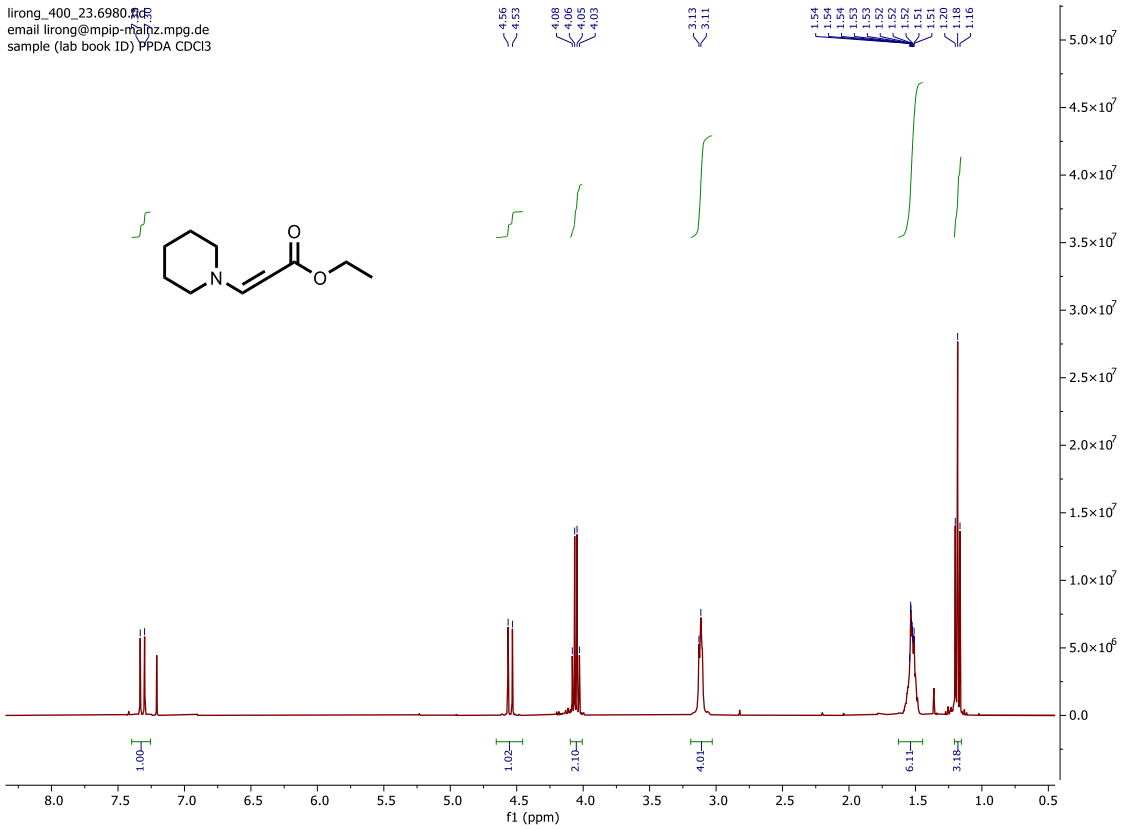

^{13}C-{^{1}H} NMR spectrum (101 MHz, $CDCl_3$) of ethyl 3-(piperidin-1-yl)acrylate

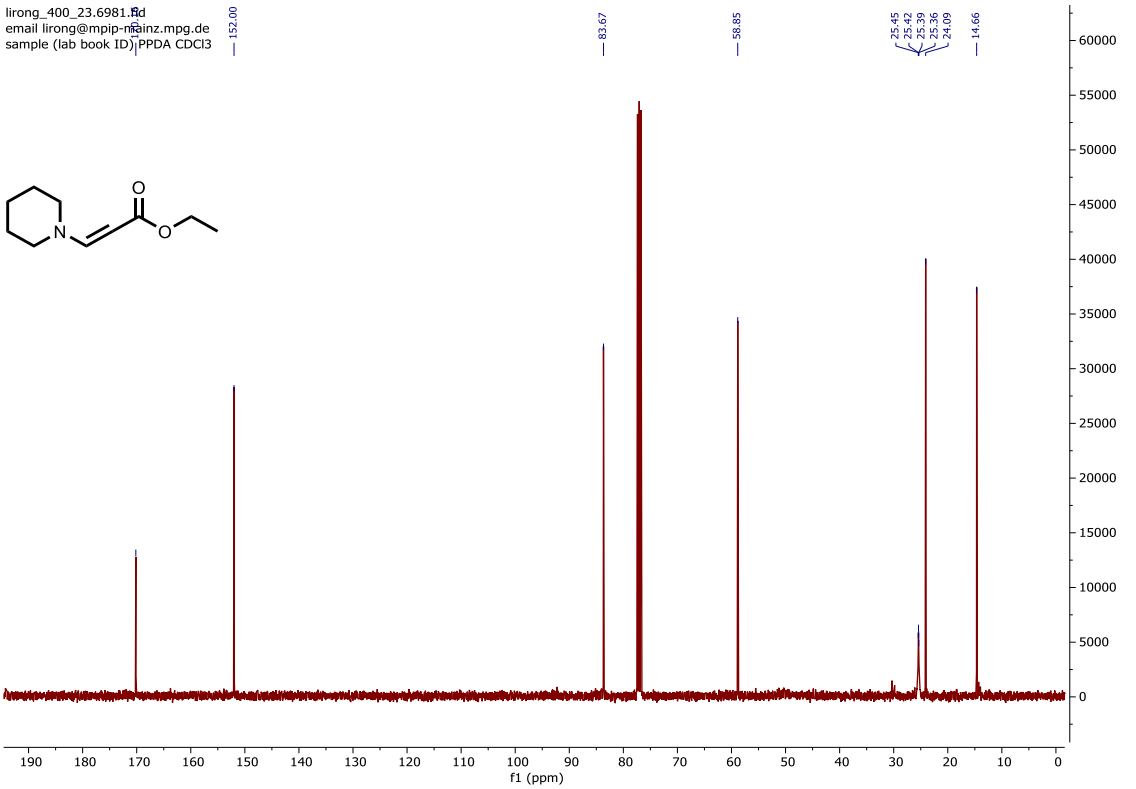

^{1}H NMR spectrum (400 MHz, $CDCl_3$) of Pro-CPT

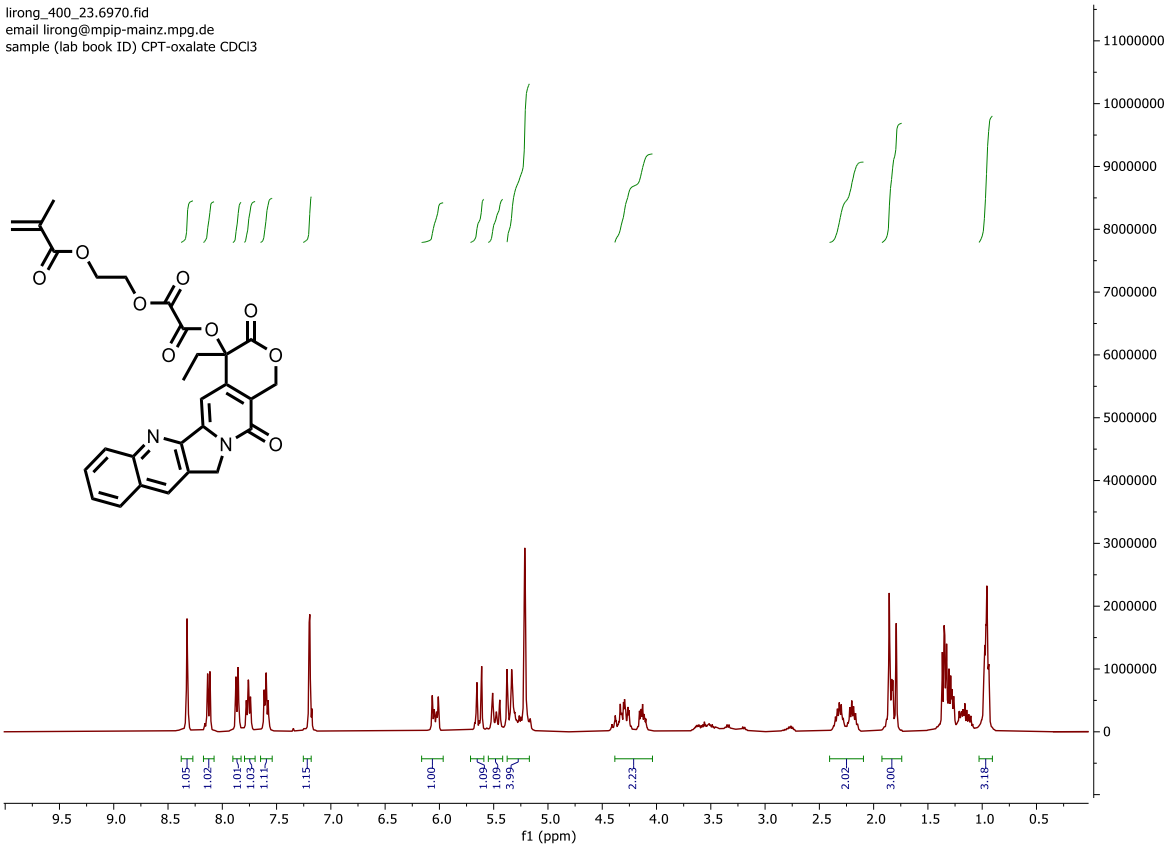

^{13}C-{^{1}H} NMR spectrum (101 MHz, $CDCl_3$) of Pro-CPT

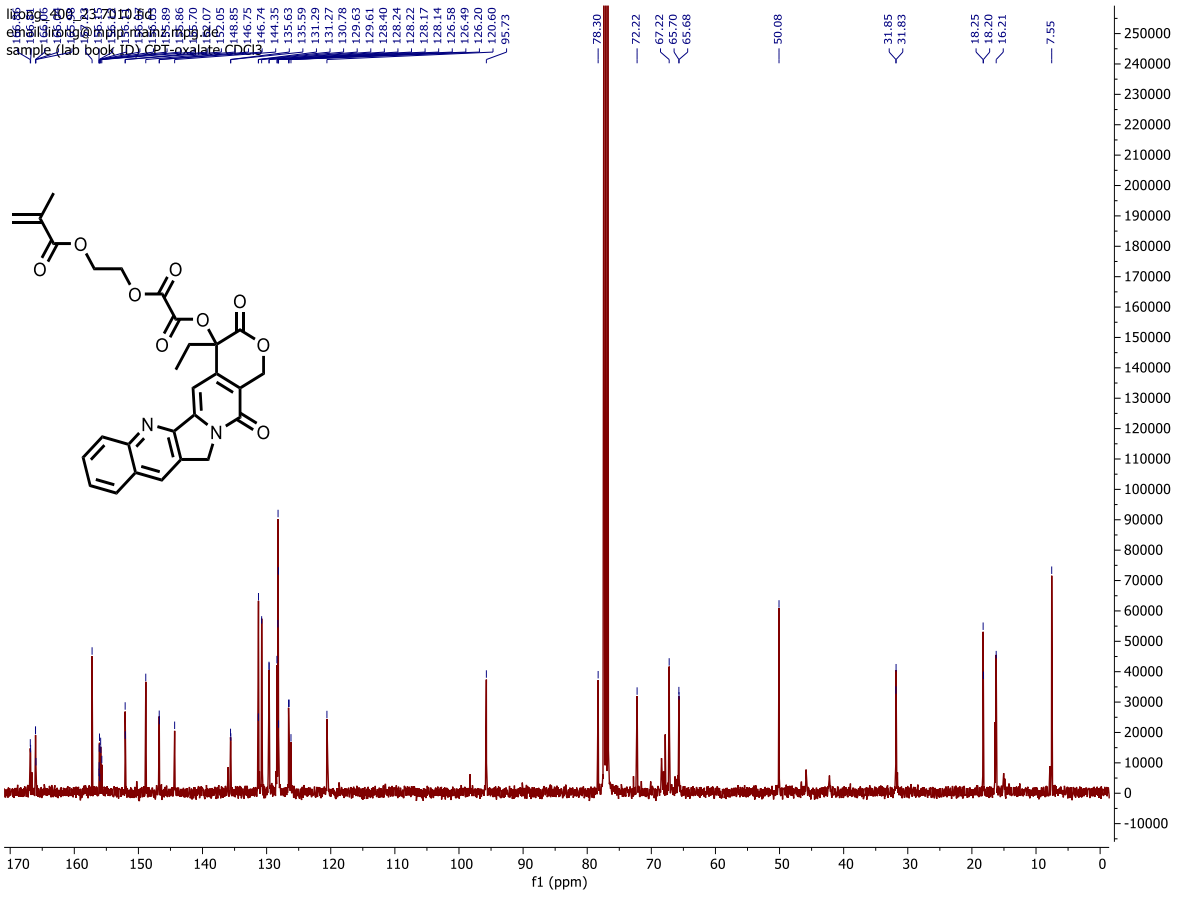

^{1}H NMR spectrum (400 MHz, $CDCl_3$) of Pro-FU

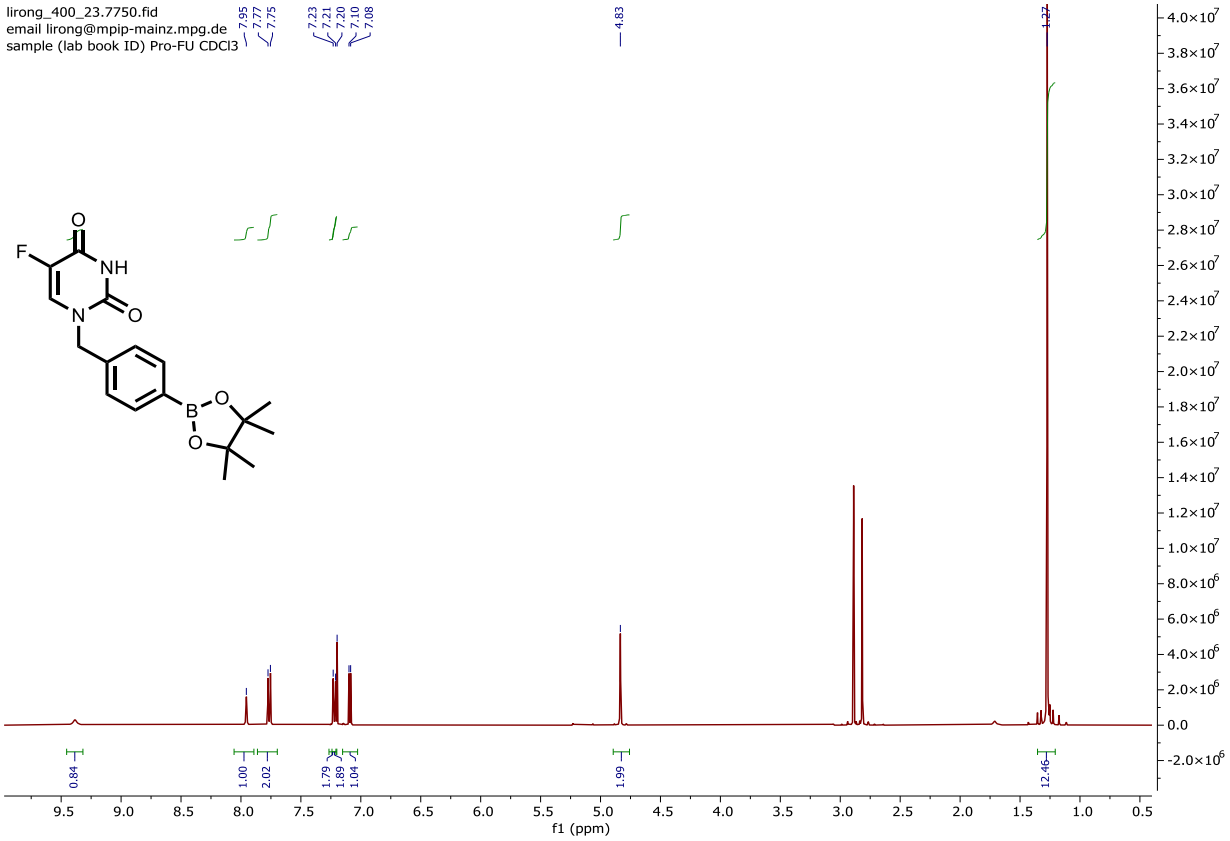

^{13}C-{^{1}H} NMR spectrum (101 MHz, $CDCl_3$) of Pro-FU

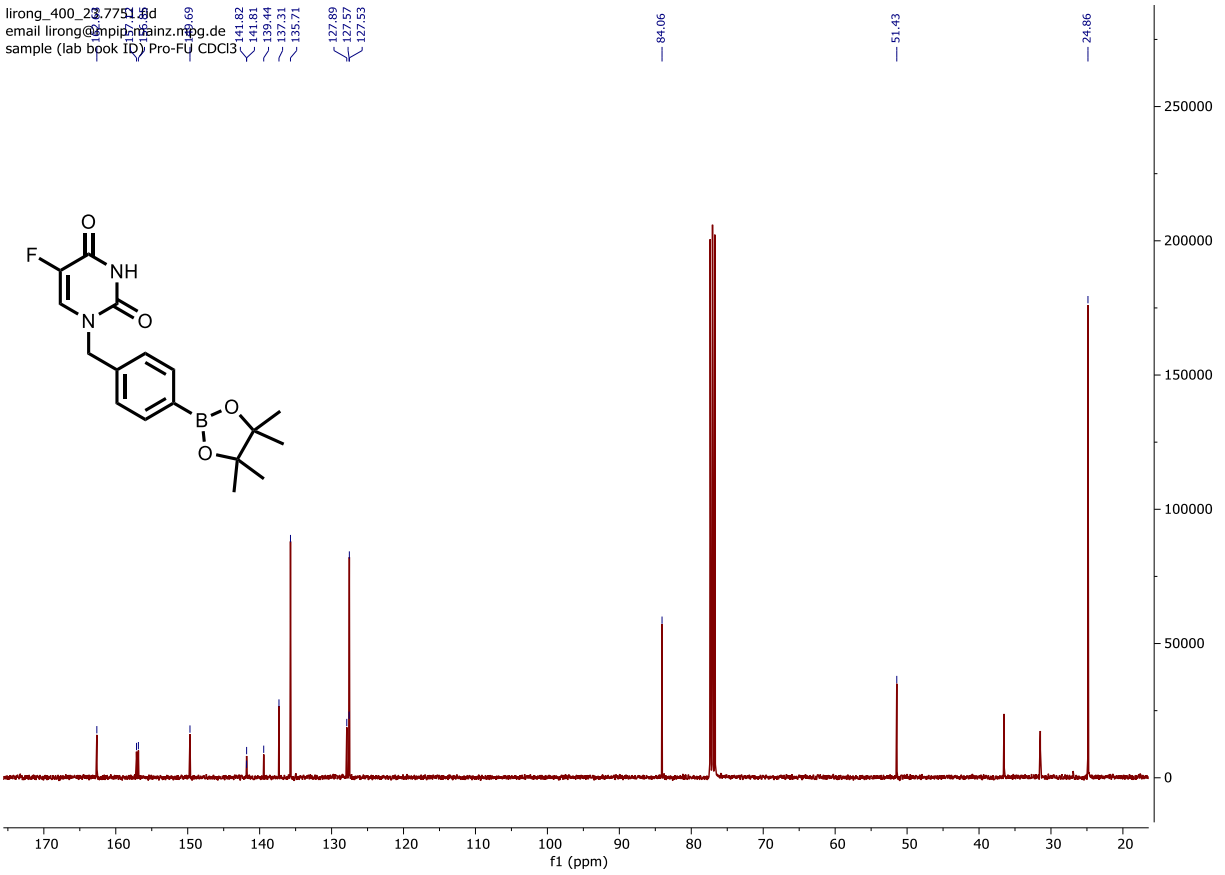

A4. Reference

[1] F. T. Geldasa, in *Solar PV Panels - Recent Advances and Future Prospects*, IntechOpen, **2022**.

[2] M. Hasanuzzaman, M. A. Islam, N. A. Rahim, Y. Yanping, in *Energy for Sustainable Development* (Eds.: MD. Hasanuzzaman, N.A. Rahim), Academic Press, **2020**, pp. 41–87.

[3] N. S. Lewis, *Chem. Rev.* **2015**, *115*, 12631–12632.

[4] T. Banerjee, F. Podjaski, J. Kröger, B. P. Biswal, B. V. Lotsch, *Nat Rev Mater* **2021**, *6*, 168–190.

[5] C. T. J. Ferguson, K. A. I. Zhang, *ACS Catal.* **2021**, *11*, 9547–9560.

[6] Z. Wang, H. Song, H. Liu, J. Ye, *Angewandte Chemie International Edition* **2020**, *59*, 8016–8035.

[7] A. Fujishima, K. Honda, *Nature* **1972**, *238*, 37–38.

[8] J. Coronado, *Green Energy and Technology* **2013**, *71*, 1–4.

[9] F. E. Osterloh, *ACS Energy Lett.* **2017**, *2*, 445–453.

[10] X. Yang, D. Wang, *ACS Appl. Energy Mater.* **2018**, *1*, 6657–6693.

[11] N. Serpone, A. V. Emeline, *J. Phys. Chem. Lett.* **2012**, *3*, 673–677.

[12] F. Zhang, X. Wang, H. Liu, C. Liu, Y. Wan, Y. Long, Z. Cai, *Applied Sciences* **2019**, *9*, 2489.

[13] J. Twilton, C. (Chip) Le, P. Zhang, M. H. Shaw, R. W. Evans, D. W. C. MacMillan, *Nat Rev Chem* **2017**, *1*, 1–19.

[14] D. M. Schultz, T. P. Yoon, *Science* **2014**, *343*, 1239176.

[15] C. K. Prier, D. A. Rankic, D. W. C. MacMillan, *Chem. Rev.* **2013**, *113*, 5322–5363.

[16] M. H. Shaw, J. Twilton, D. W. C. MacMillan, *J. Org. Chem.* **2016**, *81*, 6898–6926.

[17] S. G. E. Amos, M. Garreau, L. Buzzetti, J. Waser, *Beilstein J. Org. Chem.* **2020**, *16*, 1163–1187.

[18] A. Penzkofer, A. Beidoun, M. Daiber, *Journal of Luminescence* **1992**, *51*, 297–314.

[19] A. Penzkofer, A. Beidoun, *Chemical Physics* **1993**, *177*, 203–216.

[20] A. Penzkofer, A. Beidoun, S. Speiser, *Chemical Physics* **1993**, *170*, 139–148.

[21] D. P. Hari, B. König, *Chem. Commun.* **2014**, *50*, 6688–6699.

[22] D. M. Hedstrand, W. H. Kruizinga, R. M. Kellogg, *Tetrahedron Letters* **1978**, *19*, 1255–1258.

[23] X.-J. Yang, B. Chen, L.-Q. Zheng, L.-Z. Wu, C.-H. Tung, *Green Chem.* **2014**, *16*, 1082–1086.

[24] D.-T. Yang, Q.-Y. Meng, J.-J. Zhong, M. Xiang, Q. Liu, L.-Z. Wu, *European Journal of Organic Chemistry* **2013**, *2013*, 7528–7532.

[25] D. P. Hari, B. König, *Org. Lett.* **2011**, *13*, 3852–3855.

[26] C. W. Kee, K. M. Chan, M. W. Wong, C.-H. Tan, *Asian Journal of Organic Chemistry* **2014**, *3*, 536–544.

[27] Y.-Q. Zou, J.-R. Chen, X.-P. Liu, L.-Q. Lu, R. L. Davis, K. A. Jørgensen, W.-J. Xiao, *Angewandte Chemie International Edition* **2012**, *51*, 784–788.

[28] V. P. Srivastava, A. K. Yadav, L. D. S. Yadav, *Synlett* **2013**, *24*, 465–470.

[29] A. K. Yadav, V. P. Srivastava, L. D. S. Yadav, *New J. Chem.* **2013**, *37*, 4119–4124.

[30] A. K. Yadav, V. P. Srivastava, L. D. S. Yadav, *RSC Adv.* **2013**, *4*, 4181–4186.

[31] J. Zhang, L. Wang, Q. Liu, Z. Yang, Y. Huang, *Chem. Commun.* **2013**, *49*, 11662–11664.

[32] D. P. Hari, P. Schroll, B. König, *J Am Chem Soc* **2012**, *134*, 2958–2961.

[33] D. Cantillo, O. de Frutos, J. A. Rincón, C. Mateos, C. O. Kappe, *Org. Lett.* **2014**, *16*, 896–899.

[34] M. Neumann, S. Füldner, B. König, K. Zeitler, *Angewandte Chemie International Edition* **2011**, *50*, 951–954.

[35] D. A. Nicewicz, D. W. C. MacMillan, *Science* **2008**, *322*, 77–80.

[36] C. Lu, P. Zhang, S. Jiang, X. Wu, S. Song, M. Zhu, Z. Lou, Z. Li, F. Liu, Y. Liu, Y. Wang, Z. Le, *Applied Catalysis B: Environmental* **2017**, *200*, 378–385.

[37] S. Ghosh, N. A. Kouamé, L. Ramos, S. Remita, A. Dazzi, A. Deniset-Besseau, P. Beaunier, F. Goubard, P.-H. Aubert, H. Remita, *Nature Mater* **2015**, *14*, 505–511.

[38] C. Santhosh, A. Malathi, E. Daneshvar, P. Kollu, A. Bhatnagar, *Sci Rep* **2018**, *8*, 15531.

[39] B. C. Ma, S. Ghasimi, K. Landfester, K. A. I. Zhang, *J. Mater. Chem. B* **2016**, *4*, 5112–5118.

[40] C. Xing, Q. Xu, H. Tang, L. Liu, S. Wang, *J. Am. Chem. Soc.* **2009**, *131*, 13117–13124.

[41] Y. Li, X. Liu, L. Tan, Z. Cui, X. Yang, Y. Zheng, K. W. K. Yeung, P. K. Chu, S. Wu, *Advanced Functional Materials* **2018**, *28*, 1800299.
[42] H.-F. Jiao, J. Guo, Y. Cui, X. Yu, Y. Liao, Y. Ying, Z. Li, K. Yao, H. Huang, *Advanced Therapeutics* **2022**, *5*, 2100202.
[43] L. Xu, L. Cheng, C. Wang, R. Peng, Z. Liu, *Polym. Chem.* **2014**, *5*, 1573–1580.
[44] J. Geng, C. Sun, J. Liu, L.-D. Liao, Y. Yuan, N. Thakor, J. Wang, B. Liu, *Small* **2015**, *11*, 1603–1610.
[45] C. Zhu, L. Liu, Q. Yang, F. Lv, S. Wang, *Chem. Rev.* **2012**, *112*, 4687–4735.
[46] V. S. Vyas, F. Haase, L. Stegbauer, G. Savasci, F. Podjaski, C. Ochsenfeld, B. V. Lotsch, *Nat Commun* **2015**, *6*, 8508.
[47] Z.-A. Lan, Y. Fang, Y. Zhang, X. Wang, *Angewandte Chemie* **2018**, *130*, 479–483.
[48] G. Zhang, Z.-A. Lan, X. Wang, *Angewandte Chemie International Edition* **2016**, *55*, 15712–15727.
[49] G. Zhang, G. Li, T. Heil, S. Zafeiratos, F. Lai, A. Savateev, M. Antonietti, X. Wang, *Angewandte Chemie International Edition* **2019**, *58*, 3433–3437.
[50] K. Wang, Q. Li, B. Liu, B. Cheng, W. Ho, J. Yu, *Applied Catalysis B: Environmental* **2015**, *176–177*, 44–52.
[51] J. Albero, Y. Peng, H. García, *ACS Catal.* **2020**, *10*, 5734–5749.
[52] C. Dai, B. Liu, *Energy Environ. Sci.* **2020**, *13*, 24–52.
[53] Y.-L. Wong, J. M. Tobin, Z. Xu, F. Vilela, *J. Mater. Chem. A* **2016**, *4*, 18677–18686.
[54] J. Xiao, X. Liu, L. Pan, C. Shi, X. Zhang, J.-J. Zou, *ACS Catal.* **2020**, *10*, 12256–12283.
[55] X. Wang, K. Maeda, A. Thomas, K. Takanabe, G. Xin, J. M. Carlsson, K. Domen, M. Antonietti, *Nature Mater* **2009**, *8*, 76–80.
[56] *Applied Catalysis B: Environmental* **2020**, *269*, 118828.
[57] K. Zhang, D. Kopetzki, P. H. Seeberger, M. Antonietti, F. Vilela, *Angewandte Chemie* **2013**, *125*, 1472–1476.
[58] J. Byun, K. A. I. Zhang, *Mater. Horiz.* **2020**, *7*, 15–31.
[59] G. Bian, J. Yin, J. Zhu, *Small* **2021**, *17*, 2006043.
[60] G.-B. Wang, S. Li, C.-X. Yan, F.-C. Zhu, Q.-Q. Lin, K.-H. Xie, Y. Geng, Y.-B. Dong, *J. Mater. Chem. A* **2020**, *8*, 6957–6983.
[61] J. Guo, D. Jiang, *ACS Cent. Sci.* **2020**, *6*, 869–879.
[62] H. Wang, H. Wang, Z. Wang, L. Tang, G. Zeng, P. Xu, M. Chen, T. Xiong, C. Zhou, X. Li, D. Huang, Y. Zhu, Z. Wang, J. Tang, *Chem. Soc. Rev.* **2020**, *49*, 4135–4165.
[63] H. Shimakoshi, M. Nishi, A. Tanaka, K. Chikama, Y. Hisaeda, *Chem. Commun.* **2011**, *47*, 6548.
[64] N. Soliman, L. K. McKenzie, J. Karges, E. Bertrand, M. Tharaud, M. Jakubaszek, V. Guérineau, B. Goud, M. Hollenstein, G. Gasser, C. M. Thomas, *Chem. Sci.* **2020**, *11*, 2657–2663.
[65] V. Ibrahimova, S. A. Denisov, K. Vanvarenberg, P. Verwilst, V. Préat, J.-M. Guigner, N. D. McClenaghan, S. Lecommandoux, C.-A. Fustin, *Nanoscale* **2017**, *9*, 11180–11186.
[66] A. P. Schaap, A. L. Thayer, E. C. Blossey, D. C. Neckers, *J. Am. Chem. Soc.* **1975**, *97*, 3741–3745.
[67] M. Ballestri, E. Caruso, A. Guerrini, C. Ferroni, S. Banfi, M. Gariboldi, E. Monti, G. Sotgiu, G. Varchi, *Journal of Photochemistry and Photobiology B: Biology* **2018**, *186*, 169–177.
[68] N. Huber, R. Li, C. T. J. Ferguson, D. W. Gehrig, C. Ramanan, P. W. M. Blom, K. Landfester, K. A. I. Zhang, *Catal. Sci. Technol.* **2020**, *10*, 2092–2099.
[69] P. Zhi, Z.-W. Xi, D.-Y. Wang, W. Wang, X.-Z. Liang, F.-F. Tao, R.-P. Shen, Y.-M. Shen, *New J. Chem.* **2019**, *43*, 709–717.
[70] F. Peng, P. Zhi, H. Ji, H. Zhao, F.-Y. Kong, X.-Z. Liang, Y.-M. Shen, *RSC Adv.* **2017**, *7*, 19948–19953.
[71] W. Li, W. Zhang, X. Dong, L. Yan, R. Qi, W. Wang, Z. Xie, X. Jing, *J. Mater. Chem.* **2012**, *22*, 17445–17448.
[72] W.-J. Yoo, S. Kobayashi, *Green Chem.* **2014**, *16*, 2438–2442.

[73] J. M. Tobin, T. J. D. McCabe, A. W. Prentice, S. Holzer, G. O. Lloyd, M. J. Paterson, V. Arrighi, P. A. G. Cormack, F. Vilela, *ACS Catal.* **2017**, *7*, 4602–4612.
[74] C. T. J. Ferguson, N. Huber, T. Kuckhoff, K. A. I. Zhang, K. Landfester, *J. Mater. Chem. A* **2020**, *8*, 1072–1076.
[75] T. R. Weikl, B. Hemmateenejad, *Biochimica et Biophysica Acta (BBA) - Proteins and Proteomics* **2013**, *1834*, 867–873.
[76] D. J. Hosfield, C. D. Mol, in *Cancer Drug Design and Discovery* (Ed.: S. Neidle), Academic Press, New York, **2008**, pp. 229–252.
[77] A. C. Price, Y.-M. Zhang, C. O. Rock, S. W. White, *Structure* **2004**, *12*, 417–428.
[78] V. L. Arcus, E. J. Prentice, J. K. Hobbs, A. J. Mulholland, M. W. Van der Kamp, C. R. Pudney, E. J. Parker, L. A. Schipper, *Biochemistry* **2016**, *55*, 1681–1688.
[79] R. K. Chowhan, S. Hotumalani, H. Rahaman, L. R. Singh, *Sci Rep* **2021**, *11*, 9657.
[80] M. S. Ricci, C. A. Sarkar, E. M. Fallon, D. A. Lauffenburger, D. N. Brems, *Protein Science* **2003**, *12*, 1030–1038.
[81] P. Gupta, F. I. Khan, S. Roy, S. Anwar, R. Dahiya, M. F. Alajmi, A. Hussain, Md. T. Rehman, D. Lai, Md. I. Hassan, *Spectrochimica Acta Part A: Molecular and Biomolecular Spectroscopy* **2020**, *225*, 117453.
[82] L. Jiang, L. Wen, in *Biophotonics for Medical Applications* (Ed.: I. Meglinski), Woodhead Publishing, **2015**, pp. 25–51.
[83] Y. Michael Peyser, K. Ajtai, T. P. Burghardt, A. Muhlrad, *Biophysical Journal* **2001**, *81*, 1101–1114.
[84] C. T. J. Ferguson, N. Huber, K. Landfester, K. A. I. Zhang, *Angewandte Chemie International Edition* **2019**, *58*, 10567–10571.
[85] Q. Zuo, K. Feng, J. Zhong, Y. Mai, Y. Zhou, *CCS Chemistry* **2021**, DOI 10.31635/ccschem.020.202000486.
[86] H. Koizumi, Y. Shiraishi, S. Tojo, M. Fujitsuka, T. Majima, T. Hirai, *J. Am. Chem. Soc.* **2006**, *128*, 8751–8753.
[87] M. He, X. Yu, Y. Wang, F. Li, M. Bao, *J. Org. Chem.* **2021**, *86*, 5016–5025.
[88] H. Shigemitsu, Y. Tani, T. Tamemoto, T. Mori, X. Li, Y. Osakada, M. Fujitsuka, T. Kida, *Chem. Sci.* **2020**, *11*, 11843–11848.
[89] R. A. Olson, J. S. Levi, G. M. Scheutz, J. J. Lessard, C. A. Figg, M. N. Kamat, K. B. Basso, B. S. Sumerlin, *Macromolecules* **2021**, *54*, 4880–4888.
[90] Z. Gao, J. Liang, X. Tao, Y. Cui, T. Satoh, T. Kakuchi, Q. Duan, *Macromol. Res.* **2012**, *20*, 508–514.
[91] N. Qiu, Y. Li, S. Han, G. Cui, T. Satoh, T. Kakuchi, Q. Duan, *Journal of Photochemistry and Photobiology A: Chemistry* **2014**, *283*, 38–44.
[92] Y. Ruan, B. Gao, S. Lv, Q. Duan, *New J. Chem.* **2020**, *44*, 2781–2787.
[93] M. Chen, S. Deng, Y. Gu, J. Lin, M. J. MacLeod, J. A. Johnson, *J. Am. Chem. Soc.* **2017**, *139*, 2257–2266.
[94] J. Bianga, K. U. Künnemann, T. Gaide, A. J. Vorholt, T. Seidensticker, J. M. Dreimann, D. Vogt, *Chem. Eur. J.* **2019**, *25*, 11586–11608.
[95] N. Priyadarshani, Y. Liang, J. Suriboot, H. S. Bazzi, D. E. Bergbreiter, *ACS Macro Lett.* **2013**, *2*, 571–574.
[96] D. Rackl, P. Kreitmeier, O. Reiser, *Green Chem.* **2015**, *18*, 214–219.
[97] X. Zhang, Y. Li, X. Hao, K. Jin, R. Zhang, C. Duan, *Tetrahedron* **2018**, *74*, 7358–7363.
[98] G. Kocak, C. Tuncer, V. Bütün, *Polym. Chem.* **2016**, *8*, 144–176.
[99] F. Ofridam, M. Tarhini, N. Lebaz, E. Gagnière, D. Mangin, A. Elaïssari, *Polymers for Advanced Technologies* **2021**, 1455–1484.
[100] S. Dai, P. Ravi, K. C. Tam, *Soft Matter* **2008**, *4*, 435–449.
[101] A. E. Felber, M.-H. Dufresne, J.-C. Leroux, *Advanced Drug Delivery Reviews* **2012**, *64*, 979–992.

[102] J. Niskanen, C. Wu, M. Ostrowski, G. G. Fuller, S. Hietala, H. Tenhu, *Macromolecules* **2013**, *46*, 2331–2340.
[103] D. Selianitis, S. Pispas, *Journal of Polymer Science* **2020**, *58*, 1867–1880.
[104] D. Li, Q. He, Y. Yang, H. Möhwald, J. Li, *Macromolecules* **2008**, *41*, 7254–7256.
[105] Y. Bai, Z. Hu, J.-X. Jiang, F. Huang, *Chemistry – An Asian Journal* **2020**, *15*, 1780–1790.
[106] C. Dai, M. Panahandeh-Fard, X. Gong, C. Xue, B. Liu, *Solar RRL* **2019**, *3*, 1800255.
[107] Z. Hu, X. Zhang, Q. Yin, X. Liu, X. Jiang, Z. Chen, X. Yang, F. Huang, Y. Cao, *Nano Energy* **2019**, *60*, 775–783.
[108] H. Lu, R. Hu, H. Bai, H. Chen, F. Lv, L. Liu, S. Wang, H. Tian, *ACS Appl. Mater. Interfaces* **2017**, *9*, 10355–10359.
[109] Y. Wu, X. Zhang, Y. Xing, Z. Hu, H. Tang, W. Luo, F. Huang, Y. Cao, *ACS Materials Lett.* **2019**, *1*, 620–627.
[110] X. Yang, Z. Hu, Q. Yin, C. Shu, X.-F. Jiang, J. Zhang, X. Wang, J.-X. Jiang, F. Huang, Y. Cao, *Advanced Functional Materials* **2019**, *29*, 1808156.
[111] S. Ghasimi, K. Landfester, K. A. I. Zhang, *ChemCatChem* **2016**, *8*, 694–698.
[112] J. Byun, W. Huang, D. Wang, R. Li, K. A. I. Zhang, *Angew. Chem. Int. Ed.* **2018**, *57*, 2967–2971.
[113] J. Wang, L. Liu, L. Ying, L. Chen, *European Polymer Journal* **2017**, *93*, 87–96.
[114] W. Lü, C. Sun, Q. Lu, N. Li, D. Wu, Y. Yao, W. Chen, *Sci. China Chem.* **2012**, *55*, 1108–1114.
[115] Y. Huang, X. Li, J. Le Li, B. Zhang, T. Cai, *Macromolecules* **2018**, *51*, 7974–7982.
[116] S. Zhang, J. Li, M. Zeng, G. Zhao, J. Xu, W. Hu, X. Wang, *ACS Appl. Mater. Interfaces* **2013**, *5*, 12735–12743.
[117] B. Bayarkhuu, C. Yang, W. Wang, K. A. I. Zhang, J. Byun, *ACS Materials Lett.* **2020**, *2*, 557–562.
[118] S. Chi, C. Ji, S. Sun, H. Jiang, R. Qu, C. Sun, *Ind. Eng. Chem. Res.* **2016**, *55*, 12060–12067.
[119] H. Wang, Y. Xu, L. Jing, S. Huang, Y. Zhao, M. He, H. Xu, H. Li, *Journal of Alloys and Compounds* **2017**, *710*, 510–518.
[120] R. Djellabi, J. Ali, B. Yang, M. R. Haider, P. Su, C. L. Bianchi, X. Zhao, *Separation and Purification Technology* **2020**, *250*, 116954.
[121] J. C. S. Terra, A. Desgranges, C. Monnereau, E. H. Sanchez, J. A. De Toro, Z. Amara, A. Moores, *ACS Appl. Mater. Interfaces* **2020**, *12*, 24895–24904.
[122] M. T. Cook, P. Haddow, S. B. Kirton, W. J. McAuley, *Advanced Functional Materials* **2021**, *31*, 2008123.
[123] R. Marcilla, J. Alberto Blazquez, J. Rodriguez, J. A. Pomposo, D. Mecerreyes, *Journal of Polymer Science Part A: Polymer Chemistry* **2004**, *42*, 208–212.
[124] P. Agostinis, K. Berg, K. A. Cengel, T. H. Foster, A. W. Girotti, S. O. Gollnick, S. M. Hahn, M. R. Hamblin, A. Juzeniene, D. Kessel, M. Korbelik, J. Moan, P. Mroz, D. Nowis, J. Piette, B. C. Wilson, J. Golab, *CA: A Cancer Journal for Clinicians* **2011**, *61*, 250–281.
[125] M. K. Singh, A. Singh, in *Characterization of Polymers and Fibres* (Eds.: M.K. Singh, A. Singh), Woodhead Publishing, **2022**, pp. 321–339.
[126] H. Friebolin, J. K. Becconsall, *Basic One- and Two-Dimensional NMR Spectroscopy*, Wiley-VCH-Verl, Weinheim, **2008**.
[127] D. Baumstark, P. Pagel, J. Eiglsperger, V. Pfahlert, F. Huber, *LaboratoriumsMedizin* **2014**, *38*, 137–149.
[128] J. Keeler, *Understanding NMR Spectroscopy*, John Wiley & Sons, **2010**.
[129] M. H. Levitt, *Spin Dynamics: Basics of Nuclear Magnetic Resonance*, John Wiley & Sons, **2013**.
[130] N. Elgrishi, K. J. Rountree, B. D. McCarthy, E. S. Rountree, T. T. Eisenhart, J. L. Dempsey, *J. Chem. Educ.* **2018**, *95*, 197–206.
[131] L. Reimer, *Transmission Electron Microscopy: Physics of Image Formation and Microanalysis*, Springer, **2013**.
[132] D. B. Williams, C. B. Carter, in *Transmission Electron Microscopy: A Textbook for Materials Science* (Eds.: D.B. Williams, C.B. Carter), Springer US, Boston, MA, **1996**, pp. 3–17.
[133] Z. Wang, W. Ma, C. Chen, H. Ji, J. Zhao, *Chemical Engineering Journal* **2011**, *170*, 353–362.

[134] W. Deng, H. Zhao, F. Pan, X. Feng, B. Jung, A. Abdel-Wahab, B. Batchelor, Y. Li, *Environ. Sci. Technol.* **2017**, *51*, 13372–13379.
[135] O. Fawzi Suleiman Khasawneh, P. Palaniandy, *Environmental Technology & Innovation* **2021**, *21*, 101230.
[136] S. Kwiatkowski, B. Knap, D. Przystupski, J. Saczko, E. Kędzierska, K. Knap-Czop, J. Kotlińska, O. Michel, K. Kotowski, J. Kulbacka, *Biomedicine & Pharmacotherapy* **2018**, *106*, 1098–1107.
[137] J. H. Correia, J. A. Rodrigues, S. Pimenta, T. Dong, Z. Yang, *Pharmaceutics* **2021**, *13*, 1332.
[138] J. C. S. Simões, S. Sarpaki, P. Papadimitroulas, B. Therrien, G. Loudos, *J. Med. Chem.* **2020**, *63*, 14119–14150.
[139] S. Cao, L. Piao, X. Chen, *Trends in Chemistry* **2020**, *2*, 57–70.
[140] W. Zhao, Z. Chen, X. Yang, X. Qian, C. Liu, D. Zhou, T. Sun, M. Zhang, G. Wei, P. D. Dissanayake, Y. S. Ok, *Renewable and Sustainable Energy Reviews* **2020**, *132*, 110040.
[141] J. Kosco, M. Bidwell, H. Cha, T. Martin, C. T. Howells, M. Sachs, D. H. Anjum, S. Gonzalez Lopez, L. Zou, A. Wadsworth, W. Zhang, L. Zhang, J. Tellam, R. Sougrat, F. Laquai, D. M. DeLongchamp, J. R. Durrant, I. McCulloch, *Nat. Mater.* **2020**, *19*, 559–565.
[142] S. Liu, W. Pan, S. Wu, X. Bu, S. Xin, J. Yu, H. Xu, X. Yang, *Green Chemistry* **2019**, *21*, 2905–2910.
[143] H.-P. Liang, Q. Chen, B.-H. Han, *ACS Catal.* **2018**, *8*, 5313–5322.
[144] G. H. Lovett, S. Chen, X.-S. Xue, K. N. Houk, D. W. C. MacMillan, *J. Am. Chem. Soc.* **2019**, *141*, 20031–20036.
[145] L. Tian, N. A. Till, B. Kudisch, D. W. C. MacMillan, G. D. Scholes, *J. Am. Chem. Soc.* **2020**, *142*, 4555–4559.
[146] J. Kim, B. X. Li, R. Y.-C. Huang, J. X. Qiao, W. R. Ewing, D. W. C. MacMillan, *J. Am. Chem. Soc.* **2020**, *142*, 21260–21266.
[147] A. Mills, C. O'Rourke, *Catalysis Today* **2014**, *230*, 256–264.
[148] C. Ayed, L. C. da Silva, D. Wang, K. A. I. Zhang, *J. Mater. Chem. A* **2018**, *6*, 22145–22151.
[149] D. A. Nagib, D. W. C. MacMillan, *Nature* **2011**, *480*, 224–228.
[150] R. Pawlowski, F. Stanek, M. Stodulski, *Molecules* **2019**, *24*, 1533.
[151] Z. Li, W. Zhang, Q. Zhao, H. Gu, Y. Li, G. Zhang, F. Zhang, X. Fan, *ACS Sustainable Chem. Eng.* **2015**, *3*, 468–474.
[152] N. A. Romero, D. A. Nicewicz, *Chem. Rev.* **2016**, *116*, 10075–10166.
[153] L. Wang, W. Huang, R. Li, D. Gehrig, P. W. M. Blom, K. Landfester, K. A. I. Zhang, *Angew. Chem. Int. Ed.* **2016**, *55*, 9783–9787.
[154] R. Radjagobalou, J.-F. Blanco, L. Petrizza, M. Le Bechec, O. Dechy-Cabaret, S. Lacombe, M. Save, K. Loubiere, *ACS Sustainable Chem. Eng.* **2020**, *8*, 18568–18576.
[155] J. J. Lessard, G. M. Scheutz, A. B. Korpusik, R. A. Olson, C. A. Figg, B. S. Sumerlin, *Polym. Chem.* **2021**, *12*, 2205–2209.
[156] M. Bu, C. Cai, F. Gallou, B. H. Lipshutz, *Green Chem.* **2018**, *20*, 1233–1237.
[157] R. Wang, X. Qi, P. Schmiege, E. Coutavas, X. Li, *Science Advances* **2020**, *6*, eaaz1466.
[158] C. Narayanan, D. N. Bernard, K. Bafna, D. Gagné, P. K. Agarwal, N. Doucet, *Frontiers in Molecular Biosciences* **2018**, *5*.
[159] B. Moree, K. Connell, R. B. Mortensen, C. T. Liu, S. J. Benkovic, J. Salafsky, *Biophys J* **2015**, *109*, 806–815.
[160] J.-H. Ha, S. N. Loh, *Chemistry* **2012**, *18*, 7984–7999.
[161] S. Biswas, E. Mani, A. Mondal, A. Tiwari, S. Roy, *Soft Matter* **2016**, *12*, 1989–1997.
[162] J. D. Willott, W. M. Nielen, W. M. de Vos, *ACS Appl. Polym. Mater.* **2020**, *2*, 659–667.
[163] F. D'Agosto, J. Rieger, M. Lansalot, *Angew. Chem. Int. Ed.* **2020**, *59*, 8368–8392.
[164] T. R. Guimarães, Y. L. Bong, S. W. Thompson, G. Moad, S. Perrier, P. B. Zetterlund, *Polym. Chem.* **2021**, *12*, 122–133.
[165] T. Kuckhoff, K. Landfester, K. A. I. Zhang, C. T. J. Ferguson, *Chem. Mater.* **2021**, *33*, 9131–9138.
[166] S. Kozuch, J. M. L. Martin, *ACS Catal.* **2012**, *2*, 2787–2794.
[167] P. C. Bandara, J. Peña-Bahamonde, D. F. Rodrigues, *Sci Rep* **2020**, *10*, 9237.

[168] Y. Chen, D. An, S. Sun, J. Gao, L. Qian, *Materials* **2018**, *11*, 269.
[169] J. R. Stutzman, C. A. Luongo, S. A. McLuckey, *Journal of Mass Spectrometry* **2012**, *47*, 669–675.
[170] P. Kollman, in *New Comprehensive Biochemistry* (Ed.: M.I. Page), Elsevier, **1984**, pp. 55–71.
[171] P. Kumar, S. Banerjee, A. Radha, T. Firdoos, S. Chandra Sahoo, S. K. Pandey, *New Journal of Chemistry* **2021**, *45*, 2249–2263.
[172] S. Caron, R. W. Dugger, S. G. Ruggeri, J. A. Ragan, D. H. B. Ripin, *Chem. Rev.* **2006**, *106*, 2943–2989.
[173] S. Otsuki, T. Nonaka, N. Takashima, W. Qian, A. Ishihara, T. Imai, T. Kabe, *Energy Fuels* **2000**, *14*, 1232–1239.
[174] Y. Huang, Z. Xin, W. Yao, Q. Hu, Z. Li, L. Xiao, B. Yang, J. Zhang, *Chem. Commun.* **2018**, *54*, 13587–13590.
[175] C. Herrero, A. Quaranta, R. Ricoux, A. Trehoux, A. Mahammed, Z. Gross, F. Banse, J.-P. Mahy, *Dalton Trans.* **2015**, *45*, 706–710.
[176] M. M. Heravi, Z. Amiri, K. Kafshdarzadeh, V. Zadsirjan, *RSC Advances* **2021**, *11*, 33540–33612.
[177] T. C. Barden, in *Heterocyclic Scaffolds II: Reactions and Applications of Indoles* (Ed.: G.W. Gribble), Springer, Berlin, Heidelberg, **2010**, pp. 31–46.
[178] A. Dorababu, *RSC Med. Chem.* **2020**, *11*, 1335–1353.
[179] F. Naaz, K. Neha, M. R. Haider, S. Shafi, *Future Medicinal Chemistry* **2021**, *13*, 1795–1828.
[180] Y. Hong, Y.-Y. Zhu, Q. He, S.-X. Gu, *Bioorganic & Medicinal Chemistry* **2022**, *55*, 116597.
[181] S. Tang, Z. Zhou, Z. Jiang, W. Zhu, D. Qiao, *Molecules* **2022**, *27*, 1587.
[182] Z.-Y. Yu, J.-N. Zhao, F. Yang, X.-F. Tang, Y.-F. Wu, C.-F. Ma, B. Song, L. Yun, Q.-W. Meng, *RSC Adv.* **2020**, *10*, 4825–4831.
[183] S. Yadav, M. Srivastava, P. Rai, B. P. Tripathi, A. Mishra, J. Singh, J. Singh, *New J. Chem.* **2016**, *40*, 9694–9701.
[184] R. P. Herrera, V. Sgarzani, L. Bernardi, A. Ricci, *Angewandte Chemie International Edition* **2005**, *44*, 6576–6579.
[185] Q. Liu, Y.-N. Li, H.-H. Zhang, B. Chen, C.-H. Tung, L.-Z. Wu, *Chemistry – A European Journal* **2012**, *18*, 620–627.
[186] D. P. Hari, T. Hering, B. König, *Org. Lett.* **2012**, *14*, 5334–5337.
[187] T. Xiao, X. Dong, Y. Tang, L. Zhou, *Advanced Synthesis & Catalysis* **2012**, *354*, 3195–3199.
[188] D. P. Hari, P. Schroll, B. König, *J. Am. Chem. Soc.* **2012**, *134*, 2958–2961.
[189] J. Heuer, T. Kuckhoff, R. Li, K. Landfester, C. T. J. Ferguson, *ACS Appl. Mater. Interfaces* **2023**, *15*, 2891–2900.
[190] R. Li, J. Heuer, T. Kuckhoff, K. Landfester, C. T. J. Ferguson, *Angewandte Chemie International Edition* **2023**, *62*, e202217652.
[191] R. Li, K. Landfester, C. T. J. Ferguson, *Angewandte Chemie International Edition* **2022**, *61*, e202211132.
[192] L. Balan, J.-P. Malval, D.-J. Lougnot, **2010**.
[193] A. Ding, Y. Zhang, Y. Chen, R. Rios, J. Hu, H. Guo, *Tetrahedron Letters* **2019**, *60*, 660–663.
[194] T. Toyao, N. Ueno, K. Miyahara, Y. Matsui, T.-H. Kim, Y. Horiuchi, H. Ikeda, M. Matsuoka, *Chemical Communications* **2015**, *51*, 16103–16106.
[195] J. Luo, X. Zhang, J. Zhang, *ACS Catal.* **2015**, *5*, 2250–2254.
[196] M. Liu, Y. Luo, J. Yan, X. Xiong, X. Xing, J. S. Kim, T. Zou, *J. Am. Chem. Soc.* **2023**, *145*, 10082–10091.
[197] J. S. Basuki, A. Jacquemin, L. Esser, Y. Li, C. Boyer, T. P. Davis, *Polym. Chem.* **2014**, *5*, 2611–2620.
[198] Z. Zhou, J. Song, L. Nie, X. Chen, *Chem. Soc. Rev.* **2016**, *45*, 6597–6626.
[199] S. Wang, G. Yu, Z. Wang, O. Jacobson, L.-S. Lin, W. Yang, H. Deng, Z. He, Y. Liu, Z.-Y. Chen, X. Chen, *Angewandte Chemie International Edition* **2019**, *58*, 14758–14763.
[200] X. Zhang, S. Wang, G. Cheng, P. Yu, J. Chang, X. Chen, *Matter* **2021**, *4*, 26–53.

[201] J. F. Lovell, T. W. B. Liu, J. Chen, G. Zheng, *Chem. Rev.* **2010**, *110*, 2839–2857.
[202] L. Cheng, C. Wang, L. Feng, K. Yang, Z. Liu, *Chem. Rev.* **2014**, *114*, 10869–10939.
[203] H. O. Alsaab, M. S. Alghamdi, A. S. Alotaibi, R. Alzhrani, F. Alwuthaynani, Y. S. Althobaiti, A. H. Almalki, S. Sau, A. K. Iyer, *Cancers* **2020**, *12*, 2793.
[204] D. Bechet, P. Couleaud, C. Frochot, M.-L. Viriot, F. Guillemin, M. Barberi-Heyob, *Trends Biotechnol* **2008**, *26*, 612–621.
[205] H. Sun, Z. Zhong, *ACS Macro Lett.* **2020**, *9*, 1292–1302.
[206] R. Wei, S. Liu, S. Zhang, L. Min, S. Zhu, *Anal Cell Pathol (Amst)* **2020**, *2020*, 6283796.
[207] R. Tong, H. H. Chiang, D. S. Kohane, *Proceedings of the National Academy of Sciences* **2013**, *110*, 19048–19053.
[208] R. Tong, H. D. Hemmati, R. Langer, D. S. Kohane, *J. Am. Chem. Soc.* **2012**, *134*, 8848–8855.
[209] S. Ruan, X. Cao, X. Cun, G. Hu, Y. Zhou, Y. Zhang, L. Lu, Q. He, H. Gao, *Biomaterials* **2015**, *60*, 100–110.
[210] Q. Zhou, *Nature Nanotechnology* **2019**, *14*, 16.
[211] Y. Dong, Y. Tu, K. Wang, C. Xu, Y. Yuan, J. Wang, *Angewandte Chemie International Edition* **2020**, *59*, 7168–7172.
[212] J. Li, Y. Li, Y. Wang, W. Ke, W. Chen, W. Wang, Z. Ge, *Nano Lett.* **2017**, *17*, 6983–6990.
[213] H.-J. Li, J.-Z. Du, J. Liu, X.-J. Du, S. Shen, Y.-H. Zhu, X. Wang, X. Ye, S. Nie, J. Wang, *ACS Nano* **2016**, *10*, 6753–6761.
[214] Z. Deng, Y. Qian, Y. Yu, G. Liu, J. Hu, G. Zhang, S. Liu, *J. Am. Chem. Soc.* **2016**, *138*, 10452–10466.
[215] S. Zhou, X. Hu, R. Xia, S. Liu, Q. Pei, G. Chen, Z. Xie, X. Jing, *Angewandte Chemie International Edition* **2020**, *59*, 23198–23205.
[216] P. Kulkarni, M. K. Haldar, P. Katti, C. Dawes, S. You, Y. Choi, S. Mallik, *Bioconjugate Chem.* **2016**, *27*, 1830–1838.
[217] P. Wang, Q. Gong, J. Hu, X. Li, X. Zhang, *J. Med. Chem.* **2021**, *64*, 298–325.
[218] M. Bio, G. Nkepang, Y. You, *Chem. Commun.* **2012**, *48*, 6517–6519.
[219] Y. Yuan, C.-J. Zhang, B. Liu, *Angewandte Chemie International Edition* **2015**, *54*, 11419–11423.
[220] Z. Cao, Y. Ma, C. Sun, Z. Lu, Z. Yao, J. Wang, D. Li, Y. Yuan, X. Yang, *Chem. Mater.* **2018**, *30*, 517–525.
[221] S. Z. F. Phua, C. Xue, W. Q. Lim, G. Yang, H. Chen, Y. Zhang, C. F. Wijaya, Z. Luo, Y. Zhao, *Chem. Mater.* **2019**, *31*, 3349–3358.
[222] Y. Kuang, K. Balakrishnan, V. Gandhi, X. Peng, *J. Am. Chem. Soc.* **2011**, *133*, 19278–19281.
[223] W. Chen, Y. Han, X. Peng, *Chemistry – A European Journal* **2014**, *20*, 7410–7418.
[224] W. Chen, K. Balakrishnan, Y. Kuang, Y. Han, M. Fu, V. Gandhi, X. Peng, *J. Med. Chem.* **2014**, *57*, 4498–4510.
[225] W. Zhang, X. Hu, Q. Shen, D. Xing, *Nat Commun* **2019**, *10*, 1704.
[226] S. Bai, X. Ma, X. Shi, J. Shao, T. Zhang, Y. Wang, Y. Cheng, P. Xue, Y. Kang, Z. Xu, *ACS Appl. Mater. Interfaces* **2019**, *11*, 36130–36140.
[227] Y. Zhang, C. Ye, S. Li, A. Ding, G. Gu, H. Guo, *RSC Advances* **2017**, *7*, 13240–13243.
[228] K. Zhou, Y. Wang, X. Huang, K. Luby-Phelps, B. D. Sumer, J. Gao, *Angewandte Chemie International Edition* **2011**, *50*, 6109–6114.
[229] B. A. Webb, M. Chimenti, M. P. Jacobson, D. L. Barber, *Nat Rev Cancer* **2011**, *11*, 671–677.
[230] C. Wu, N. Corrigan, C.-H. Lim, K. Jung, J. Zhu, G. Miyake, J. Xu, C. Boyer, *Macromolecules* **2019**, *52*, 236–248.
[231] B. Fan, W. Peng, Y. Zhang, P. Liu, J. Shen, *Biomater. Sci.* **2023**, *11*, 4930–4937.
[232] D. B. Longley, D. P. Harkin, P. G. Johnston, *Nat Rev Cancer* **2003**, *3*, 330–338.
[233] G. D. Heggie, J. P. Sommadossi, D. S. Cross, W. J. Huster, R. B. Diasio, *Cancer Res* **1987**, *47*, 2203–2206.
[234] M. Scartozzi, E. Maccaroni, R. Giampieri, M. Pistelli, A. Bittoni, M. Del Prete, R. Berardi, S. Cascinu, *Pharmacogenomics* **2011**, *12*, 251–265.

[235] J. S. Macdonald, *Oncology (Williston Park)* **1999**, *13*, 33–34.
[236] J. Shelton, X. Lu, J. A. Hollenbaugh, J. H. Cho, F. Amblard, R. F. Schinazi, *Chem. Rev.* **2016**, *116*, 14379–14455.
[237] Y. Ai, O. N. Obianom, M. Kuser, Y. Li, Y. Shu, F. Xue, *ACS Med. Chem. Lett.* **2019**, *10*, 127–131.
[238] Y. Li, Q. N. Bui, L. T. M. Duy, H. Y. Yang, D. S. Lee, *Biomacromolecules* **2018**, *19*, 2062–2070.
[239] C. Ash, M. Dubec, K. Donne, T. Bashford, *Lasers Med Sci* **2017**, *32*, 1909–1918.
[240] R. W. Davis IV, E. Snyder, J. Miller, S. Carter, C. Houser, A. Klampatsa, S. M. Albelda, K. A. Cengel, T. M. Busch, *Photochemistry and Photobiology* **2019**, *95*, 430–438.
[241] T.-C. Chen, L. Huang, C.-C. Liu, P.-J. Chao, F.-H. Lin, *Process Biochemistry* **2012**, *47*, 1903–1908.
[242] L. Jiang, H. Bai, L. Liu, F. Lv, X. Ren, S. Wang, *Angew Chem Int Ed* **2019**, *58*, 10660–10665.
[243] E. Zhang, Y. Huang, S. Wang, *Drug Deliv. and Transl. Res.* **2021**, *11*, 1451–1455.
[244] H. Yuan, H. Chong, B. Wang, C. Zhu, L. Liu, Q. Yang, F. Lv, S. Wang, *J. Am. Chem. Soc.* **2012**, *134*, 13184–13187.
[245] A. L. Rose, T. D. Waite, *Anal. Chem.* **2001**, *73*, 5909–5920.

A5. List of Publications

(1) **R. Li**, J. Heuer, T. Kuckhoff, K. Landfester, C. Ferguson, Angew. Chem.Int. Ed. 2023, 62, e202217652. https://doi.org/10.1002/anie.202217652

(2) **R. Li**, K. Landfester, C. Ferguson, Angew. Chem.Int. Ed. 2022, 61, e202211132. https://doi.org/10.1002/anie.202211132

(3) J. Heuer, T. Kuckhoff, **R. Li**, K. Landfester, C. Ferguson, ACS Appl. Mater. Interfaces 2023, 15, 2, 2891–2900. https://doi.org/10.1021/acsami.2c17607

(4) T. Kuckhoff, J. Heuer, **R. Li**, K. A. I. Zhang, K. Landfester, C. Ferguson, RSC Appl. Polym., 2024. https://doi.org/10.1039/D3LP00162H

(5) **R. Li**, X. Q. Zhang, V. Mailänder, K. Landfester, C. Ferguson, Therapeutic Application of Responsive Organic Photocatalytic Polymers Enabling in situ Drug Activation (submitted).

(6) **R. Li**, K. Landfester, C. Ferguson, Magnetically Recyclable Polymer Photocatalytic Materials for Sustainable Photocatalysis (submitted).